Artificial Neural Network-Based All-Sky Power Estimation and Fault Detection in Photovoltaic Modules

Kian Jazayeri

Submitted to the
Institute of Graduate Studies and Research
in partial fulfillment of the requirements for the degree of

Doctor of Philosophy
in
Electrical and Electronic Engineering

Eastern Mediterranean University
January 2018
Gazimağusa, North Cyprus

Approval of the Institute of Graduate Studies and Research

Assoc. Prof. Dr. Ali Hakan Ulusoy
Acting Director

I certify that this thesis satisfies the requirements as a thesis for the degree of Doctor of Philosophy in Electrical and Electronic Engineering.

Prof. Dr. Hasan Demirel
Chair, Department of Electrical and Electronic Engineering

We certify that we have read this thesis and that in our opinion it is fully adequate in scope and quality as a thesis for the degree of Doctor of Philosophy in Electrical and Electronic Engineering.

Prof. Dr. Şener Uysal
Supervisor

Examining Committee

1. Prof. Dr. Şule Erten Ela _____
2. Prof. Dr. Osman Kükrer _____
3. Prof. Dr. Adnan Sözen _____
4. Prof. Dr. Serhat Şeker _____
5. Prof. Dr. Şener Uysal _____

ABSTRACT

The objective of this study is to develop an Artificial Neural Network (ANN) based system for output power estimation and fault detection in PV modules in a minute by minute basis. Such system, after being trained on sample data paths in a supervised manner, is ought to be capable of real-time output power estimation and fault detection in PV modules. The process of data acquisition is carried out during a three-month interval, from Nov. 1st, 2015 to Jan. 31st, 2016 using sensitive measurement equipment and precise mathematical formulas. Resultantly, around 30,000 healthy and faulty per-minute accurate data paths containing the solar altitude and azimuth angles, incident angle, irradiance level (W/m^2), PV module output power (W/min) and PV module surface temperature (°C) are acquired and normalized in the range 0 to 1 in order to be fed as input to different ANNs. In order to simulate the faulty operation conditions, the PV module is coated with glasses of different shades of gray color.

Two different ANNs of Multi-Layer Perceptron type, namely being the Estimation Artificial Neural Network (EANN) and Detection Artificial Neural Network (DANN) are developed for PV power estimation and fault detection purposes, respectively. Both ANNs are of three-layer fully-connected feed-forward architecture, with input, hidden and output layers. Log-sigmoid activation function is deployed in both ANNs' hidden layers, while softmax transfer function is utilized in the DANN output layer to solve binary classification problems which lead to fault detections in a PV module. The training process of the ANNs is carried out based on Bayesian Regularization (BR) back-propagation algorithm, using the mentioned collected data paths in a supervised way by providing the ANNs with training output targets in each training

epoch. After the training goal for both ANNs is satisfied, the ANNs go through a rigorous testing process with new and unseen input data and no more output targets in order to measure their generalization capabilities. At the end of the testing process, the ANNs are ready to be implemented in real life situations.

The ANNs' implementation is carried out during a 15-day interval from Feb. 1st, to Feb. 15th, 2016. The mentioned interval contains highly meteorologically fluctuating wintry days, providing context for a rigorous performance examinations of the mentioned ANNs. During the implementation period, six different fault simulations namely being the lightgray, dimgray and darkslategray shadings as well as the light, moderate and heavy dirt and dust coverings are homogeneously applied to the surface of the PV module. The first two of the mentioned fault simulations had been used during the ANNs training data acquisition process, but the rest four faults are only demonstrated in the implementation period in order to measure the generalization capabilities of the ANNs for unseen situations. Expectedly, the lightgray shading – light dirt and dust covering, the dimgray shading – moderate dirt and dust covering and the darkslategray shading – heavy dirt and dust covering fault simulation pairs led to almost similar amounts of drops in the PV module output power, whilst the homogeneous fault application technique made the power drops independent of the internal architecture of the PV module.

The 15-day per-minute implementation period resulted in 6222 PV module power estimation and fault detection acts carried out by the EANN and DANN. The overall EANN average MAPE between the estimated and the measured PV module output power values is 4.44%, and the DANN sensitivity, specificity, and overall accuracy rates are 97.6%, 99.7%, and 98.6%, respectively. The results are promising and the

developed and verified PV module-level output power estimation and fault detection system is expected to be deployed in broader PV fleets after taking the developmental requirements into consideration, thus increasing the efficiency and decreasing the support and maintenance costs of the PV systems in long term.

Keywords: Renewable Energy, Solar Energy, Photovoltaic, Artificial Intelligence, Artificial Neural Network, Output Estimation, Fault Detection

ÖZ

Bu tez çalışmasında, güneş panellerinde dakikadaki çıkış gücünün tahmini ve hata tespiti için Yapay Sinir Ağı (YSA)'na dayalı bir sistemin geliştirilmesi amaçlanmıştır. Böyle bir sistem, denetimli bir şekilde örnek veriler kullanılarak eğitildikten sonra, güneş panellerinde gerçek zamanlı çıkış gücü tahmini ve hata tespiti yapma kabiliyetine sahip olmalıdır. Tez çalışması için toplanan veriler 01/Ekim/2015 - 31/Ocak/2016 tarihleri arasındaki üç aylık bir zaman dilimi içerisinde hassas olarak ölçülmüş ve matematiksel bağıntılar kullanılarak tespit edilmiştir. Sonuç olarak, YSA'nı eğitmek üzere girdi olarak güneş yükseklik ve azimut açıları, güneş ışınlarının geliş açısı, güneş radyasyon düzeyi (W/m^2), güneş paneli çıkış gücü (W/dakika) ve güneş paneli yüzey sıcaklık (°C) verilerini içeren yaklaşık olarak 30,000 veri elde edilip toplanan veriler 0 – 1 değer aralığında normalleştirilmiştir. Hatalı çalışma koşullarının simülasyonu için güneş panelinin yüzeyi, gri renginin çeşitli tonlarına sahip camlar ile kaplanmıştır.

Güneş paneli çıkış gücü tahmini ve hata tespiti amaçları için sırasıyla Tahmin Yapay Sinir Ağı (TYSA) ve Saptama Yapay Sinir Ağı (SYSA) olmak üzere Çok Katmanlı algılayıcı tipi iki farklı YSA geliştirilmiştir. Her iki YSA çok katmanlı ileri beslemeli mimariye ve girdi, gizli ve çıktı katmanı olmak üzere üç katmana sahiptir. Her iki YSA'nın gizli katmanlarında log-sigmoid aktivasyon fonksiyonundan yararlanılmış olup aynı zamanda bir güneş panelinde hata tespiti ile sonuçlanan ikili sınıflandırma problemlerinin çözülmesi için SYSA'nın çıktı katmanında softmax transfer fonksiyonu kullanılmıştır. YSA'nın eğitme süreci, Bayes Düzenleme (BD) geri yayılımlı algoritma esas alınmak suretiyle daha önce bahsedilen toplanan veri yolları

kullanılarak her bir eğitim devresinde YSA'ya eğitimin çıktı hedefleri sunularak denetimli bir şekilde gerçekleştirilmektedir. Her iki YSA için eğitim amaçlarına ulaşıldığında, genelleme kabiliyetleri ölçülmek üzere YSA'lar yeni ve daha önce kullanılmamış olan girdi verileri kullanılarak herhangi bir çıktı hedefi sunulmadan çok sıkı bir test sürecine tabi tutulmaktadır. Test sürecinin sonunda YSA'lar gerçek koşullar altında uygulanmaya hazır hale gelmiş bulunmaktadır.

YSA'nın uygulama aşaması 01/Şubat/2016 – 15/Şubat/2016 tarihleri arasında 15 günlük bir zaman aralığı içerisinde gerçekleştirilmiştir. Bahsi geçen zaman aralığı meteorolojik açıdan yüksek oranda değişkenlik gösteren kış günlerini kapsamakta olup belirtilen YSA için karmaşık bir performans incelemesi imkânını sağlamaktadır. Uygulama zaman aralığı içerisinde açık gri, koyu gri ve koyu barut grisi gölgelemeler ile birlikte hafif, orta ve yoğun derecelerdeki toz ve toprak kaplamaları olmak üzere altı farklı hata simülasyonu güneş panelinin yüzeyi üzerinde homojen bir şekilde uygulanmıştır. Bahsi geçen hata simülasyonlarından ilk ikisi YSA'nın eğitim için veri toplama süreci içerisinde kullanılmış olup geriye kalan diğer dört hata çeşidi ise YSA'nın görülmemiş koşullar altındaki genelleme kabiliyetinin ölçülmesi amacıyla yalnızca uygulama dönemi içerisinde kullanılmıştır. Homojen hata uygulama tekniği, çıkış gücündeki azalmaların güneş panelinin iç mimarisinden bağımsız olmasını sağlar iken, beklendiği gibi açık gri gölgeleme – hafif toz ve toprak kaplaması, koyu gri gölgeleme – orta yoğunluk derecesine sahip toz ve toprak kaplaması ve koyu barut grisi gölgeleme – yoğun toz ve toprak kaplaması hata simülasyon çiftleri güneş panelinin çıkış gücünde neredeyse benzer oranlarda azalmaya yol açmıştır.

15 günlük dakika bazlı uygulama süresi TYSA ve SYSA tarafından gerçekleştirilen toplam 6222 güneş paneli çıkış gücü tahmin ve hata tespit eylemi ile sonuçlanmıştır.

TYSA için tahmin edilen ile ölçülen güneş paneli çıkış güç değerleri arasındaki ortalama mutlak yüzdesel hata (OMYH) oranı toplam %4.44 olup SYSA'nın hassasiyet, özgüllük ve toplam doğruluk oranları ise sırasıyla %97.6, %99.7 ve %98.6 olmaktadır. Elde edilen sonuçlar ileriki uygulamalar açısından ümit verici olup geliştirilen ve doğrulanan güneş paneli düzeyli çıkış gücü tahmin ve hata tespit sisteminin, gelişimsel gereksinimlerin dikkate alınmasının ardından, sayısal açıdan daha fazla güneş panelinden oluşan güneş enerji sistemlerinde kullanılması ve dolaysıyla uzun vadede güneş enerjisi sistemlerinin verimlerini yükseltmesi ve destek ve bakım masraflarını azaltması beklenmektedir.

Anahtar Kelimeler: Yenilenebilir Enerji, Güneş Enerjisi, Yapay Zekâ, Yapay Sinir Ağları, Çıkış Gücü Tahmini, Hata Tespiti

Dedicated to science;

ACKNOWLEDGEMENT

First and foremost, I would like to express my sincere appreciation to my supervisor Prof. Dr. Şener Uysal for his professional and kind guidance and assistance through the various stages of this study.

It is a great pleasure to acknowledge the advice and support of the Head of the Electrical and Electronic Engineering Department Prof. Dr. Hasan Demirel and the honorable jury members, Prof. Dr. Şule Erten Ela, Prof. Dr. Osman Kükrer, Prof. Dr. Adnan Sözen and Prof. Dr. Serhat Şeker.

Words are not enough to extend my gratitude to my dear father and mother for their limitless love, motivation and support throughout my life.

Last but not least, I would like to give my endless thanks to my dear brother and best friend Moein, whom this study could not have been completed without his absolute support.

TABLE OF CONTENTS

LIST OF TABLES

LIST OF FIGURES

LIST OF SYMBOLS AND ABBREVIATIONS

I_0	The Reverse Saturation Current (A)
I_D	The Current Passing through the Diode
I_L	The Photo-generated Current (A)
I_{SH}	The Current Passing through the Shunt Resistor
$T_{ambient}$	Ambient Temperature
V_j	The Voltage across the Diode and the Shunt Resistor
Z_s	The Solar Zenith Angle
$j`$	The Julian Day Angle
j'	The Day Angle
w_0^l	Artificial Neural Network Weight
z_0^l	Artificial Bias Neuron
α_m	Module Azimuth Angle (North: 0°, East: 90°)
γ_s	The Solar Altitude Angle
λ_R	Time Zone Longitude (East Positive)
C	The Summer Time Improvement Parameter (Normally set to 1 for the Countries in Which the Summer Time is applied)
E_{tot}	The Irradiance Level
G_0	The Intensity of the Irradiance Hitting a Horizontal Surface outside the Earth's Atmosphere
G_{od}	The Daily Irradiation from Sunrise to Sunset (Wh/m^2)
I	Total Output Current (A)
I_{sc}	Short Circuit Current
j	The Julian Day Number

K_t	Clearness Index
$P_{\max}$	Maximum Power
T	The Absolute Temperature
V_{oc}	Open Circuit Voltage
δ	The Solar Declination Angle
ΔT_{GMT}	The Difference of Local Time from Greenwich Mean Time (GMT)
ω	The Hour Angle
T	PV Module Surface Temperature
V	The Voltage at the output Terminals
k	Boltzman`s Constant
n	Diode Ideality Factor
q	Elementary Charge (The Electric Charge Carried by a Single Proton)
β	Tilt Angle of the Solar Collector (Horizontal: 0°)
θ	The Angle of Incidence
λ	Longitude (East Positive)
φ	The Latitude of the Observation Point
AC	Alternative Current
ACC	Accuracy
AM	Air Mass
BOS	Balance of System Equipment
BR	Bayesian Regularization
CET	Central Europe Time
CT	Civil Time
DC	Direct Current
EoT	Equation of Time

ET	The Equation of Time
FF	Fill Factor
FN	False Negative
FNR	False Negative Rate (Miss or ‘Type II Error’)
FP	False Positive
FPR	False Positive Rate (False Alarm or ‘Type I Error’)
GMT	Greenwich Mean Time
LAT	Local Apparent Time
LM	Levenberg-Marquardt
LMT	Local Mean Time
LST	Local Solar Time
LSTM	Local Standard Time Meridian
LT	Local Time
MAE	Mean Absolute Error
MAPE	Mean Absolute Percentage Error
MLP	Multi-Layer Perceptron
N	The number of faulty points in data (Condition Negative)
NOCT	The Nominal Operating Cell Temperature
P	The number of healthy points in data (Condition Positive)
RBF	Radial Basis Function
RCI	Reference Clearness Index
RNN	Recurrent Neural Network
STC	Standard Test Conditions
TC	Time Correction factor
TN	True Negative

TNR	True Negative Rate (Correct Rejection)
TP	True Positive
TPR	True Positive Rate (Hit)
UT	Universal Time

Chapter 1

INTRODUCTION

Solar energy emerges as a promising renewable resource to meet the modern world energy requirements. The world is currently consuming about 17 terawatts (TW) of energy annually and this number is expected to increase to 30 TW by 2050. This means that there will be a demand of >10 TW renewable energy to stabilize the CO_2 in the atmosphere by mid-century [1].

Solar radiation is converted to Direct Current (DC) electricity in solar cells by the Photovoltaic (PV) effect which was discovered in 1839 by Becquerel. The PV effect is described as the potential difference generation between junctions of different materials. Such potential difference is caused as a response to a visible or non-visible radiation. What happens by the PV effect can roughly be defined as follows; Photons are absorbed in semiconductor material and generate charge carriers which are separated in the junctions and are collected at the terminals of the junctions. The solar spectrum consists of different wavelengths and the photons in each wavelength have different amounts of energy. The photons in the sunlight hitting the surface of a solar cell may be absorbed, reflected back or passed through. The PV effect is caused by the absorbed photons, which transfer their energy to the electrons in the solar cell material. This energy transfer excites the electrons from the valence band into the conduction band of energy and lets them move freely through the semiconductor material. What makes the photo-generation possible is the fact that most of the photons existing in

solar radiation hitting the earth have energies higher than the semiconductor material band gap and can excite the electrons in the material (from valence band to conduction band). Figure 1.1 demonstrates the energy bands structure of a semiconductor material.

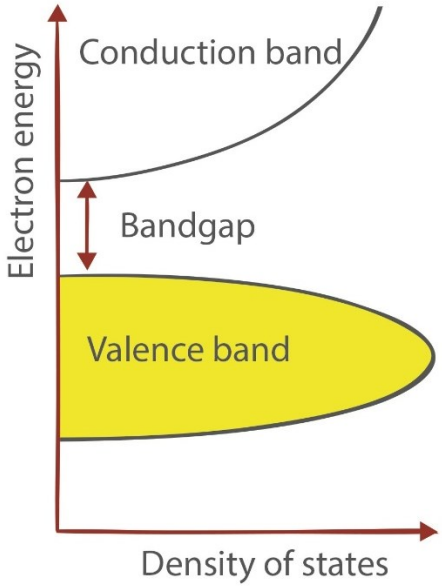

Figure 1.1: Energy Bands Structure of a Semiconductor Material

As previously mentioned, the PV effect was discovered in late 19th century but it took a long time for solar cells made of crystalline Silicon (c-Si) to achieve a relatively sufficient efficiency of 6-10% and serve the space programs and satellites in the 1950s [1]. The first solid state photovoltaic cell made of semiconductor selenium and coated by a very thin gold layer to form the junctions was introduced by Charles Fritts in 1883. Russian physicist Aleksander Stoletov made the first photoelectric cell based on outer photoelectric effect. The underlying mechanism of light instigated carrier excitation was defined by Albert Einstein in 1905, granting him the physics Nobel Prize in 1921. Russel Ohl presented the modern junction semiconductor solar cell in 1946. The first practical photovoltaic cells were developed in Bell Laboratories in 1954 and were appended to Vanguard I satellite in 1958.

It was after the 1970s energy crisis that the PV research and development (R&D) was accelerated. Elliot Barmen's researches that led to produce solar cells with lower costs in 1973 is one of these R&D efforts. Crystalline Silicon (c-Si) is the most common semiconductor material used in solar cell production. These cells are mostly shaped as Si wafers and ribbons. However, the reliability and stability of the Si cells comes at a high production price. The complexity of module assembly and cell manufacturing and the demand for highly purified silicon, as well as limited number of manufacturing units all lead to high production cost. The Si material is separated into the following classes based on crystallinity and crystal size;

- Monocrystalline Silicon (c-Si)
- Poly-crystalline Silicon or Multi-crystalline Silicon (pc-Si or mc-Si)
- Ribbon Silicon
- Mono-like-multi-silicon

Thin film is the second commonly used material in solar cell manufacturing. Thin film solar cells are heavier, less efficient and more area per watt production occupying compared to crystalline cells, but have the advantage of lower material usage. The thin film solar cells are generally made of Cadmium Telluride (CdTe), Copper Indium Gallium Selenide (CIGS) and Amorphous Silicon (A-Si).

There are also other solar cell technologies, like organic cells, dye-sensitized cells and light-concentration based Gallium Arsenide (GaAs) cell which are not very popular due to several disadvantages. For example the GaAs solar cells are not preferred due to their very high manufacturing costs, even though they have been reported to exhibit more than 40% efficiency under concentrated sunlight.

As a result of the mentioned trade-offs, the compound semiconductor and polycrystalline Si (pc-Si) solar cells were developed to meet the desirable efficiency and costs for high production capacities and large-scale terrestrial installations. The PV technology is currently at a “tipping point” taking that the “energy security and independence, environment, electrical grid integrity and protection have brought us to the threshold [2]”. The PV R&D activities with research-device scope is presented in Figures 1.2-a and 1.2-b.

Multi-megawatt PV power generation plants triggered the rapid growth of the PV market in the 1980s. Currently Si technologies lead by 94% of global market sales [2], the research on Si is of first priority and several Si cell designs have reached >20% efficiencies. The Si PV cell efficiency advancements can be categorized into four stages, based on technology solutions and cell structures. The first advancement of Si PV cells belongs to the “semiconductor-era” (1950s) which led to production of cells with 15% efficiency. The second advancement occurred in the 1970s due to the attainments in microelectronics which allowed Si PV cell fabrication with 17% efficiency. Nevertheless, the greatest achievement in high efficiency Si solar cell production belongs to the third (1980s) and fourth (2000+) stages where the technology almost earned 25% efficiency. The last advancements were achieved due to the cell structure improvements described in [3]. Further advancements are required to close the performance gaps between the research and the manufactured cells and also to create appropriate R&D basis for next-generation Si PV cells as well as other PV technologies.

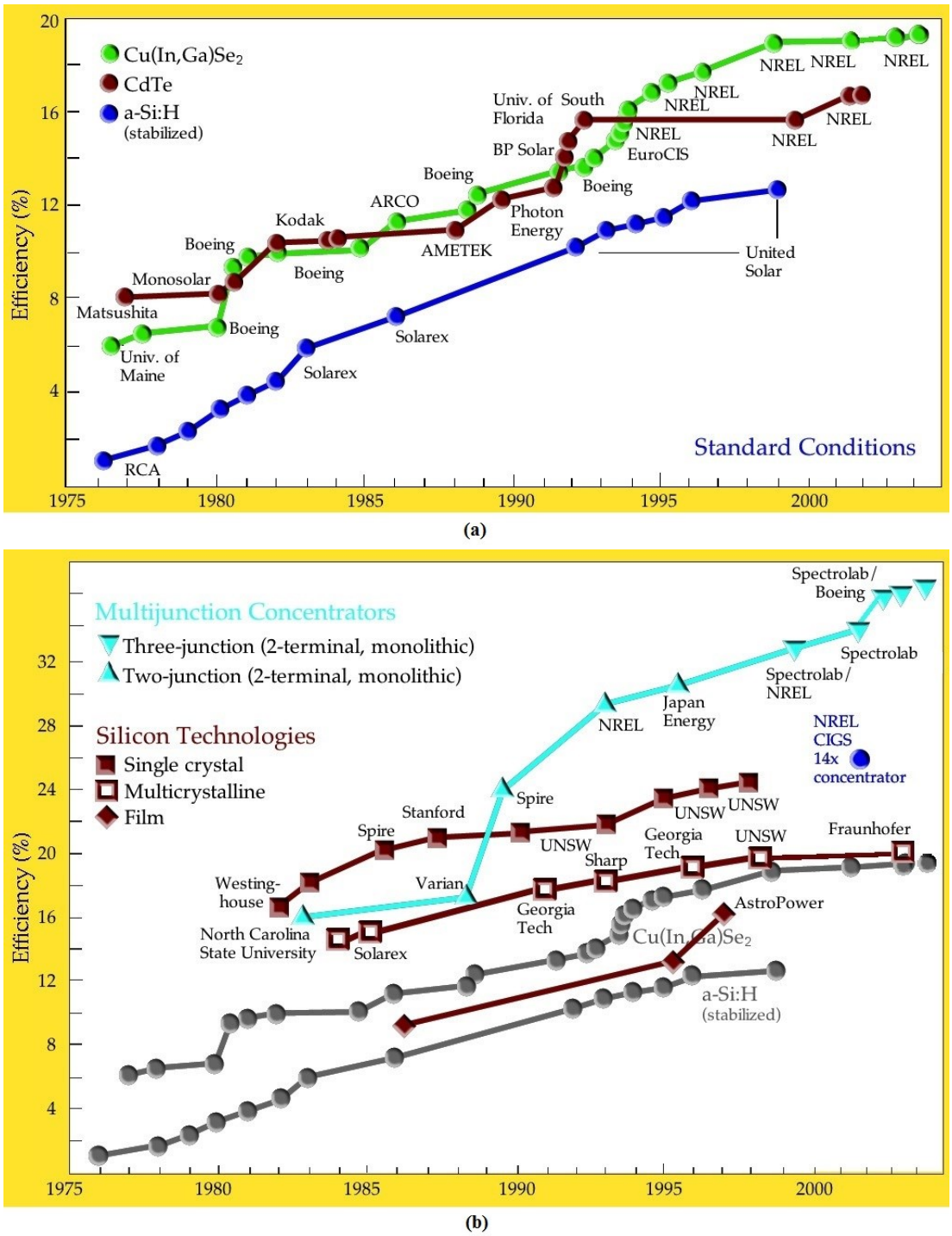

Figure 1.2: Evolution of Research Solar Cell Efficiencies; (a) Thin-Film Technologies; (b) Si and Concentrators, Comparing Them to the Thin Films [2]

The electronic characteristics of a solar cell can be defined as a mathematical model which is equivalent to the electronic circuit shown in Figure 1.3.

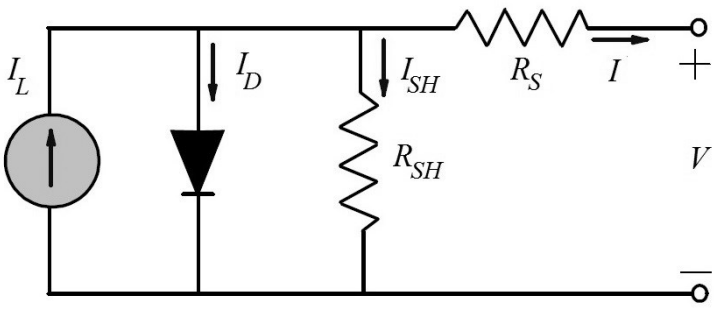

Figure 1.3: Equivalent Electronic Circuit of a Solar Cell

The above circuit would model the solar cell as a current source only connected to a diode in parallel as a demonstration of an ideal situation, while the real-life experiments suggest that the solar cells are not practically ideal. To overcome this matter, the solar cell electronic circuit is modified by the addition of a shunt and a series resistor.

The proposed electronic circuit determines the electrical current generated by a solar cell as the subtraction of the current passing through the diode and the shunt resistor from the current generated by the current source. The current equation of a solar cell is described in the following equation;

$$I = I_L - I_D - I_{SH} \tag{1.1}$$

where,

I : Total output current (A)

I_L : The photogenerated current (A)

I_D : The current passing through the diode

I_{SH} : The current passing through the shunt resistor

The solar cell voltage equation is described as follows;

$$V_j = V + IR_s \tag{1.2}$$

where,

V_j : The voltage across the diode and the shunt resistor

V : The voltage at the output terminals

I : The output current

The current passing through the diode is given by;

$$I_D = I_0 \left\{ exp \left[\frac{q(V + IR_S)}{nKT} \right] - 1 \right\} \tag{1.3}$$

where,

I_0 : The reverse saturation current (A)

n : Diode ideality factor

q : Elementary charge (the electric charge carried by a single proton)

k : Boltzman`s constant

T : The absolute temperature

Finally, the current passing through the shunt resistor is defined as;

$$I_{SH} = \frac{V + IR_S}{R_{SH}} \tag{1.4}$$

As the overall combination of the above equations, the solar cell characteristic equation is defined by;

$$I = I_L - I_0 \left\{ exp \left[\frac{q(V + IR_S)}{nKT} \right] - 1 \right\} - \frac{V + IR_S}{R_{SH}} \tag{1.5}$$

Various characteristic factors and limitations are to be considered during solar cell design process. Some of these characteristic factors are short circuit current (I_{sc}), open circuit voltage (V_{oc}) and fill factor, which are briefly explained as follows;

I_{sc} is defined as the maximum current a solar cell with shorted terminals can generate. As previously described by the PV effect, the energy of photons existing in the sunlight hitting the surface of a solar cell, excites the electrons and makes them freely move through the semiconductor material. As a matter of fact, the maximum I_{sc} is generated by each photon of the sunlight contributing to one electron flow to the load. Again as previously mentioned, the photon energy must be bigger than the band gap of the semiconductor material (the gap between the valence and the conduction bands) so that it can excite electrons to move through this band. This fact implies that the band gap of the semiconductor material determines the I_{sc} of a solar cell. A solar cell made of some semiconductor material with a large band gap absorbs less photons and generates less I_{sc} while a solar cell made of small band gap semiconductor material absorbs more photon and produces higher amount of I_{sc}.

V_{oc} is given as the maximum voltage acquired from a solar cell with open circuited terminals. Photons with higher energies than the band gap of the solar cell semiconductor material are absorbed and excite the electrons from the valence to the conduction band, thus increasing their potential. Therefore, the maximum V_{oc} of a solar cell is defined by the band gap energy of the compounding material. The higher the material band gap energy, the greater the generated V_{oc} and vice versa.

The fill factor of a solar cell is an extent of the squareness of the cell I-V curve and is described as;

$$FF = \frac{V_{OC} - \ln(V_{OC} + 0{,}72)}{V_{OC} + 1} \tag{1.6}$$

where,

$V_{OC} = \frac{nkT}{q} \ln(\frac{I_L}{I_0} + 1)$: Normalized open circuit voltage

Different interconnections of PV cells form PV modules, which can be organized to form PV arrays and systems in several ways. A simple illustration of PV cell, module and array structures is given in Figure 1.4.

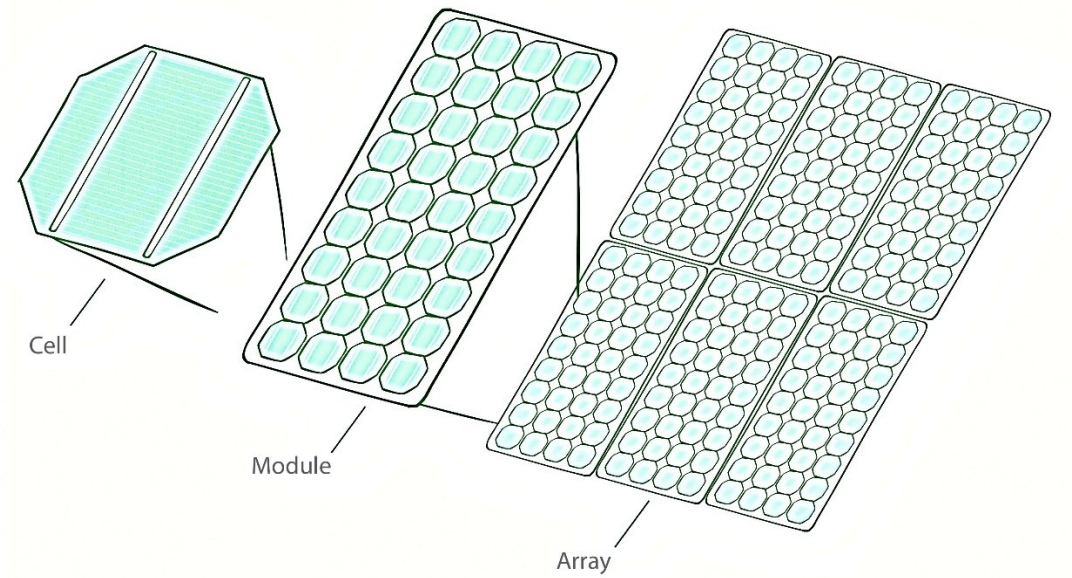

Figure 1.4: PV Cell, Module and Array Structures

Different PV systems are designed and implemented for various applications to meet part or all of the electrical energy requirements. The PV systems may or may not be connected to a power utility and are categorized as stand-alone and grid-connected systems. The stand-alone PV systems operate independently and usually are directly connected to a DC load. Since these systems are not connected to any power utility, they can only supply electricity under direct sunshine. However, it is also possible to equip a stand-alone PV system with battery backups so the batteries are charged during clear daylight hours and supply the load during night or overcast sky situation.

As mentioned, the other PV system category refers to PV systems that are connected to some electrical power utility. Such PV systems are connected together with an electrical utility to the applications so that in cases when all the required electrical energy cannot be produced by the PV system, the shortcoming is removed by the main utility supply.

The grid-interactive PV system designs can be classified in two general categories: The systems with and without battery backups. The grid-interactive PV systems without battery backup are commonly connected to main power facility. In such systems the energy is supplied to the users from PV facility during clear daylight hours while the energy demands during night or overcast hours are met by the main power facility. Figure 1.5 demonstrates the general view of such system.

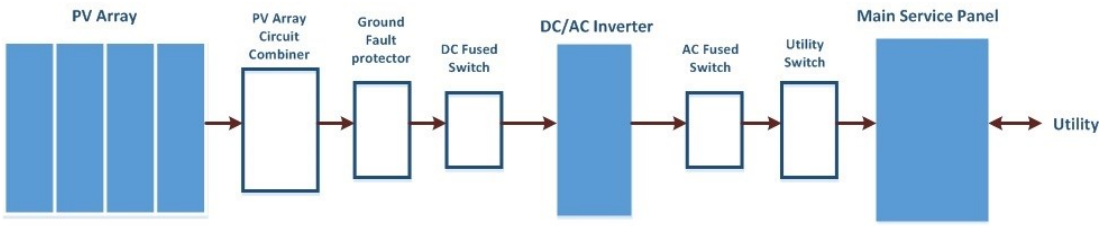

Figure 1.5: Grid-Interactive PV System without Battery Backup

The principal parts of the system demonstrated above are PV Arrays, Balance of System Equipment (BOS), DC-AC inverters, Meters and Switches. As mentioned earlier, a composition of PV modules (or panels) with various interconnection types form a PV array. The BOS includes parts like mounting and wiring systems that are utilized in connecting the PV modules and arrays to the other parts of the application ground. Some wiring system components are disconnected for DC-AC sides of the inverter, ground-fault protection elements and over current protection elements. Again as mentioned earlier, the PV modules produce DC electricity. This energy needs to be

converted into Alternative Current (AC) electricity in order to be used in various applications. This conversion is performed by the DC-AC converters. The metering and measurement equipment are deployed for system performance monitoring purposes. Finally some switching equipment are used in order to facilitate the exchange between the PV system and the power facility in certain situations.

The other general category corresponds to grid-interactive PV systems with battery backup which utilize backup battery banks to handle critical load circuits in tense situations of grid power outage. In such situations, the system automatically disconnects from the electrical grid and connects to the battery assembly in order to supply the critical load circuits. The batteries are charged during the clear sunlight hours. In situations of grid power outage the critical load circuits are fed by both the PV system and battery bank in daylight clear sky or only by the previously charged battery bank during night or overcast sky hours. The energy consumption rate of the critical load circuits and the backup battery bank capacity determines the duration of the critical load supply. Such PV systems with battery backups contain extra component like batteries and battery enclosures, battery charge controllers and separate subpanels for critical loads as compared to the first category PV systems (systems without battery backup). The general view of a grid-interactive PV system with battery backup is given below.

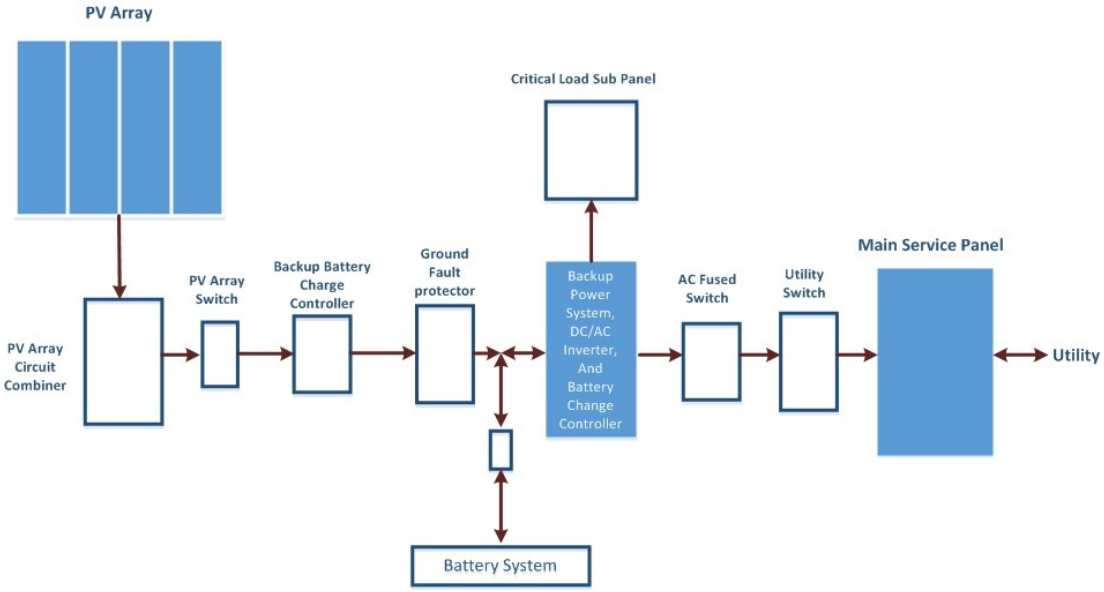

Figure 1.6: Grid-Interactive PV System with Battery Backup

While the PV module output power generation depends on the intensity of sunlight received on the module surface, this intensity varies based on factors like date and time, along with cloudiness index as an obstacle. There are also several extra factors that affect the power generation of a PV module, the most important of which may be named as the Standard Test Conditions (STC), temperature, dirt and dust, mismatch and wiring losses and DC-AC conversion losses.

The STC refers to condition in which PV module can produce the upmost output power. The STC for PV operation is defined as solar cell temperature being 25°C, solar irradiance being 1000 W/m^2 and solar spectrum being filtered by passing through atmosphere of Air Mass (AM) =1.5. While it is possible to maintain the STC for indoor PV applications, most of the outdoor PV applications are running in non-STC condition due to existence of usual losses. The losses are reportedly around 5% [4], causing the rated solar cell output decreasing to 95%.

The PV module surface temperature increases under direct sunlight and the PV module power generation tendency decreases with increasing surface temperature. This issue will be explained comprehensively in section 2. The highest PV output drop caused by increasing module surface temperature is reported to be around 89% [4].

Dirt and dust accumulation on PV modules is another factor decreasing the PV output power. The details of dirt and dust accumulation on PV module surface is described thoroughly in section 4 and also may be investigated in [5], [6]. The upmost PV power reduction by dirt and dust accumulation on PV surface is reported to be around 93% [4].

Although a PV array is constructed by connecting several PV modules, the output power generated by a PV array is not the summation of the output power generated by each contributing PV module in real-life practical applications. One reason is the performance differences of the contributing PV modules which is called module mismatch. In general the module mismatch cause no more than 2% reduction to a PV array [4] while some other drops may occur in the array due to connection resistances and wiring losses which lead to power drops around 3% [4].

As previously described, the PV module generates DC power which needs to be converted into AC power for most of the applications. This conversion is carried out by DC-AC inverters. Not surprisingly, the inverter operations and the wiring connections of the PV array to the inverters are also sources of some output losses. The inverter losses are around 10% of the total generated power [4].

Taking all of the above opposing factors into consideration, a PV module with rated power output of 100 Watts may face a power drop of 33 Watts on a clear day under direct sunshine due to several possible losses.

Despite significant growth of the PV industry in order to meet the rapidly growing modern world energy demand, the supervision techniques for PV systems have not received sufficient consideration. This issue is highlighted taking that the PV systems in lower output levels are mostly operating without appropriate monitoring mechanisms [7]. Considering the above, developing supervision techniques for low output PV systems is highly emphasized.

Artificial Intelligence (AI) techniques are diversely deployed in real-life applications due to their strong reasoning, fault tolerance, flexibility and generalization capabilities. AI can be described as the demonstration of human intelligence on a machine and consists of various branches which are given in Figure 1.7, as well as several combinations of the mentioned branches called Hybrid Systems (HSs). AI techniques may be further reviewed in [8-13].

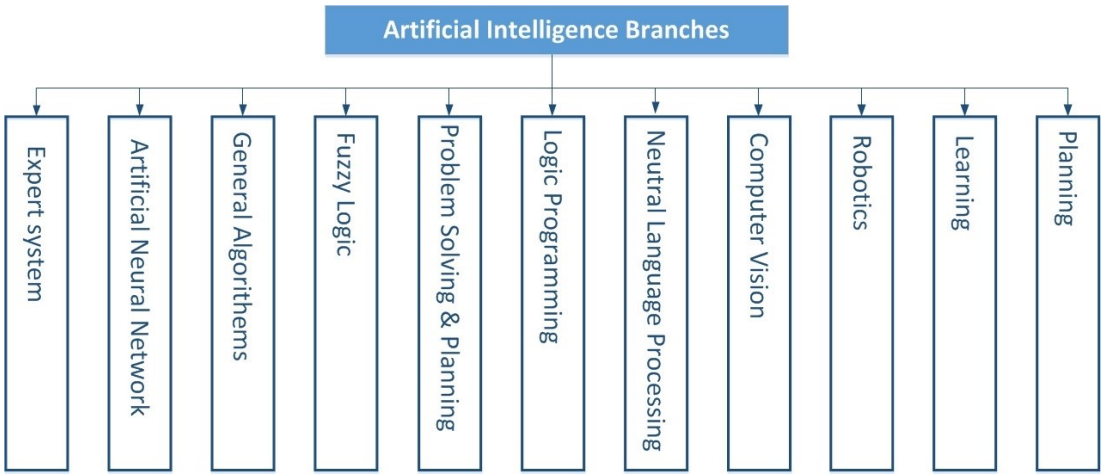

Figure 1.7: Artificial Intelligence Branches

Artificial Neural Network (ANN), which is one of the most popular branches of AI, is a mathematical paradigm simulating the behavior of biological neural network. The Nucleus (neuron center) which is the main part of a biological neuron is interconnected with other neuron centers to form a biological neural network. The Synaptic connection between the nuclei is maintained via Dendrites and Axons. The architecture of a biological neuron is demonstrated in Figure 1.8.

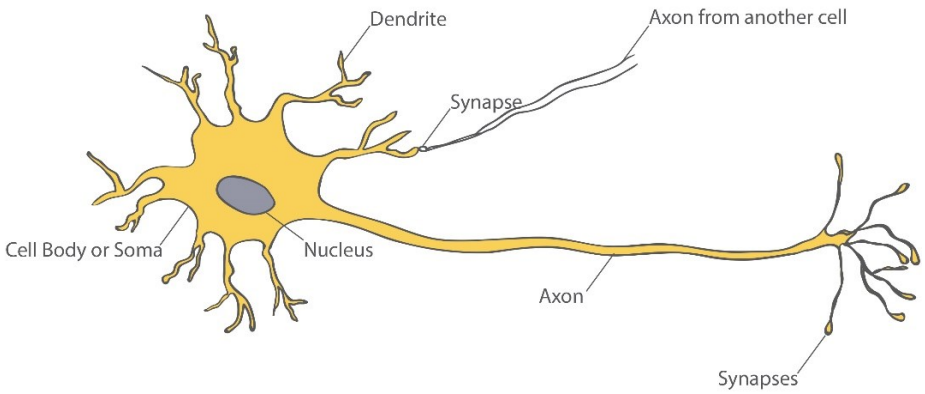

Figure 1.8: Biological Neuron Architecture

The biological neuron demonstrated in Figure 1.8 can receive electrical pulses fired by other neurons through its synapses. When the electrical pulses (signals) received on a neuron exceed a certain threshold, the neuron is activated and emits an electrical pulse through its axon. Other neurons can receive the emitted pulse.

The synaptic connections between neurons and the required thresholds for neuron activations may change during the life time of neurons. A sequence of changing synaptic connections and activation thresholds enables the process of learning. A simplified illustration of biological neuron is given in Figure 1.9.

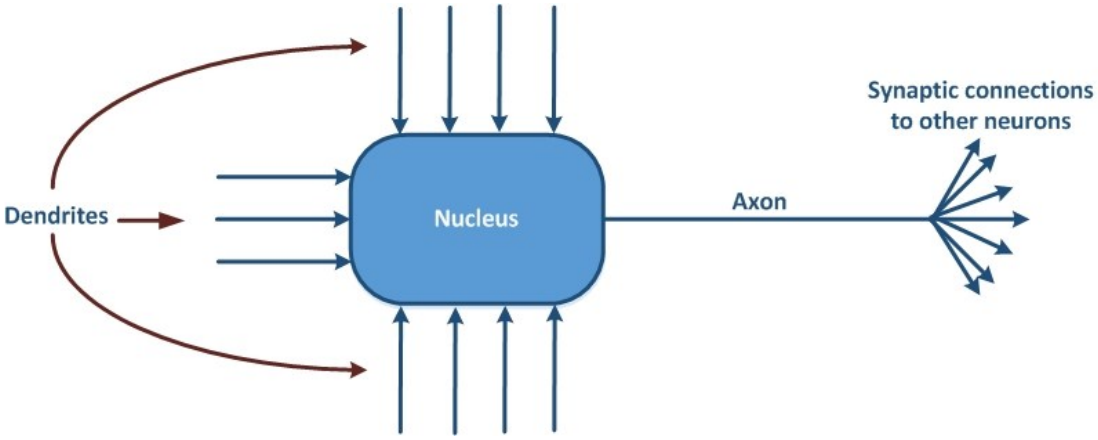

Figure 1.9: Simplified Biological Neuron Architecture

Although it is far from reality to create an artificial brain, ANN as a collection of individually interconnected artificial neurons (which are inspired by biological neurons) is developed to solve many real-life practical problems in various fields. Each artificial neuron has associated inputs (x_i), weights (w_i) and threshold (θ) as demonstrated in Figure 1.10.

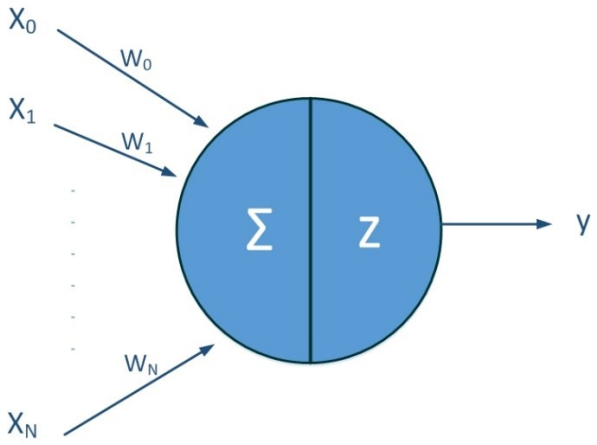

Figure 1.10: Artificial Neuron

The information traverses through these processing units and the activation function (of the layer to which the unit belongs) determines the output based on the input-weight summation. The most commonly used activation functions are given in equation 1.7 and equation 1.8, respectively.

$$\text{Linear: } z = \sum_{i=0}^{N} w_i x_i + \theta \tag{1.7}$$

$$\text{Sigmoid: } f(z) = \frac{1}{1+e^{-z}} \tag{1.8}$$

ANNs are not programmed to carry out specific tasks, but they are trained with data sets and learn the patterns of the training inputs presented to them. The most common ANN architecture is the multi-layer feed-forward (Figure 1.11) with back-propagation training algorithm. In this architecture, the training data is traversed in forward direction through the network to reach the output layer and the training error is calculated as the comparison of the estimated output and the target output which is presented to the network to investigate the learning process. The calculated error is back-propagated in the network and the weights (which are set to random small values at the beginning of the training process) are re-adjusted. This procedure is repeated until the training error falls below a pre-set threshold.

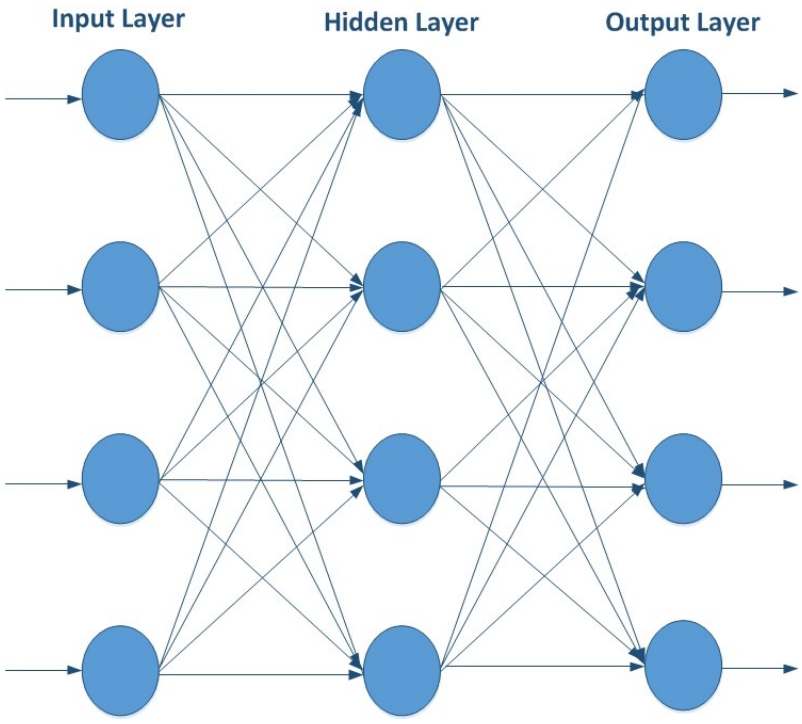

Figure 1.11: Multi-Layer Feed-Forward ANN Architecture

ANNs, as human brain-inspired simplified mathematical models, can learn from examples and make generalizations for new and unseen inputs, thus remove the need for sophisticated mathematical formulas and expensive physical models. ANNs being robust in terms of fault tolerance, dealing with noisy data and making high-speed generalizations, are widely utilized in several PV system modeling, estimation and prediction applications. A review of some ANN-based PV system estimation applications is given below.

The minimum and maximum air temperature, precipitation, day-length and clear-sky radiation are used as inputs to develop an ANN for daily solar radiation estimation in [14]. The authors report the Root Mean Square Error (RMSE) of the proposed system to be averagely 3.28 MJ/m^2 and claim that the system can be deployed in diverse locations in existence of the temperature and precipitation information. Another ANN similar to the one mentioned above with one additional input, day of the year is developed in [15]. The issue that the direct measurement equipment are not available everywhere is pointed and an ANN for global solar radiation estimation in such locations is designed in [16]. The average values of pressure, temperature, humidity, wind speed and sunshine duration along with the geographical location and month of year are fed to the proposed ANN, yielding an accuracy of 93% reportedly. A similar approach is proposed in [17] where solar radiation data collected from 13 different locations across India is used for developing an ANN for global solar radiation estimation. The author indicate that the developed ANN shows promising estimation ability for locations without direct measurement and monitoring equipment. The global solar radiation is also modeled in [18] using a Recurrent Neural Network (RNN) for various Spanish locations with satisfying precision. RNN specifications may be surveyed in [19,20].

Radial Basis Function (RBF) networks are utilized in [21] and [22] for daily and monthly mean daily solar radiation values, respectively. The latter presents location information (latitude, longitude and altitude) and sunshine duration to the network and claims high generalization capability for new locations not included in the network training data sets. Comprehensive details of the RBF neural network structures may be investigated in [23,24].

ANN and Adaptive Neuro-Fuzzy Inference System (ANFIS) techniques for hourly solar radiation estimation with previously mentioned common meteorological parameters as inputs are compared in [25]. The authors report the ANN with Levenberg-Marquardt (LM) algorithm as the best estimation model. Also it is indicated that the overall performances of both the ANN and ANFIS models are boosted when the information of wind speed is available as input. RNN and Multi-Layer Perceptron (MLP) techniques for solar radiation synthetic series generation are compared in [26,27] where the MLP technique is reportedly outperformed RNN in terms of estimation accuracy. ANFIS and MLP features may be extensively reviewed in [28-35].

ANN-based solar potential estimation in Turkey is carried out in [36,37]. Similar to previous examples, the inputs to the developed ANN are raw geographical (latitude, longitude and altitude) and meteorological (sunshine duration and temperature) information, alongside with the month of year. Figure 1.12 demonstrates the proposed ANN architecture. The data has been collected from 17 stations across Turkey during a two-year interval, with the data of 11 stations being used for training of the ANN. After the training phase, the developed ANN is tested by the data collected from the rest 6 stations. The results are reportedly promising (MAPE < 6.7%) and the study

provides the possibility of deciding the location and the appropriate technology for solar system installations in Turkey.

A solar radiation map for clearness index estimation in Spain is developed in [38] using MLP. As shown in Figure 1.13 the inputs to the proposed MLP are the irradiation history, clearness index and the hour order of the clearness index (K_t). While the classical methods remain insufficient for generating maps in locations where no solar information is available, the proposed MLP is claimed to be able to draw maps in existence of the hourly solar radiations as the only required input.

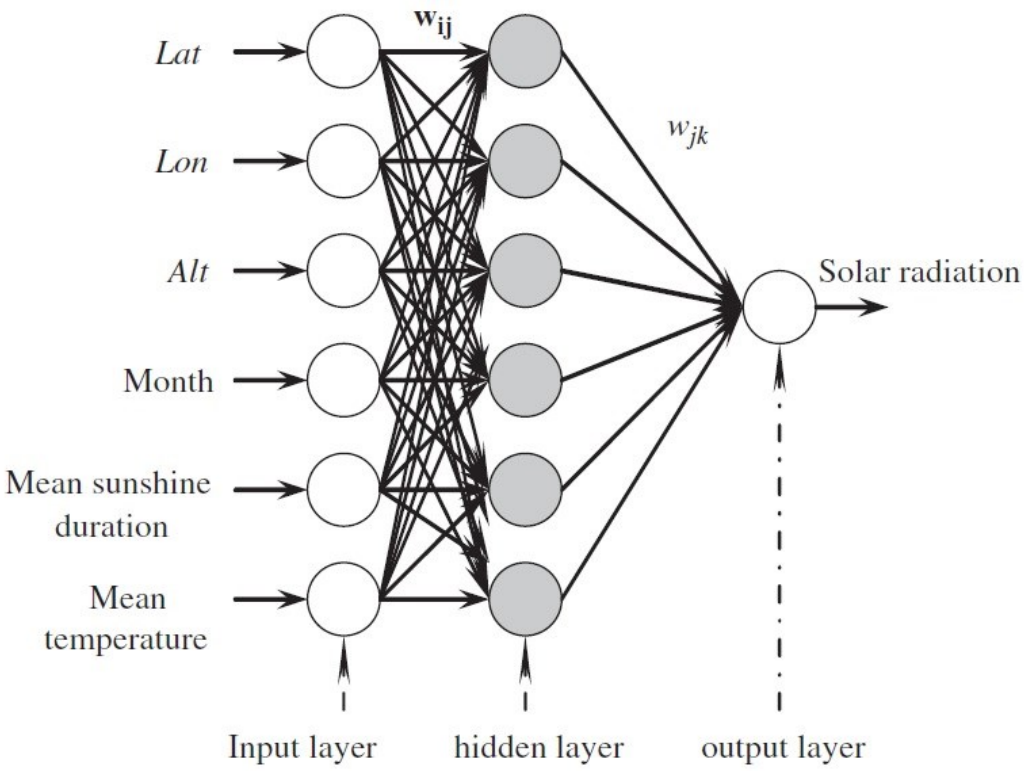

Figure 1.12: ANN Architecture for Solar Radiation Estimation [36]

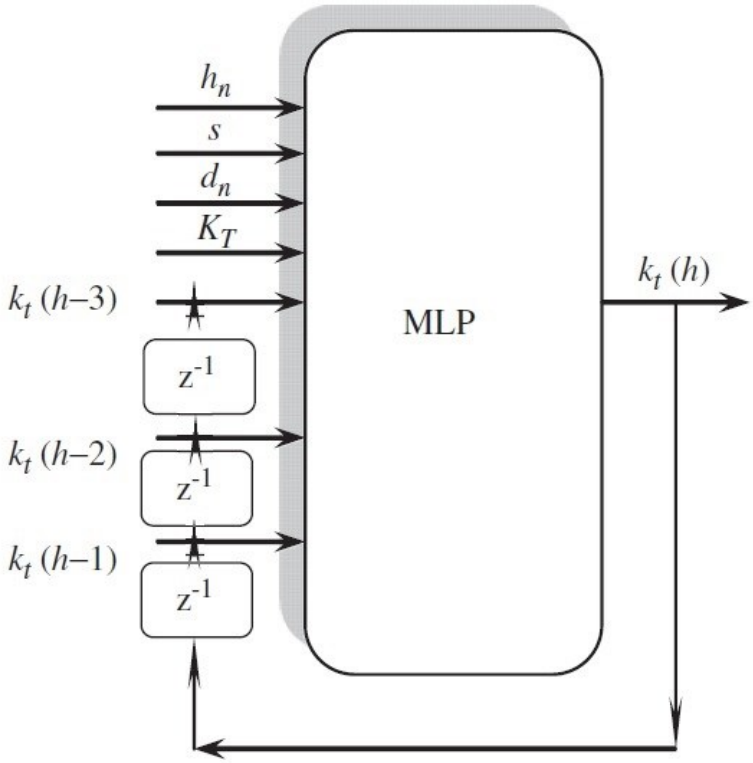

Figure 1.13: MLP Architecture for Clearness Index Estimation [38]

ANN and linear regression models for hourly and daily diffuse fraction estimation in Egypt are compared in [39]. According to the authors, the ANN model outperforms linear regression models with estimations precision of 95%, 93% and 96% for infrared, ultraviolet and global insolation, respectively, in flat areas. Also the ANN model is utilized to estimate the above mentioned parameters in Aswan and the results are reported to be very promising. Taking that the data of Aswan was not included in the ANN training sets, highlights the robostness of the proposed ANN model in generalization of unseen data.

An ANN model for beam solar radiation estimation which is defined as Reference Clearness Index (RCI) is proposed in [40]. The monthly mean daily beam solar radiation estimation is carried out in India and the RMSE between the ANN model and

the measured results are reported to be averagely 2.22%. Figure 1.14 shows the proposed ANN architecture.

Summarizing the above, AI techniques are widely utilized in diverse PV and meteorological applications as robust and promising alternatives to classical methods and approaches of overcoming the problems and shortcomings when dealing with missing or noisy data, modeling and predicting data in locations without measurement and monitoring equipment, generalizing and extending the estimations to new locations with previously unseen data, etc. According to [41] the number of applications of each AI branch in the PV and meorological fields are given in Table 1. Obviously it can be noted the the majority of the applications are accociated with ANNs.

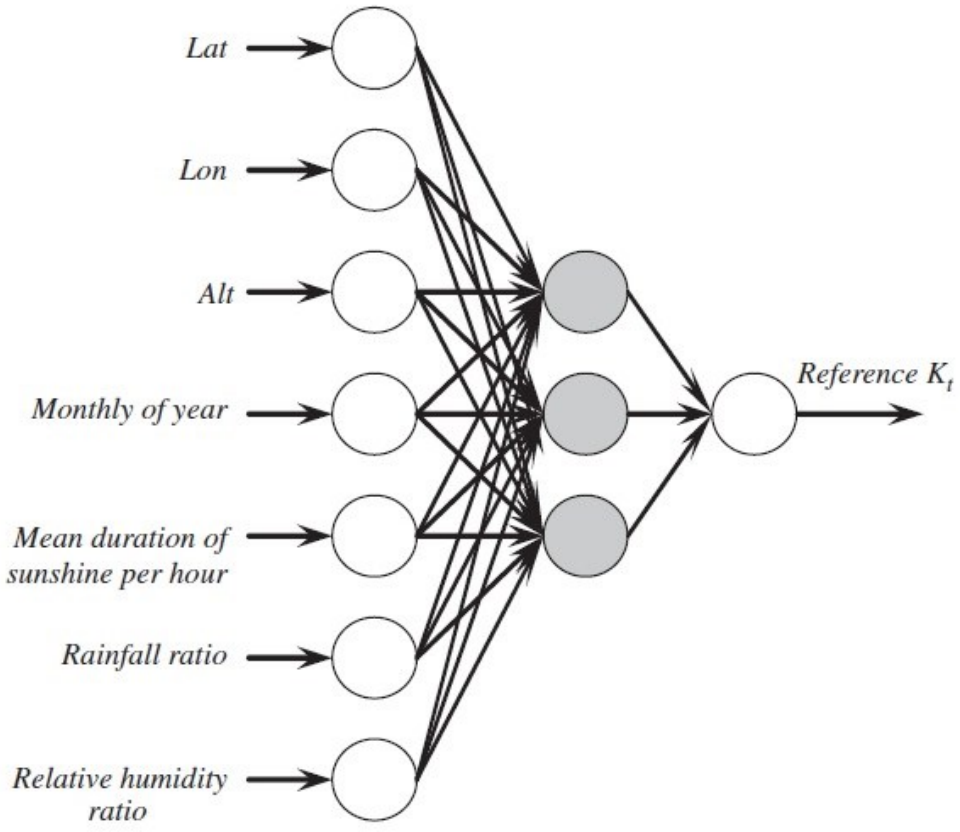

Figure 1.14: ANN Architecture for Beam Solar Radiation Prediction [40]

Several ANNs are developed for monthly, daily and hourly global solar radiation modeling and estimation, clearness index prediction, temperature and humidity forecasting, etc. Some of these applications are mentioned in this section. A comprehensive list of these applications may be investigated in [41].

RBF neural network is used to predict the output characteristics of a commercial PV module. The proposed RBF neural networks (shown in Figure 1.15-a and 1.15-b) are aimed to enhance the estimation accuracy of the output I-V and P-V curves by receiving the solar irradiation and temperature data as inputs [42].

Table 1.1: Summary of the numbers of applications presented in PV and meteorological data [41]

AI technique	**Area**	**Number of applications**
Neural networks	Modeling and prediction of solar radiation Wind speed forecasting Temperature forecasting Weather forecasting (temperature, humidity, etc.) Clearness index forecasting Insolation modeling and prediction	48
Fuzzy logic	Modeling and prediction of solar radiation	3
Neuro-fuzzy (ANFIS)	Prediction of clearness index K_t	3
Wavelet and neural network	Forecasting of solar radiation (for missing data) Generation of hourly wind speed	5
ANN with Markov chain	Prediction of daily global solar radiation	2

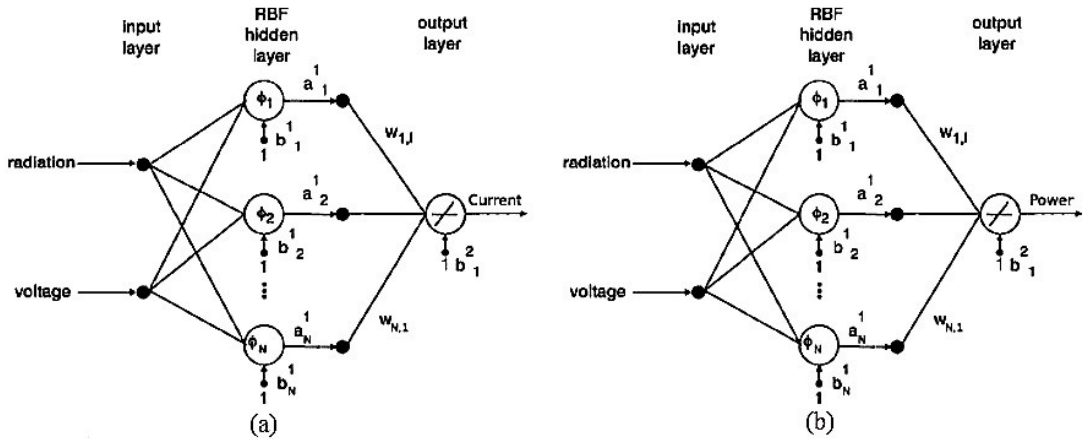

Figure 1.15: RBF Neural Networks for PV Module Output Characteristics Estimation [42]

Different ANN architectures are developed for PV output power estimation [43]. In the mentioned study, the output power of two PV modules using different ANN topologies with inputs given in Figure 1.16 are estimated. According to the authors, the MLP topology outperforms other ANNs in terms of estimation accuracy.

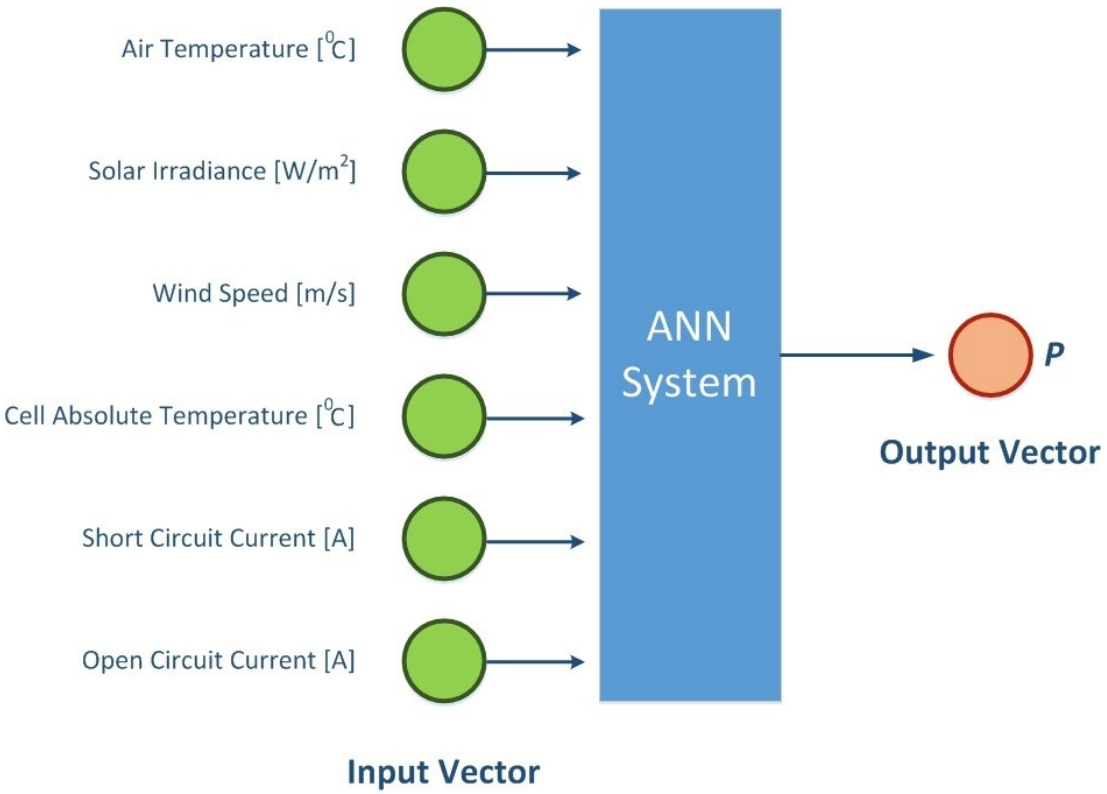

Figure 1.16: Input and Output Vector Definitions of the Developed ANNs [44]

A similar study is carried out in [45] where again different ANN topologies with minimum temperature, maximum temperature, mean temperature and solar irradiance as inputs are utilized for output power estimation of a PV module. The authors indicate that the feed-forward MLP topology with back-propagation shows the best performance in PV module output power estimation.

As described in the above examples, ANNs are being widely utilized in PV systems, mostly for irradiance estimations and rarely for PV output power predictions. Nevertheless, in most of the cases the inputs to the developed ANNs are raw location, time and meteorolocial data like latitude, longitude, altitude, month and day of year, etc. In this study, more definitive functions of the mentioned parameters namely being the solar altitude, azimuth and incidence angles, which precisely indicate the Sun's position in the sky, alongside with real-time and synchronous measurements of irradiance (W/m^2) and PV module output power (W/min) as well as the calculated PV module surface temperature values are presented to the proposed ANNs.

In this study, calibrated and sensitive measurement equipment are utilized for well-detailed and highly accurate data acquisition which will be comprehensively described in the next section. Nevertheless, regardless of how well-detailed, accurate and straight-forward-looking the inputs are, the PV module output power cannot be precisely described based on first physical principles. Especially the effect of the PV module surface temperature highly complicates the PV module output power estimation process. The PV module output power increases with increasing irradiance, while the PV power generation tendency decreases with increasing module temperature, which is again directly caused by increasing irradiance received on the module surface. Although a fine analytical or physical model can be employed for PV

power estimation and fault detection at an adequate accuracy level, the need for a qualified and eligible machine learning technique for highly-precise PV module output power estimation and fault detection is emphasized by taking the above issues into consideration. The focus of this study is to give insight of competency of the well-recognized MLP machine learning technique with appropriate back-propagation algorithm for PV power estimation and fault detection applications in existence of sufficient amount of input data sets.

A general review of various PV system faults and corresponding fault detection and mitigation approaches is provided in [46]. Several simulation-based fault detection models for small PV systems are developed in [47,48]. PV system fault detection approaches based on climate data retrieved from satellite observations are introduced in [49,50]. Other approaches such as data-driven, graph-based and wireless sensor-based fault detection, represented in [51-53], also address the PV system monitoring challenge.

Online fault detection of PV systems using a one-equation model with irradiance and PV module surface temperature is developed in [54]. In order to examine the accuracy of the model, the authors compare it with feed-forward ANN models and conclude that although ANNs perform better, the performance of the one-equation model is also satisfactory.

In this study, two ANNs for PV module output power estimation and fault detection are developed. The details regarding data acquisition and ANN training, testing and implementation processes are comprehensively presented in the following sections.

1.1 Thesis Contribution

As previously discussed, ANNs are widely being deployed in solar system supervision and monitoring, but in most cases the inputs to the mentioned ANNs are raw data such as latitude, longitude, altitude, month, day, and time values. In this study, instead of directly feeding raw input data to the ANNs, the input data is processed and parameters like the solar altitude and azimuth angle as well as the angle of incidence which are functions of latitude, longitude, altitude, month, day, and time are provided to the ANNs as inputs. Most ANN practitioners agree on the fact that the ANNs perform better when provided by more definitive input paths and functions rather than just random and raw values.

On the other hand, the per-minute measurements of PV module output power (W/min), irradiance (W/m^2) and PV module surface temperature are other inputs to the system developed in this study. Calibrated and sensitive measurement equipment are utilized for highly precise data acquisition, but regardless of how well-detailed, precise and straight-forward-looking the inputs are, the PV module output power generation cannot be described by the first physical principles. The PV module surface temperature highly complicates the PV module output power estimation. The PV module output power increases by increasing irradiance level, but in parallel the PV module power generation tendency decreases with increasing PV module surface temperature which is a direct result of increasing irradiance level. In other words, the irradiance level plays both positive and negative effect in PV module output power generation at the same time which cannot be thoroughly described using an analytical or physical model. The need for a highly qualified and eligible machine learning technique that can handle all the possible contradictions is highlighted by taking the

above into consideration. The aim of this study is to provide a comprehensive analysis of the well-recognized MLP (Multi-Layer Perceptron) machine learning technique with the robust Bayesian Regularization (BR) backpropagation approach in PV module output power estimation and fault detection. The measured PV module output power is fed to an ANN in order to detect any possible fault on PV module surface, for the first time, in this study. The full versions of our previously published studies that led to achieve the goals of this work are presented in the Appendices section.

Such PV module-level approach may be deployed in broader PV fleets by taking developmental requirements into consideration. The utilization of the PV output power estimation and fault detection system expectedly yields higher efficiency and lower support and maintenance costs for PV systems in long term.

Chapter 2

DATA ACQUISITION

The data sets used in this study consist of highly accurate experimental measurements and synchronized calculations collected during a three-month period from Nov. 1st, 2015 to Jan. 31st, 2016. A South oriented, 45° tilted monocrystalline silicon solar panel (P_{max}: 40 W, V_{OC}: 21.6 V, I_{SC}: 2.56 A) located at 35° 8' 51" N, 33° 53' 58" E, with 1 meter elevation from the sea level and a pyranometer at same location with same tilt and alignment are used for real-time measurement purposes. The Sun's position in the sky, the solar angle of incidence and the solar panel surface temperature are also calculated synchronously. Before proceeding to the data acquisition process, a preliminary review of solar energy characteristics and principals are beneficial to readers.

2.1 Solar Energy Characteristics

It is always desirable for anyone dealing with solar energy applications in any geographical location to be able to estimate the solar radiation intensity that is received on the Earth surface and is converted into energy by the solar systems. The spectral form of the solar energy determines the direction of sunlight beams (in terms of directly or diffusely emitted beams), as well as the geographical and time distribution of solar energy. Any estimation regarding the solar energy intensity should be made by considering the mentioned spectral form. There are several objects contained in the Earth atmosphere such as natural and artificial aerosols, cloud layers, etc. The interference of such factors make the estimation of solar radiation intensity at the

Earth's surface much more difficult as compared to the same estimation at the outer edge of the atmosphere.

The solar radiation estimation process can be explained in three main parts which are the position of the Earth and the Sun in our solar system, time systems and also the manner by which solar radiation passes through the atmosphere and reach the Earth's surface. The first part which deals with determination of the Earth's and the Sun's position in the solar system or more simply the Sun's position in the sky will be comprehensively explained due to its significant importance in solar radiation estimations. The latter two parts, time systems and solar beam behavior, will also be described briefly through this section. However, before proceeding to further definitions, a solar terminology overview is useful for readers.

2.1.1 Terminology

Some of the most common solar energy terms are briefly described as follows;

- ***Solar Radiation***: The complete spectrum of solar electromagnetic radiation emission.
- ***Insolation***: A quantitative rate which determines the amount of solar radiation received on a given surface area. The insolation (also called solar irradiation) may be measured in unit of Watts hour per meter square (Wh/m^2).
- ***Solar constant***: There is a significant difference in solar radiation intensity before and after entering the Earth's atmosphere due to the previously mentioned factors. The irradiance level of 1366 W/m^2 measured at the outer edge of the Earth's atmosphere (the solar constant) is reduced when received at the Earth's surface due to several interactions with different particles in the

atmosphere. The amount of 1000 W/m^2 is considered as the solar irradiance under Standard Test Condition (STC).

Annual Mean Insolation: As the name suggest, it is a measure of average solar power received on the Earth's surface in one year. The annual mean insolation maps of the World, Europe and Cyprus are given in Figures 2.1, 2.2 and 2.3, respectively.

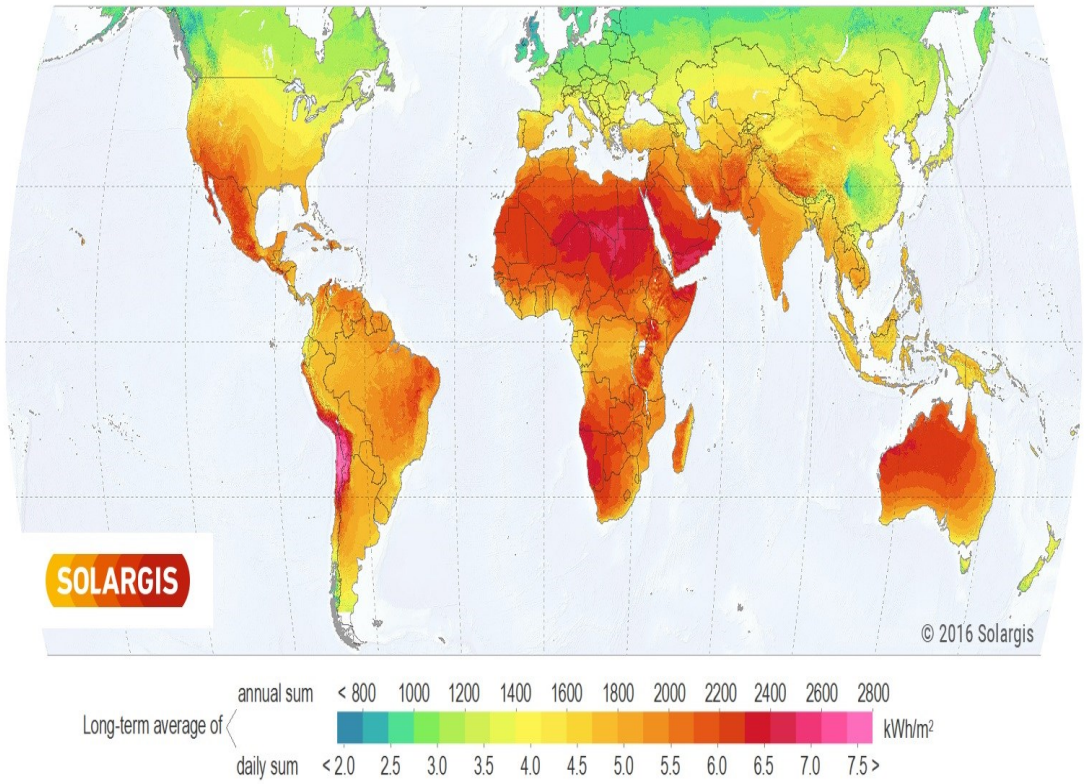

Figure 2.1: Annual Mean Insolation in the World [55]

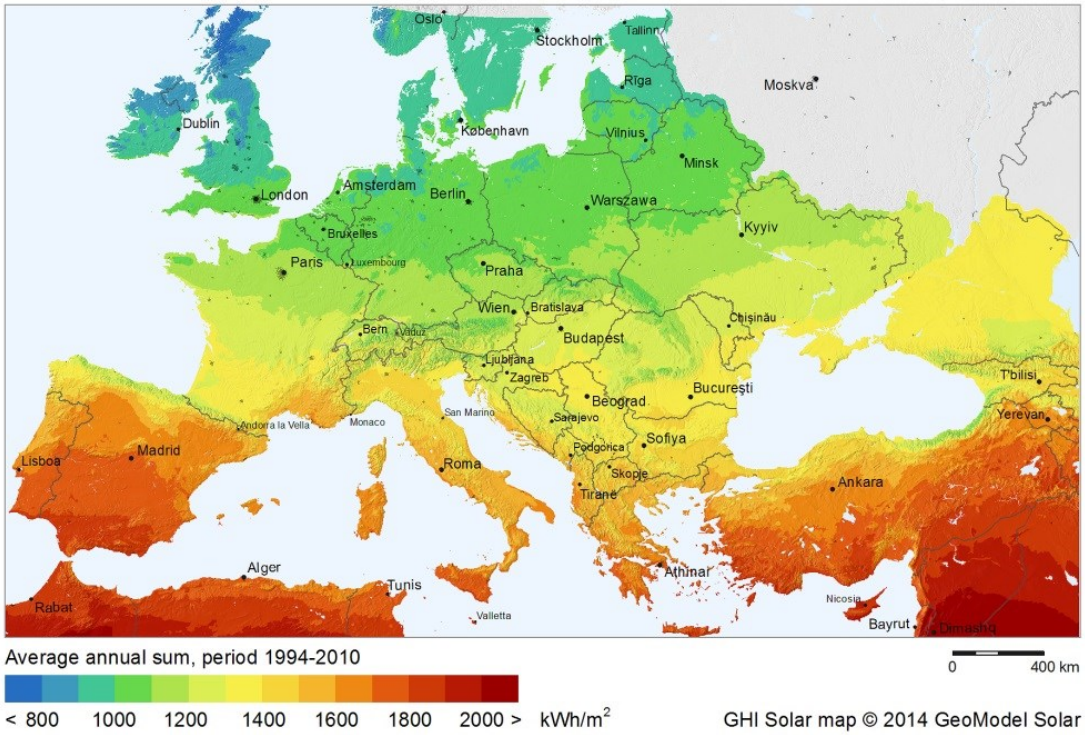

Figure 2.2: Annual Mean Insolation in Europe [55]

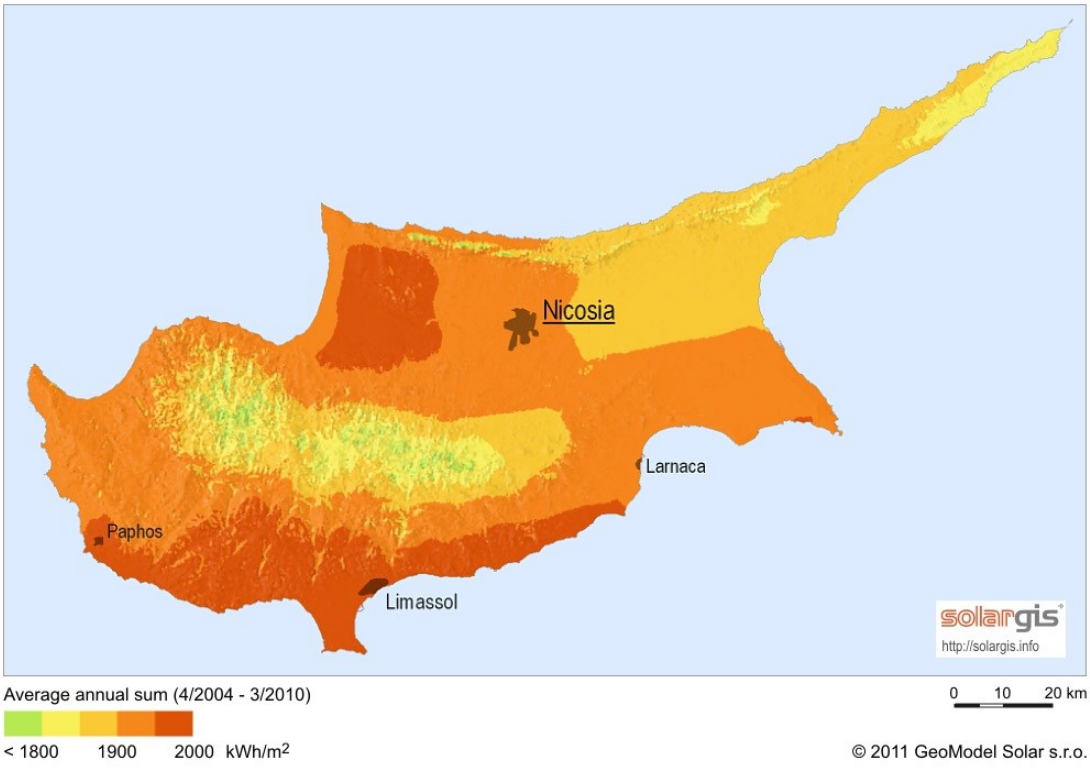

Figure 2.3: Annual Mean Insolation in Cyprus [55]

2.1.2 Solar Irradiance Spectrum

The range and intensity of the solar radiation wavelengths is rummaged via the solar irradiance spectrum. The solar radiation wavelengths range from 0.2 μm to 2.0 μm, while the wavelengths visible by human eye range between 0.4-0.8 μm (which correspond to colors violet and red). Figure 2.4 illustrates the solar irradiance spectrum and the human eye visible part within it. As obvious in the figure, the solar irradiance peaks around 0.5 μm.

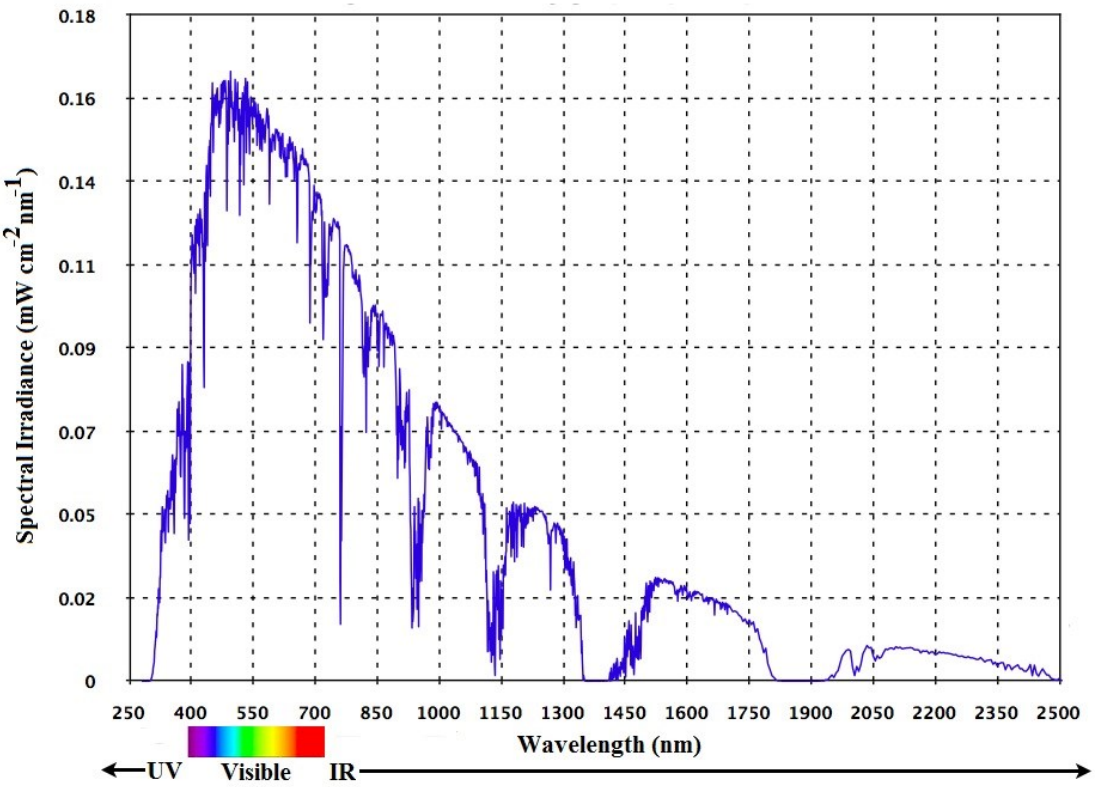

Figure 2.4: Spectrum of Solar Irradiance

2.1.3 Time Systems

Time systems are of significant importance in solar radiation estimation taking that the Sun's movement can be described as a function of time. Various time systems are characterized, the most significant of which are the Civil Time (CT), the Local Apparent Time (LAT), and the Universal Time (UT).

The CT is generally defined by latitude and longitude, by which the wavelength and the sunrise/sunset times are, respectively, determined. The time system also called the Local Mean Time (LMT) is introduced to ease the calculation for vast geographical area coverage. The LAT, also called the solar time, is mostly deployed in solar applications as an alternative to the CT. In LAT the solar noon is defined as the time at which the Sun passes the South axis which corresponds the highest elevation of the Sun in the sky. In this system, the sunrise/sunset times are independent of the longitude, oppositely to the CT. In UT, the Greenwich longitude (defined as zero) is the reference longitude. At longitude zero (Greenwich) there are differences between CT and LAT, as a consequence of the Earth's motion about its North axis, which is described by time equations. The time equation value varies based on the Julian day, which is illustrated in Figure 2.5.

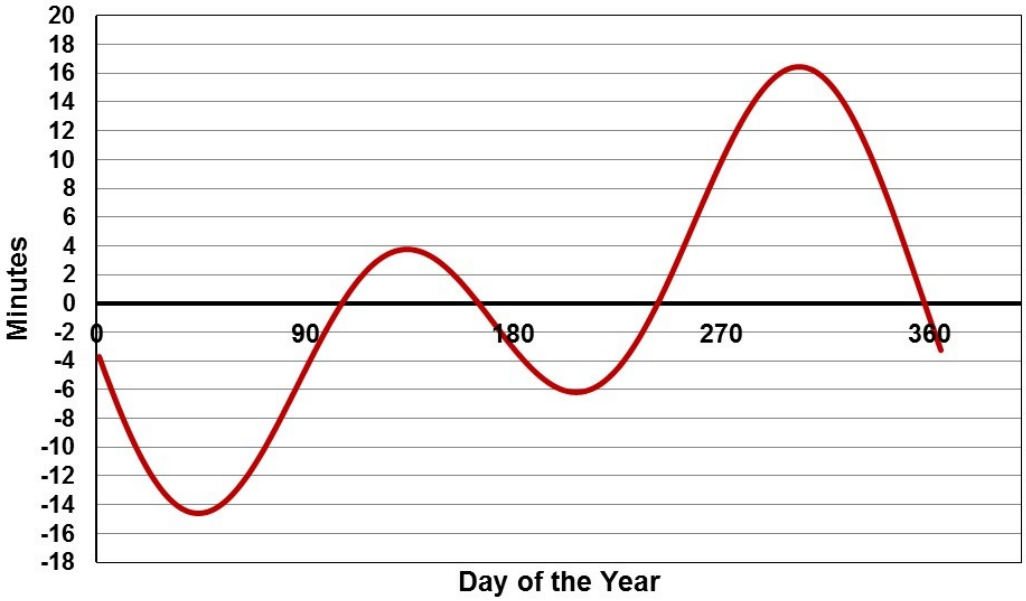

Figure 2.5: The Equation of Time Values [56]

The Julian day factor is comprehensively described further on in the Sun's position calculations. If Greenwich Mean Time (GMT) is taken as the observation point time zone, each degree of the longitude towards West refers to -4 minutes. The Central Europe Time (CET) leads the GMT by one hour. The relationship between the mentioned time zones is given by;

$$LAT = LMT + \frac{EoT+\lambda-\lambda_R}{15} - C \ (decimal\ hours) \tag{2.1}$$

where,

EoT : The equation of time

λ : Longitude (East Positive)

λ_R : Time Zone Longitude (East Positive)

C : The summer time improvement parameter (normally set to 1 for the countries in which the summer time is applied)

2.1.4 Extraterrestrial Solar Radiation

As previously described, the solar radiation intensity at the outer edge of the Earth's atmosphere is 1366 W/m^2. The Northern hemisphere is closer and further to the Sun in winter and summer, respectively, as a consequence of the Earth turning around the Sun in an elliptical orbit. 'Perihelion' happens on January 2nd and refers to the Earth's closest position to the Sun and 'Aphelion' happens on July 2nd when the Earth is in the furthest position to the Sun. The mentioned movement pattern is illustrated in Figure 2.6.

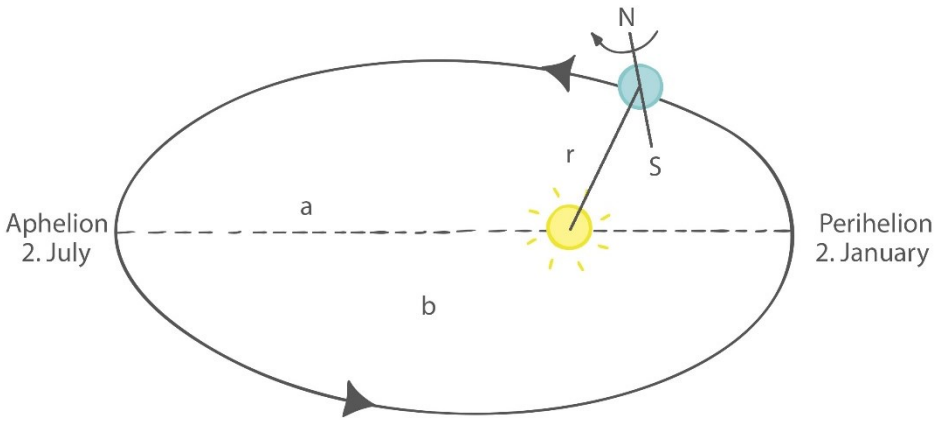

Figure 2.6: The Earth-Sun Movement Pattern

The distance between the Earth and the Sun may vary by ±1.7%. The solar constant value also changes by 1 W/m^2 in 11.2 years. The intensity of the irradiance hitting a horizontal surface outside the Earth's atmosphere is indicated by G_0 and calculated as follows;

$$G_0 = 1367\varepsilon \, sin(\delta_s) \; W/m^2 \tag{2.2}$$

where,

ε : The improvement parameter for solar range

δ_s : Altitude Angle of the sun

The following equation gives the correction factor to the mean solar range, ε;

$$\varepsilon = 1 + 0.0334\cos(j' - 2.80^{\circ}) \tag{2.3}$$

where,

j' : The day angle

G_{od} is described as the daily irradiation from sunrise to sunset measured in Wh/m^2. Figure 2.7 illustrates the G_{od} against latitude and Julian day number and Figure 2.8 shows the average solar irradiation received at the Earth's atmosphere.

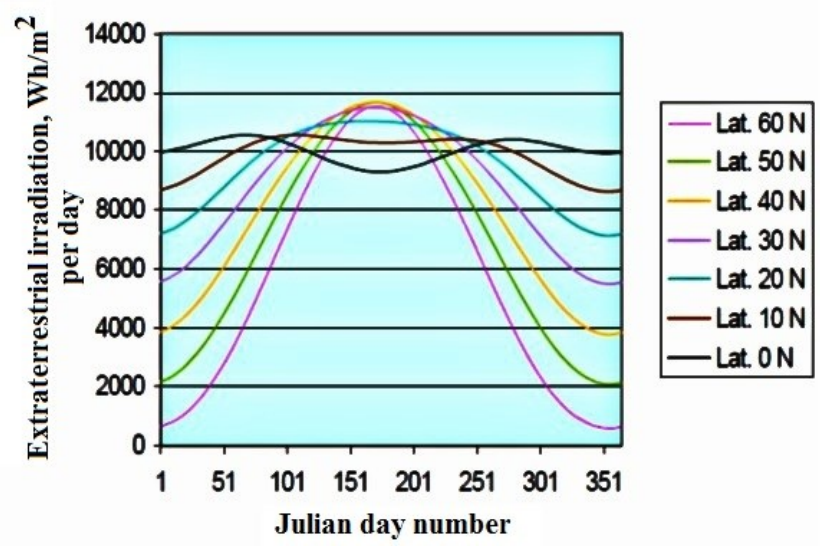

Figure 2.7: The Variations in G_{od} as a Function of the Julian Day Number and Latitude [56]

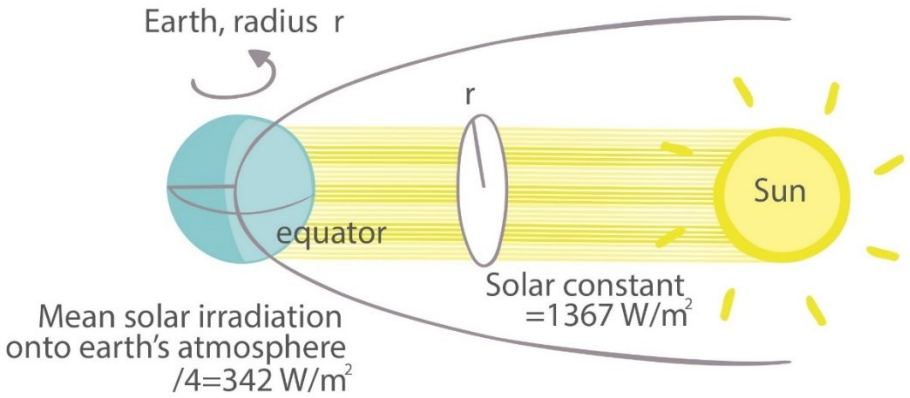

Figure 2.8: The Average Irradiance Hitting the Earth`s Atmosphere

2.1.5 Behavior of Sunlight Beams at the Earth's Surface

The solar beams go through several interactions while passing the atmosphere and reaching at the Earth's surface. The solar radiation intensity that is received on the Earth's surface after all those interactions is called the global irradiance. The most important fact for the solar practitioners is that the sunlight beams are decomposed into three components after passing the atmosphere. These are namely direct, diffuse and albedo components. The solar cells installed on the Earth's surface are interacting with all the mentioned solar radiation components.

The diffuse portion of solar radiation, as the name suggests, is the fraction of solar beams diffused (or scattered) by clouds, aerosols or other particles existing in the Earth's atmosphere. It can be easily predicted that on a cloudy day the solar cells that are installed in places without direct sunlight, are dominantly affected by the diffuse portion of the solar beams, while the cells that see the sunlight directly are mostly affected by the direct beams as a matter of fact. As previously mentioned, the last significant portion of the solar radiation corresponds to the beams that are reflected from the Earth's surface or from the objects on the Earth's surface. This last component, called the albedo component, generally has a minor effect on the solar cell performance but its effect becomes significant in locations near seashores or snowy mountains (like the Swiss Alps) due to the remarkable reflection of the solar beams from the sea or snow. The three solar radiation components are demonstrated in Figure 2.9.

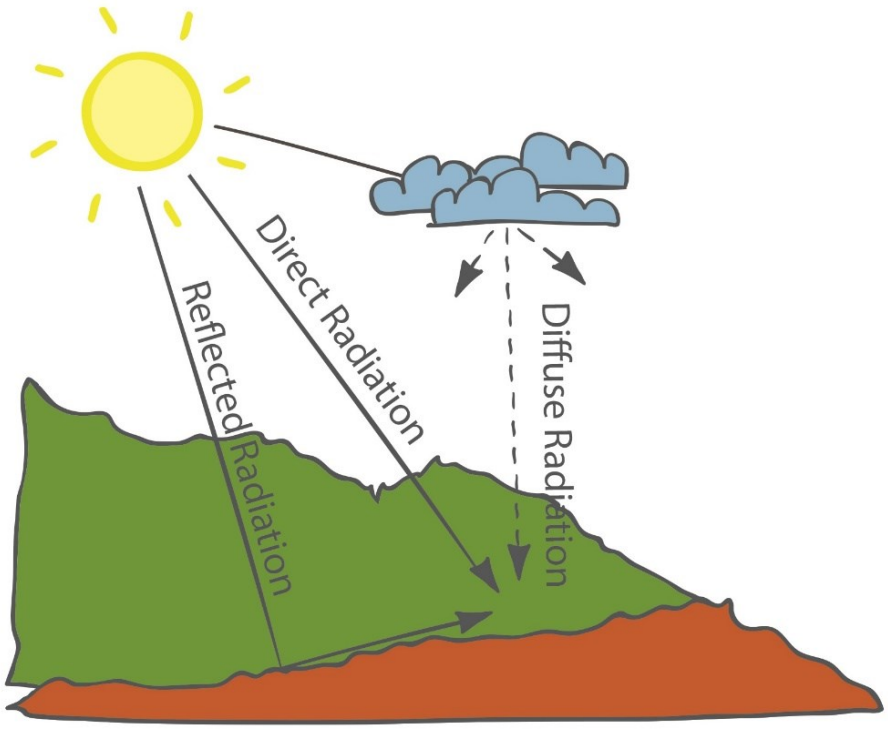

Figure 2.9: The Direct, Diffuse and Albedo Components of Solar Radiation

The solar beams go through several interactions with particles existing in the Earth's atmosphere which makes it difficult to estimate the global solar radiation received on the Earth's surface, especially on cloudy days. Particles like aerosols, water vapor, etc. in the atmosphere have different effects on solar beams, as some of these particles absorb and the others scatter the beams.

Generally, out of 100% of the solar beams entering the Earth's atmosphere;

- %20 are absorbed within the atmosphere.
- %23 diffused back to the space.
- %57 pass the atmosphere and reach the Earth`s surface.

The 57% of the solar beams reaching the Earth's surface is shared as 49% being absorbed and the rest 8% being reflected by the ground albedo effect.

2.2 The Sun's Position in the Sky

It is much needed to calculate the Sun's position in several solar energy research and application processes. The Sun's position in the sky is defined by the solar altitude and azimuth angles [55]. A general illustration of the Sun's position from the point of view of an observer on the Earth is given in Figure 2.10.

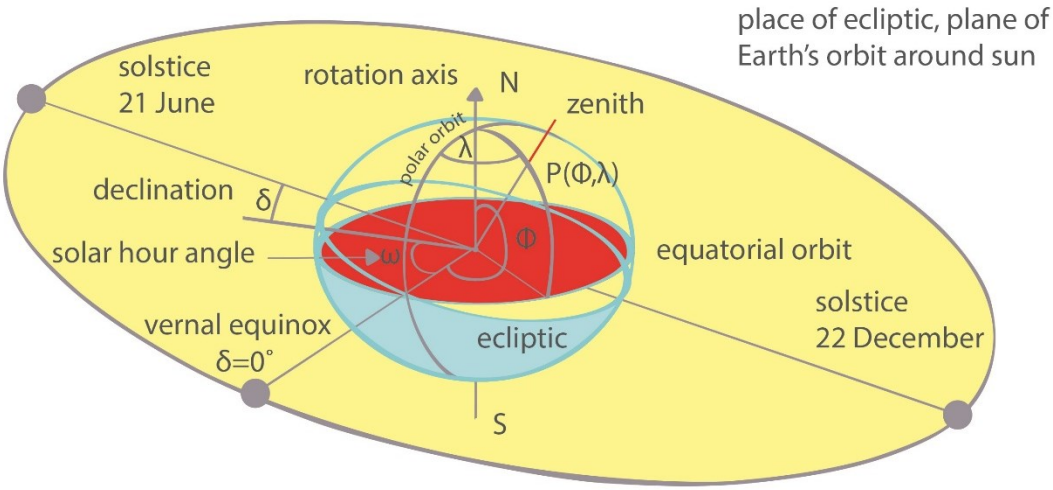

Figure 2.10: The Sun's Position as Observed from the Earth

The Sun's position estimation for every geographical location at any time instant is of crucial importance for solar researchers and practitioners. The main parameter used in such calculation are listed as follows;

- The latitude of the observation point
- The Julian day number
- The hour angle corresponding to the specific time instant

Each day of a year can be indicated by a number. Such enumeration can be carried out by the Julian day number according to Table 2.1.

Table 2.1: The Julian day number of the i^{th} day in a year

Month	**Julian Day Number**	**Leap Year**
January	i	
February	31+i	
March	59+i	(+1)
April	90+i	(+1)
May	120+i	(+1)
June	151+i	(+1)
July	181+i	(+1)
August	212+i	(+1)
September	243+i	(+1)
October	273+i	(+1)
November	304+i	(+1)
December	334+i	(+1)

The hour angle, ω, is used to define the time of day in degrees. It is set to zero for solar noon and shifted by 15° cycles for each hour. The hour angle can be calculated as;

$$\omega = 15(LST - 12) \tag{2.2.1}$$

The Local Solar Time (LST) slightly varies from the Local Time (LT) due to the atypicality of the Earth's orbit and the human regulations (such as time zone settings and daylight saving applications). The LST is expressed as;

$$LST = LT + \frac{TC}{60} \tag{2.2.2}$$

$$TC = 4(Longitude - LSTM) + EoT \tag{2.2.3}$$

$$EoT = 9.87\sin(2B) - 7.53\cos(B) - 1.5\sin(B) \quad (2.2.4)$$

$$B = \frac{360}{365}(j - 81) \quad (2.2.5)$$

$$LSTM = 15^\circ . \Delta T_{GMT} \quad (2.2.6)$$

where,

TC : Time Correction factor

EoT : Equation of Time

LSTM : Local Standard Time Meridian

ΔT_{GMT} : The difference of local time from Greenwich Mean Time (GMT)

2.2.1 The Declination Angle

One of the most significant factors in calculation of the Sun-Earth relationship is the declination angle which is represented by δ. The Sun's declination is a continually varying function of time. The declination measure changes throughout a day, but since it is a very small value, the daily declination rate is accepted as a constant. In order to calculate the solar declination for an instance, the only required parameter is the number of day in a year which is expressed by the Julian day number as previously discussed. Equation (2.2.7) is simply used for solar declination angle calculation.

$$\delta = \sin^{-1}\{0.3978\sin(j` - 80.2^0 + 1.92(\sin(j` - 2.80^0)))\} \quad (2.2.7)$$

$$j` = j \times 365.25 \quad (2.2.8)$$

where,

j : The Julian day number

$j`$: The Julian day angle

2.2.2 The Solar Altitude Angle

The solar altitude angle which determines the Sun's height or elevation in the sky is expressed as;

$$\gamma_s = \sin^{-1}(\sin\varphi\sin\delta + \cos\varphi\cos\delta\cos\omega) \quad (2.2.9)$$

where,

φ : The latitude of the observation point

δ : The solar declination angle, degrees

ω : The solar hour angle

The solar zenith angle is the complement of the solar altitude angle and is represented as;

$$Z_s = 90 - \gamma_s \quad (2.2.10)$$

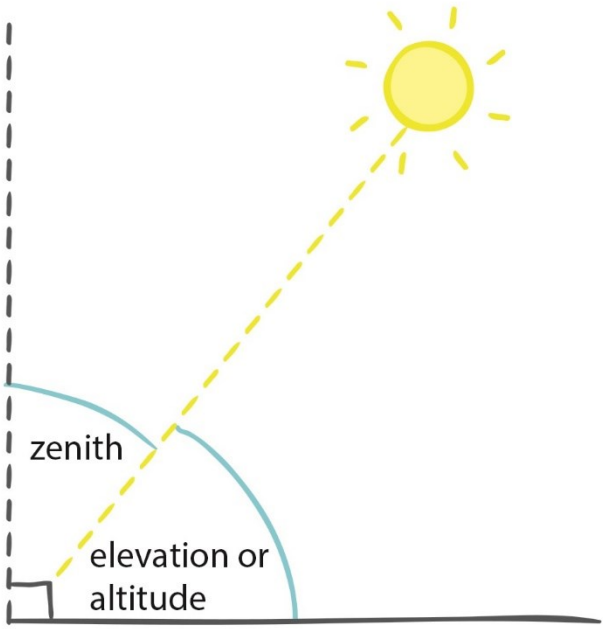

Figure 2.11: The Solar Altitude and Zenith Angles

The angle values which are calculated minute by minute on each data acquisition day are normalized in the range of 0-1 in order to be configured as appropriate inputs to the proposed ANNs. The normalization process yields data close to 1 for angle values that have the utmost effect on PV module power generation and data close to 0 vice versa. The normalized solar altitude angle values calculated minute by minute on Nov. 12th, 2015 as a typical data acquisition period are demonstrated in Figure 2.12.

As demonstrated in Figure 2.12, the normalized solar altitude angle takes on its highest values (indicating the Sun being in highest elevation in the sky) around solar noon.

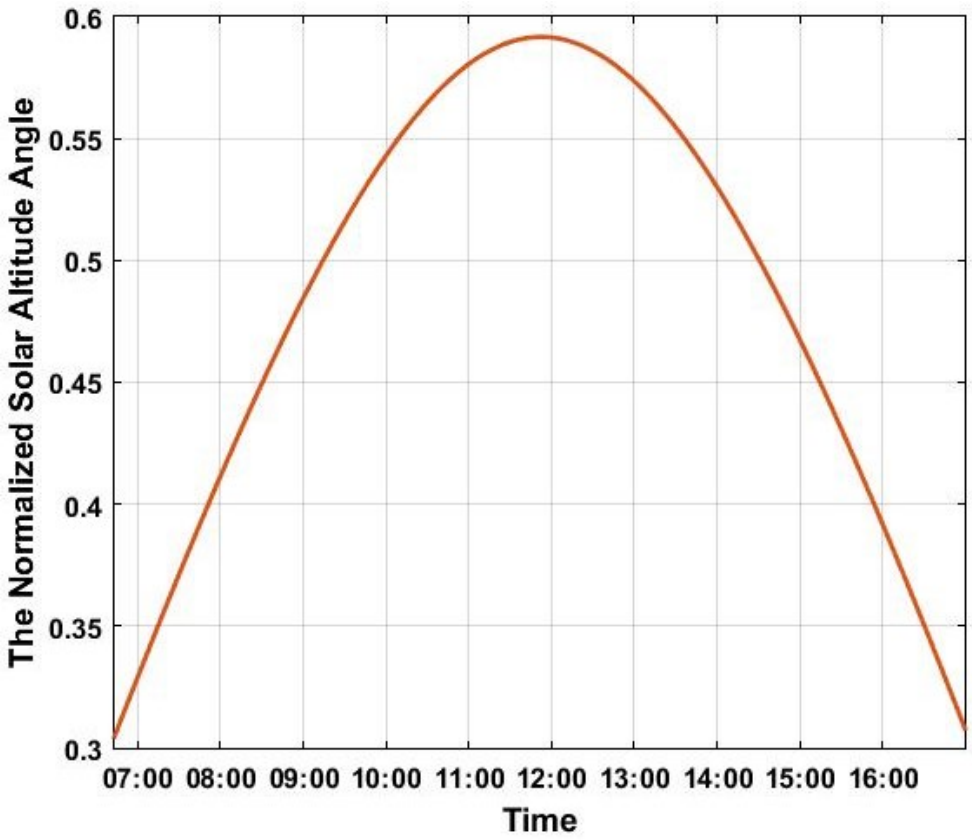

Figure 2.12: The Normalized Solar Altitude Angle Values Calculated on Nov. 12th, 2015

2.2.3 The Solar Azimuth Angle

The solar azimuth angle, which determines the Sun's deviation from North axis, is another important parameter in calculating the Sun's position in the sky. The solar azimuth angle is represented by the following equations;

$$\begin{cases} \alpha_s = 180 - \cos^{-1}(\cos \alpha_s) & \text{If } \sin \alpha_s < 0 \\ \alpha_s = 180 + \cos^{-1}(\cos \alpha_s) & \text{If } \sin \alpha_s > 0 \end{cases} \quad (2.2.11)$$

where,

$$\cos \alpha_s = (\sin \varphi \sin \gamma_s - \sin \delta) / \cos \varphi \cos \gamma_s \quad (2.2.12)$$

$$\sin \alpha_s = \cos \alpha_s \sin \omega / \cos \gamma_s \quad (2.2.13)$$

The solar azimuth angle is illustrated in Figure 2.13.

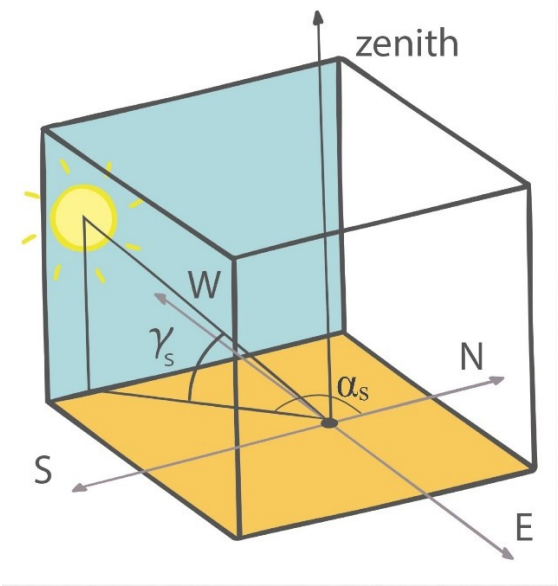

Figure 2.13: The Solar Azimuth Angle

Likewise the solar altitude angle, the solar azimuth angle values are also calculated on a minute by minute basis during the data acquisition period and the calculated angle values are normalized between 0 and 1 in order to be shaped as desirable ANN inputs. The normalization process is again carried out based on the effect of the angle value on the PV module power output (since the PV module is South oriented, the

normalized value takes on 1 when the Sun is exactly in South direction corresponding to the solar azimuth angle 180° and the normalized value takes on 0 when the Sun is in North direction with azimuth angle 0°).

The normalized solar azimuth angle values calculated minute by minute on Nov. 12th, 2015 as a typical data acquisition period are demonstrated in Figure 2.14. As demonstrated in the figure, the normalized solar azimuth angle peaks at solar noon indicating that the Sun is exactly in South direction.

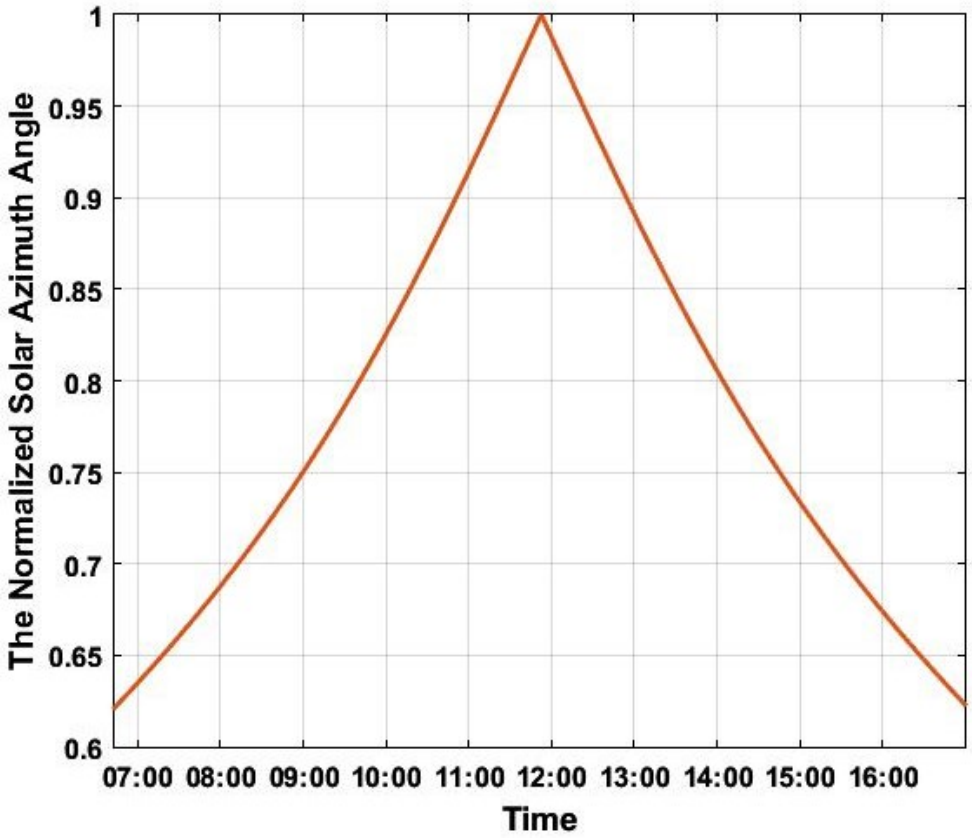

Figure 2.14: The Normalized Solar Azimuth Angle Values Calculated on Nov. 12th, 2015

2.2.4 Solar Angle of Incidence

The angle of incidence is defined as the angle between the emitted solar beams and a perpendicular vector on a PV module surface that receive the radiation. The accurate

calculation of this angle is of significant importance for the solar energy researchers and practitioners since the maximum power a PV module can produce is directly related to the cosine of this angle. The angle of incidence can be calculated by the following equation;

$$\theta = \cos^{-1}[\cos(\beta)\cos(Z_s) + \sin(\beta)\sin(Z_s)\cos(\alpha_s - \alpha_m)] \quad (2.2.14)$$

where,

β : Tilt angle of the solar collector (Horizontal: 0°)

Z_s : Zenith Angle of the Sun

α_m : Module azimuth angle (North: 0°, East: 90°)

A demonstration of the angle of incidence with respect to the Sun's position in the sky and the module azimuth angle is given in Figure 2.15.

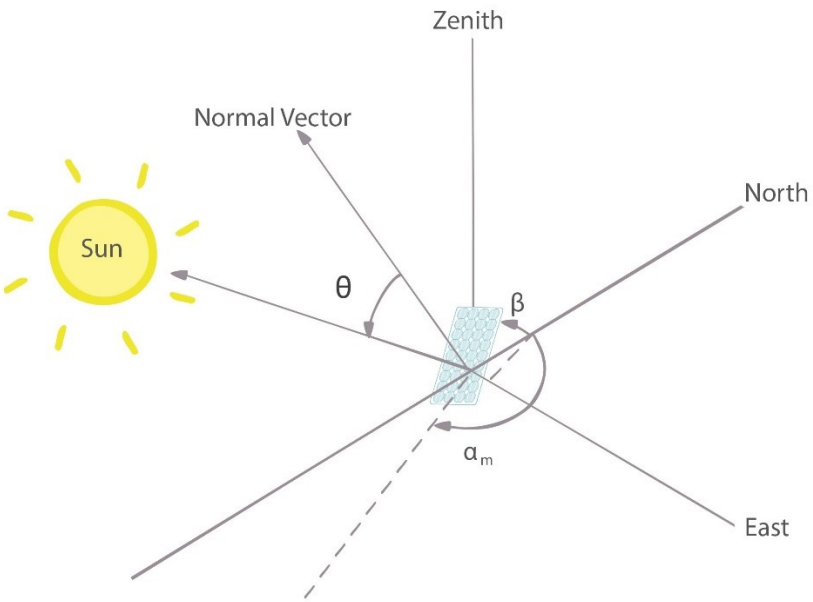

Figure 2.15: The angle of Incidence

The normalization of this last angle is carried out in the same manner of the previous angle value normalizations. Since the utmost effect of the Sun's position in the sky

corresponds to the solar beams hitting the surface of a PV module perpendicularly, the normalized incidence angle takes on value 1 when the incidence angle value is 0° and decreases to 0 as the angle between solar beams and PV module perpendicular vector increases. The normalized solar azimuth angle values calculated minute by minute on Nov. 12th, 2015 as a typical data acquisition period are demonstrated in Figure 2.16. The figure shows that the normalized incidence angle is at its highest position around solar noon when to solar beams hit the PV module surface perpendicularly.

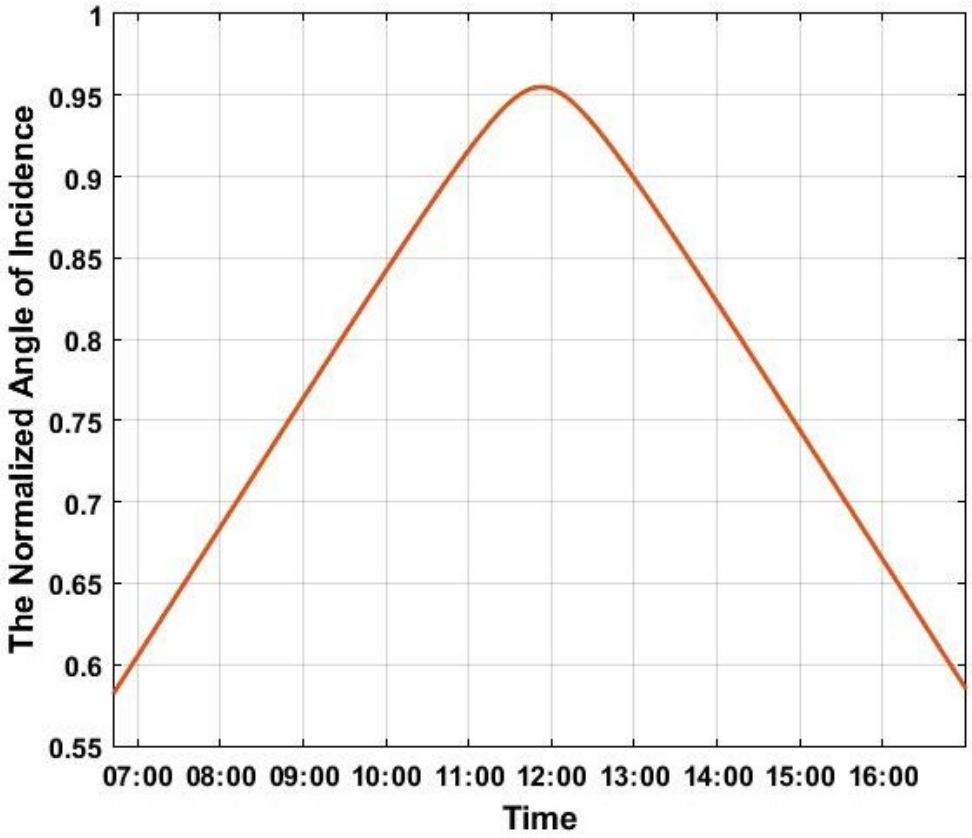

Figure 2.16: The Normalized Solar Azimuth Angle Values Calculated on Nov. 12th, 2015.

2.2.5 PV Module Output Power

The generated power of a South oriented 45° tilted PV module directly feeding a constant resistive load is measured (in W) during the mentioned three-month interval on per-minute basis and logged after being normalized in the range 0-1. The

normalized PV module output power is used as ANN target output and ANN input for estimation and fault detection purposes, respectively. The normalized PV module output values logged on Nov. 12th, 2015, Dec. 17th, 2015 and Jan. 12th, 2016 corresponding to typical clear, overcast and partly cloudy data acquisition periods are given in Figure 2.17.

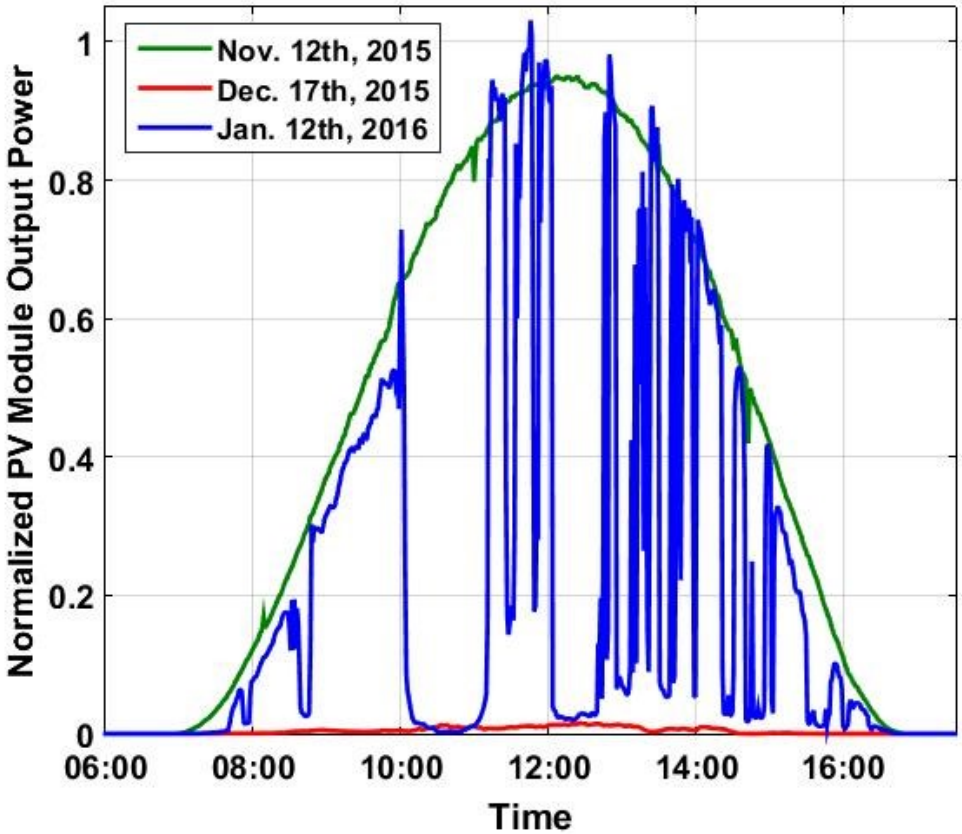

Figure 2.17: The Normalized PV Module Output Power Values, Measured per-minute in (W) on Nov. 12th, 2015, Dec. 17th and Jan. 12th, 2015

2.2.6 The Irradiance Level

A pyranometer at same location with same tilt and alignment of the PV module is used for minute by minute measurement of irradiance level (in W/m^2) during the three-month data acquisition period. The collected data is normalized in the range 0-1 to be prepaid as proper ANN input. The normalized irradiance values logged on Nov. 12th,

2015, Dec. 17th, 2015 and Jan. 12th, 2016 corresponding to typical clear, overcast and partly cloudy data acquisition periods are given in Figure 2.18.

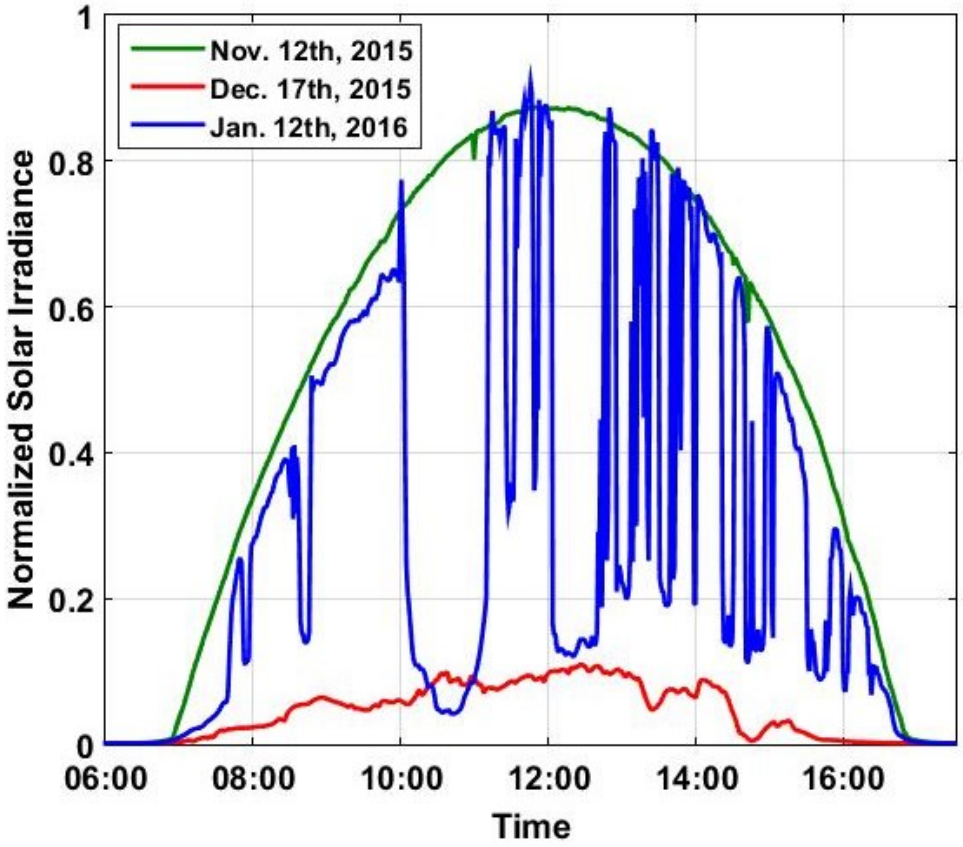

Figure 2.18: The Normalized Irradiance Values, Measured Minute by Minute in (W/m^2) on Nov. 12th, 2015, Dec. 17th and Jan. 12th, 2015

2.2.7 PV Module Surface Temperature

Another important parameter in determination of a PV module output power is the PV module surface temperature. As discussed earlier, electrical power is generated as solar beams hit the surface of a PV module by the PV effect. However, another effect of solar beams hitting the surface of a PV module is the increment of the PV module surface (and PV cell) temperature. Taking the fact that the power generation trend of a PV module decreases with increasing cell temperature, the temperature issue gains significant importance in PV power estimation. There are several ways of PV module surface temperature measurement, the most straight forward one being the direct usage

of surface temperature sensors. Nevertheless, alternative methods of surface temperature prediction or calculation suggest less sensor dependent systems. For example the ANN based PV module surface temperature estimation is carried out in [57].

Another method for PV module surface temperature determination is suggested in [58], where the PV module surface temperature can be calculated as a function of the Nominal Operating Cell Temperature (NOCT), ambient temperature and irradiance level (E_{tot}) using the following formula;

$$T = T_{ambient} + ((NOCT - 20°C)(E_{tot}/800\ Wm^{-2})) \quad (2.17)$$

As previously mentioned, the PV power generation tendency decreses with increasing cell temperature. Therefore, the normalization process of this parameter in the range 0-1 is performed accordingly, yielding values close to 1 for lower surface temperatures and valuess close to 0 for higher temperature (in other words, higher normalized values for higher PV power generation and vice versa).

The meteorological information obtained real-timely from the Larnaca international airport (LCLK) and the synchronizedly measured irradiance values are used for the PV module surface temperature calculation. The normalized PV module surface temperature values calculated on Nov. 12th, 2015, Dec. 17th, 2015 and Jan. 12th, 2016 corresponding to clear, overcast and partly cloudy days, respectively, are given in Figure 2.19.

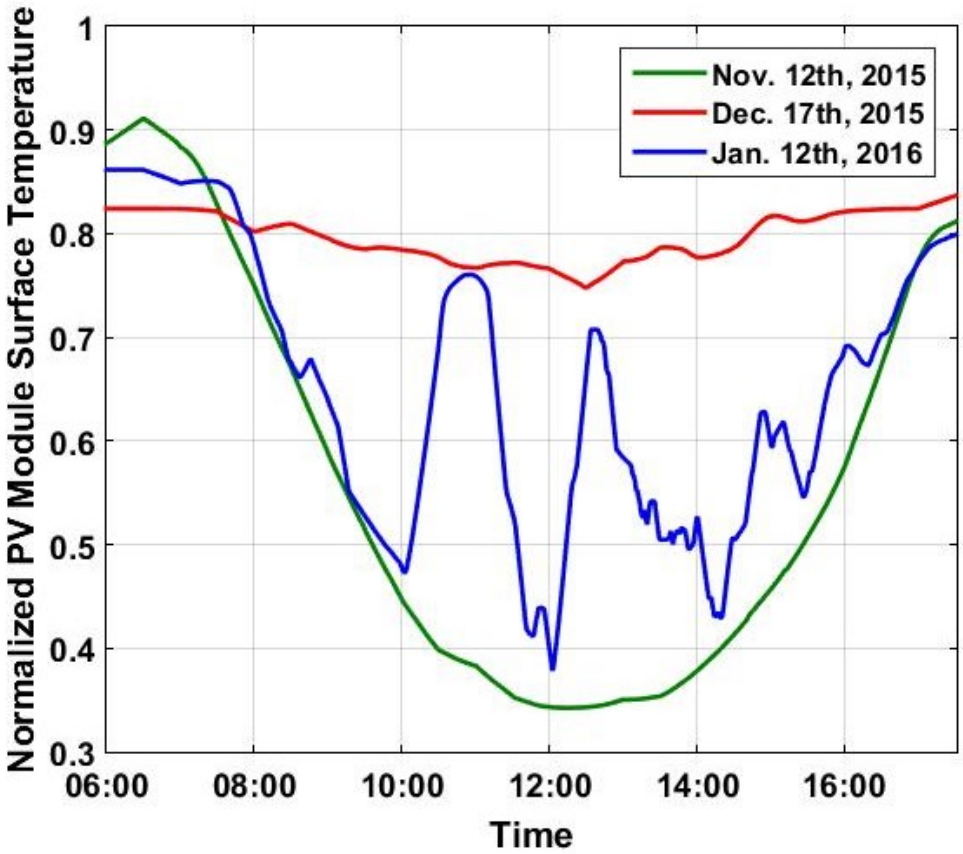

Figure 2.19: The Normalized PV Module Surface Temperature Values, Calculated Minute by Minute in (°C) on Nov. 12th, 2015, Dec. 17th and Jan. 12th, 2015

Summarizing the above, the PV module output power (W) and the irradiance rate (W/m^2) are measured minute by minute while the Sun's position in the sky, the incidence angle and the PV module surface temperature values are calculated real-timely and synchronously during the three-month data acquisition interval from Nov. 1st, 2015 to Jan. 31st, 2016.

The collected data is normalized in the range 0-1 in order to be formed as suitable input/output data for the ANNs. The details of ANN development with the above mentioned input/outputs for PV module power estimation and fault detection will be comprehensively described in the following chapter.

Chapter 3

INVESTIGATION OF THE APPROPRIATE ANN

The scope of this study is to develop an artificial neural network-based method for PV module output power estimation and fault detection. It is intended to investigate the competency of the well-known Multi-Layer Perceptrons (MLPs) with appropriate back-propagation techniques and sufficient input amount. In this regard, two ANNs are eventually evolved for PV power estimation and fault detection objectives after preliminary research and development stages. The comprehensive details of creation and validation of the proposed ANNs are given in this section.

The competency of the Levenberg-Marquardt (LM) and the Bayesian Regularization (BR) back-propagation algorithms are investigated for PV module power estimation. The normalized values of the solar altitude angle, the solar azimuth angle, the angle of incidence, the irradiance level and the PV module surface temperature collected during Nov. 1st, to Nov. 25th, 2015 are fed to the ANNs as input values. While the input data set corresponds to severe meteorologically fluctuating intervals, the noise in data is tolerable due to the sensitivity of the utilized measurement equipment and accuracy of the calculations. The target output presented to the ANNs during the learning phase is the normalized PV module output power collected during the mentioned interval. All input/output data sets are consisting per-minute accurate measurements and calculations. The two ANNs are both of feed-forward MLP architectures with one

hidden layer consisting of 15 neurons. The ANN architecture shown in Figure 3.1 is constructed for further analysis.

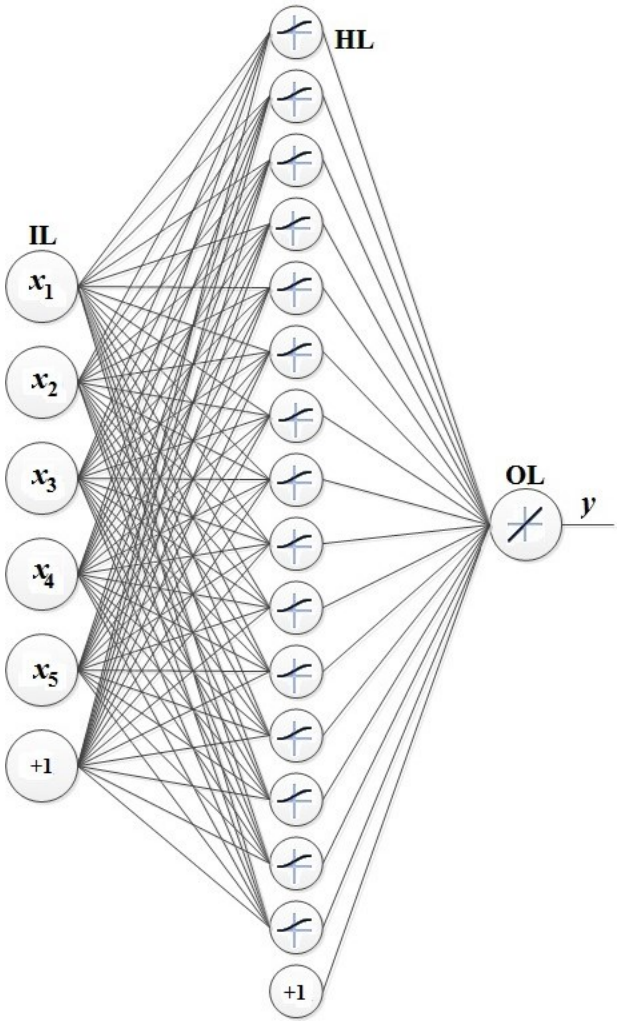

Figure 3.1: The Proposed ANN Architecture. (x_1: Normalized γ_s, x_2: Normalized α_s, x_3: Normalized θ, x_4: Normalized E_{tot}, x_5: Normalized T, y: Normalized PV Module Output Power, IL: Input Layer, HL: Hidden Layer, OL: Output Layer

The reason that 15 is decided to be the size of the proposed ANNs' hidden layer is that it is experimentally validated that a lesser size lacks the desirable estimation accuracy while a larger size is highly computational time and memory consuming with no more contribution to the estimation accuracy. The transfer or activation functions are log-sigmoid and purelin in hidden and output layers, respectively. The mentioned

activation functions are formulated in equations (3.1) and (3.2) and illustrated in Figure 3.2.

$$logsig(n) = \frac{1}{1 + e^{-n}} \tag{3.1}$$

$$purelin(n) = n \tag{3.2}$$

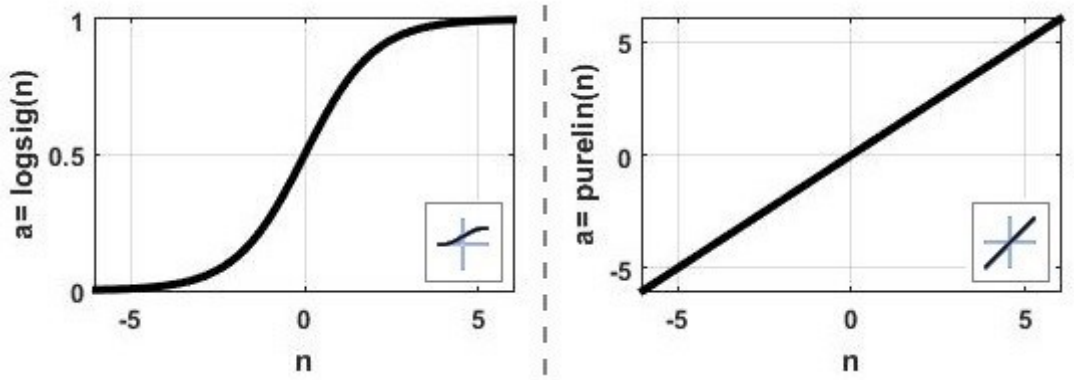

Figure 3.2: ANN Hidden and Output Layer Activation Functions

Random small values are assigned to the network weights and the inputs are fed to the input layer at the beginning of the ANN training process. Since the network is of feed-forward architecture, the input data only propagates in one direction through the network layers until it reaches the output layer. At this stage, the error is calculated based on the specified error function to compare the resultant output and the target output. The target output is used to supervise the learning process of the ANN. Furthermore, the calculated error is back-propagated in the network and the weights are adjusted according to the weight update rules. Both error functions and network weight update rules are specified by the selected training algorithm. This process is repeated until the training error falls below a pre-set threshold. The training error threshold should neither be too loose nor too tight, and should be set appropriately in order to save the network from either being under-fitted or over-fitted. An under-fitted

network lacks precision while an over-fitted network accustoms to the training inputs and fails in generalizing outputs for new and unseen inputs.

The effectiveness of the BR algorithm is better expressed by the fact that the algorithm eliminates the redundant network weights (weights that do not affect the problem solution) and performs better in passing the local minima obstacles. Also the BR algorithm does not require cross validation (as opposed to the LM algorithm) which saves a significant part of data from being reserved for validation process. Also the BR algorithm saves the ANNs from being over-trained or over-fitted.

As mentioned before, the ANN training, testing and validation data sets were acquired during Nov.1st to Nov. 25th, 2015 and the ANN implementation period is selected as Nov. 26th, to Dec. 7th, 2015. 10695 combinations of data, each consisting of 5 inputs and 1 output, are presented to the ANNs as training input and target output during the supervised ANN training, testing and validation processes. The 5 training inputs being the normalized values of the solar altitude and azimuth angles, angle of incidence, irradiance and PV module surface temperature are presented at the input layer in each iteration. The normalized input values are processed through the hidden layer by log-sigmoid activation function and are passed to the output layer containing a single neuron with linear transfer function. At this stage, the resultant output is compared to the target output (which is in the range 0-1) and after the error is calculated by the corresponding error or cost function, it is back-propagated in the network and the corresponding update rule is applied to the network weights in order to decrease the error for the next iteration. After several epochs of error back-propagation and network weight adjustments the pre-set training error threshold is satisfied and the network becomes ready to make generalization for new inputs without any target output

presented. As previously described, the objective is to save the ANNs from being under-fitted or over-fitted. The training goal is very significant in this case. A loose training goal develops a weak network incapable of making accurate estimations and a tight training goal forces the network to produce outputs highly similar to the training targets and results in development of a network incapable of making generalization for new inputs. In this regard, the minimum gradient of 1.0e-10 is set as the training goal for both ANNs in order to obtain both precision and generalization capabilities at the same time.

The first ANN is created and 70% (7487 paths) of the data collected during data acquisition period is allocated to the ANN training phase. Inputs and targets are presented to the network in this phase and the network weights are adjusted based on the LM algorithm. In order to measure the generalization capabilities of the ANN, another 15% (1604 paths) of data is presented to the network during the validation phase. At this point, the network is supposed to be ready to make estimations and generalization. Therefore, the testing phase is initiated independently than the training and validation phases with the remaining 15% (1604 paths) of data in order to measure the performance of the network. In this last phase, no output targets are presented to the network in order to rate the network estimation and generalization capabilities. This whole process ends when the validation procedure stops making more generalizations.

The same procedure is followed for development of the second ANN. As mentioned before, the BR algorithm does not require validation processes, thus 85% (9091 paths) and 15% (1604 paths) of the collected data are allotted to the second ANN training and testing processes, respectively. It is clear that the BR algorithm has saved 1604

paths of data from being reserved for validation purposes. The mentioned paths are also added to the training data sets and the whole process stops at the pre-set 1000 back-propagation epochs limit. Figure 3.3 shows the regression plots of the two ANNs with different training algorithms.

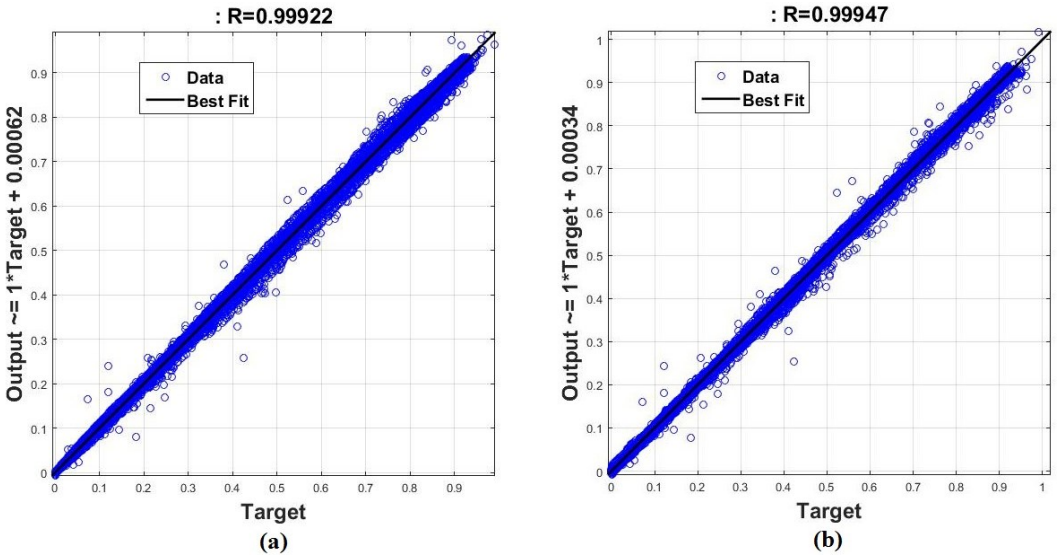

Figure 3.3: The Regression Plots of (a) Levenberg-Marquardt and (b) Bayesian Regularization Training Backpropagation Algorithms

The performance details of the ANN training, testing and validation processes for LM and BR are given in Table 3.1. The Mean Absolute Error (MAE) and the Mean Absolute Percentage Error (MAPE) values between the ANN predicted and the measured PV module output power values for the ANNs implementation period from Nov. 26th, to Dec. 7th, 2015 are given in Table 3.2. In order to have reasonable and robust MAPE calculations, the overcast sky days are excluded from Table 3.2. (In an overcast sky day when almost no electrical power is generated by a PV module, a measured power value of '0 W' and an estimated power value of '0.001 W' yield 100% MAPE, which makes no sense in terms of statistical analysis).

Table 3.1: Performance metrics of the Levenberg-Marquardt (LM) and the Bayesian Regularization (BR) training backpropagation algorithms

Performance Metrics	**Levenberg-Marquardt (LM) Algorithm**	**Bayesian Regularization (BR) Algorithm**
Best Training Performance	1.2549e-04	1.0211e-04
Best Validation Performance	1.3365e-04	Not applied in BR
Best Testing Performance	1.0787e-04	1.0418e-04
No. of Training Epochs	162	1000
Best Training Epoch	154	1000
Minimum Gradient	6.2957e-06	1.2496e-08
Training Time (in Seconds)	16.27	114.53

Table 3.2: The Mean Absolute Error (MAE) and the Mean Absolute Percentage Error (MAPE) between the Estimated and the Measured PV Module Output Power Values for Different ANN Implementation Periods

ANN Implementation Period	**Mean Absolute Error(LM) (mW)**	**Mean Absolute Error(BR) (mW)**	**Mean Absolute Percentage Error (LM)**	**Mean Absolute Percentage Error (BR)**
November 26th, 2015	1.45	1.42	7.05%	5.87%
November 27th, 2015	1.12	0.94	5.62%	5.43%
November 28th, 2015	1.58	1.04	5.74%	4.54%
November 29th, 2015	1.82	1.29	9.74%	6.28%
December 2nd, 2015	1.7	0.93	7.33%	4.77%
December 7th, 2015	2.16	0.71	3.18%	2.06%
Average	1.64	1.05	6.44%	4.83%

The developed ANNs with LM and BR algorithms are implemented from Nov.26th, to Dec. 7th, 2015. The meteorological conditions during the mentioned period varies from smooth clear to highly fluctuating partly cloudy conditions. The aim is to investigate the PV module output power estimation capabilities of the ANNs with different training algorithms. For better expression of the ANN performances, scatter graphs of ANN-estimated vs. real-timely measured PV module output power for sample implementation days, Nov. 26th, Nov. 28th, and Dec. 7th, 2015, with highly fluctuating partly cloudy, partly cloudy and clear sky weather conditions, respectively, are given in Figure 3.4-a, 3.4-b and 3.4-c. Also the plots of the BR-based ANN-estimated and the measured PV output power for the same days are given in Figure 3.5-a, 3.5-b and 3.5-c.

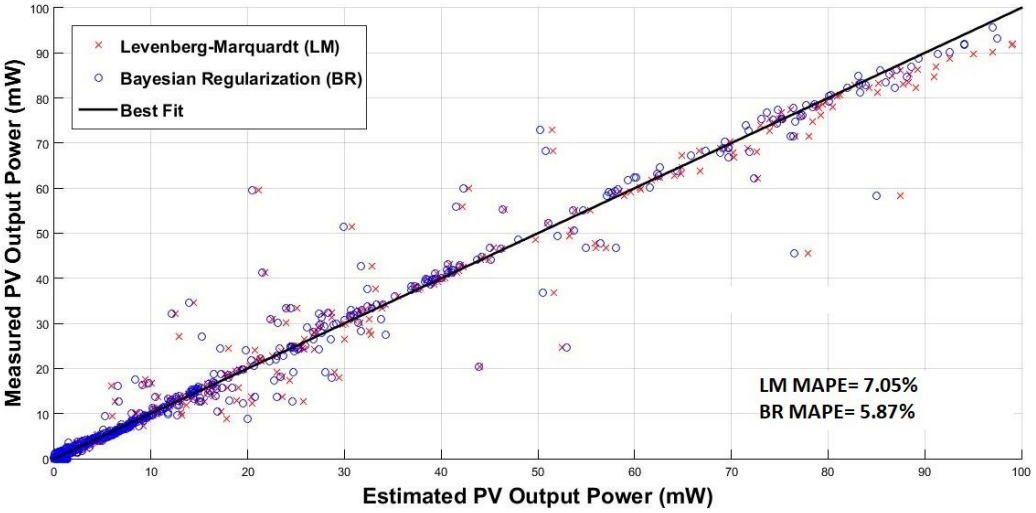

(a)

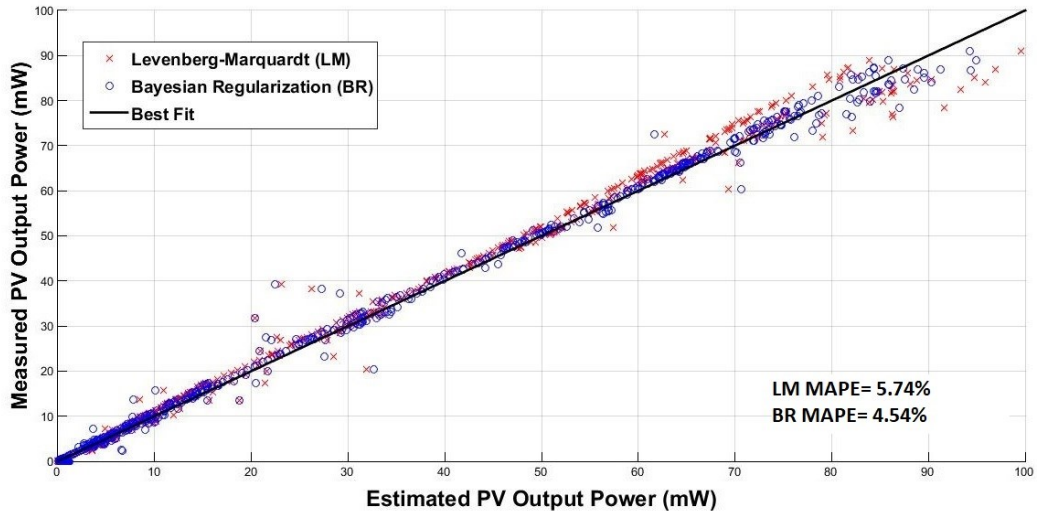

(b)

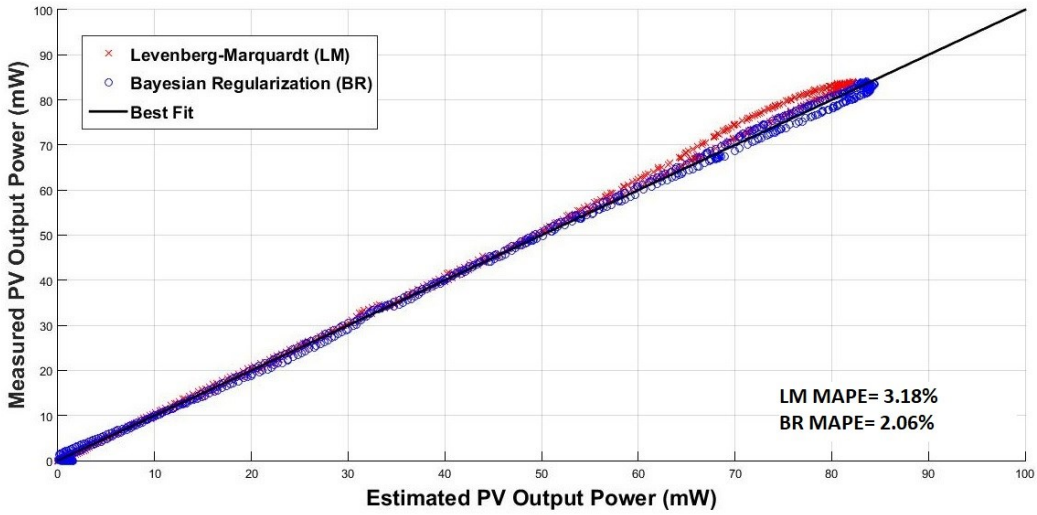

(c)

Figure 3.4: The Measured vs. the Estimated PV Module Output Values for ANNs Implemented by the LM and the BR Algorithms on (a) November 26th, 2015, (b) November 28th, 2015 and (c) December 7th, 2015

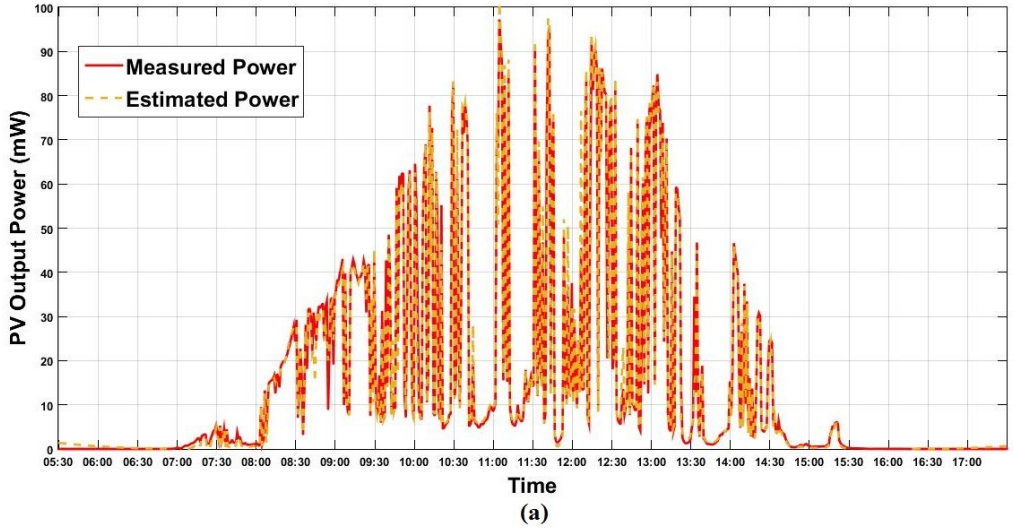

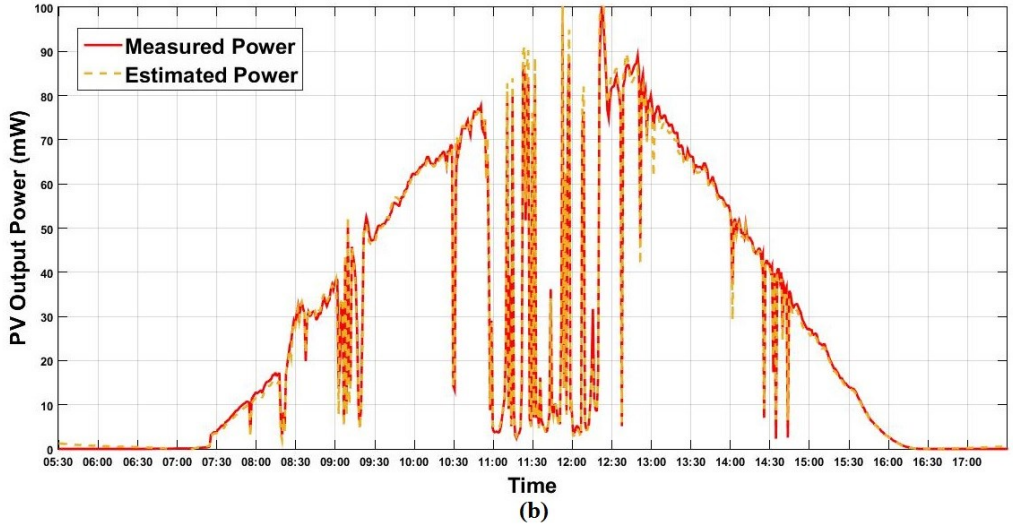

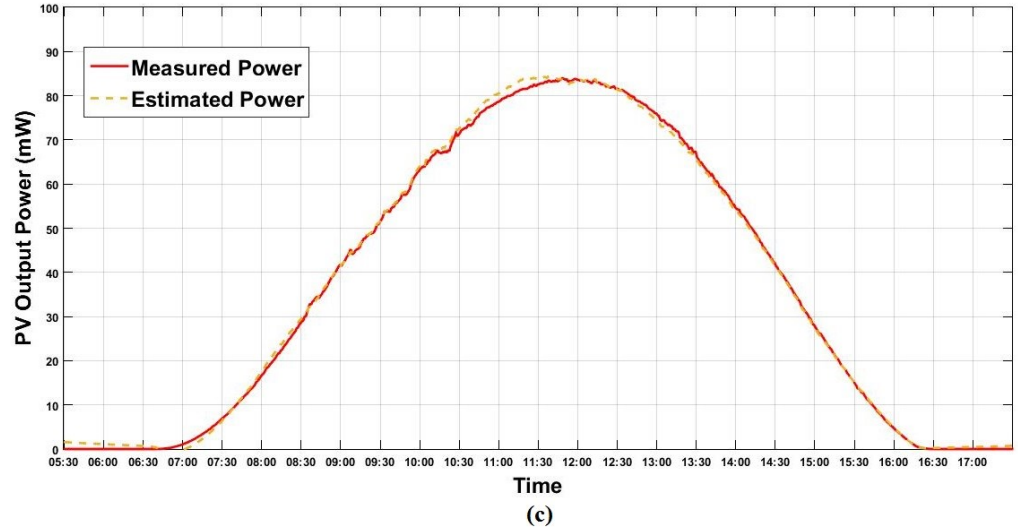

Figure 3.5: The Measured and the Estimated PV Module Output Power Values for ANN Implemented by BR Algorithm on (a) November 26th, 2015, (b) November 28th, 2015 and (c) December 7th, 2015

It is obviously expressed by the scatter graphs of Figure 3.4 that the BR algorithm outperforms the LM algorithm in terms of ANN development for PV module output power estimation. The results were expectable taking that the BR training back-propagation algorithm is known to work well with relatively large-sized, noisy and rigid data as previously mentioned. Although the indicated performance improvement for a single PV module output power estimation may appear to be relatively small, such improvement gains significant importance when the application is expanded to broader PV fleets after taking necessary developmental considerations. The average MAE and MAPE between the estimated and the measured PV module generated power for the ANN implementation period (Nov.26th, to Dec.7th, 2015) are calculated as 1.64 (mW) and 6.44%, respectively, for the ANN with the LM algorithm, while these values are decreased to 1.05 (mW) and 4.83% by utilizing the BR as the training algorithm for the ANN. Taking the above accuracy metrics into consideration, it is concluded that the BR back-propagation algorithm is the right choice for ANN-based PV module output power estimation applications.

3.1 Development of a Preliminary Artificial Neural Network

At this stage, a possible approach would be directly proceeding to develop the final ANNs for PV module output power estimation and fault detection. However, it is intended to launch a preliminary ANN (hereinafter called 'PANN') using a portion of collected data in order to investigate any possible deficiency or difficulty as well as to have statistical measures of ANN implementations with different data sizes. The latter would determine either increasing the data size beyond a certain point provides significant improvement to the ANN performance or some convergence is achieved in terms of ANN estimation accuracy with sufficiently-sized data.

In this part, over 20,000 paths of data collected during a two-month period from Nov. 1st, to Dec. 31st, 2015 is used as a fraction of total data, in order to train, test and implement an ANN for PV module output power estimation. The developed ANN is of the same architecture demonstrated in figure 3.1, with the previously described and examined BR back-propagation training algorithms and the same input/output data of the normalized values of per-minute measurements and calculations utilized for ANNs developed in this section.

After the three-layer ANN with log-sigmoid and purelin activation functions in the hidden and the output layer is launched, 85% (17581 paths) of data collected during the mentioned two-month period is fed as training inputs to the ANN input layer and the training process is carried out based on BR back-propagation algorithm. Minimum gradient of 1.0e-12 is set as the training performance goal. A more rigorous training goal is set for this ANN compared to the previously developed ANNs, and also the training data size is increased to more than double, therefore it is of no surprise that the network went through a tougher training process and satisfied the desired training goal in 1169 back-propagation epochs. As previously mentioned the BR algorithm does not require cross validation process so the rest 15% (3103 paths) of data is allotted to the testing phase. In the testing phase no target output is presented to the network in order to examine the generalization capabilities and precision of the ANN. The performance plot of the ANN training and testing process showing the best training performance (3.4032e-04) achieved at epoch 1169 is given in Figure 3.6. The regression plot of the ANN training and testing processes is given in Figure 3.7, and the performance metrics of the ANN training and testing processes is given in Table 3.3.

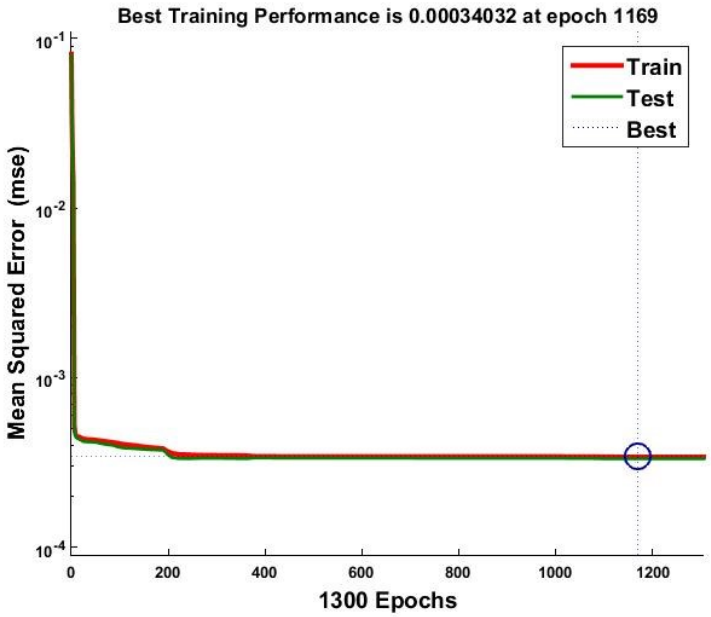

Figure 3.6: The Performance Plot of the ANN Training and Testing Processes

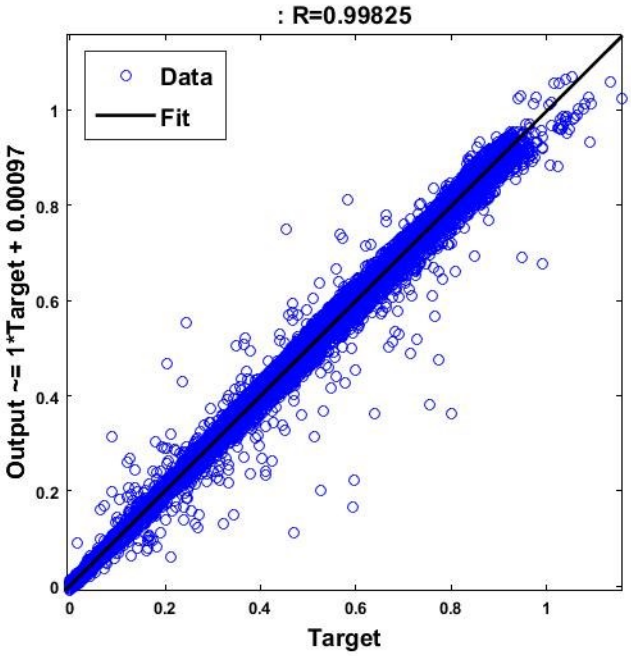

Figure 3.7: The Regression Plot of the ANN Training and Testing Processes

Table 3.3: Performance metrics of the ANN training and testing processes

Training Function	**'trainbr'**
Best Training Performance	3.4032e-04
Best Testing Performance	3.3219e-04
No. of Training Epochs	1300
Best Training Epoch	1169
Minimum Gradient	9.0682e-09
Training Time (in Seconds)	277.16

3.2 Implementation of the PANN

The developed PANN is implemented in a 15-day period from Jan 1st, to Jan. 15th, 2016 corresponding to highly various meteorological conditions ranging from clear to overcast sky situations. The measured and the PANN-estimated PV module output values are compared during this interval, while the monitoring results for highly meteorologically similar consecutive days are excluded from further analysis. In order to proceed to analytical results, on each day of the PANN implementation during 5:30 to 17:30 the previously mentioned normalized input values are collected minute by minute and fed to the PANN and the ANN output is derived, while the PV module output power is also measured and logged synchronously. After reconstructing the ANN output from its normalized form, at the end of each day 721 pairs of data consisting of ANN-estimated and experimentally measured PV module output power are established. In order to better represent the ANN performance, a scatter graph of per-minute comparisons of the estimated vs. the measured PV module output power values during Jan 1st, to Jan 15th, 2016 is given in Figure 3.8.

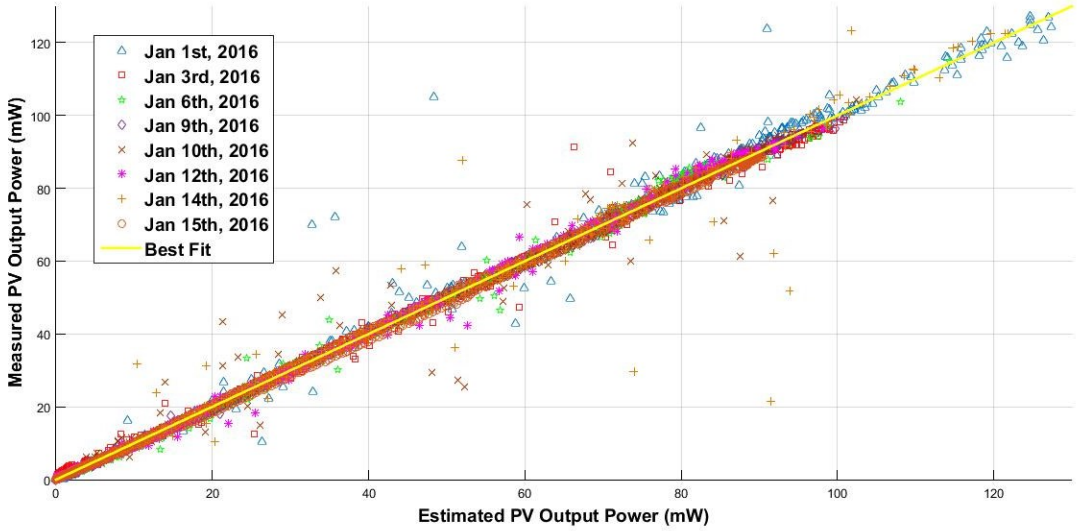

Figure 3.8: The estimated vs. the measured PV output power values (mW) for different ANN implementation days

The PANN-estimated and the measured PV module output power values for Jan. 1st, Jan. 10th, and Jan. 15th, 2016, corresponding to various meteorological conditions are demonstrated in Figure 3.9-a, 3.9-b, 3.9-c, and hourly averages of irradiance level, measured and estimated PV power, Mean Absolute Error (MAE) and Mean Absolute Percentage Error (MAPE) between the measured and the estimated power values for the same interval are given in Table 3.4. For this analysis, the mean of each mentioned parameter for each hour from 5:30 to 17:30 on each PANN implementation day is calculated. In order to obtain statistically reasonable values, the MAPE calculations for solar altitude angle below 5.5° which correspond to almost zero output power are omitted. The MAE and the MAPE between the measured and the estimated PV module output power values for PANN implementation days are given in Table 3.5.

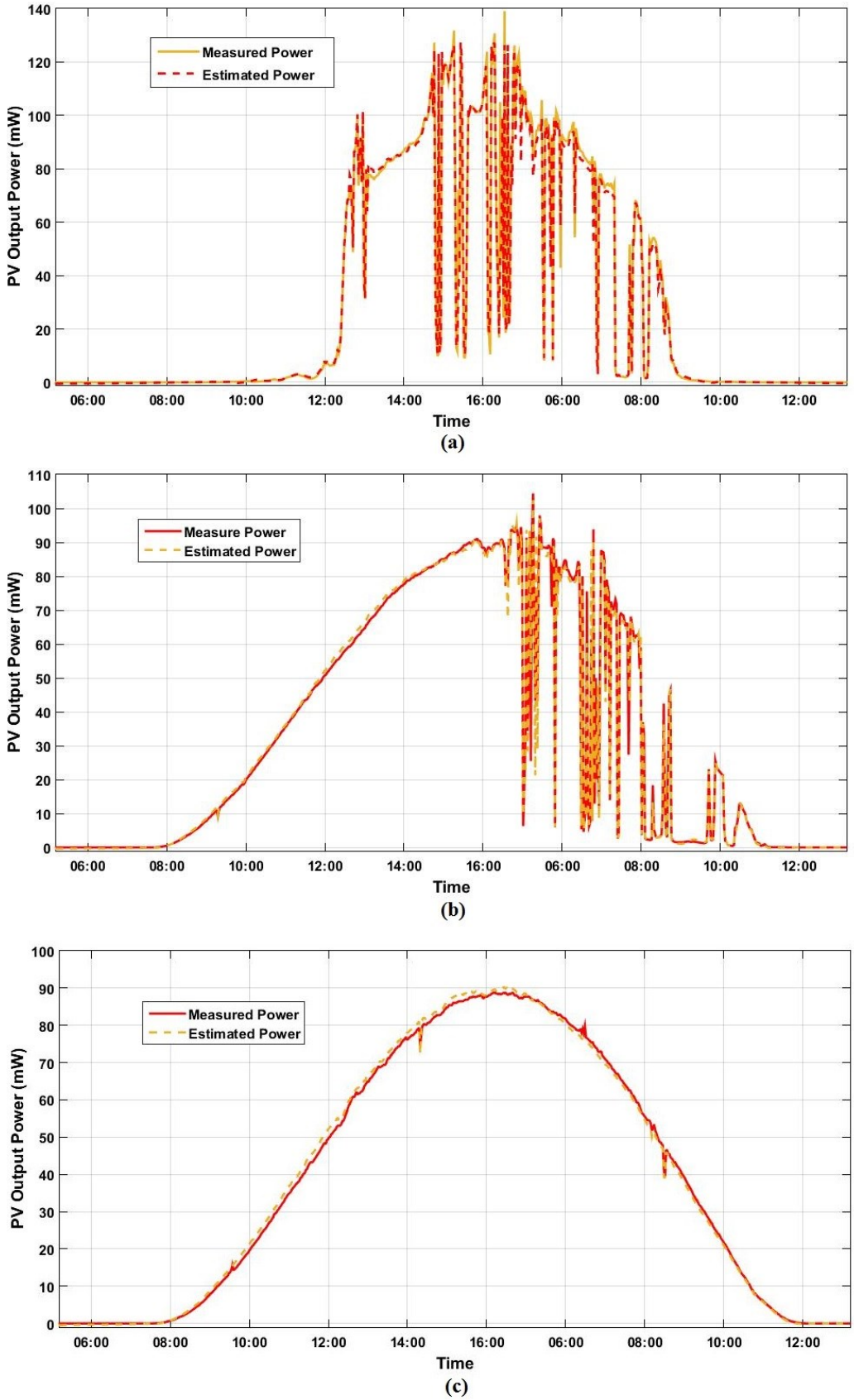

Figure 3.9: The Measured vs. the Estimated PV Module Output Power Values for ANN Implementations on (a) Jan. 1st, (b) Jan. 10th, and (c) Jan. 15th, 2016

Table 3.4: Hourly averages of irradiance level, measured and estimated PV power, Mean Absolute Error (MAE) and Mean Absolute Percentage Error (MAPE) between the measured and the estimated power values for the ANN implementation days during Jan. 1st to Jan 15th, 2016

	5:30-6:29	**6:30-7:29**	**7:30-8:29**	**8:30-9:29**	**9:30-10:29**	**10:30-11:29**	**11:30-12:29**	**12:30-13:29**	**13:30-14:29**	**14:30-15:29**	**15:30-16:29**	**16:30-17:30**
Irradiance (W/m^2)	1.94	36.96	273.50	532.25	761.34	809.12	857.30	901.38	791.42	518.07	260.66	15.35
Measured PV Power (mW)	(≈ 0)	0.27	7.66	26.01	51.02	62.70	70.19	72.68	56.17	26.43	6.96	(≈ 0)
Estimated PV Power (mW)	(≈ 0)	0.19	8.04	26.71	52.18	62.88	69.87	71.91	55.21	25.60	6.69	(≈ 0)
Mean Absolute Error (mW) (MAE)	(≈ 0)	0.10	0.38	0.71	1.15	0.71	0.69	1.52	1.21	0.84	0.27	(≈ 0)
Mean Absolute Percentage Error (MAPE)	---	---	%5.17	%2.84	%2.20	%1.14	%1.02	%2.10	%2.10	%3.34	%6.28	---

Table 3.5: The MAE and the MAPE between the measured and the estimated PV module output power values

	Mean Absolute Error (mW) (MAE)	**Mean Absolute Percentage Error (MAPE)**
Jan. 1st, 2016	1.32	4.76%
Jan. 3rd, 2016	0.86	3.43%
Jan 6th, 2016	0.97	4.00%
Jan 9th, 2016	0.66	2.78%
Jan 10th, 2016	1.22	3.70%
Jan 12th, 2016	0.68	5.16%
Jan 14th, 2016	1.29	4.56%
Jan 15th, 2016	0.98	4.01%
Average	0.9975	4.05%

The PANN implementation during Jan 1st, to Jan 15th, 2016, corresponding to highly fluctuating meteorological conditions, yields an average MAE and average MAPE between the measured and the estimated PV module output power values of 0.9975 (mW) and 4.05%, respectively. The performance of the PANN with BR training algorithm is expectedly promising and provides conceivability for development of the final ANNs with full training data to be utilized for the PV module output power estimation and fault detection.

Chapter 4

DEVELOPMENT OF THE ULTIMATE ANNS

In this final section, the development process of the ultimate ANNs for PV module output power estimation and fault detection is comprehensively described. The details of suitable ANN input/output measurements and calculations, as well as the appropriate ANN architecture and algorithms are thoroughly reviewed in previous sections. Also a preliminary ANN is developed and implemented in order to figure out any possible inconvenience prior to proceeding to final ANN designs. The final ANNs are developed considering all the mentioned investigations, with training data collected in a per-minute basis during a three-month period from Nov. 1st, 2015 to Jan 31st, 2016, corresponding to highly variable winter meteorological conditions. Around 30,000 paths of healthy and faulty data are rigorously acquired during the mentioned time interval in order to be fed to different ANNs for estimation and detection purposes. The details of artificial fault applications on PV module, as well as the development and implementation processes of the ANNs are given through this section.

4.1 Artificial Fault Application on PV Module

Around 30,000 paths of healthy and faulty data are collected during data acquisition period. Healthy data, which refers to the data collected during normal operation periods of the PV module is used for development of an ANN (similar to the PANN, described in sub-section 3.2.1) for PV module output power estimation. Faulty data, which correspond to data collected during faulty PV module operation intervals is

mixed with the healthy data in order to develop an ANN for PV module fault detection. There are several possible sources of fault associating with PV module operation which are reviewed in the introduction section with corresponding references. In this study coating glasses of different shades of gray color are used in the data acquisition phase in order to simulate faulty PV module operation conditions. Other faults are also applied to the PV module in the ANN implementation period in order to test the generalization capability of the system for unseen faults.

The two coating glasses used to simulate faulty PV module operation conditions, are of two different shades of gray color. The glasses hereinafter called 'lightgray' and 'dimgray' to express their transparency levels, are used to cover the PV module surface and simulate faulty operation situations caused by shading effects and dirt/dust accumulation on panel surface. In order to better express the PV module output power degradation by each artificial fault (lightgray and dimgray coating glasses), a comparison is carried out based on the faulty PV module output values and the expected fault-free PV module output values. The expected fault-free PV module output power values are obtained using the ultimate ANN developed for PV power estimation (to be described in next sub-section). In this regard the inputs corresponding to the faulty PV module operation period is fed to an ANN only trained on healthy data and the ANN output, which is expectedly higher than the measured PV output power is logged as the expected fault-free operation output power. The performance analysis of the measured and the expected PV module output power, obtained by averaging the mentioned values acquired during the fault application intervals, is given in Table 4.1, the plots of the measured and the expected PV module output power for sample fault application days are given in Figure 4.1, and a scatter graph of the

measured vs. the estimated PV module output power for overall faulty operation intervals is given in Figure 4.2.

Table 4.1: The performance analysis of the PV module output power during the overall faulty operation intervals

	Maximum Measured Power (mW)	**Maximum Expected Power (mW)**	**Mean Absolute Error (MAE) (mW)**	**Mean Absolute Percentage Error (MAPE)**
Lightgray	114.52	140.74	13.72	≈ 25%
Dimgray	54.95	128.87	24.82	≈ 55%

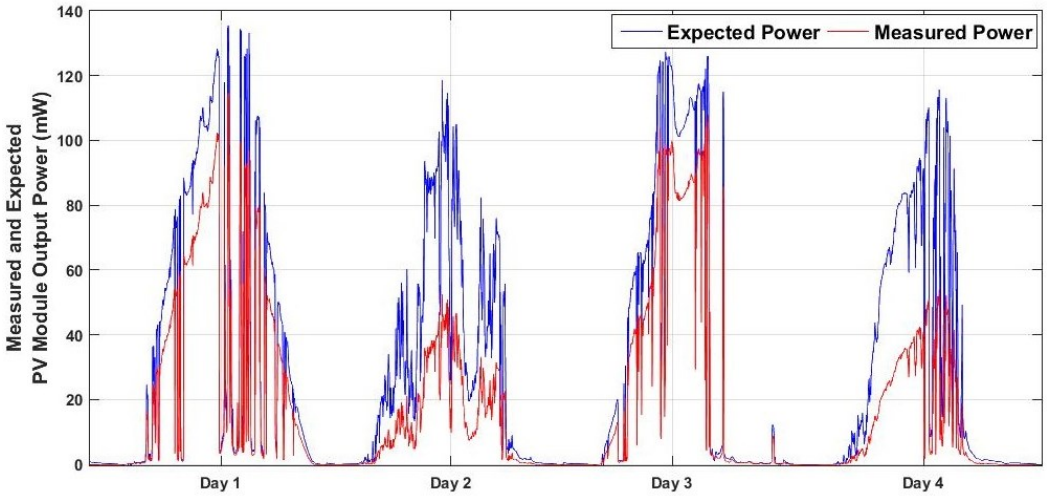

Figure 4.1: The Measured vs. the Expected PV Module Output Power for Sample Days of Faulty Operation Under Lightgray (Day 1 and Day 3) and Dimgray (Day 2 and Day 4) Shading Conditions

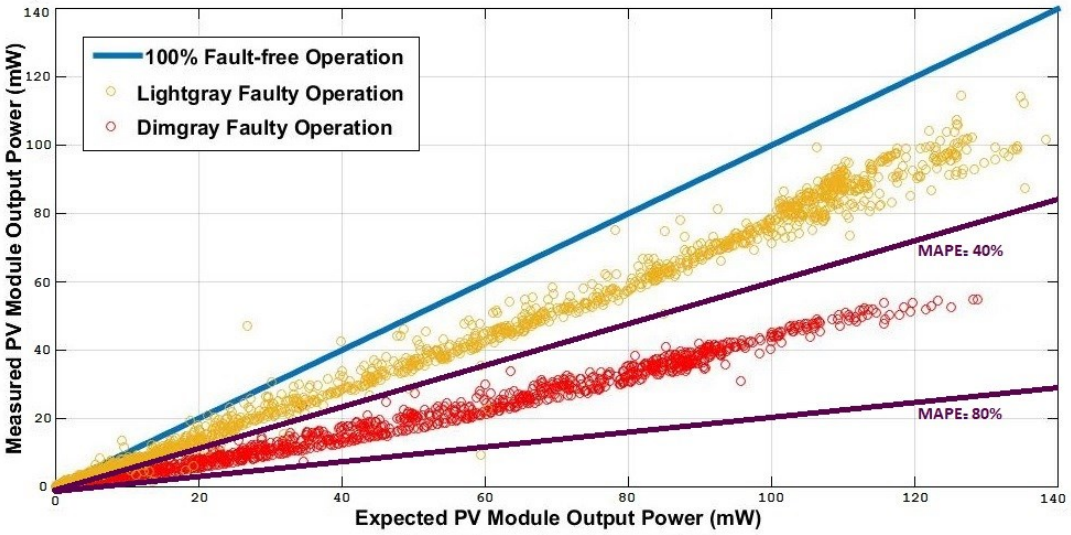

Figure 4.2: The Measured vs. the Estimated PV Module Output Power for Overall Faulty Operation Intervals

The mentioned coating glasses cover the entire PV module surface homogenously. The homogeneous fault application to a PV module surface makes the resulting output power degradation independent of the internal PV module architecture. As discussed in [59], PV modules are formed by a collection of PV cells interconnected in series and/or parallel in order to meet eligible voltage and current requirements. PV arrays are also formed by different interconnections of PV modules. Further analysis of various interconnection architecture effects on PV output characteristics may be investigated in [60,62]. The series-parallel, bridge-link and total-cross-tied, illustrated in Figure 4.3, are the most commonly utilized configurations in PV application. Considering that all of the mentioned architectures are expanded versions of series and parallel interconnections, behavioral investigation of the series and parallel interconnected PV cell/modules gains significant importance in PV power generation analysis.

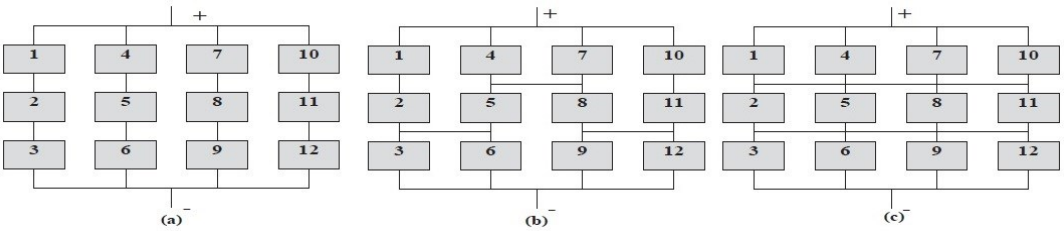

Figure 4.3: The (a) Series-Parallel, (b) Bridge-Link and (c) Total-Cross-Tied Configurations of PV Cells/Modules

- ***Series Connection of PV Cells***

  A series connection of PV cells is maintained in order to meet eligible voltage requirements. The voltage, current and power produced by series connected PV cells is expressed as follows;

$$V_{output} = \sum_{i=1}^{n} V_i \tag{4.1.1}$$

$$I_{output} = I_1 = I_2 = \cdots = I_j \tag{4.1.2}$$

$$P_{output} = V_{output} \times I_{output} = \sum_{i=1}^{n} V_i \times I_j \tag{4.1.3}$$

  The series connected cells produce higher amount of voltage values, but even if one cell in the configuration is subjected to damage, shading effects, etc. and lacks in producing the same current amount as other normal operating cells, the whole string current is limited to the current produced by the faulty operating cell. Therefore, the total power output generation of a series cell configuration is dependent to the operation of each contributing cell.

- ***Parallel Connection of PV Cells***

  Parallel connected PV cells/modules are configured in order to meet desirable current values. The voltage, current and power characteristics of parallel connected PV cells are given as;

$$V_{output} = V_1 = V_2 = \cdots = V_i \tag{4.1.4}$$

$$I_{output} = \sum_{j=1}^{n} I_j \tag{4.1.5}$$

$$P_{output} = V_{output} \times I_{output} = \sum_{j=1}^{n} V_i \times I_j \tag{4.1.6}$$

The parallel connected PV cells/modules are not as sensitive to faults as the series connected cells/modules. In essence, the faulty operation of one cell/module in a parallel connected configuration yields lesser overall output power loss comparing to series configuration.

As briefly described, the reaction of a PV module to non-homogenous fault condition, such as one or more shaded/damaged cell(s), depends on the internal PV module configuration in terms of PV cell interconnections. The ideal situation, which is far from reality, is that there be a bypass diode connected to each cell in a PV module, so that the faulty operation of each cell being bypassed and the overall PV module output power degrade only by the proportion of faulty operating cells to the total number of cells containing in the module. However, this is not applicable and faulty operation of one or more cells results in higher output power degradations in commercial PV modules compared to the imaginary ideal PV module.

Also besides making the PV module output power independent of the internal architecture, the homogeneous fault application investigated in this study provides the possibility of expanding the proposed PV module-level fault detection to broader levels after taking necessary developmental observations.

4.2 Development of ANN for PV Module Output Power Estimation

A three-layer fully-connected feed-forward neural network with log-sigmoid and purelin transfer functions in hidden and output layers is developed for PV module output power estimation purposes. The ultimate network illustrated in Figure 4.4 will be called the EANN (Estimation Artificial Neural Network) hereinafter.

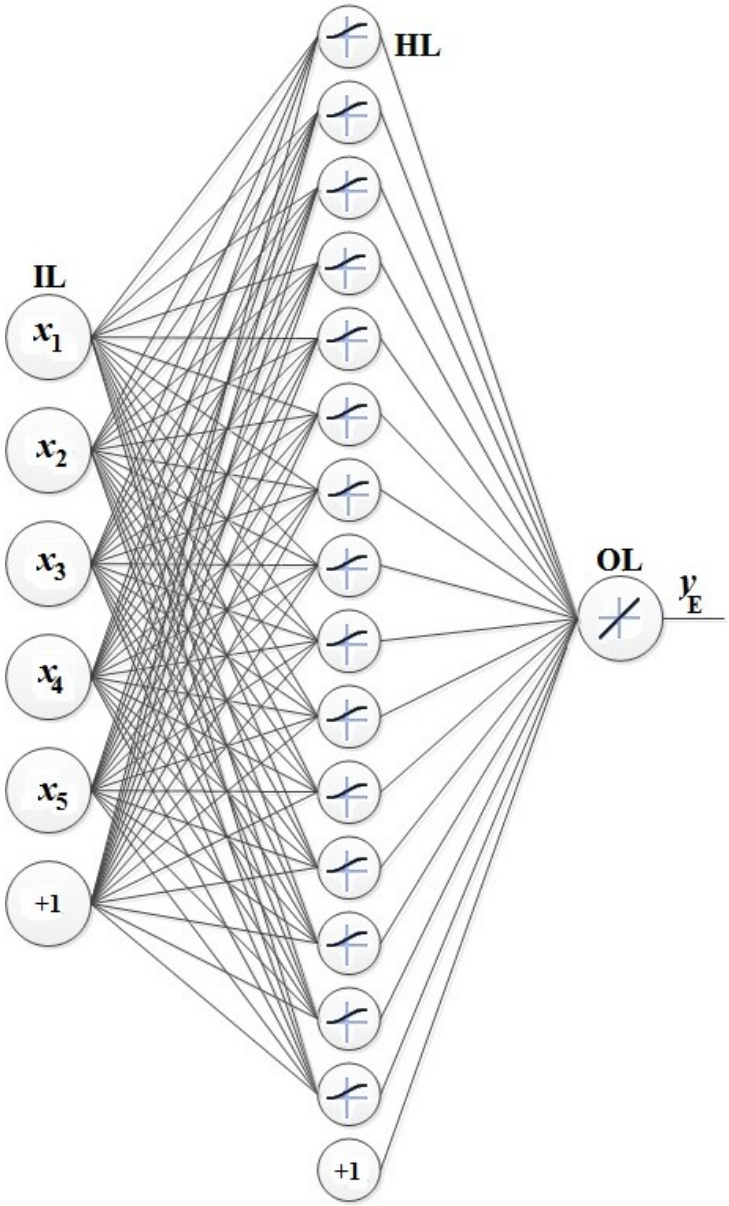

Figure 4.4: The Proposed EANN Architecture. (x_1: Normalized γ_s, x_2: Normalized α_s, x_3: Normalized θ, x_4: Normalized E_{tot}, x_5: Normalized T, y_E: Normalized PV Module Output Power, IL: Input Layer, HL: Hidden Layer, OL: Output Layer

As illustrated in Figure 4.4, there is a bias neuron in input and hidden layers of ANN. A bias neuron emitting +1 is connected to all the next layer neurons to shift the activation function curve to left or right. The effect of a bias neuron expressed as z_0^l is associated with a weight w_0^l (l indicates the layer in which the bias neuron exists) is that the weighted sum is equivalent to the bias when all the previous layer neurons have zero reaction. The phenomenon is explained in equations 4.2.1-4.2.2 and Figure 4.2.2. Further details about the effect of bias neuron may be investigated in [63]-[65].

$$\gamma_i^l = \sum_{j=0}^{N_{l-1}} w_{ij}^l \, z_j^{l-1} \tag{4.2.1}$$

$$\gamma_i^l = w_{i0}^l, if \; z_1^{l-1} = z_2^{l-1} = \cdots = z_{N_{l-1}}^{l-1} = 0 \tag{4.2.2}$$

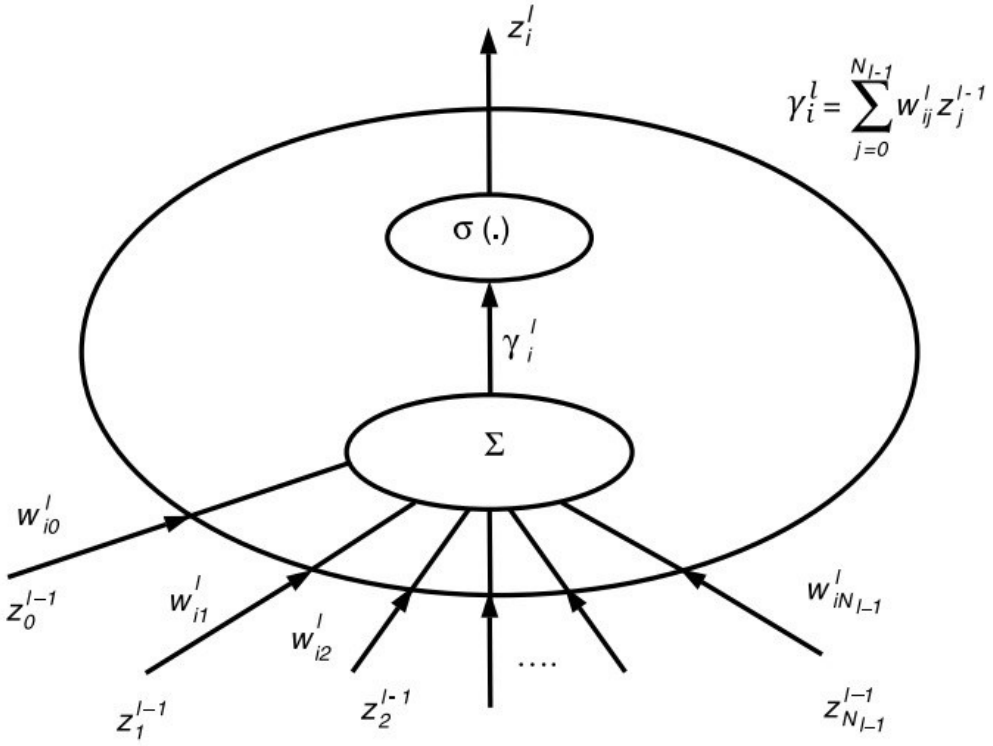

Figure 4.5: A Typical i^{th} Hidden Neuron of i^{th} Layer with Additional Weight Parameter Called Bias [63]

As previously mentioned, ultimate data to be fed to the ANNs is collected within a three-month period from Nov. 1st, 2015 to Jan 31st, 2016. During this period, the data corresponding to healthy and faulty operation intervals of the PV module is acquired. The healthy data collected during the mentioned period, represented as 22272 paths of the normalized values of the solar altitude and azimuth angles, solar incidence angle, irradiance and PV module surface temperature as training inputs and the normalized values of the PV module output power as training target outputs are presented to the EANN during the training and testing processes.

85% (18931 paths) of the healthy data is fed to the EANN during the training phase, which is performed by the BR back-propagation training algorithm. As discussed earlier, the BR algorithm performs well with noisy and rigid data in existence of adequate amounts of training data and also the algorithm does not require validation process and saves the network from being over-fitted. The EANN is trained with a performance gradient goal of 1.0e-12. The testing process is carried out independently on 15% (3341 paths) of the healthy data where the target outputs are no more presented to the network in order to measure the estimation and generalization capabilities of the network. The overall training and testing performance of the EANN may be investigated in Figures 4.6 and 4.7.

The developed EANN is implemented during a 15-day period from Feb 1st, to Feb 15th, 2016. During this period the PV module is operated both under normal and faulty conditions. The details of faulty operation intervals of the PV module is given in the next sub-section where the development of an ANN for fault detection in the PV modules is explained. So far, the result of per-minute implementation of the EANN in

healthy intervals of the implementation period (2962 points) is given in figure 4.8 as a graph of the measured vs. the estimated PV module output power.

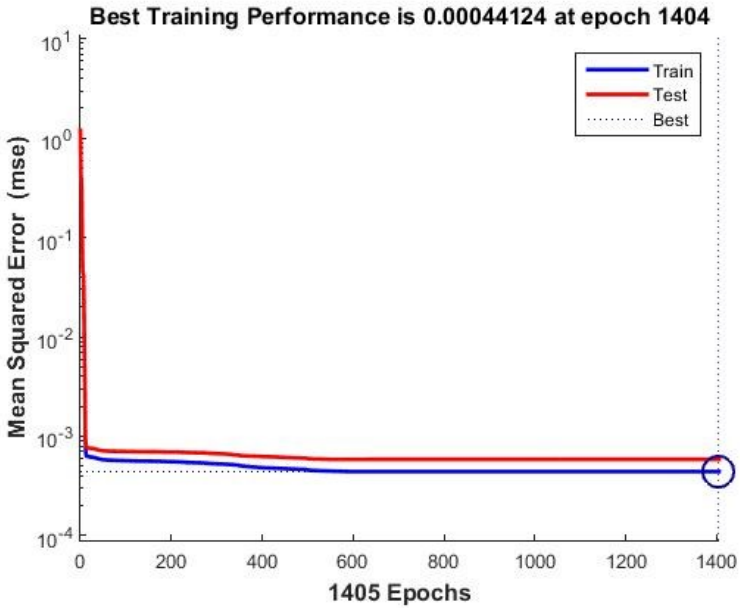

Figure 4.6: The Performance Plot of the EANN Training and Testing Processes

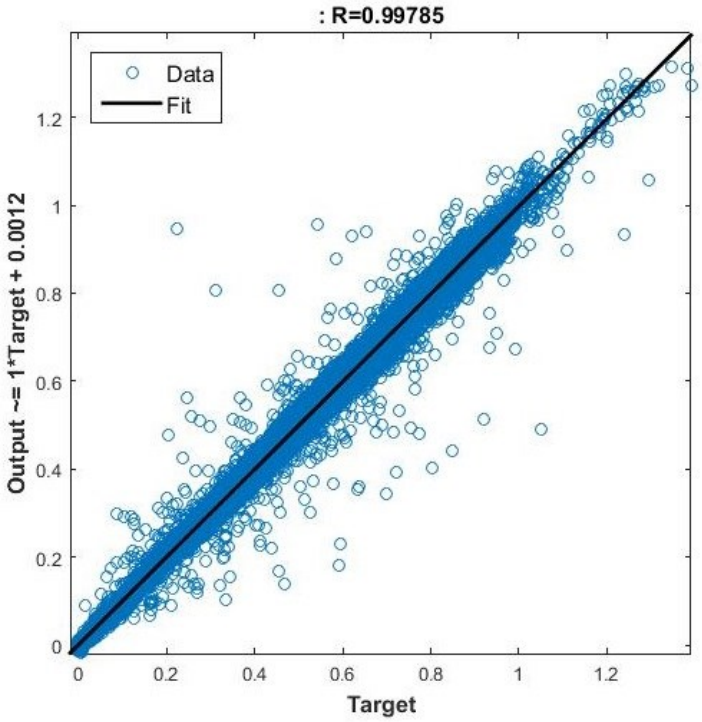

Figure 4.7: The Regression Plot of the ANN Training and Testing Processes

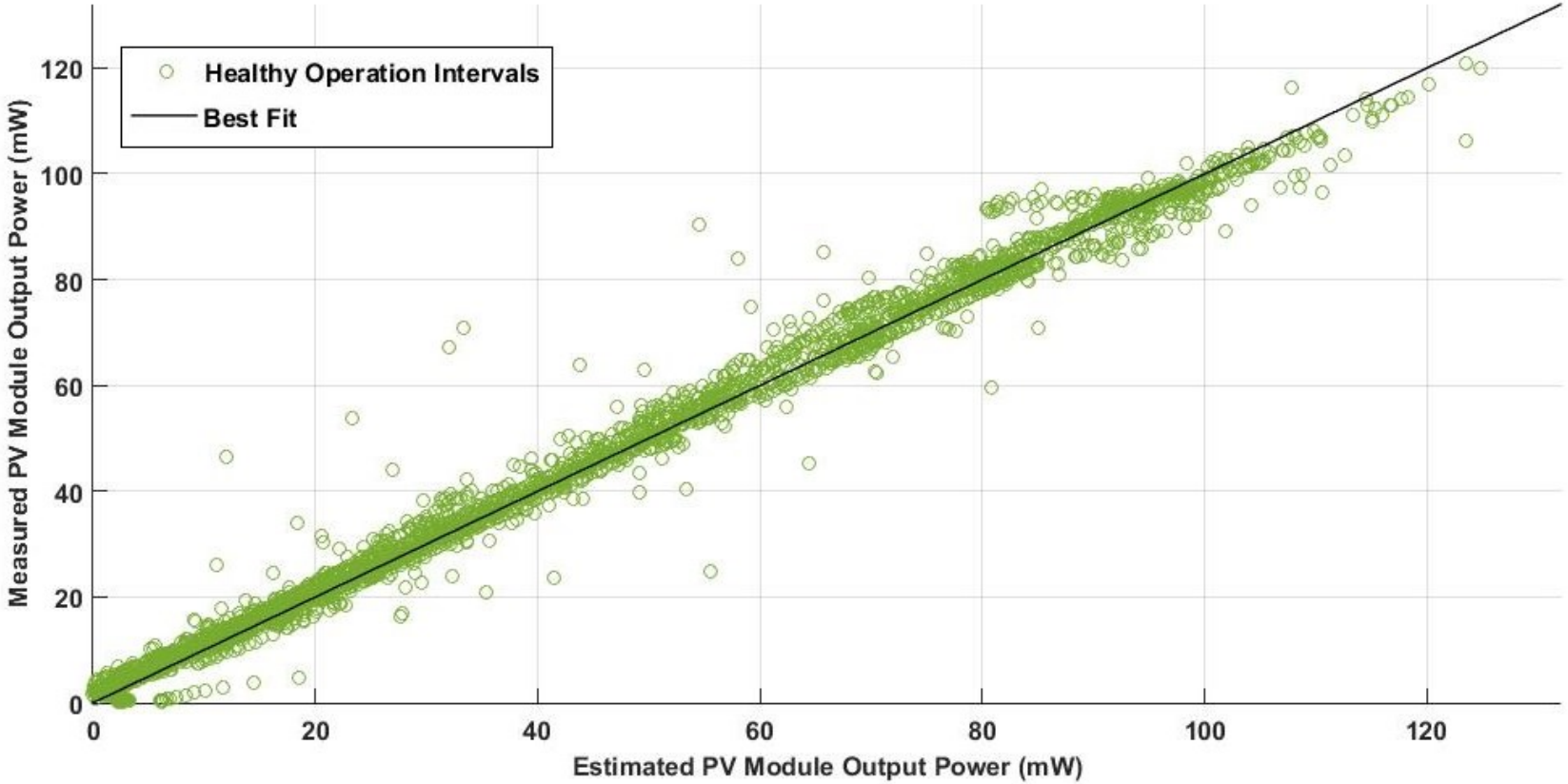

Figure 4.8: The Estimated vs. the Measured PV Output Power Values (mW) for the EANN Implementation Period (Normal PV Module Operation Intervals during Feb. 1st, to Feb. 15th, 2016)

4.3 Development of ANN for PV Module Fault Detection

A three-layer fully-connected feed-forward ANN with log-sigmoid and softmax transfer functions in the hidden and output layers is developed for PV module fault detection purposes. The ANN illustrated in Figure 4.3.1 will be called the DANN (Detection Artificial Neural Network) hereinafter.

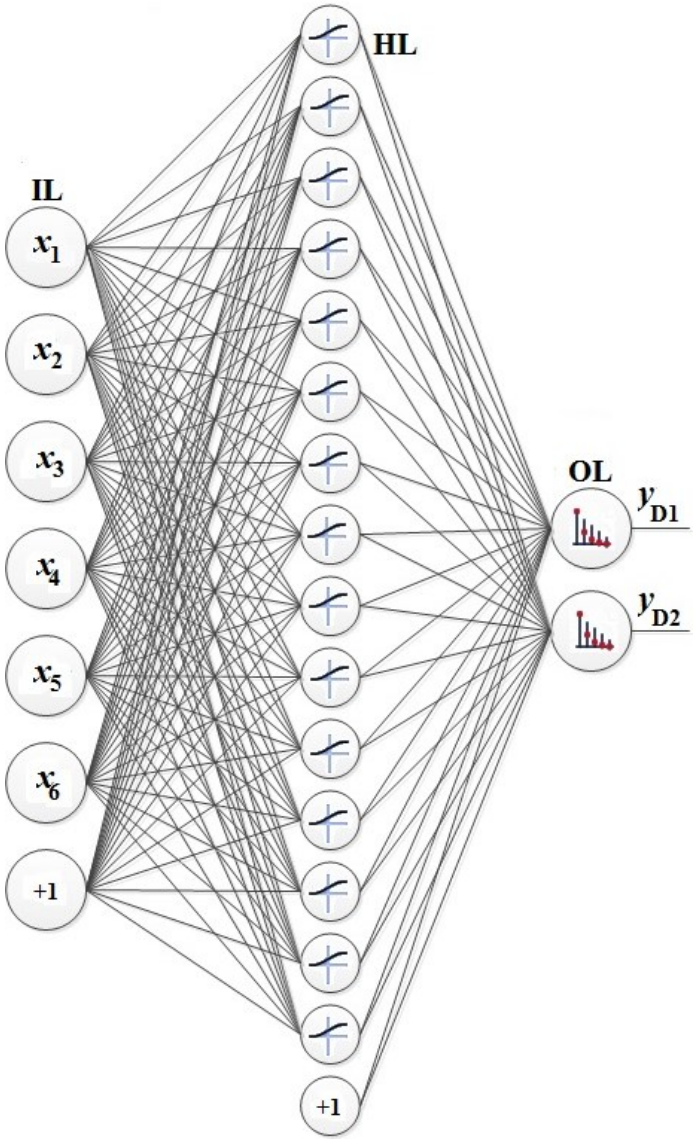

Figure 4.9: The Proposed DANN Architecture. (x_1: normalized γ_s, x_2: Normalized α_s, x_3: Normalized θ, x_4: Normalized E_{tot}, x_5: Normalized T, x_6: Normalized P_{out}, y_{D1}: First Classification Output, y_{D2}: Second Classification Output, IL: Input Layer, HL: Hidden Layer, OL: Output Layer)

As demonstrated in figure 4.9, the DANN output layer consists of two neurons with softmax transfer function. The softmax function in the output layer acts as a classifier by squashing the inputs coming from the hidden layer neurons into two real values. As the result of the classification, the output neurons are assigned two values in the range 0-1 that always add up to 1. The mentioned softmax transfer/activation function is represented in equation 4.3.1 and Figure 4.10.

$$softmax(n_i) = \frac{e^{n_i}}{\sum_{j=1}^{J} e^{n_j}} \, , for \; i = 0 \ldots J \tag{4.3.1}$$

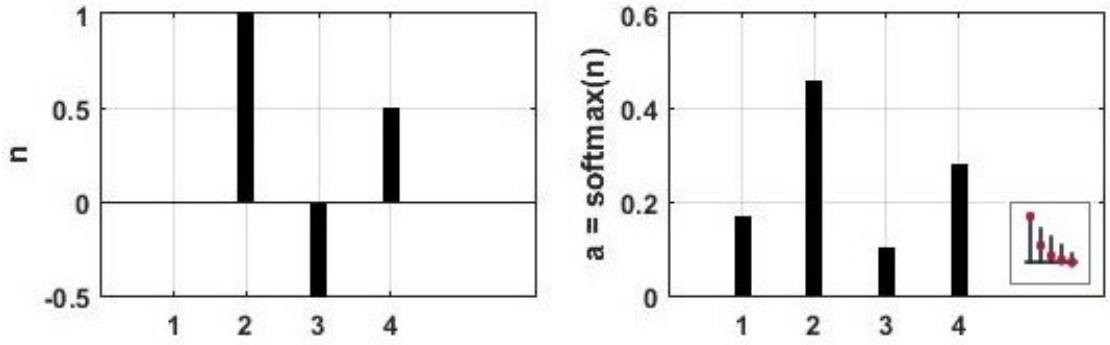

Figure 4.10: The Softmax Transfer Function

The complete data acquired within the data collection period (Nov. 1st, 2015 to Jan. 31st, 2016) consisting 22272 healthy and 7344 faulty paths corresponding to normal and faulty PV module operation intervals are presented to the DANN during the training and testing period. The classification network has two outputs, therefore the training target needs to be two dimensional. The vectors [1 0] and [0 1] representing healthy and faulty training target outputs are provided to the DANN in order to supervise the classification training process. 85% (25174 paths) of the healthy and faulty data are presented to the DANN during the training process which is carried on by the BR algorithm and the network is evolved to solve the binary classification problem with classes '10' and '01' corresponding to the normal and faulty PV module

operation conditions, respectively. The DANN is trained with a performance gradient goal of 1.0e-12. The rest 15% (4442 paths) of data is allotted to the testing process where the target vectors are no more provided to the DANN in order to measure the classification capabilities of the developed network. As given in the confusion matrix in figure 4.11, the developed DANN achieved an overall training and testing classification precision of 99.9%.

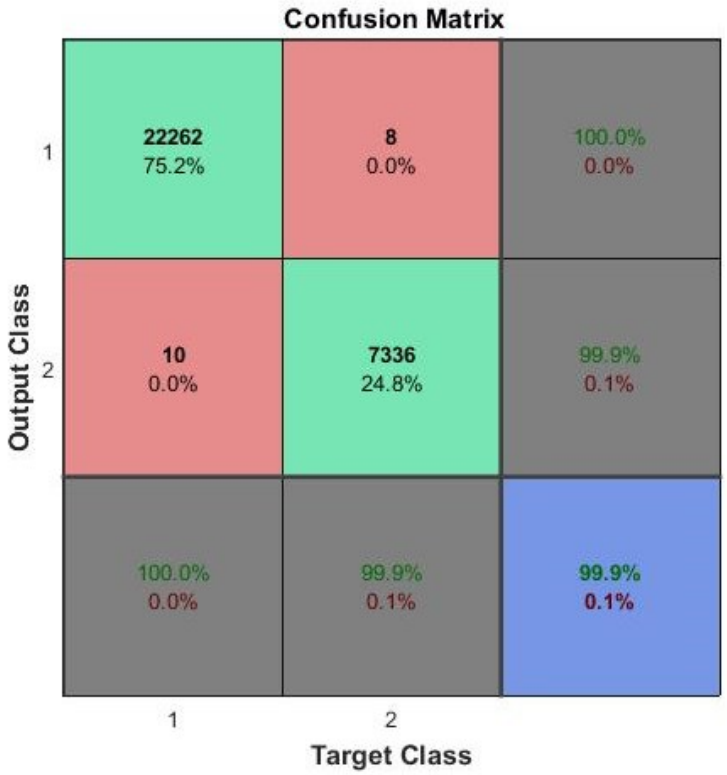

Figure 4.11: The DANN Training and Testing Classification Confusion Matrix

The green blocks in the figure correspond to the true positive and true negative points and the red blocks correspond to the false positive and false negative points. The details about classification confusion matrix will be comprehensively given through this section.

4.4 Implementation of the Ultimate ANNs

The proposed PV module output power estimation and fault detection method is implemented by deploying the developed EANN and DANN during a 15-day interval from Feb. 1st to Feb. 15th, 2016. On the first day of February 2016, the EANN and DANN started their synchronized performance for PV power estimation and fault detection. Everyday starting at solar altitude angle value 0° (almost corresponding to sunrise instance), the EANN starts its operation and when the solar altitude angle reaches 10°, the DANN also starts operating synchronously. The reason that the DANN is not deployed for the solar altitude angle values below 10° is the fact that the input data corresponding to the mentioned angle values below 10° have a very noisy and uncertain nature (not surprisingly for twilight moments) and performing fault detection operation in these periods is pointless. During the operation of the ANNs, the normalized values of the solar altitude, azimuth and incidence angles, the irradiance level and the PV module surface temperature are provided as inputs to the EANN, while the mentioned input values alongside with the normalized measured PV module output power are fed to the DANN as inputs, all in a minute by minute basis. The estimated PV module output power is reconstructed from the normalized EANN output y_E and is logged in per-minute foundation. On the other hand, the two outputs of the DANN are saved in parallel as y_{D1} and y_{D2}.

As discussed earlier, the PV module fault detection is performed based on a binary classification approach. The softmax activation function in the output layer of the DANN squashes the incoming inputs from the hidden layer into two real numbers which are logged as y_{D1} and y_{D2}. In the implementation phase, the decision for fault detection is made with respect to the value of $y_D = y_{D1} - y_{D2}$. Since the training target

vectors [1 0] and [0 1] were presented to the DANN during its training process, the y_D parameter takes on values close to 1 for normal PV module operation and values close to -1 for PV module faulty operation intervals. At this point a threshold is applied to the y_D and the positive and negative y_D values are set as indicators of normal and faulty PV module operation conditions, respectively.

At this stage an important notice is necessary for the reader in order to prevent a possible confusion. In the standard estimation and detection theory terminology, positive/negative status indicates the presence/absence of fault. In our approach, the decision parameter y_D takes on positive values within normal PV module operation intervals and negative values during faulty PV module operation intervals (i.e., for absence and presence of fault, respectively). It is of significant importance to note that the y_D is just a local parameter indicating the operation condition of the PV module and the estimation and detection theory terminology is continued to be used hereinafter without any conversions.

- **A Brief Introduction to the Estimation and Detection Theory:**

In terms of estimation and detection theory, a fault detection algorithm can be simplified to the form that is expressed in Table 4.2.

Table 4.2: A simple fault detection algorithm

	Respond 'Present'	**Respond 'Absent'**
Fault 'Present'	Hit	Miss
Fault 'Absent'	False Alarm	Correct Rejection

Further parameters are introduced in order to express the simple approach suggested in Table 4.2 in terms of the estimation and detection terminology.

$$\text{True Positive Rate (Hit): } TPR = \frac{TP}{P} = \frac{TP}{TP+FN} \tag{4.4.1}$$

$$\text{True Negative Rate (Correct Rejection): } TNR = \frac{TN}{N} = \frac{TN}{FP+TN} \tag{4.4.2}$$

$$\text{False Positive Rate (False Alarm): } FPR = \frac{FP}{N} = \frac{FP}{FP+TN} = 1 - TNR \tag{4.4.3}$$

$$\text{False Negative Rate (Miss): } FNR = \frac{FN}{P} = \frac{FN}{TP+FN} = 1 - TPR \tag{4.4.4}$$

$$\text{Accuracy: } ACC = \frac{TP+TN}{P+N} \tag{4.4.5}$$

where,

TP*:* True Positive (Corresponding to 'Hit')

TN*:* True Negative (Corresponding to 'Correct Rejection')

FP*:* False Positive (Corresponding to 'False Alarm' or 'Type I Error')

FN*:* False Negative (Corresponding to 'Miss' or 'Type II Error')

P*:* The number of healthy points in data (Condition Positive)

N*:* The number of faulty points in data (Condition Negative)

The TPR and the TNR are also referred to as the sensitivity and the specificity (of the system/method), respectively. A confusion matrix with different fields is given in Figure 4.12 in order to better express the estimation and detection theory terminology described in this chapter.

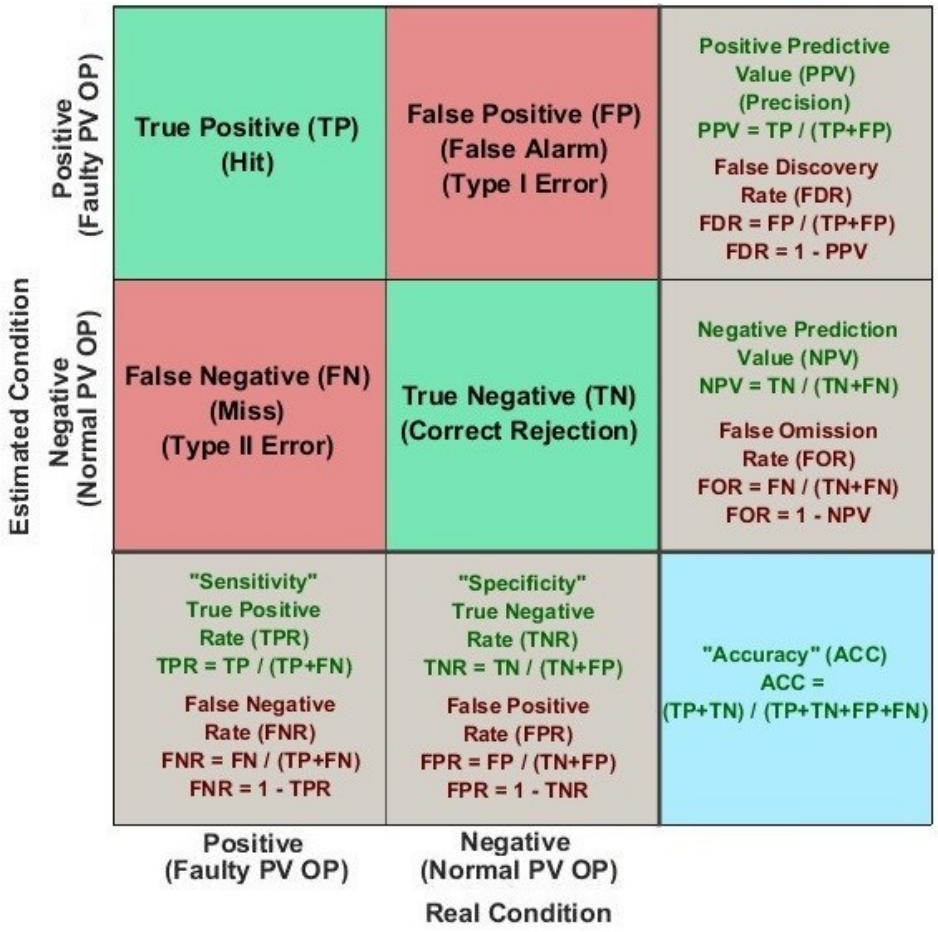

Figure 4.12: The Estimation and Detection Theory Confusion Matrix

After the previous brief introductory part, proceeding to the proposed PV module estimation and detection method is continued. As discussed earlier, a well-trained ANN should be neither under-fitted nor over-fitted. Also it was mentioned that one of the most significant features of the BR training algorithm is that it saves the network from being over-fitted and lacking generalization for new and unseen inputs.

Two coating glasses with different transparency levels for PV fault simulation purposes (referred to as the ‘lightgray’ and the ‘dimgray’ shading faults) have been utilized during the faulty data acquisition periods for training the DANN. In order to examine the generalization capabilities of the DANN, a darker coating glass (hereinafter called ‘darkslategray’) for shading fault simulation as well as real dirt and

dust covering applications to the surface of the PV module in three different intensities (henceforth called the ‘light’, ‘moderate’ and ‘heavy’ dirt and dust coverings) are used during the ANNs implementation period.

Not surprisingly, it is observed that the amount of the PV module output power degradation caused by the homogeneous light, moderate and heavy dirt and dust accumulation on PV module surface is adequately analogous to that caused by the homogeneous lightgray, dimgray and darkslategray shading applications, respectively.

Before proceeding to the general performance overview of the developed estimation and detection method, it is intended to rigorously investigate the performance of the proposed method under a highly fluctuating meteorological condition in order to obtain a precise insight of its sensitivity and specificity levels. For this purpose, an interval at about 14:30 to 15:30 in the afternoon Feb. 1st, 2016 with extremely oscillating partly cloudy weather condition is selected and homogeneous ‘lightgray’ and ‘dimgray’ shadings are applied to the PV module surface in 1-minute, 3-minute and 5-minute terms during the mentioned interval.

Figure 4.4.2 demonstrates the outcome of the experiment. The EANN and DANN are utilized synchronously for solar altitude angle values above 10° on Feb. 1st, 2016 (as the first day of the ANNs implementation period). The measured and the estimated PV module output power values for the entire day is given in Figure 4.13-a and the previously described detailed sensitivity and specificity experiment for the mentioned afternoon interval is given in Figure 4.13-b.

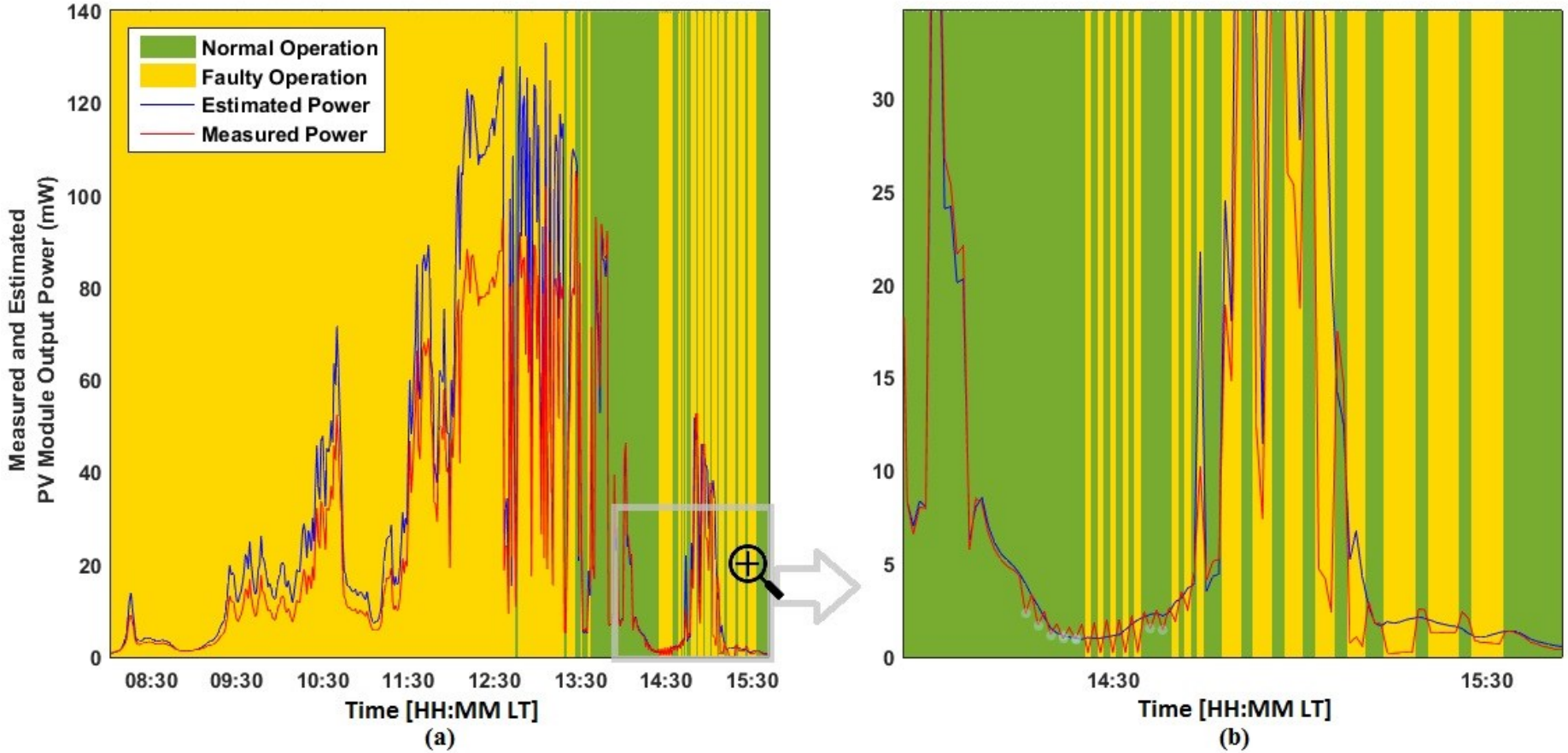

Figure 4.13: The Measured and the Estimated PV Module Output Power Collected During the Fault Detection System Implementation Period on Feb. 1st, 2016

As demonstrated in Figure 4.13-b, all the faulty points caused by the 'dimgray' shading application are accurately detected, whilst a few faulty points corresponding to the 'lightgray' shading application are missed. The missed points, which are all liaise with irradiance levels lower than 150 W/m^2, are marked by whitish highlighting color in Figure 4.13-b.

The experiment well-satisfies its initial objective, which was exploring the essence of situations leading to a missed point (also referred to as the false negative or the type II error point) in the developed PV module fault detection system. The experiment results suggest that such missed faulty points as well as possible false alarmed healthy points are most likely occurring under extremely fluctuating partly cloudy weather conditions with irradiance levels lower than 150 W/m^2.

For the next 14 days of the ANNs implementation period (Feb. 2nd, to Feb. 15th, 2016), different artificial fault states are applied to the PV module in the following manner. For each day, one fault type is applied to the module at a time around solar noon (for instance, one fault type is enforced to a normal performing PV module around solar noon, or an existing fault on a faulty operating PV module is removed around solar noon and the module continues to operate normally for the rest of the day). Such fault application method yields almost equal normal and faulty PV module operation intervals for each implementation day (starting and ending by the solar altitude angle value 10°) with a certain fault type under variable meteorological conditions. There are two motives behind the mentioned fault application method. Firstly, having almost equal amount of healthy and faulty data with one certain fault type for each implementation day is more convenient in terms of further statistical analysis, and secondly, the collected data during the implementation period becomes suitable for

possible future studies where these healthy and faulty data may be used to train future ANNs without the risk of confusing the fault types or even mixing the faulty and the healthy data.

The EANN and DANN implementation performances can be investigated by comparing the measured and the estimated PV module output power values and also by monitoring the detection confusion matrices for each implementation day. The estimation and detection verification results for three sample implementation days (Feb. 7th, Feb. 9th and Feb 12th, 2016) are given in Figure 4.14, 4.15 and 4.16 where the measured and the EANN-estimated PV module output power values alongside the DANN confusion matrices for each day are presented.

As suggested by the examination results for the mentioned days, the 'moderate dirt and dust' covering fault application to the PV module on Feb. 7th, 2016 yields 100% detection accuracy (Figure 4.14), while the 'lightgray' shading and the 'heavy dirt and dust covering' faults, applied to the PV module on Feb. 9th, and Feb. 12th, 2016, respectively, do not sustain such excellent detection rate due to some false alarmed or missed points (type I and type II detection errors). However, the detection rate degradations for the mentioned sample days are not significant and the PV module fault detection examination results in these days are well satisfying with accuracy rates of 97.7% and 99.8%, respectively. The sensitivity and specificity experiment performed on Feb. 1st, 2016 was suggesting the temper of the situations leading to the missed and the false alarmed points. As it is obvious from the Figures 4.15 and 4.16, the false negative and false positive points correspond to extremely fluctuating weather conditions causing immediate and significant power drops, as well as low irradiance conditions causing uncertainty of data.

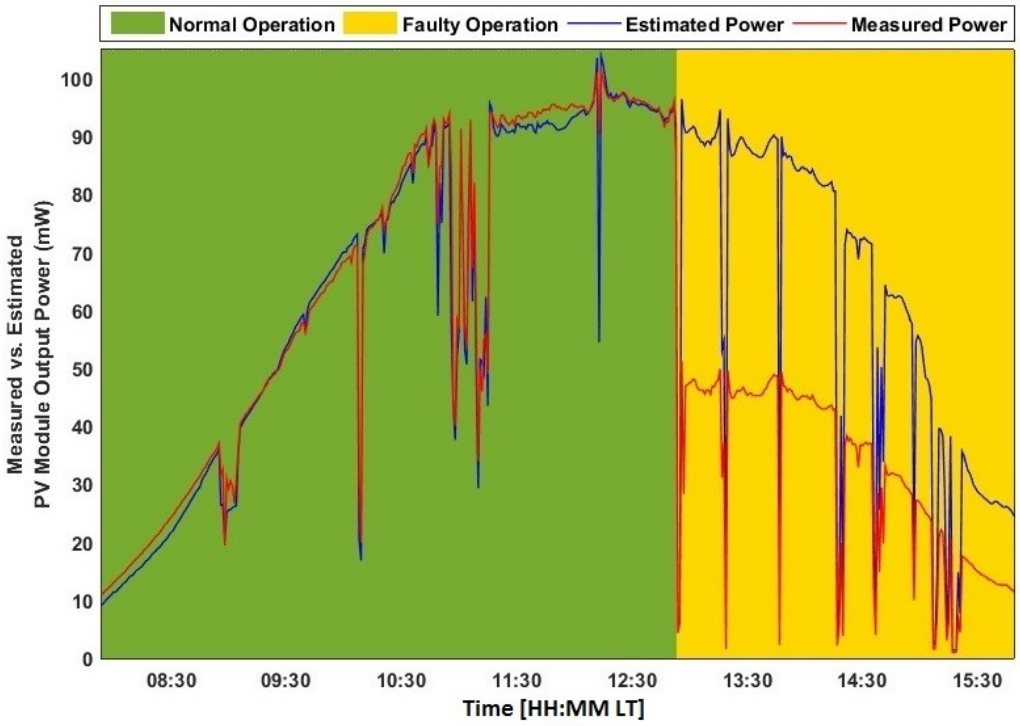

(a)

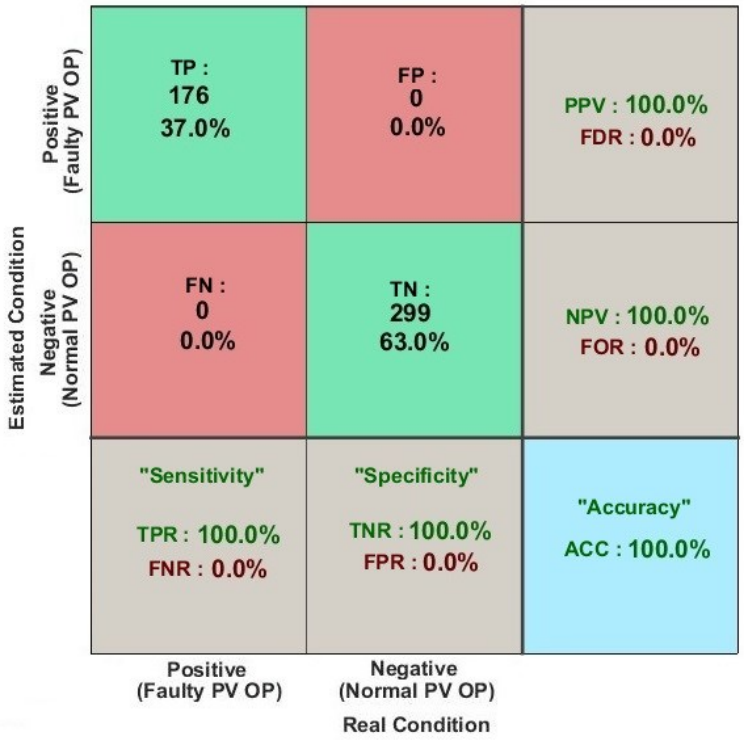

(b)

Figure 4.14: (a) The Measured and the EANN-Estimated PV Module Output Power Values (mW) and Fault Detection by DANN and (b) the Corresponding Confusion Matrices Recorded During Fault Detection System Implementation Period on Feb. 7th, 2016 with 'Moderate and Dust' Covering Fault Type

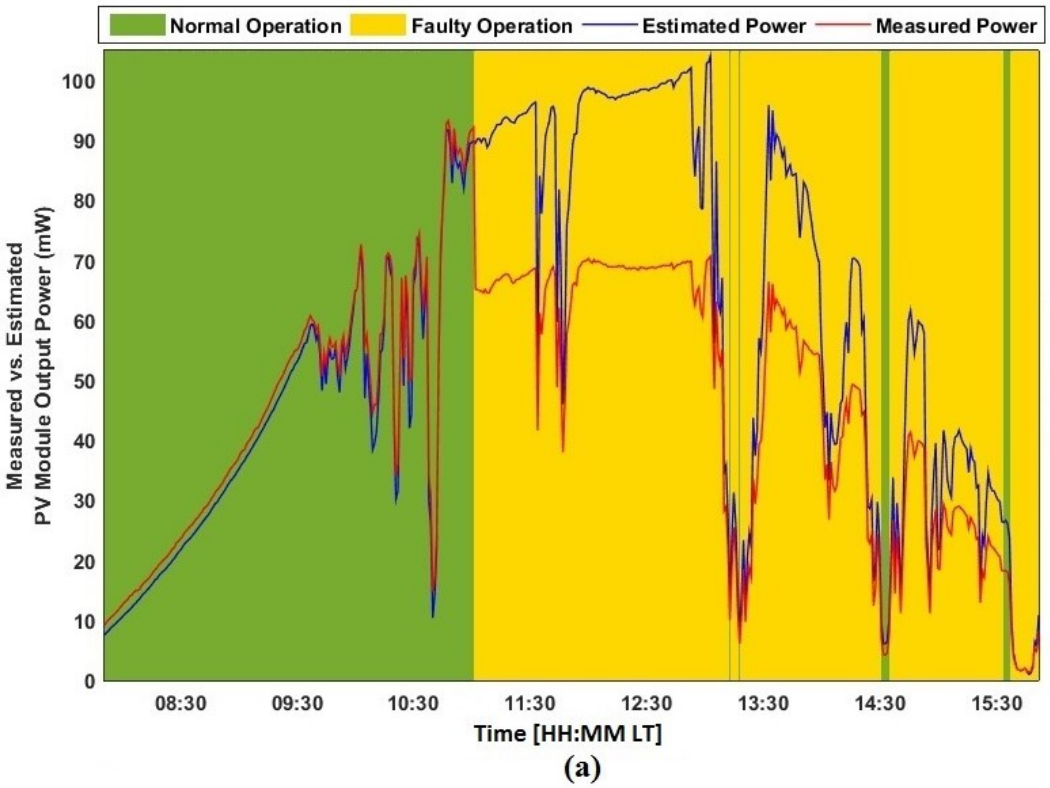

(a)

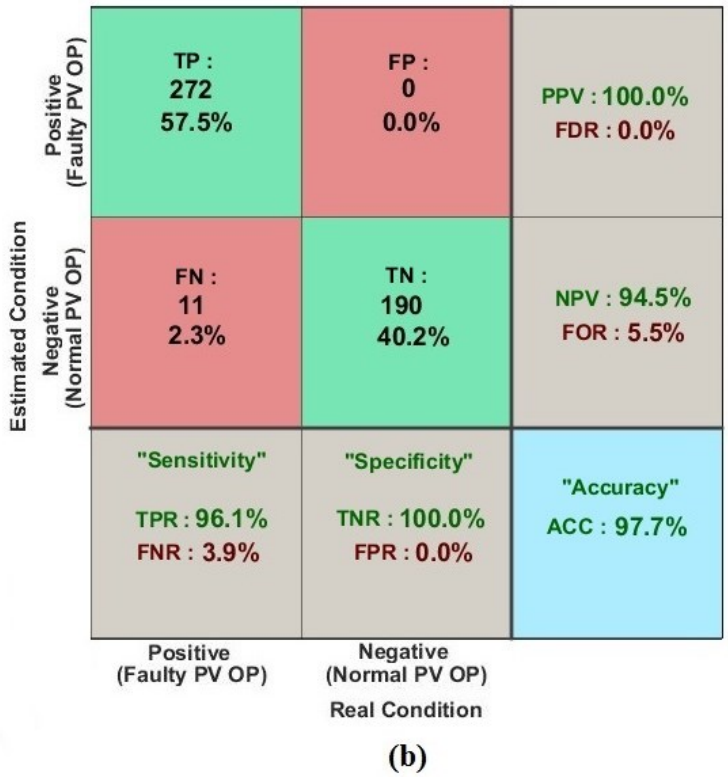

(b)

Figure 4.15: (a) The Measured and the EANN-Estimated PV Module Output Power Values (mW) and Fault Detection by DANN and (b) the Corresponding Confusion Matrices Recorded During Fault Detection System Implementation Period on Feb. 9th, 2016 with 'Lightgray Shading' Fault Type

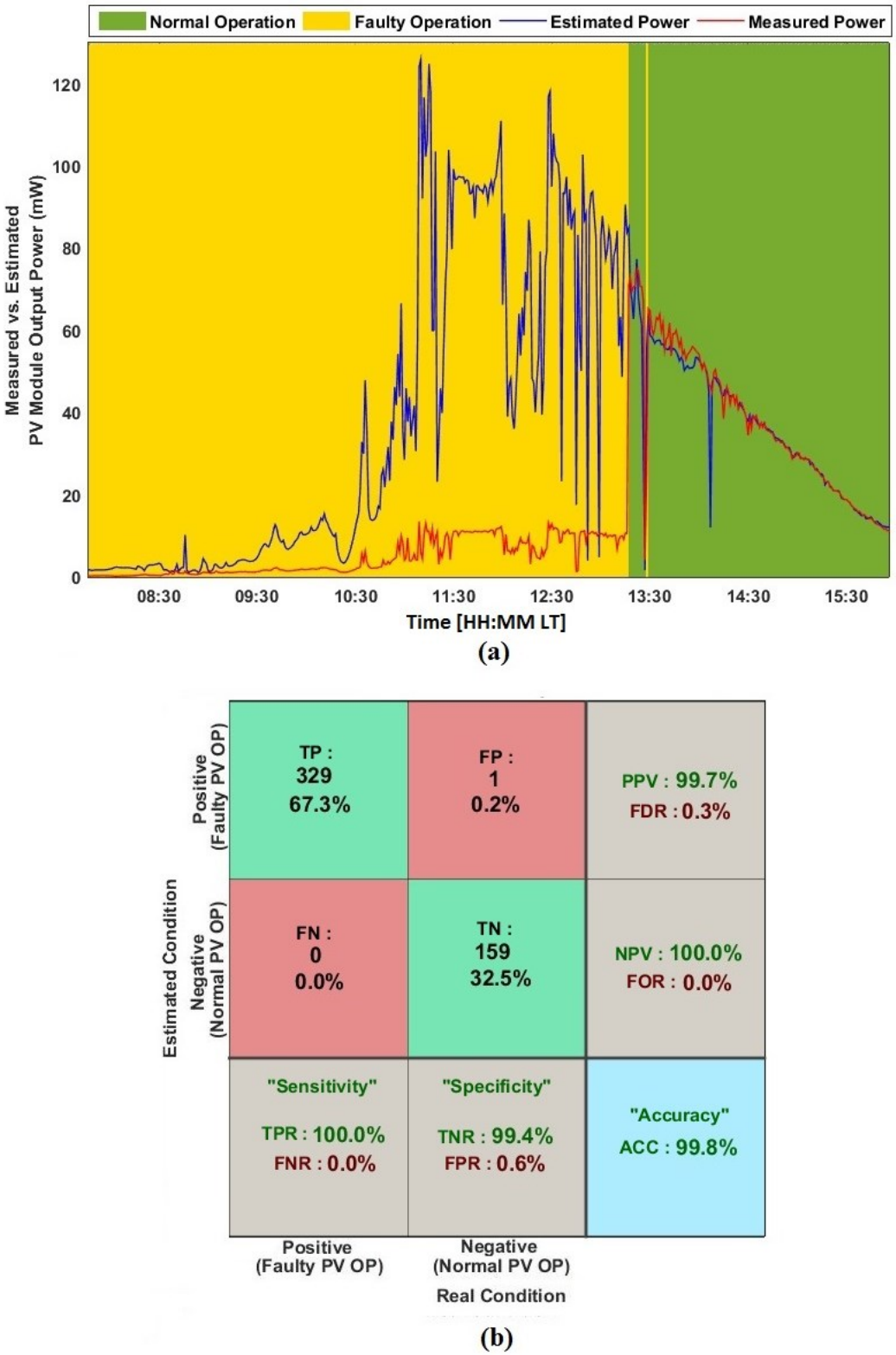

Figure 4.16: (a) The Measured and the EANN-Estimated PV Module Output Power Values (mW) and Fault Detection by DANN and (b) the Corresponding Confusion Matrices Recorded During Fault Detection System Implementation Period on Feb. 12th, 2016 with 'Heavy Dirt and Dust' Covering Fault Type

As mentioned earlier, the PV module output power estimation and fault detection system, powered by the EANN and DANN, is implemented during a 15-day interval from Feb. 1st, to Feb. 15th, 2016. In the mentioned interval, the PV module is operated under heathy and faulty conditions and the ANNs outputs are acquired minute by minute. The per-minute outputs of the ANNs yield overall 6222 values, out of which 2962 values correspond to the healthy operation periods and 3260 values correspond to faulty performance periods of the PV module.

The faulty PV module performance intervals are simulated using six different fault applications being the 'lightgray', 'dimgray' and 'darkslategray' shading applications, alongside the 'light', 'moderate' and 'heavy' dirt and dust coverings. The first two of the mentioned fault types were used during the trainging phase of the ANNs, but the rest four were only deployed during the ANNs implementation phase in order to achieve a measure of generalization capabilities of the networks.

Before proceeding to a general overview of the EANN and DANN performances, an interesting yet not surprising matter is presented to the readers. Out of the six different fault types applied to the PV module, the 'lightgray shading - light dirt and dust covering', the 'dimgray shading- moderate dirt and dust covering' and the 'darkslategray shading- heavy dirt and dust covering' fault application pairs are almost causing equal degradation amounts to the PV module output power, as expected.

To better express the similar effects of the mentioned fault application pairs, the scatter graphs of the EANN-estimated vs. the measured PV module output power values for the operation intervals under each mentioned fault application pair is given separately in Figure 4.17-a, b and c.

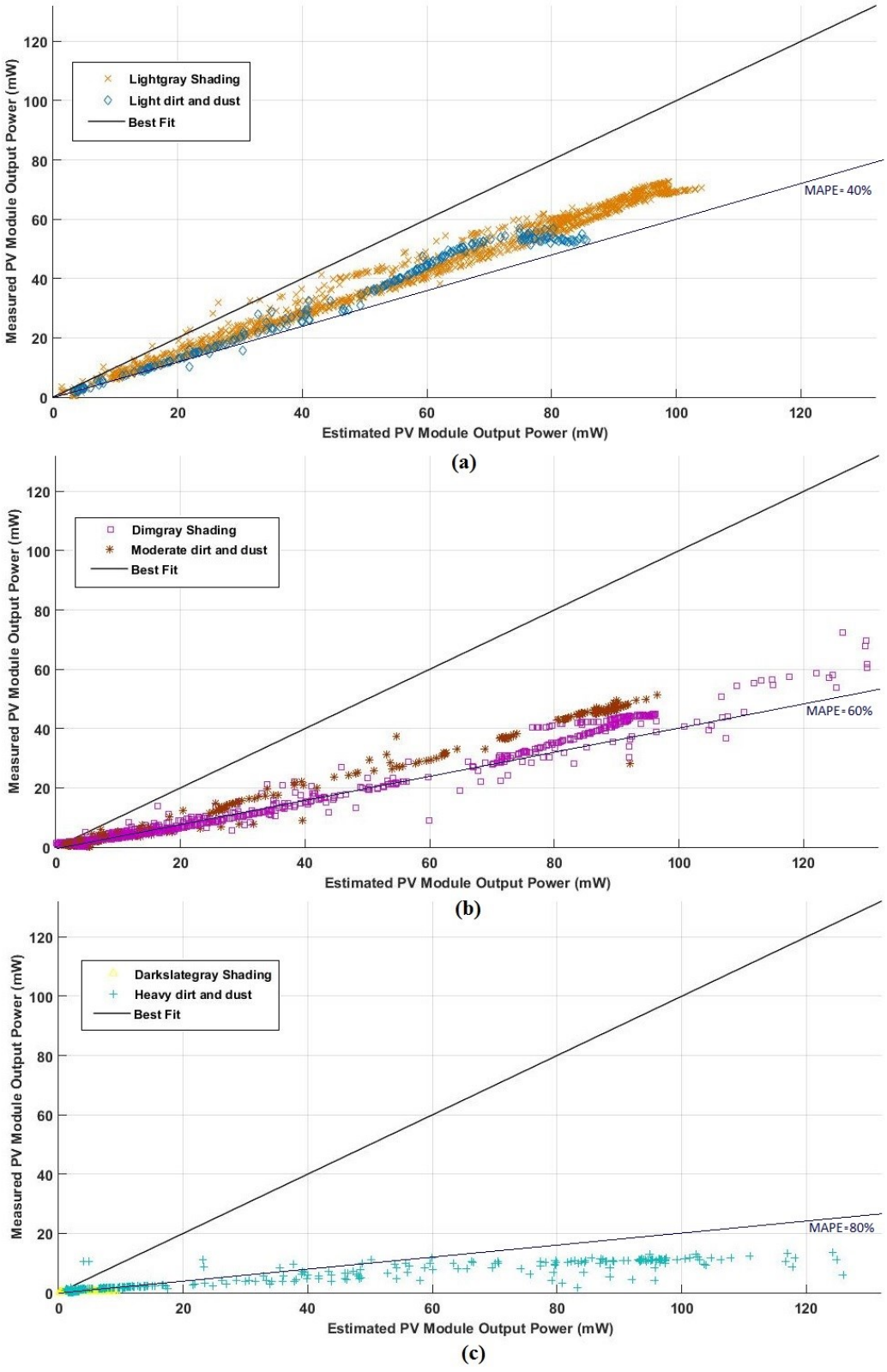

Figure 4.17: Similar Effects of Different Fault Application Pairs on PV Module Output Power

At this point, the general performance overview of the EANN and DANN performance during the implementation period Feb. 1st, to Feb. 15th, 2016 is investigated. As discussed earlier, during this period each day is divided into two parts and one the previously mentioned fault applications is performed to the PV module either before or after an instance around solar noon, yielding nearly equal amounts of healthy and faulty data (2962 and 3260 healthy and faulty values), respectively.

The performance of the EANN in terms of the PV module output power estimation accuracy under both normal and faulty operation conditions is given as a scatter graph in Figure 4.18, containing all the 6222 values (each corresponding to a data acquisition minute) of the healthy and faulty points. It is obvious from the figure that the healthy points corresponding to the normal PV module operation intervals during the mentioned 15-day period settle around the 'best fit' line, while the faulty points fall under this line. Also as illustrated in Figures 4.17-a, b and c, it can be observed that the PV power degradation values due to the mentioned fault applications can heuristically be categorized into three parts. The points corresponding to the 'lightgray shading - light dirt and dust covering' fault application pair fall immediately under the healthy points and the best fit line. The next points to fall lower than the mentioned points are related to the 'dimgray shading- moderate dirt and dust covering' fault application pair and finally the points located close to the bottom of the scatter graph, lower than all other points, correspond to the 'darkslategray shading- heavy dirt and dust covering' fault application pair.

The daily mean MAE and MAPE between the EANN-estimated and the measured PV module output power, the DANN accuracy, the fault application type and the applied fault transmissivity for each implementation day is given in Table 4.3.

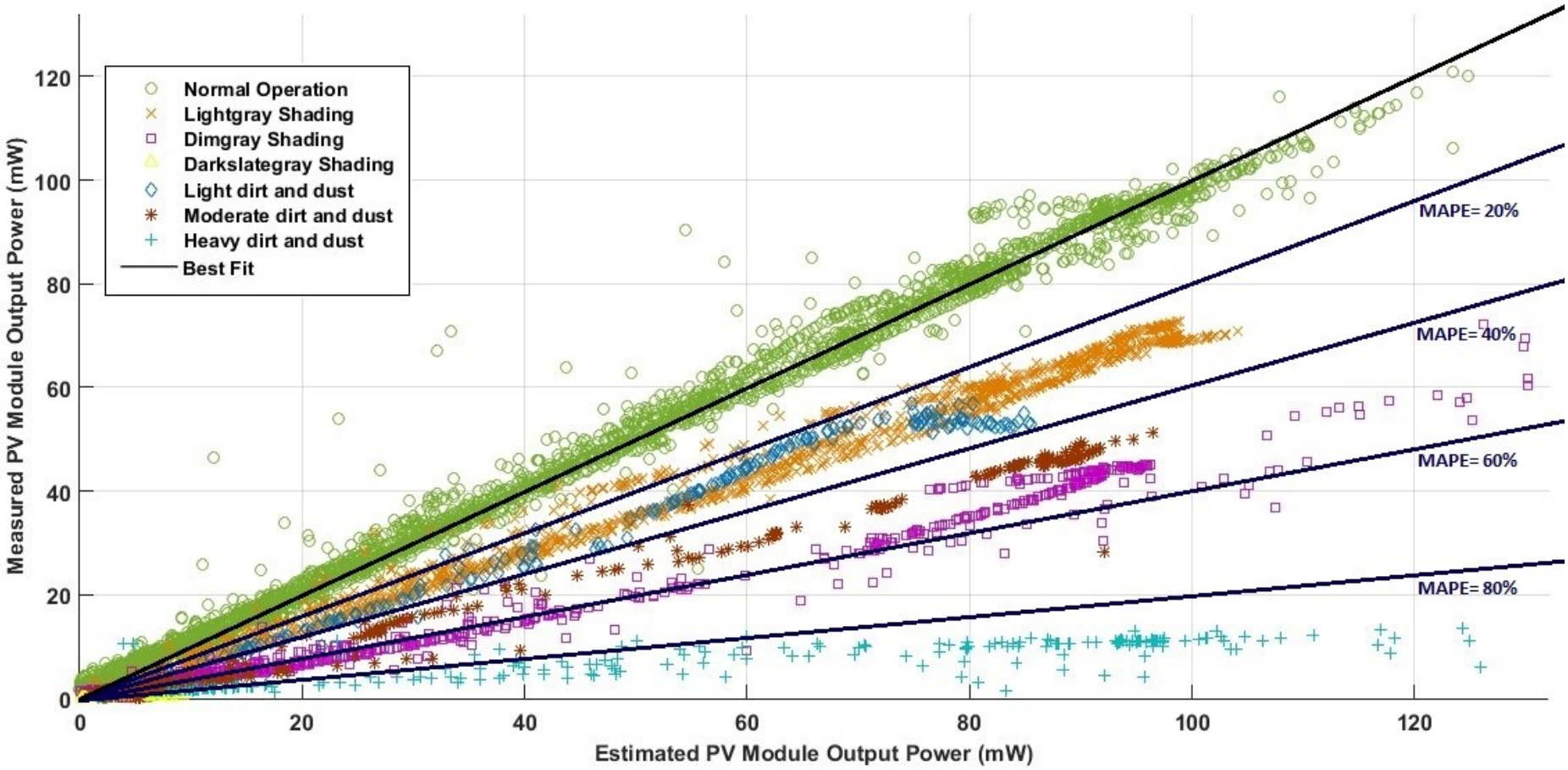

Figure 4.18: The Measured and the Estimated PV Module Output Power Recorded on All the PV Module Fault Detection System Implementation Moments (6222 points) During Feb 2nd, to Feb. 15th, 2016

Table 4.3: The Average MAE and MAPE between the measured and the estimated PV module output power, the DANN accuracy, the applied fault types and different fault transmissivity values during the fault detection system implementation period

	EANN Mean Absolute Error (MAE) (mW)	**EANN Mean Absolute Percentage Error (MAPE)**	**DANN Accuracy**	**Applied Fault Type**	**Applied Fault Transmissivity**
Feb. 2nd, 2016	1.71	2.25%	99.4%	Lightgray Shading	77%
Feb. 3rd, 2016	2.33	4.54%	100%	Dimgray Shading	48%
Feb. 4th, 2016	2.51	5.31%	100%	Lightgray Shading	77%
Feb. 5th, 2016	0.96	2.53%	88.8%	Ligh Dirt and Dust Covering	≈ 75-80%
Feb. 6th, 2016	1.69	5.82%	100%	Dimgray Shading	48%
Feb. 7th, 2016	1.99	4.27%	100%	Moderate Dirt and Dust Covering	≈ 50-55%
Feb. 8th, 2016	2.73	4.87%	99.8%	Lightgray Shading	77%
Feb. 9th, 2016	2.20	6.90%	97.7%	Lightgray Shading	77%
Feb. 10th, 2016	2.22	5.77%	99.8%	Darkslategray Shading	27%
Feb. 11th, 2016	2.24	4.73%	97.6%	Moderate Dirt and Dust Covering	≈ 50-55%
Feb. 12th, 2016	2.03	3.06%	99.8%	Heavy Dirt and Dust Covering	≈ 25-30%
Feb. 14th, 2016	1.40	5.44%	100%	Dimgray Shading	48%
Feb. 15th, 2016	1.39	2.23%	98.8%	Lightgray Shading	77%
Average	1.95	4.44%	98.6%		

In order to analyze the performance results of the DANN, an ultimate confusion matrix containing all the true and false positive and negative points alongside other estimation and detection theory parameters is given in Figure 4.19.

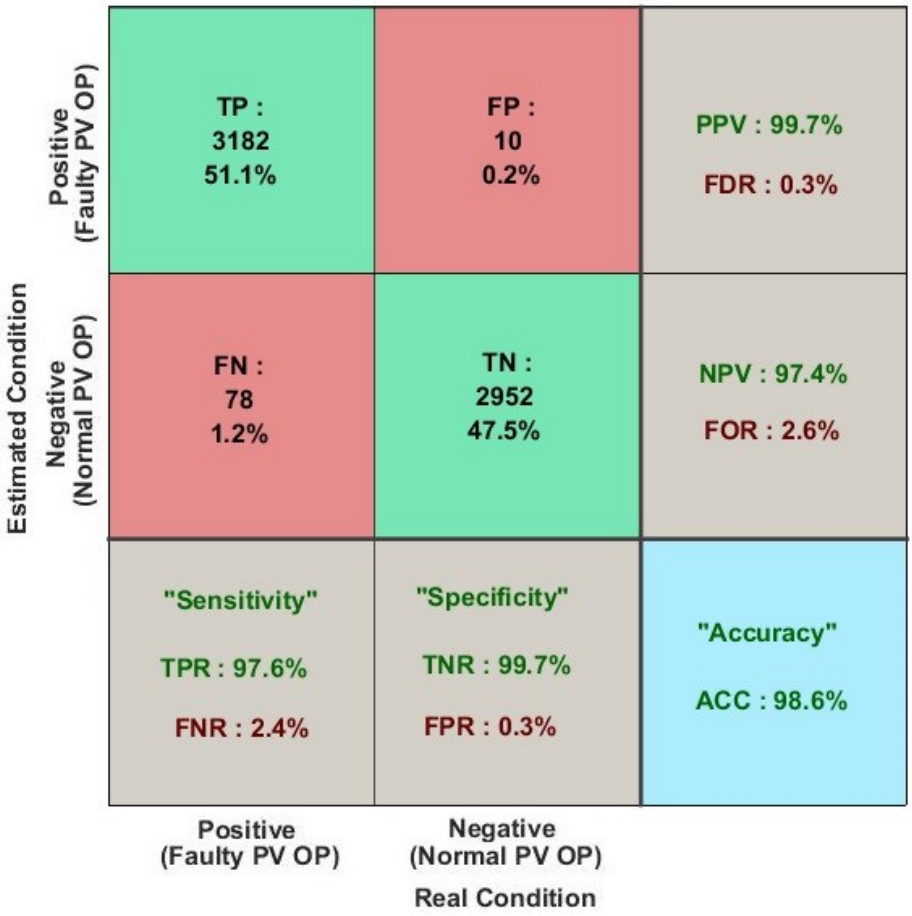

Figure 4.19: The Ultimate Confusion Matrix Representing the DANN Performance

As represented in Figure 4.19, out of overall 6222 DANN implementation points, 6134 points are corresponding to true decisions (3182 true positive/hit and 2952 true negative/correct rejection points), while only 88 points are related to false decisions (10 false positive/false alarm/ type I error and 78 false negative/miss/type II error). The fact that the number of missed points are higher than the number of false alarmed points causes the sensitivity of the DANN being slightly lower than its specificity. An

overall evaluation represents the DANN performance by sensitivity, specificity and accuracy rates of 97.6%, 99.7% and 98.6%, respectively.

Chapter 5

CONCLUSIONS

In this thesis, we have developed an ANN-based intelligent system for PV module output power estimation and fault detection. The required data for training and testing the proposed ANNs, being irradiance level, PV module output power, solar altitude angle, solar azimuth angle, incidence angle and PV module surface temperature, are either measured by highly sensitive measurement equipment or calculated rigorously in a minute by minute basis during a three-month period from Nov. 1st, 2015 to Jan. 31st, 2016. The resulting data sets acquired under normal and faulty operation intervals of the PV module are normalized in the range 0-1 and presented to the ANNs as input/outputs.

Investigation for the most appropriate ANN architectures and training algorithms are also carried out. As a comprehensive comparison between the Levenberg-Marquardt (LM) and the Bayesian Regularization (BR) back-propagation algorithms as the two most widely utilized ANN training methods, the BR algorithm is selected to be utilized in the ANNs training and testing phases due to its robustness in dealing with noisy and rigid data and avoiding network over-fitting and local minima problems, as well as the fact that the BR algorithm does not require validation process which allows all the data to be allotted to the ANNs training and testing processes. Furthermore, the feed-forward Multi-Layer Perceptron (MLP) architecture with three layers as the input, hidden and output layers is selected as the ultimate ANN architecture to be developed

and the number of hidden neurons are set to 15, as it is observed experimentally that a smaller layer size lacks in estimation and detection capabilities, while a larger layer size does not contribute to networks accuracies anymore and consumes much more amounts of time and memory for training and testing processes.

Moreover, before proceeding to the development of the ultimate ANNs for PV module output power estimation and fault detection, a preliminary ANN called PANN is constructed with part of data only for estimation purposes in order to monitor the performance of the mentioned network architecture and the BR training algorithm, and also to detect any shortcomings or problems regarding the performance of the network. Whilst no inconveniences observed, the PANN performance results also gave insight regarding the appropriate data size for the ultimate ANNs to be developed.

Finally, two ANNs namely being the Estimation Artificial Neural Network (EANN) and the Detection Artificial Neural Network (DANN) are developed with the mentioned architecture and algorithm. The log-sigmoid and purelin activation functions are assigned to the EANN hidden and output layers, respectively, and the EANN is trained and tested only on the healthy data acquired during the normal operation intervals of the PV module during the three-month data acquisition period, in order to become capable of estimating the PV module output power under normal operation conditions.

On the other hand, the log-sigmoid and softmax transfer functions are assigned to the DANN hidden and output layers, respectively, and the DANN is trained and tested on both healthy and faulty data acquired during the normal and faulty PV module operation intervals during data acquisition period. Six different fault types, namely

being the ‘lightgray’, ‘dimgray’ and ‘darkslategray’ shadings as well as the ‘light’, ‘moderate’ and ‘heavy’ dirt and dust coverings, are applied to the PV module to simulate faulty operation situations. The first two of the mentioned fault types are presented to the DANN during the training and testing process, while the rest four are kept for the ANNs implementation period in order to measure the generalization capabilities of the DANN for new and unseen fault types.

The EANN and DANN are implemented during a 15-day period from Feb. 1st, to Feb. 15th, 2016. On each day, per-minute measured and calculated values of the mentioned input/output data are presented to the ANNs and the networks are operated synchronously for solar altitude angle values above 10°. The results of implementing the ANNs in the mentioned period yields overall 6222 points (each corresponding to an implementation minute) with DANN performance accuracy rate of 98.6% and EANN average MAPE between the estimated and the measured values of 4.44% level.

Considering the mentioned metrics, the performance analysis results of the EANN and DANN for the implementation period from Feb. 1st, to Feb. 15th, 2016 are highly satisfying and much promising considering further possible expansion of the proposed method to broader PV fleets in the future.

REFERENCES

[1] T. M. Razykov, C. S. Ferekides, D. Morel, E. Stefanakos, and H. S. Ullal, "Solar photovoltaic electricity : Current status and future prospects," *Sol. Energy*, vol. 85, no. 8, pp. 1580–1608, 2011.

[2] L. L. Kazmerski, "Photovoltaics R & D : At the Tipping Point," *NREL Tech. Rep.*, pp. 1–6, 2005.

[3] M. A. Green, J. Zhao, A. Wang, and S. R. Wenham, "Progress and Outlook for High Efficiency Crystalline Silicon Solar Cells," *Sol. Energy Mat. Sol. Cells*, 2001.

[4] Endecon Engineering and I. Regional Economic Research, "A Guide to Photovoltaic (PV) System Design and Installation," 2001.

[5] S. Mekhilef, R. Saidur, and M. Kamalisarvestani, "Effect of dust, humidity and air velocity on efficiency of photovoltaic cells," *Renewable and Sustainable Energy Reviews*. 2012.

[6] M. Mani and R. Pillai, "Impact of dust on solar photovoltaic (PV) performance: Research status, challenges and recommendations," *Renew. Sustain. Energy Rev.*, vol. 14, no. 9, pp. 3124–3131, 2010.

[7] A. Chouder and S. Silvestre, "Automatic supervision and fault detection of PV systems based on power losses analysis," *Energy Convers. Manag.*, vol. 51, pp.

1929–1937, 2010.

[8] S. A. Oke, “A literature review on artificial intelligence,” *Int. J. Inf. Manag. Sci.*, vol. 19, no. 4, pp. 535–570, 2008.

[9] E. S. Brunette, R. C. Flemmer, and C. L. Flemmer, “A review of artificial intelligence,” in *ICARA 2009 - Proceedings of the 4th International Conference on Autonomous Robots and Agents*, 2009, pp. 385–392.

[10] J. A. Akrimi, A. R. Ahmad, L. E. George, and S. Aziz, “Review of Artificial Intelligence,” *Int. J. Sci. Res.*, vol. 2, no. 2, pp. 2319–7064, 2013.

[11] C. Tsatsoulis, “A review of artificial intelligence in simulation,” *ACM SIGART Bull.*, vol. 2, no. 1, pp. 115–121, 1990.

[12] A. S. Drigas and R. E. Ioannidou, “A Review on Artificial Intelligence in Special Education,” in *Communications in Computer and Information Science*, 2013, vol. 278, pp. 385–391.

[13] A. Kablan, “A Review of Artificial Intelligence Techniques in Trading Systems,” *Bus. Rev. Journal, Cambridge, US*, vol. 14, no. ISSN: 1553-5827, pp. 222–229, 2010.

[14] D. Elizondo, G. Hoogenboom, and R. McClendon, “Development of a neural network model to predict daily solar radiation,” *Agric. For. Meteorol.*, vol. 71, pp. 115–132, 1994.

[15] D. Williams and F. Zazueta, “Solar radiation estimation via neural network,” in *Sixth international conference on computers in agriculture*, 1994, pp. 140–146.

[16] S. Alawi and H. Hinai, “An ANN-based approach for predicting global radiation in locations with no direct measurement instrumentation,” *Renew. Energy*, vol. 14, no. 1–4, pp. 199–204, 1998.

[17] K. Reddy and R. Manish, “Solar resource estimation using artificial neural networks and compariosn with other correlation models,” *Energy Convers. Manag.*, vol. 44, pp. 2519–2530, 2003.

[18] L. Hontoria, J. Riesco, P. Zufiriz, and J. Aguilera, “Application of neural networks in the solar radiation field. Obtainment of solar radiation maps,” in *16th European photovoltaic for chemical engineers*, 2000, pp. 385–408.

[19] M. Schuster and K. K. Paliwal, “Bidirectional recurrent neural networks,” *IEEE Trans. Signal Process.*, vol. 45, no. 11, pp. 2673–2681, 1997.

[20] Z. C. Lipton, J. Berkowitz, and C. Elkan, “A Critical Review of Recurrent Neural Networks for Sequence Learning,” *arXiv Prepr. arXiv1506.00019*, pp. 1–38, 2015.

[21] A. Guessoum, S. Boubkeur, and A. Maafi, “A global radiation model using radial basis function neural network,” in *world renewable energy congress*, 1998, pp. 332–336.

[22] M. Mohandes, A. Balghonaim, M. Kassas, S. Rehman, and T. Halawani, “Use of radial basis functions for estimating monthly mean daily solar radiation,” *Sol. Energy*, vol. 68, no. 2, pp. 161–168, 2000.

[23] Q. Que and M. Belkin, “Back to the Future: Radial Basis Function Networks Revisited,” in *AISTATS*, 2016, pp. 1375–1383.

[24] C. C. Lee, P. C. Chung, J. R. Tsai, and C. I. Chang, “Robust radial basis function neural networks,” *IEEE Trans. Syst. Man, Cybern. Part B Cybern.*, vol. 29, no. 6, pp. 674–85, Jan. 1999.

[25] A. Sfetsos and A. Coonick, “Univariate and multivariate forecasting of hourly solar radiation with artificial intelligence techniques,” *Sol. Energy*, vol. 68, no. 2, pp. 169–178, 2000.

[26] L. Hontoria, J. Aguilera, J. Riesco, and P. Zufiriz, “Recurrent neural supervised models for generating solar radiation synthetic series,” *J. Intell. Robot. Syst.*, vol. 31, pp. 201–221, 2001.

[27] L. Hontoria, J. Aguilera, and P. Zufiriz, “Generation of hourly irradiation synthetic series using the neural network multilayer perceptron,” *Sol. Energy*, vol. 72, no. 5, pp. 441–446, 2002.

[28] J. S. R. Jang, “ANFIS: Adaptive-Network-Based Fuzzy Inference System,” *IEEE Trans. Syst. Man Cybern.*, vol. 23, no. 3, pp. 665–685, 1993.

[29] J.-S. R. Jang, C.-T. Sun, and E. MizutaniR, *Neuro-Fuzzy and Soft Computing: A Computational Approach to Learning and Machine Intelligence*. Prentice Hall, 1997.

[30] N. Walia, H. Singh, and A. Sharma, "ANFIS : Adaptive Neuro-Fuzzy Inference System- A Survey," *Int. J. Comput. Appl.*, vol. 123, no. 13, pp. 32–38, 2015.

[31] J. Echanobe, I. del Campo, and G. Bosque, "An adaptive neuro-fuzzy system for efficient implementations," *Inf. Sci. (Ny).*, vol. 178, no. 9, pp. 2150–2162, May 2008.

[32] J. Tang, C. Deng, and G. Huang, "Extreme Learning Machine for Multilayer Perceptron," *IEEE Trans. Neural Networks Learn. Syst.*, vol. PP, no. 1, pp. 1–13, 2015.

[33] T. W. Rauber and K. Berns, "Kernel multilayer perceptron," in *Proceedings - 24th SIBGRAPI Conference on Graphics, Patterns and Images*, 2011, pp. 337–343.

[34] A. G. Parlos, B. Fernandez, A. F. Atiya, J. Muthusami, and W. K. Tsai, "An Accelerated Learning Algorithm for Multilayer Perceptron Networks," *IEEE Trans. Neural Networks*, vol. 5, no. 3, pp. 493–497, 1994.

[35] M. T. Manry, "Recent Developments in Multilayer Perceptron Neural Networks," *Eng. Sci.*, pp. 1–15, 2005.

[36] A. Sözen, E. Arcaklioglu, and M. Özalp, “Estimation of solar potential in Turkey by artificial neural networks using meteorological and geographical data,” *Energy Convers. Manag.*, vol. 45, no. 18–19, pp. 3033–3052, Nov. 2004.

[37] A. Sozen, E. Arcaklioglu, M. Ozalp, and E. Kanit, “Use of artificial neural networks for mapping the solar potential in Turkey,” *Appl. Energy*, vol. 77, pp. 273–286, 2004.

[38] L. Hontoria, J. Aguilera, and P. Zufiriz, “An application of the multilayer perceptron: solar radiation maps in Spain,” *Sol. Energy*, vol. 79, pp. 523–530, 2005.

[39] H. Elminir, Y. Azzam, and F. Younes, “Prediction of hourly and daily diffuse fractionusing neural network, as compared to linear regression models,” *Energy*, vol. 32, pp. 1513–1523, 2007.

[40] S. Alam, S. C. Kaushik, and S. N. Garg, “Computation of beam solar radiation at normal incidence using artificial neural network,” *Renew. Energy*, vol. 31, no. 10, pp. 1483–1491, Aug. 2006.

[41] A. Mellit and S. A. Kalogirou, “Artificial intelligence techniques for photovoltaic applications: A review,” *Progress in Energy and Combustion Science*, vol. 34, no. 5. pp. 574–632, 2008.

[42] F. Bonanno, G. Capizzi, C. Napoli, G. Graditi, and G. M. Tina, “A radial basis function neural network based approach for the electrical characteristics

estimation of a photovoltaic module," *Appl. Energy*, vol. 97, pp. 956–961, 2012.

[43] V. Lo Brano, G. Ciulla, and M. Di Falco, "Artificial Neural Networks to Predict the Power Output of a PV Panel," *Int. J. Photoenergy*, vol. 2014, pp. 1–12, 2014.

[44] V. Lo Brano, G. Ciulla, and M. Di Falco, "Artificial neural networks to predict the power output of a PV panel," *Int. J. Photoenergy*, vol. 2014, pp. 1–12, 2014.

[45] A. Saberian, H. Hizam, M. Radzi, M. Kadir, and M. Mirzaei, "Modelling and Prediction of Photovoltaic Power Output Using Artificial Neural Networks," *Int. J. Photoenergy*, vol. 2014, pp. 1–10, 2014.

[46] M. Alam, F. Khan, J. Johnson, and J. Flicker, "A Comprehensive Review of Catastrophic Faults in PV Arrays: Types, Detection, and Mitigation Techniques," *IEEE J. Photovoltaics*, vol. 5, no. 3, pp. 982–997, 2015.

[47] N. Gokmen, E. Karatepe, B. Celik, and S. Silvestre, "Simple diagnostic approach for determining of faulted PV modules in string based PV arrays," *Sol. Energy*, vol. 86, pp. 3364–3377, 2012.

[48] S. Silvestre, A. Chouder, and E. Karatepe, "Automatic fault detection in grid connected PV systems," *Sol. Energy*, vol. 94, pp. 119–127, 2013.

[49] S. Stettler, P. Toggweiler, and J. Remund, "SPYCE: sattellite photovoltaic yield control and evaluation," in *Proceedings of the 21st European photovoltaic solar energy conference*, 2006, pp. 2613–2616.

[50] A. Drews *et al.*, "Monitoring and remote failure detection of grid-connected PV systems based on sattelite observations," *Sol. Energy*, vol. 81, pp. 548–564, 2007.

[51] J. Chen and F. Yang, "Data-driven subspace-based adaptive fault detection for solar power generation systems," *IET Control Theory Appl.*, vol. 7, no. 11, pp. 1498–1508, 2013.

[52] Y. Zhao, R. Ball, J. Mosesian, J. de Palma, and B. Lehman, "Graph-Based Semi-supervised Learning for Fault Detection and Classification in Solar Photovoltaic Arrays," *IEEE Trans. Power Electron.*, vol. 30, no. 5, pp. 2848–2858, 2015.

[53] P. Guerriero, F. Di Napoli, G. Vallone, V. Dalessandro, and S. Daliento, "Monitoring and diagnostics of PV plants by a wireless self-powered sensor for individual panels," *IEEE J. Photovoltaics*, vol. 6, no. 1, pp. 286–294, Jan. 2016.

[54] R. Platon, J. Martel, N. Woodruff, and T. Y. Chau, "Online Fault Detection in PV Systems," *IEEE Trans. Sustain. Energy*, vol. 6, no. 4, pp. 1200–1207, 2015.

[55] Solargis apps. [online] Available at: http://solargis.info [Accessed 17 Oct. 2017].

[56] K. Scharmer and J. Greif, *The European Solar Radiation Atlas, Vol.1: Fundamentals and Maps*. Paris, France: Les Presses de l`Ecole des Mines, 2000.

[57] I. Ceylan, O. Erkaymaz, E. Gedik, and A. E. Gurel, "The prediction of

photovoltaic module temperature with artificial neural networks," *Case Stud. Therm. Eng.*, vol. 3, pp. 11–20, 2014.

[58] S. S. Hegedus and A. Luque, *Handbook of photovoltaic science and engineering*. West Sussex, UK: Wiley, 2003.

[59] M. Jazayeri, S. Uysal, K. Jazayeri, and S. Yapici, "Experimental analysis of effects of connection type on PV system performance," *Proc. 2013 Int. Conf. Renew. Energy Res. Appl. ICRERA 2013*, no. October, pp. 190–195, 2013.

[60] T.-C. Yu and T.-S. Chien, "Analysis and simulation of characteristics and maximum power point tracking for photovoltaic systems," *2009 Int. Conf. Power Electron. Drive Syst.*, pp. 1339–1344, 2009.

[61] E. Karatepe, M. Boztepe, and M. Çolak, "Development of a suitable model for characterizing photovoltaic arrays with shaded solar cells," *Sol. Energy*, vol. 81, no. 8, pp. 977–992, Aug. 2007.

[62] A. D. Hansen, P. Sørensen, and L. H. Hansen, *Models for a Stand-Alone PV System*, vol. 1219, no. December. 2000.

[63] K. C. Gupta, "Neural Network Structures," *Neural Networks RF Microw. Des.*, pp. 61–103, 2000.

[64] V. L. Berardi and G. P. Zhang, "An empirical investigation of bias and variance in time series forecasting: Modeling considerations and error evaluation," *IEEE*

Trans. Neural Networks, vol. 14, no. 3, pp. 668–679, May 2003.

[65] M. Stevenson, R. Winter, and B. Widrow, "Sensitivity of Feedforward Neural Networks to Weight Errors," *IEEE Trans. Neural Networks*, vol. 1, no. 1, pp. 71–80, 1990.

APPENDICES

Appendix A: Artificial Neural Network-Based All-Sky Power Estimation and Fault Detection in Photovoltaic Modules

Kian Jazayeri, Moein Jazayeri, Sener Uysal, "Artificial neural network-based all-sky power estimation and fault detection in photovoltaic modules," Journal of Photonics for Energy, vol. 7, no. 2, 2017.

Abstract. The development of a system for output power estimation and fault detection in photovoltaic (PV) modules using an artificial neural network (ANN) is presented. Over 30,000 healthy and faulty data sets containing per-minute measurements of PV module output power (W) and irradiance (W/m^2) along with real-time calculations of the Sun's position in the sky and the PV module surface temperature, collected during a three-month period, are fed to different ANNs as training paths. The first ANN being trained on healthy data is used for PV module output power estimation and the second ANN, which is trained on both healthy and faulty data, is utilized for PV module fault detection. The proposed PV module-level fault detection algorithm can expectedly be deployed in broader PV fleets by taking developmental considerations. The machine-learning-based automated system provides the possibility of all-sky real-time monitoring and fault detection of PV modules under any meteorological condition. Utilizing the proposed system, any power loss caused by damaged cells, shading conditions, accumulated dirt and dust on module surface, etc., is detected and reported immediately, potentially yielding increased reliability and efficiency of the PV systems and decreased support and maintenance costs. [DOI: 10.1117/1.JPE.7.025501]

Keywords: artificial intelligence; artificial neural networks; fault detection; renewable energy sources; solar energy; sustainable development.

Paper 17017 received Jan. 24, 2017; accepted for publication Apr. 4, 2017; published online Apr. 19, 2017.

Artificial neural network-based all-sky power estimation and fault detection in photovoltaic modules

Kian Jazayeri,* Moein Jazayeri, and Sener Uysal
Eastern Mediterranean University, Department of Electrical and Electronic Engineering, Famagusta, Turkey

Abstract. The development of a system for output power estimation and fault detection in photovoltaic (PV) modules using an artificial neural network (ANN) is presented. Over 30,000 healthy and faulty data sets containing per-minute measurements of PV module output power (W) and irradiance (W/m^2) along with real-time calculations of the Sun's position in the sky and the PV module surface temperature, collected during a three-month period, are fed to different ANNs as training paths. The first ANN being trained on healthy data is used for PV module output power estimation and the second ANN, which is trained on both healthy and faulty data, is utilized for PV module fault detection. The proposed PV module-level fault detection algorithm can expectedly be deployed in broader PV fleets by taking developmental considerations. The machine-learning-based automated system provides the possibility of all-sky real-time monitoring and fault detection of PV modules under any meteorological condition. Utilizing the proposed system, any power loss caused by damaged cells, shading conditions, accumulated dirt and dust on module surface, etc., is detected and reported immediately, potentially yielding increased reliability and efficiency of the PV systems and decreased support and maintenance costs. [DOI: 10.1117/1.JPE.7.025501]

Keywords: artificial intelligence; artificial neural networks; fault detection; renewable energy sources; solar energy; sustainable development.

Paper 17017 received Jan. 24, 2017; accepted for publication Apr. 4, 2017; published online Apr. 19, 2017.

1 Introduction

Solar energy is a renewable and sustainable resource that emerges to meet the modern world's growing energy requirements. The Sun's radiations transform to direct current (DC) electricity by the photovoltaic (PV) effect. PV cells are interconnected to form PV modules (solar panels) and the PV modules are organized to build PV arrays and systems. The importance of developing supervision and monitoring techniques for PV systems is highlighted considering the amplifying world energy demands and the limitations and threats associated with the traditional energy resources. However, despite the significant growth of PV industry in the modern world, the supervision and fault detection of PV systems have not received the same consideration. Especially, PV systems in lower output levels are mostly running without a proper monitoring mechanism.

Artificial intelligence (AI) techniques are deployed in diverse applications due to their strong reasoning, fault tolerance, flexibility, and generalization capabilities. As one of the most popular branches of (AI), artificial neural network (ANN), which is a mathematical paradigm imitating the behavior of a biological neural network, is being utilized to solve many practical problems in different fields. ANNs being a collection of individually interconnected processing units act as parallel-distributed computing networks. Despite conventional computers that are programmed to carry out specific functions, ANNs, which can be considered as human brain-like mathematical models, can learn from examples and remove the need to use complex mathematical formulas

*Address all correspondence to: Kian Jazayeri, E-mail: kian.jazayeri@cc.emu.edu.tr

1947-7988/2017/$25.00 © 2017 SPIE

or expensive physical models. ANNs are fault tolerant, can work with noisy data, and provide high-speed generalization capabilities for unseen inputs. ANNs are widely deployed in various PV system modeling, estimation, and prediction applications. Some of the ANN applications for estimation purposes in PV systems are given as follows.

ANNs are developed for predicting hourly, daily, and monthly solar radiation.[1–12] An ANN with geographical and meteorological data (latitude, longitude, altitude, month, mean sunshine duration, and mean temperature) as inputs is developed,[13,14] for the estimation of solar potential in Turkey. A solar radiation map for Spain is developed using a multilayer perceptron (MLP).[15] The inputs are solar irradiance and clearness index, and the methodology is extendable to other locations only with the irradiance information of the corresponding zone where the map is going to be prepared. A comparison of ANN and linear regression models for prediction of hourly and daily diffuse fraction in Egypt is proposed in Ref. 16. According to the authors, the ANN model outperformed the linear regression model with prediction accuracies of 95%, 93%, and 96% for infrared, ultraviolet, and global insolation, respectively.

A radial basis function neural network is developed to predict the output characteristics of a commercial PV module by reading the data of solar irradiance and temperature.[17] Different topologies of ANNs are utilized for the output power forecasting of PV modules.[18] The output power of two PV test modules is estimated using ANNs trained on ambient temperature, solar irradiance, and wind speed data in the above-mentioned study. The authors conclude that MLP topology provides the best performance in terms of the prediction error. A similar study is carried out in Ref. 19, where different ANN architectures with inputs of minimum temperature, maximum temperature, mean temperature, and solar irradiance are employed for output power estimation of a solar panel. The authors indicate that the feed-forward MLP with a backpropagation training algorithm has shown the best performance in PV module power estimation.

As expressed in the above examples, ANNs have widely been employed in PV systems mostly for irradiance estimations and rarely for PV output power estimations. However, in most of the cases, the raw data of latitude, longitude, altitude, month, day, and time values are provided to the ANNs. It was demonstrated that with the aim of physical parameters the PV output power forecast by means of hybrid models is enhanced.[20–22] In our study, the per-minute calculations of the Sun's position in the sky, expressed by the solar altitude, azimuth and incidence angles, which are more expressive functions of the above-mentioned parameters, alongside with the synchronous measurements of the solar irradiance (W/m^2) and the PV module output power are presented to the ANNs as inputs. ANN experts and practitioners have always been agreed on the fact that ANNs learn and perform more robustly when provided with preprocessed and meaningful data rather than raw and unprocessed data.

In this study, well-detailed and highly accurate data are acquired using appropriate and highly sensitive measurement equipment. The details of the data acquisition process will be described in Sec. 2. However, no matter how well-detailed and straight-forward-looking the inputs are, the PV performance cannot be accurately modeled based on first physical principles. Especially, the effect of the PV module surface temperature complicates the relation between the solar irradiance and the PV output power as the PV power generation tendency decreases with increasing PV module surface temperature, which is caused by increasing irradiance. Even though a competent analytical or physical model can be utilized for PV power estimation and fault detection to an adequate level, the need for using a qualified machine learning technique for highly accurate PV module output power estimation and fault detection is highlighted by taking the above into consideration. The scope of this study is to give insight of the competency of the well-known MLP approach with an eligible backpropagation algorithm in PV power estimation and fault detection applications in existence of sufficient inputs. Although it may seem a straight-forward approach, this is the first time that the PV module output power and the irradiance level (alongside other inputs) are being presented together to a classifier ANN to determine any fault or power drop in the PV performance accurately and immediately. Furthermore, this study gains robustness by utilizing an appropriate ANN backpropagation training algorithm as the result of our earlier study,[23] which comprehensively compares the effect of using the Bayesian regularization (BR) and the Levenberg–Marquardt (LM) backpropagation algorithms and concludes that the BR algorithm outperforms the LM algorithm in ANN-based PV module output power estimation applications, as the average mean absolute error (MAE) and the mean absolute

percentage error (MAPE) between the estimated and the measured PV module output power values for ANN implementation period from November 26 to December 7, 2015, are respectively 1.64 (mW) and 6.44%, for the LM algorithm, which are reduced to 1.05 (mW) and 4.83% by the BR algorithm. The estimation improvement of the BR algorithm is highlighted by the fact that the proposed PV power estimation algorithm can be extended to broader PV fleets after taking necessary developmental considerations.

A comprehensive review of several PV system faults and the corresponding detection and mitigation techniques is given in Ref. 24. Different fault detection methods for small PV systems are developed based on simulation models.[25–27] Climate data retrieved from satellite observations are also used in modeling PV system fault detection methods.[28,29] Data-driven, graph-based, and wireless sensor-based fault detection methods are other approaches that address PV system supervision issue.[30–32]

A simple one-equation model using solar irradiance and PV module surface temperature as inputs is developed for online fault detection in PV systems.[33] The model is implemented by 10-min measurements and hourly averages. According to the authors, the models based on hourly averages are more accurate than the models using 10-min measurements, and at certain irradiance intervals, a fault detection rate of 90% is achieved. To determine the accuracy level of the above-mentioned one-equation model, the authors compare it with feed-forward ANN models and conclude that although the ANNs are better, the accuracy of the one-equation model is satisfactory.

In this study, two ANNs for output power estimation and fault detection of PV modules are developed. The comprehensive details of the data acquisition and the ANN training, testing, and implementation processes are presented in the following sections.

2 Data Acquisition Process

The data sets used in this study contain per-minute accurate experimental measurements and real-time calculations. A south oriented, 45-deg tilted monocrystalline silicon solar panel (P_{max}:40 W, V_{OC}:21.6 V, and I_{SC}:2.56 A) located at 35°8′51″ N, 33°53′58″ E, with 1-m elevation from the sea level and a pyranometer at the same location with the same tilt and alignment are used for field measurement purposes. The Sun's position in the sky, the solar angle of incidence, and the solar panel surface temperature are also calculated in real time. The details of data acquirement and storage are given as follows.

As described in Ref. 34, the Sun's position in the sky is expressed by the solar altitude angle and the solar azimuth angle. The solar altitude angle indicates the Sun's elevation in the sky and is expressed as

$$\gamma_s = \sin^{-1}(\sin\varphi \sin\delta + \cos\varphi \cos\delta \cos\omega), \tag{1}$$

where ω is the solar hour angle and δ is the solar declination angle.

The solar azimuth angle indicates the Sun's deviation from the north axis and is represented as

$$\begin{cases} \alpha_s = 180 - \cos^{-1}(\cos\alpha_s) & \text{If } \sin\alpha_s < 0 \\ \alpha_s = 180 + \cos^{-1}(\cos\alpha_s) & \text{If } \sin\alpha_s > 0 \end{cases}, \tag{2}$$

where

$$\cos\alpha_s = (\sin\varphi \sin\gamma_s - \sin\delta)/\cos\varphi \cos\gamma_s, \tag{3}$$

$$\sin\alpha_s = \cos\alpha_s \sin\omega/\cos\gamma_s, \tag{4}$$

where α_s is the solar azimuth angle and γ_s is the solar altitude angle.

The angle of incidence, which is the angle between the sunlight beams and a vector perpendicular to the surface of a solar panel, is given as

$$\theta = \cos^{-1}\begin{bmatrix} \cos(\beta)\cos(Z_s) + \\ \sin(\beta)\sin(Z_s)\cos(\alpha_s - \alpha_m) \end{bmatrix}, \tag{5}$$

where β is the module tilt angle, Z_s is the solar zenith angle, and α_m is the module azimuth angle.

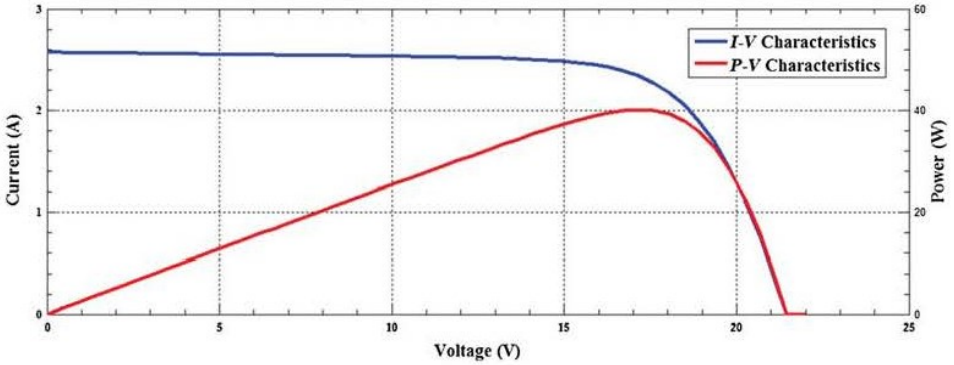

Fig. 1 The PV module $I-V$ characteristics for different temperatures and irradiances.

The minute-by-minute calculations of the above-mentioned parameters are done based on the local solar time, and the resulting data are normalized in the range of 0 to 1 to be fed as inputs to the proposed neural networks. The normalization process, which is done based on the minimum and maximum of the data, yields data close to 1 for the values of each input having higher impact on the PV module output power generation, and data close to 0, vice versa. The calibration of all the inputs is carried out based on the case-specific experimental values.

The output power of a south oriented, 45-deg tilted "Euro Plus Solar" made monocrystalline silicon PV module (P_{max}: 40 W, V_{OC}: 21.6 V, and I_{SC}: 2.56 A) located at 35°8′51″ N, 33°53′58″ E, directly feeding a constant resistive DC load (17 W, 4.7 ΩJ), is measured (mW) per minute and logged after being normalized between 0 and 1. The PV module $I-V$ characteristics for different temperatures and irradiances are given in Fig. 1.

The irradiance level is also measured (W/m^2), normalized in the range of 0 to 1, and logged once a minute using the pyranometer. The last leg of the data collection process is the acquisition of the PV module surface temperature data that is calculated based on the per-minute ambient temperature ($T_{ambient}$) values (°C) obtained from the Larnaca International Airport weather station. As described in Ref. 35, the PV module surface temperature can be calculated as a function of the nominal operating cell temperature (NOCT) and the ambient temperature using

$$T = T_{ambient} + [(\mathrm{NOCT} - 20°\mathrm{C})(E_{tot}/800\ \mathrm{Wm^{-2}})], \tag{6}$$

where E_{tot} is the global solar irradiance.

Since the PV module output power generation tendency reduces with increasing PV module surface temperature, the normalization process of this last parameter is done accordingly before being fed to the ANN, yielding values close to 1 and values close to 0 for lower and higher PV module surface temperatures, respectively. In other words, the normalized PV module output temperature is close to 1 during morning and afternoon hours when the surface temperature is low and close to 0 around noon when the surface temperature is high.

Summarizing the above, the PV module output power and the irradiance level are measured, and the Sun's position in the sky, the solar incidence angle, and the PV module surface temperature values are calculated in real time on a per-minute basis and are logged after all being normalized in the range of 0 to 1, yielding desirable data for the ANNs training procedure. The normalized values of solar irradiance, PV module surface temperature, and PV module output power for three sample data acquisition days are given in Fig. 2.

It is intended to use the above-mentioned data for training two ANNs for output power estimation and fault detection of PV modules. The first ANN, which is used for PV power estimation, is trained on healthy data collected during the normal operation intervals of the PV module, but the second ANN utilized for PV module fault detection needs to be trained on both healthy and faulty data collected during normal and faulty operation periods of the PV module, respectively. To simulate the faulty operation conditions of PV modules, coating glasses with different shades of gray color are used. Two coating glasses, hereinafter referred to as lightgray and dimgray to represent their transparence levels, are used to simulate the faulty PV

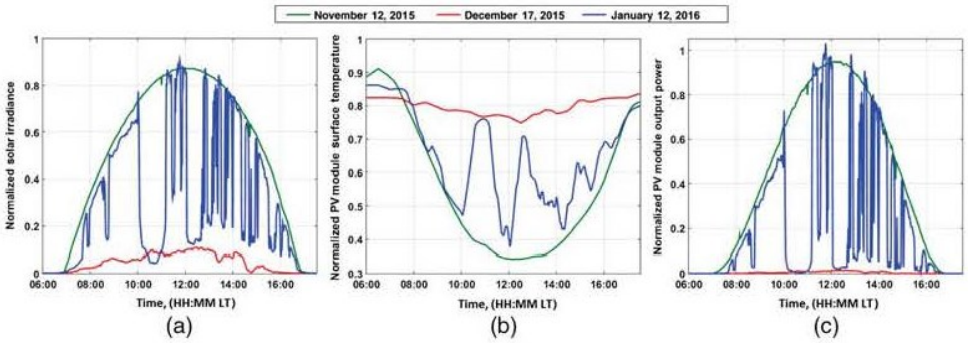

Fig. 2 The normalized values of the (a) solar irradiance, (b) PV module surface temperature, and (c) PV module output power collected on three sample data acquisition periods (November 12, 2015, December 17, 2015, and January 12, 2016).

Table 1 The performance analysis of the PV module output power during the overall faulty operation intervals.

	Maximum measured power (mW)	Maximum expected power (mW)	MAE (mW)	MAPE (%)
Lightgray	114.52	140.74	13.72	≈25
Dimgray	54.95	128.87	24.82	≈55

module operation conditions caused by shading effects, dirt or dust accumulation on the module surface, etc.

To express the PV module output power degradation caused by each above-mentioned fault condition, the performance analysis of the PV module output power during the overall faulty operation intervals is carried out in terms of comparing the measured and the expected PV module output power values, which is represented in Table 1.

The expected power values are values that would be obtained by fault removal and are estimated using the ANN described in Sec. 3.1.

The homogenously distributed fault application to the PV module makes the output power degradation independent of the PV module internal architecture. The response of different PV modules to nonhomogeneous faults, such as one or several damaged cell(s), varies based on the module's internal architecture in terms of the number of bypass diodes in the module. The ideal situation is that there be a bypass diode for each cell in a PV module so that the effect of any shaded or damaged cell can be overpassed immediately and the overall module output decreases only by the fraction of one to the number of cells in the module. However, this is not the case in real-life situations where the shading of one cell may result in significantly higher output power losses in a commercial PV module. The principal motive of homogeneous artificial fault application is for generalization and extension of the approach to be a promising PV module fault detection method, independent of the type, characteristics, and internal architecture of the PV modules on which the method is applied.

On the other hand, applying uniform fault conditions to the PV module utilized in this study expectedly provides the possibility of extending the proposed fault detection algorithm to broader PV fleets after taking developmental considerations.

3 Development of the Artificial Neural Networks

Two ANNs are developed in this study for PV module power estimation and fault detection purposes. The evolvement processes of the proposed ANNs are explained comprehensively as follows.

3.1 *Artificial Neural Network Development for Photovoltaic Module Power Estimation*

A three-layer fully connected feed-forward ANN with log-sigmoid activation function in the hidden layer and linear activation function (purelin) in the output layer is created for PV module output power estimation. The above-mentioned network will be addressed as the estimation artificial neural network (EANN) throughout the text. The number of hidden neurons is decided as 15, which grants the EANN desirable estimation accuracy while not exceeding reasonable computation time and memory allocation limits. The ANN hidden layer size (15 hidden neurons) is decided experimentally as it is observed that a smaller hidden layer lacks in maintaining the desired ANN output accuracy and a larger hidden layer lacks in performance (in terms of lower calculation speed and higher memory allocation) while not contributing much to the ANN output accuracy anymore. The healthy data collected within the normal operation intervals of the PV module during November 1, 2015, to January 31, 2016, period are fed to the EANN in training and testing phases. The EANN is aimed to be utilized in the PV module fault detection period from February 1 to February 15, 2016, which contains normal and faulty PV module operation intervals. 30,778 data paths containing the normalized values of the solar altitude and azimuth angles, solar angle of incidence, irradiance, and PV module surface temperature as training inputs and the normalized values of the PV module output power as the training target outputs are provided to the EANN at these phases.

The training process of the EANN is carried out on 85% (26, 161 paths) of the healthy data by the BR backpropagation algorithm. The BR algorithm provides robust performance in handling noisy and difficult data in existence of sufficient training inputs. The algorithm effectively eliminates the network weights that have lower impact on the problem solution and offers significant performance in avoiding local minima obstacles. The algorithm does not require cross-validation, which prevents part of the data to be reserved for validation purposes. Also the BR algorithm prevents the network from overtraining and overfitting. Comprehensive details regarding the BR backpropagation algorithm principles and axioms may be investigated in Refs. 36 and 37. The performance gradient goal is set to 1.0×10^{-12} for the EANN training procedure. The testing procedure is performed independently on 15% (4617 paths) of the healthy data. In the testing phase, the target outputs are not presented to the EANN to measure the estimation and generalization abilities of the network. The overall training and testing regression performance of 99.78% is achieved by the EANN.

3.2 *Artificial Neural Network Development for Photovoltaic Module Fault Detection*

A three-layer fully connected feed-forward ANN with log-sigmoid activation function in the hidden layer and softmax activation function in the output layer is developed for PV module fault detection. The above-mentioned network will be called the detection artificial neural network (DANN) throughout the text. The number of hidden neurons is again set to 15 (for the same reason explained in Sec. 3.1). The output layer consists of two neurons with softmax activation functions as classifiers that squash the inputs from the hidden layer into a real value in the range of 0 to 1. The values of the output neurons always add up to 1. The healthy and faulty data collected within the normal and the faulty PV module operation periods, respectively, during November 1, 2015, to January 31, 2016, interval are fed to the DANN as training and testing data.

22,272 healthy and 7344 faulty data paths containing the normalized values of the solar altitude and azimuth angles, solar angle of incidence, irradiance, PV module surface temperature, and PV module output power are fed to the DANN as training and testing inputs, and vectors [1 0] and [0 1] are provided to the DANN as the healthy and faulty target outputs, respectively. The neural network is trained by the BR algorithm on 85% (25,174 paths) of the healthy and faulty data to solve the binary classification problem with the class 10 indicating normal operation and the class 01 indicating faulty operation of the PV module. The performance gradient goal is set to 1.0×10^{-12} for the DANN training procedure. The testing procedure is performed independently on 15% (4442 paths) of the healthy and faulty data. In the testing phase, the target

vectors are not presented to the DANN to measure the classification abilities of the network. The overall training and testing classification accuracy of 99.8% is achieved by the DANN.

4 Implementation of the Photovoltaic Module Power Estimation and Fault Detection System

The proposed PV module output power estimation and fault detection system is implemented during February 1 to February 15, 2016. The range of power drops caused by the artificially applied deficiencies is wide enough ("20% to 75%" corresponding to deficiencies transmissivity range "80% to 25%") to be called a fault. The EANN and the DANN developed and described in Sec. 3 are utilized in the proposed system. Starting from February 1, 2016, the PV module is operated under normal and faulty conditions and the EANN and DANN are employed in parallel for estimation and detection purposes. On each day starting as the solar altitude angle reaches 0 deg (which approximately refers to the sunrise moment), the normalized values of the solar altitude, azimuth and incidence angles, the irradiance level, and the PV module surface temperature are fed to the EANN and the estimated PV module output power is reconstructed from the normalized EANN output (y_E) on a per-minute basis. Also starting when the solar altitude angle reaches 10 deg, the DANN is utilized synchronously. The DANN utilization for solar altitude angles lower than 10 deg is prevented due to the uncertainty of data on these intervals. The normalized values of the solar altitude, azimuth and incidence angles, the irradiance level, the PV module surface temperature, and the measured PV module output power are fed to the DANN and the two outputs of the DANN are calculated and logged as y_{D1} and y_{D2}.

As described in Sec. 3, the PV module fault detection is carried out based on a binary classification approach. The output target vectors [1 0] and [0 1] are provided to the DANN during the training phase with 10 and 01 states being representatives for normal and faulty PV module operation conditions, respectively. During the DANN implementation, the decision is made based on the value of $y_D = y_{D1} - y_{D2}$. The parameter y_D takes on values $1 - \varepsilon$ to 1 during the normal PV module operation periods and -1 to $-1 + \varepsilon$within the faulty PV module operation periods. A threshold is applied to the parameter y_D to specify the positive and the negative values of y_D as the indicators of the normal and the faulty PV module operation conditions, respectively.

At this point, a note is necessary to avoid possible confusion. In detection and estimation theory terminology, positive state corresponds to existence of fault and negative state refers to absence of fault. In our system, y_D parameter takes on positive values during normal PV operation (absence of fault) and negative values vice versa. The y_D variable is just an indicator of the PV module operation condition and the detection and estimation theory terminology will be used hereinafter without any changes.

To simulate faulty PV module operation, in addition to the lightgray and dimgray coating glasses described in Sec. 2, a darker coating glass called darkslategray to indicate its transparence level, as well as real dirt and dust coverings, are used during the fault detection system implementation period to examine the system performance with new and unseen fault conditions. It is observed that the effect of homogeneous light, moderate and heavy dirt, and dust accumulation on the PV module surface is very similar to the effect of homogeneous lightgray, dimgray, and darkslategray shading conditions, respectively. To better demonstrate the sensitivity of the system, the lightgray and dimgray shading conditions are applied homogeneously to the PV module in 1-, 3-, and 5-min intervals during a fluctuating partly cloudy weather condition interval at about 14:30 to 15:30 in the afternoon February 1, 2016. The result of the above-mentioned experiment is shown in Fig. 3 where the measured and the estimated PV module output power for solar altitude angles above 10 deg for February 1, 2016, are given in Fig. 3(a) and the above-mentioned afternoon interval when the sensitivity experiment was carried out is selected and shown in Fig. 3(b).

As it is obvious from Fig. 3(b), all the faulty points corresponding to the dimgray shading condition are detected correctly while some of the faulty points regarding the lightgray shadings are missed. These missed points, which are highlighted by whitish color in Fig. 3(b), correspond to irradiance levels lower than 150 W/m^2.

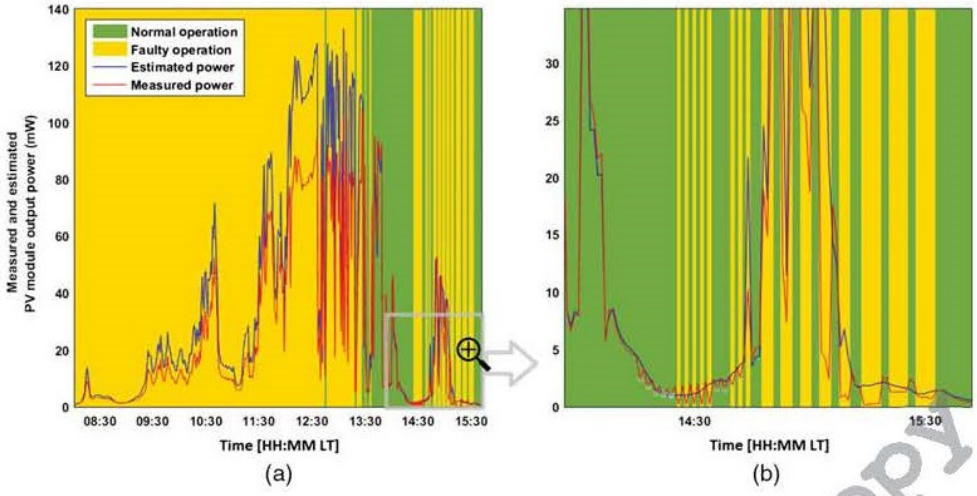

Fig. 3 The measured and the estimated PV module output power collected during the fault detection system implementation period on February 1, 2016.

The above-mentioned experiment provides insight of the nature of conditions that lead to a missing faulty point in the fault detection system. Such missing faulty points as well as false alarmed healthy points can also occur during very highly fluctuating partly cloudy weather conditions. For the following fault detection implementation, days starting from February 2, 2016, different fault conditions are applied to the PV module once a day around solar noon. In other words, a fault condition is applied to the normal operating PV module or the fault is removed from the faulty PV module around solar noon, so for each implementation day, the PV module is normally and faulty operated under variable irradiance levels starting and ending with a solar altitude angle of 10 deg.

There are two reasons for such application. First, applying a single type of fault condition for half of each implementation day leads to more accurate statistical performance analysis of the fault detection system and, second, the healthy and the faulty data acquired during each

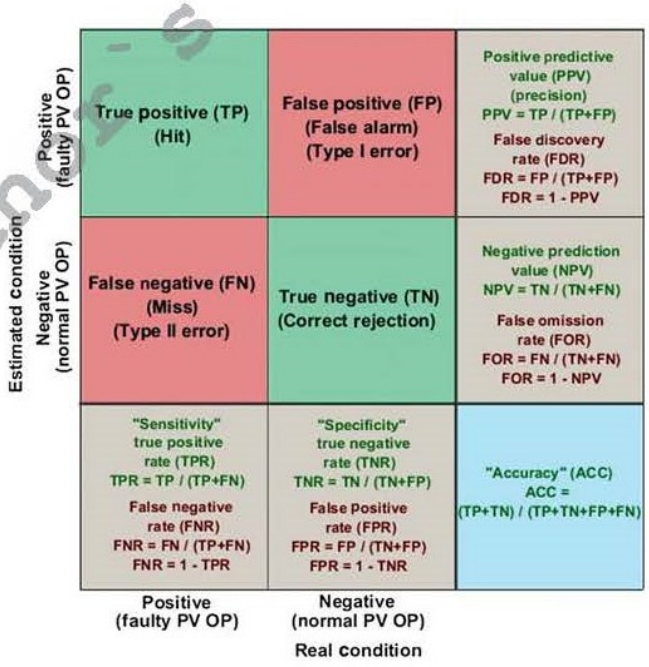

Fig. 4 A confusion matrix containing the detection and estimation theory terminology for each corresponding field.

implementation day can be further used as training data for the neural networks in future studies without the risk of mixing the fault types or even mixing the faulty and healthy data.

A confusion matrix consisting of different fields containing the corresponding detection and estimation terminology for each field is given in Fig. 4. The terminology used in this matrix will be further referred to for statistical analysis purposes throughout this paper.

The measured and the estimated PV module output power values (mW) recorded on three sample fault detection system implementation days (February 7, February 9, and February 12, 2016) and the confusion matrices for the above-mentioned periods are given in Figs. 5(a), 5(b), and 5(c). The applied fault on the above-mentioned sample days are moderate dirt and dust covering, lightgray shading, and heavy dirt and dust covering, respectively.

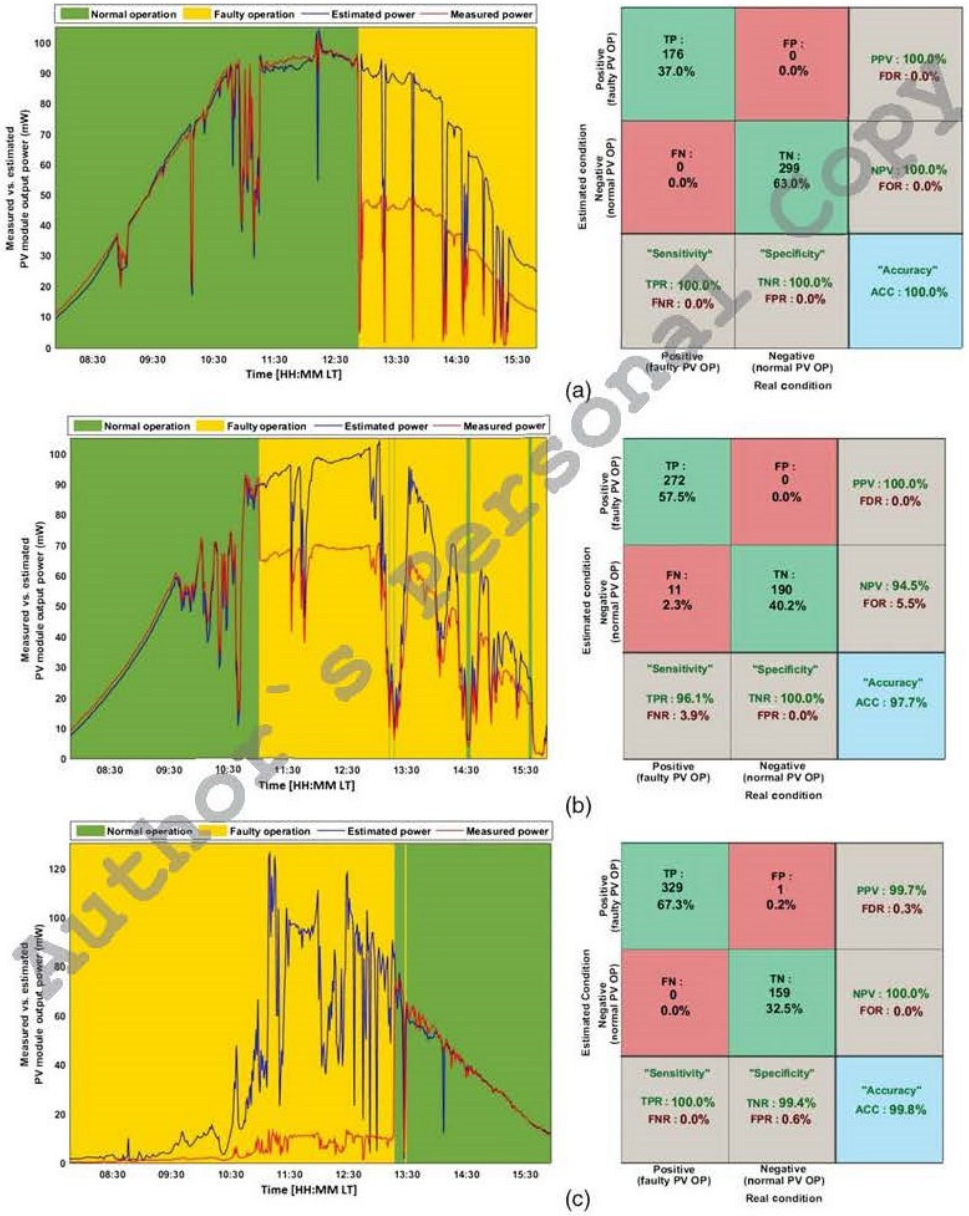

Fig. 5 The measured and the estimated PV module output power values (mW) and fault detection by DANN (left side) and the corresponding confusion matrices (right side) recorded during fault detection system implementation periods on (a) February 7, (b) February 9, and (c) February 12, 2016, with (a) moderate dirt and dust covering, (b) lightgray shading, and (c) heavy dirt and dust covering fault types, respectively.

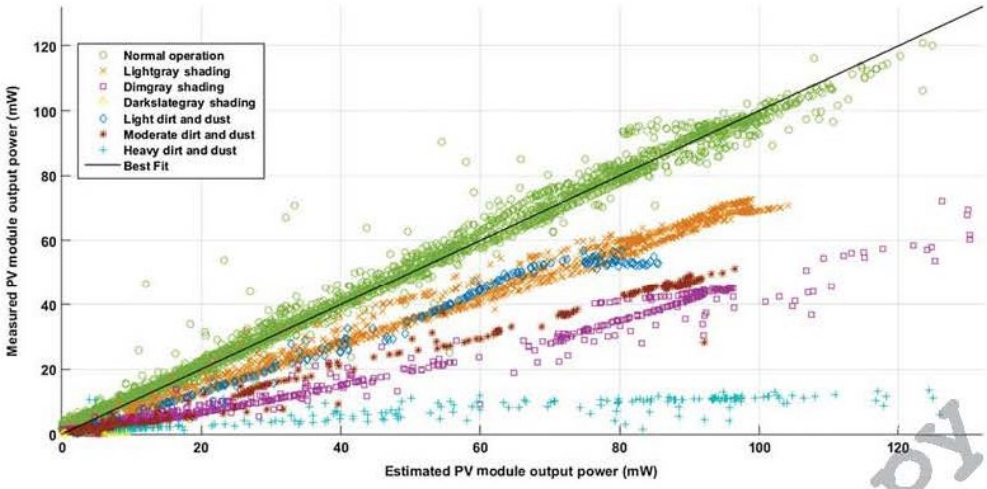

Fig. 6 The measured and the estimated PV module output power recorded on all the PV module fault detection system implementation moments (6222 points) during February 2 to February 15, 2016.

As it is obvious from the figures, the moderate dirt and dust covering fault application to the PV module on February 7, 2016 [Fig. 5(a)] results in 100% fault detection accuracy while the lightgray and heavy dirt and dust covering fault applications on the next sample days [Figs. 5(b) and 5(c)] lack in maintaining such excellent accuracy due to the existence of some missed faulty or false alarmed healthy points. However, the performances of the above-mentioned sample days with accuracy rates of 97.7% and 99.8% are satisfying. As it is apparent in Figs. 5(b) and 5(c), the misses and false alarms occur during highly fluctuating weather conditions, which cause significant power drops. Also in low irradiance levels inaccuracies may occur due to the uncertainty of data. The scatter graph of the measured and the estimated PV module output power (mW) for all the implementation moments during February 2 to February 15, 2016 (6222 points) are given in Fig. 6. As it was mentioned earlier, nearly half of each day in the above-mentioned period is specified to normal PV module operation (2962 points), while the other half is distinguished for the application of different fault types on the PV module (3260 points).

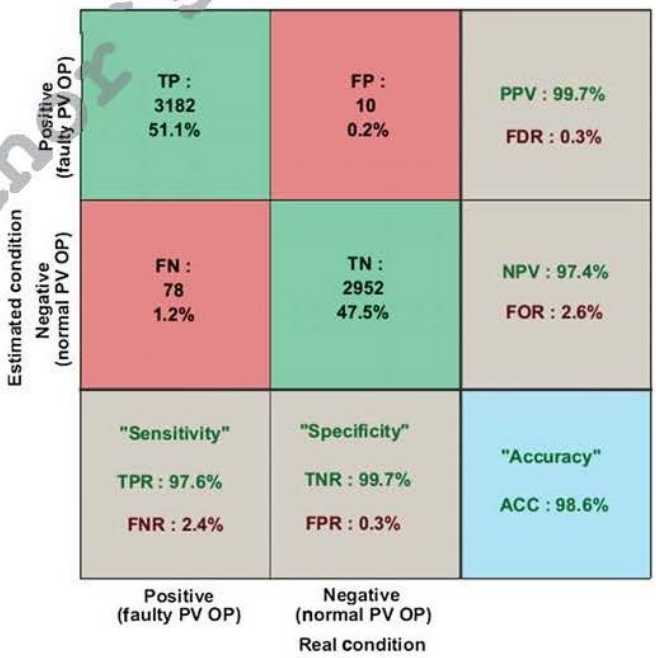

Fig. 7 The overall confusion matrix for the PV module fault detection system.

Table 2 The average MAE and MAPE between the measured and the estimated PV module output power, the DANN accuracy, the applied fault types, and different fault transmissivity values during the fault detection system implementation period.

	EANN (MAE) (mW)	EANN MAPE (%)	DANN accuracy (%)	Applied fault type	Applied fault transmissivity (%)
February 2, 2016	1.71	2.25	99.4	Lightgray shading	77
February 3, 2016	2.33	4.54	100	Dimgray shading	48
February 4, 2016	2.51	5.31	100	Lightgray shading	77
February 5, 2016	0.96	2.53	88.8	Light dirt and dust covering	≈75 to 80
February 6, 2016	1.69	5.82	100	Dimgray shading	48
February 7, 2016	1.99	4.27	100	Moderate dirt and dust covering	≈50 to 55
February 8, 2016	2.73	4.87	99.8	Lightgray shading	77
February 9, 2016	2.20	6.90	97.7	Lightgray shading	77
February 10, 2016	2.22	5.77	99.8	Darkslategray shading	27
February 11, 2016	2.24	4.73	97.6	Moderate dirt and dust covering	≈50 to 55
February 12, 2016	2.03	3.06	99.8	Heavy dirt and dust covering	≈25 to 30
February 14, 2016	1.40	5.44	100	Dimgray shading	48
February 15, 2016	1.39	2.23	98.8	Lightgray shading	77
Average	1.95	4.44	98.6		

Six different fault types, namely, being lightgray, dimgray, and darkslategray shadings as well as light, moderate, and heavy dirt and dust coverings, are applied to the PV module during the implementation period. The first two of the above-mentioned fault types were used during the DANN training data collection and the remaining four fault types are completely new and unseen for the fault detection system. As it was expected, the normal PV module operation points lie near the best-fit line on the scatter graph while the faulty points fall below this line. The effect of applying each fault type on the PV module and also the similarity levels of different fault types may be investigated in Fig. 7.

The daily average MAE and MAPE between the measured and the estimated PV module output power values during February 2 to February 15, 2016, are given in Table 2 and the overall confusion matrix, indicating the total number of hits, correct rejections, misses and false alarms, as well as other performance metrics of the PV module fault detection system is shown in Fig. 7.

5 Conclusions

The development of an ANN-based fault detection system for PV modules is described in this study. The above-mentioned system uses two ANNs (EANN and DANN) for PV module power estimation and fault detection purposes. The inputs to the system are per-minute measurements of the PV module output power (mW) and the irradiance level (W/m^2) along with the real-time calculations of the solar altitude, azimuth and incidence angles, and the PV module surface temperature (°C). The ANNs are trained and tested on data collected during a three-month interval from November 1, 2015, to January 31, 2016, and the PV module fault detection system is implemented during the February 1 to February 15, 2016, period. The results of implementation of the fault detection system show sensitivity, specificity, and overall accuracy rates of 97.6%, 99.7%, and 98.6%, respectively. The PV module fault detection system is prepared and implemented using homogeneous fault conditions, which makes the fault detection independent of

the internal PV module architecture. This paper mainly contributes to introduce a fault detection approach for PV systems that is already tested on a small scale PV application and conceivably can be deployed in broader PV fleets with maximum power point tracking after taking necessary developmental considerations. The way the PV module fault detection system is independent of internal module architecture, expectedly leads to further PV array configuration independency without loss of generality and yields sustainability promises. Utilizing the PV module fault detection system, any power loss due to damaged cells, shading conditions, dirt or dust accumulations on panel surface, etc., is detected and reported immediately under any meteorological condition, supposedly yielding increased PV system efficiency and decreased maintenance and support costs in the long term.

References

1. D. Elizondo and G. Hoogenboom, "Development of a neural network model to predict daily solar radiation," *Agric. For. Meteorol.* **71**, 115–132 (1994).
2. D. B. Williams and F. S. Zazueta, "Solar radiation estimation via neural network," in *Proc. 6th Int. Conf. on Computers in Agriculture*, p. 1143 (1997).
3. S. M. Al-Alawi and H. A. Al-Hinai, "An ANN-based approach for predicting global radiation in locations with no direct measurement instrumentation," *Renewable Energy* **14**(1–4), 199–204 (1998).
4. A. Guessoum, S. Boubkeur, and A. Maafi, "A global radiation model using radial basis function neural network," in *World Renewable Energy Congress*, pp. 332–336 (1998).
5. M. Mohandes et al., "Use of radial basis functions for estimating monthly mean daily solar radiation," *Sol. Energy* **68**(2), 161–168 (2000).
6. L. Hontoria et al., "Application of neural networks in the solar radiation field. Obtainment of solar radiation maps," in *16th European Photovoltaic for Chemical Engineers*, pp. 385–408 (2000).
7. A. Sfetsos and A. H. Coonick, "Univariate and multivariate forecasting of hourly solar radiation with artificial intelligence techniques," *Sol. Energy* **68**(2), 169–178 (2000).
8. G. Mihalakakou, M. Santamouris, and D. Asimakopoulos, "The total solar radiation time series simulation in Athens," *Theor. Appl. Climatol.* **66**, 185–197 (2000).
9. L. Hontoria et al., "Recurrent neural supervised models for generating solar radiation synthetic series," *J. Intell. Rob. Syst.* **31**(1–3), 201–221 (2001).
10. L. Hontoria, J. Aguilera, and P. Zufiria, "Generation of hourly irradiation synthetic series using the neural network multilayer perceptron," *Sol. Energy* **72**(5), 441–446 (2002).
11. A. S. S. Dorvlo, J. A. Jervase, and A. Al-Lawati, "Solar radiation estimation using artificial neural networks," *Appl. Energy* **71**, 307–319 (2002).
12. K. Reddy and R. Manish, "Solar resource estimation using artificial neural networks and comparison with other correlation models," *Energy Convers. Manage.* **44**, 2519–2530 (2003).
13. A. Sözen, E. Arcaklioglu, and M. Özalp, "Estimation of solar potential in Turkey by artificial neural networks using meteorological and geographical data," *Energy Convers. Manage.* **45**(18–19), 3033–3052 (2004).
14. A. Sözen et al., "Use of artificial neural networks for mapping of solar potential in Turkey," *Appl. Energy* **77**(3), 273–286 (2004).
15. L. Hontoria, J. Aguilera, and P. Zufiria, "An application of the multilayer perceptron: solar radiation maps in Spain," *Sol. Energy* **79**(5), 523–530 (2005).
16. H. K. Elminir, Y. A. Azzam, and F. I. Younes, "Prediction of hourly and daily diffuse fraction using neural network, as compared to linear regression models," *Energy* **32**(8), 1513–1523 (2007).
17. F. Bonanno et al., "A radial basis function neural network based approach for the electrical characteristics estimation of a photovoltaic module," *Appl. Energy* **97**, 956–961 (2012).
18. V. Lo Brano, G. Ciulla, and M. Di Falco, "Artificial neural networks to predict the power output of a PV panel," *Int. J. Photoenergy* **2014**, 1–12 (2014).
19. A. Saberian et al., "Modelling and prediction of photovoltaic power output using artificial neural networks," *Int. J. Photoenergy* **2014**, 1–10 (2014).

20. A. Gandelli et al., "Hybrid model analysis and validation for PV energy production forecasting," in *Proc. of the Int. Joint Conf. on Neural Networks* (2014).
21. F. Almonacid et al., "A methodology based on dynamic artificial neural network for short-term forecasting of the power output of a PV generator," *Energy Convers. Manage.* **85**, 389–398 (2014).
22. A. Bracale et al., "A Bayesian method for short-term probabilistic forecasting of photovoltaic generation in smart grid operation and control," *Energies* **6**(2), 733–747 (2013).
23. K. Jazayeri, M. Jazayeri, and S. Uysal, "Comparative analysis of Levenberg–Marquardt and Bayesian regularization backpropagation algorithms in photovoltaic power estimation using artificial neural network," *Lect. Notes Comput. Sci.* **9728**, 80–95 (2016).
24. M. K. Alam et al., "A comprehensive review of catastrophic faults in PV arrays: types, detection, and mitigation techniques," *IEEE J. Photovoltaics* **5**(3), 982–997 (2015).
25. A. Chouder and S. Silvestre, "Automatic supervision and fault detection of PV systems based on power losses analysis," *Energy Convers. Manage.* **51**(10), 1929–1937 (2010).
26. N. Gokmen et al., "Simple diagnostic approach for determining of faulted PV modules in string based PV arrays," *Sol. Energy* **86**(11), 3364–3377 (2012).
27. S. Silvestre, A. Chouder, and E. Karatepe, "Automatic fault detection in grid connected PV systems," *Sol. Energy* **94**, 119–127 (2013).
28. S. Stettler, P. Toggweiler, and J. Remund, "SPYCE: satellite photovoltaic yield control and evaluation," in *Proc. of the 21st European Photovoltaic Solar Energy Conf.*, pp. 2613–2616 (2006).
29. A. Drews et al., "Monitoring and remote failure detection of grid-connected PV systems based on satellite observations," *Sol. Energy* **81**, 548–564 (2007).
30. J. Chen and F. Yang, "Data-driven subspace-based adaptive fault detection for solar power generation systems," *IET Control Theory Appl.* **7**(11), 1498–1508 (2013).
31. Y. Zhao et al., "Graph-based semi-supervised learning for fault detection and classification in solar photovoltaic arrays," *IEEE Trans. Power Electron.* **30**(5), 2848–2858 (2015).
32. P. Guerriero et al., "Monitoring and diagnostics of PV plants by a wireless self-powered sensor for individual panels," *IEEE J. Photovoltaics* **6**(1), 286–294 (2016).
33. R. Platon et al., "Online fault detection in PV systems," *IEEE Trans. Sustainable Energy* **6**(4), 1200–1207 (2015).
34. K. Scharmer and J. Greif, *The European Solar Radiation Atlas: Fundamentals and Maps*, Vol. **1**, Les Presses de l'Ecole des Mines, Paris, France (2000).
35. A. Luque and S. Hegedus, *"Handbook of Photovoltaics Science and Engineering*, Wiley, West Sussex, United Kingdom (2003).
36. W. L. Buntine and A. S. Weigend, "Bayesian back-propagation," *Complex Syst.* **5**, 603–643 (1991).
37. D. J. C. MacKay, "Bayesian interpolation," *Neural Comput.* **4**(3), 415–447 (1992).

Biographies for the authors are not available.

Appendix B: Generation of Spatially Dispersed Irradiance Time-Series Based on Real Cloud Patterns

Moein Jazayeri, Kian Jazayeri, Sener Uysal, "Generation of spatially dispersed irradiance time-series based on real cloud patterns", Elsevier Solar Energy Journal, 2017.

ABSTRACT

Clouds, being complex components of the atmosphere, have significant effects on power generation by photovoltaic (PV) systems. For example, shadows caused by the cloud coverage over a geographically distributed PV power plant may cause significant fluctuations in power generation by leaving a number of PV panels unable to generate power and contribute to power generation by the plant at each time instant. Thus, investigation of the mentioned effects on PV power generation requires realistic spatial irradiance information. Such information should be evaluated based on the existing real cloud coverage and its light transmission characteristics. This also provides the opportunity to select appropriate coping strategies against the mentioned negative effects of partial shading on PV plant's power output. This paper presents a modeling approach which generates Spatially Dispersed Irradiance Profiles (SDIPs) for PV arrays based on existing cloud patterns derived from local sky images taken at the application sites. The model gets the direct, diffuse and global irradiance values incident on a horizontal surface, which are primarily obtained utilizing a solar irradiance model (the Morf (2013) model), along with local sky images captured at the application sites and cloud transmittance values, as input data and yields site-specific Spatially Dispersed Irradiance Profiles (SDIPs) incident on the surface of inclined PV panels within PV application areas, as a result of process of the inputs. Utilization of local sky images and cloud transmittance values for different cloud types creates the opportunity for precise analysis of interactions of sunlight with the existing cloud type and hence, obtaining unique and site-specific irradiance profiles according to the existing cloud type and distribution in the sky. The model firstly detects the cloudy and clear-sky parts in the sky image and then instantly utilizes the most appropriate ellipse on the cloud layer associated with each solar panel through which the beam irradiance is received by the panel. The model also considers the light transmission characteristics of different cloud types as the parameter affecting the beam irradiance. The diffuse and ground-reflected irradiance components are assumed to be spatially constant and thus identical for all solar panels. Cloud base heights, as provided in the International Cloud Atlas (1987), are also utilized to calculate the ground area covered by each sky image. Daily irradiance sequences for different observation points in a PV array are simulated under partly cloudy sky conditions using a set of sky images and utilized for validation purpose of the proposed algorithm. It is demonstrated that instantaneous irradiance values, as well as daily irradiance sequences, differ from point to point in a geographically distributed PV application site depending on the distribution of clouds in the sky. The mentioned variable characteristic of the irradiance sequences received at different observation points, as well as the model's capability to reflect the mentioned variabilities, is verified using irradiance data derived from satellite observations. The performance of the proposed model is validated using variability index (VI) metric as a measure of irradiance variability during a day. The modeled VI values are validated against the measured VI values for a reference point located at the center point of the generated irradiance profiles. Daily VI values calculated for both measured and simulated 1-min global horizontal irradiance (GHI) data are compared for a population of totally 117 days during April – August time period. The results of comparison show statistics of mean bias error (MBE) of 0.16, root mean square error (RMSE) of 2.394, correlation coefficient of 0.94 and mean absolute error (MAE) of 1.91. The validation results demonstrate capability and accuracy of the proposed model for estimation of irradiance values under cloudy sky conditions.

Solar Energy 158 (2017) 977–994

Contents lists available at ScienceDirect

Solar Energy

journal homepage: www.elsevier.com/locate/solener

Generation of spatially dispersed irradiance time-series based on real cloud patterns

Moein Jazayeri*, Kian Jazayeri, Sener Uysal

Electrical and Electronic Engineering Department, Eastern Mediterranean University, Famagusta, Via Mersin 10, Turkey

ARTICLE INFO

Keywords:
Spatially dispersed irradiance profile
Irradiance estimation
Partial shading analysis
PV fleet
Solar energy
Solar irradiance

ABSTRACT

Clouds, being complex components of the atmosphere, have significant effects on power generation by photovoltaic (PV) systems. For example, shadows caused by the cloud coverage over a geographically distributed PV power plant may cause significant fluctuations in power generation by leaving a number of PV panels unable to generate power and contribute to power generation by the plant at each time instant. Thus, investigation of the mentioned effects on PV power generation requires realistic spatial irradiance information. Such information should be evaluated based on the existing real cloud coverage and its light transmission characteristics. This also provides the opportunity to select appropriate coping strategies against the mentioned negative effects of partial shading on PV plant's power output. This paper presents a modeling approach which generates Spatially Dispersed Irradiance Profiles (SDIPs) for PV arrays based on existing cloud patterns derived from local sky images taken at the application sites. The model gets the direct, diffuse and global irradiance values incident on a horizontal surface, which are primarily obtained utilizing a solar irradiance model (the Morf (2013) model), along with local sky images captured at the application sites and cloud transmittance values, as input data and yields site-specific Spatially Dispersed Irradiance Profiles (SDIPs) incident on the surface of inclined PV panels within PV application areas, as a result of process of the inputs. Utilization of local sky images and cloud transmittance values for different cloud types creates the opportunity for precise analysis of interactions of sunlight with the existing cloud type and hence, obtaining unique and site-specific irradiance profiles according to the existing cloud type and distribution in the sky. The model firstly detects the cloudy and clear-sky parts in the sky image and then instantly utilizes the most appropriate ellipse on the cloud layer associated with each solar panel through which the beam irradiance is received by the panel. The model also considers the light transmission characteristics of different cloud types as the parameter affecting the beam irradiance. The diffuse and ground-reflected irradiance components are assumed to be spatially constant and thus identical for all solar panels. Cloud base heights, as provided in the International Cloud Atlas (1987), are also utilized to calculate the ground area covered by each sky image. Daily irradiance sequences for different observation points in a PV array are simulated under partly cloudy sky conditions using a set of sky images and utilized for validation purpose of the proposed algorithm. It is demonstrated that instantaneous irradiance values, as well as daily irradiance sequences, differ from point to point in a geographically distributed PV application site depending on the distribution of clouds in the sky. The mentioned variable characteristic of the irradiance sequences received at different observation points, as well as the model's capability to reflect the mentioned variabilities, is verified using irradiance data derived from satellite observations. The performance of the proposed model is validated using variability index (VI) metric as a measure of irradiance variability during a day. The modeled VI values are validated against the measured VI values for a reference point located at the center point of the generated irradiance profiles. Daily VI values calculated for both measured and simulated 1-min global horizontal irradiance (GHI) data are compared for a population of totally 117 days during April – August time period. The results of comparison show statistics of mean bias error (MBE) of 0.16, root mean square error (RMSE) of 2.394, correlation coefficient of 0.94 and mean absolute error (MAE) of 1.91. The validation results demonstrate capability and accuracy of the proposed model for estimation of irradiance values under cloudy sky conditions.

* Corresponding author.
E-mail addresses: moein.jazayeri@cc.emu.edu.tr (M. Jazayeri), kian.jazayeri@cc.emu.edu.tr (K. Jazayeri), sener.uysal@emu.edu.tr (S. Uysal).

http://dx.doi.org/10.1016/j.solener.2017.10.026
Received 14 June 2016; Received in revised form 2 October 2017; Accepted 7 October 2017

Nomenclature

AM	Air mass
a,b	Ångström-Prescott regression coefficients
$cc(t)$	Cloud cover [Oktas, tenths]
$\overline{cc}$	Average cloud cover [Oktas, tenths]
$cc_e(t)$	Ellipse enclosed cloud cover (EECC) [Oktas, tenths]
$C_x(t)$	Coordinate of ellipse center on X axis
$C_y(t)$	Coordinate of ellipse center on Y axis
$\overline{D_o}$	Mean daily clear-sky diffuse fraction
$D_x(t)$	Major axis of ellipse
$D_y(t)$	Minor axis of ellipse
e	Eccentricity of ellipse
$G(t)$	Cloudy sky horizontal irradiance [W/m^2]
$G_b(t)$	Clear-sky horizontal beam irradiance [W/m^2]
$G_{b\beta}(t)$	Clear-sky inclined beam irradiance [W/m^2]
$G_{d\beta}(t)$	Clear-sky inclined diffuse irradiance [W/m^2]
$G_g(t)$	Array point cloudy sky horizontal irradiance [W/m^2]
$G_{g\beta}(t)$	Array point cloudy sky inclined irradiance [W/m^2]
$G_o(t)$	Clear-sky horizontal irradiance [W/m^2]
$G_{o\beta}(t)$	Clear-sky inclined irradiance [W/m^2]
$G_{r\beta}(t)$	Clear-sky ground reflected irradiance [W/m^2]
$G_{x,y}(t)$	Irradiance at point (x,y) [W/m^2]
$G_\beta(t)$	Cloudy sky inclined irradiance [W/m^2]
$G_0(t)$	Extraterrestrial solar irradiance [W/m^2]
ΔG	Irradiance increment [W/m^2]
h	Elevation above sea level
H	Daily horizontal global irradiation [J/m^2]
$\overline{H_o}$	Mean daily clear-sky horizontal global irradiation [J/m^2]
H_0	Daily irradiation outside the earth's atmosphere [J/m^2]
$\overline{H_b}$	Mean daily clear-sky horizontal beam irradiation [J/m^2]
$\overline{K_d}$	Mean daily clear-sky diffuse clearness index
LT	Local time
LST	Local solar time
m	Image size for cloud pattern
R_b	Ratio between beam irradiance on inclined and horizontal surface
R_{cc}	Range of cloud cover [Oktas, tenths]
R_{cc_e}	Range of EECC [Oktas, tenths]
R_d	Ratio between diffuse irradiance on inclined and horizontal surface
R_G	Range of array point irradiance values [W/m^2]
$SIF(t)$	Stochastic insolation function
$\overline{H_d}$	Mean daily clear-sky horizontal Diffuse irradiation [J/m^2]
k,l	PV array size
$\overline{K_o}$	Mean daily clear-sky clearness index
$\overline{K_b}$	Mean daily clear-sky beam clearness index
SS	Sunset
φ	Latitude
x',y'	Cloud transmittance coefficient
α	Solar azimuth angle [degrees]
β	PV module tilt angle [degrees]
γ_s	Solar altitude angle [degrees]
δ	Solar declination angle[degrees]
θ_s	Solar incidence angle [degrees]
θ_z	Solar zenith angle [degrees]
μ_G	Mean of array irradiance values
$G_d(t)$	Clear-sky horizontal diffuse solar irradiance [W/m^2]
ρ	Ground reflectivity
$\bar{\tau}$	Cloud Transmission factor
τ_c	Cloud transmittance
τ	Time interval between irradiance measurements
ω	Hour angle
θ_p	Pixel zenith angle [degrees]
α_p	Pixel azimuth angle [degrees]

1. Introduction

High dependency of solar energy applications on the incident solar irradiance causes a vital need to obtain precise knowledge regarding solar irradiance levels received by each individual PV module within the application areas to create the opportunity for appropriate design and management of PV systems. Large-scale centralized PV power plants or PV plants distributed on a wide geographical area can be considered as examples of such applications. Power generation in such plants is also highly dependent on the non-identical irradiance levels incident on the surface of PV panels within the PV power plant, that are caused by cloud passages. Dependence of power generation in PV power plants on the received non-identical irradiance values caused by the real-time passing clouds is one of the main reasons for the need to the site-specific irradiance data. Unavailability of instantaneous data or limitations associated with the measurement stations have led to development of solar radiation estimation and/or simulation models. Numerous models have successfully been developed for clear-sky solar irradiance where the main emphasis is put on modeling of the beam component of the irradiance due to its importance for solar energy systems.

Clouds, at the same time, as some complex elements of the climate, have significant impacts on the incident irradiance. Thus, a good model, from PV system's point of view, should necessarily account for cloud properties to include the effects of interactions of the existing clouds with the incoming solar irradiance. The output of such a model being capable of estimation of solar irradiance under cloudy sky conditions can be considered as a reliable input for the desired PV applications.

The goal of this paper is to develop a model to generate spatially dispersed irradiance profiles incident on PV power plants extended in a wide geographical area or distributed PV power plants, taking into account the existing cloud coverage at the intended application sites. In this way, precise information on the amount of solar irradiance received by each individual solar panel within the PV power plant can be obtained at each desired instant of time. Consequently, estimation of power production and taking necessary actions to cope with negative effects caused by non-identical irradiance levels received by different solar panels in a PV plant is facilitated. As it is discussed in the further parts of the paper, the developed model mainly utilizes clear-sky global irradiance as well as the direct and diffuse irradiance components and accounts for light transmission characteristics of the existing cloud coverage to generate the mentioned irradiance profiles.

As mentioned previously, since the beam or direct irradiance component is more important from solar energy employing system design point of view, emphasis is mostly put on estimation of the mentioned irradiance component. Models introduced in the literature for estimation of direct or beam component of solar irradiance are mainly categorized under two groups as (Wong and Chow, 2001);

(1) Parametric Models
(2) Decomposition Models

(ASHRAE, 1999; Iqbal, 1983; Davies and McKay, 1989; Gueymard, 1993) are some of widely utilized parametric models while (Liu and Jordan, 1960; Erbs et al., 1982; Reindl et al., 1990a; Skartveit and Olseth, 1987; Louche et al., 1991) are provided as examples of decomposition models in the literature. Parametric models require detailed information regarding the atmospheric conditions such as cloud type, cloud coverage and distribution in the sky, sunshine duration, etc., while decomposition models only utilize global irradiance to estimate direct and diffuse irradiance components. The ASHRAE model is widely utilized due to its simplicity over the other models while a

review by Gueymard (2012) has shown that the Iqbal model is the most accurate model compared to the other parametric models. Evaluation results reported by Wong and Chow (2001) show that ASHRAE model provides lower accuracy in diffuse irradiance predictions compared to the Iqbal model as it does not include the ground reflected irradiance and aerosol-generated diffuse irradiance. As discussed in detail in further parts of the paper, this study primarily employs a model which utilizes various parameters such as cloud coverage, sunshine duration and cloud transmittance in order to estimate direct, diffuse and global irradiance components on a horizontal surface. At the second stage, the mentioned irradiance components are utilized, as inputs, by the model which is proposed in order to develop spatially dispersed irradiance profiles for PV application areas.

Cloud coverage dramatically affects atmospheric light transmission and is most often expressed in Oktas describing the amount of the sky which is covered by clouds (Jones, 1992). Cloud cover data is readily available for many meteorological stations being generally provided as hourly or 3-hourly observations, where 0 and 8 Oktas correspond respectively to totally clear and overcast sky dome. The mentioned considerations require the measurements of cloud cover and its properties to be dealt with by solar radiation models. Cloud properties can be analyzed under two main aspects; Dynamic and Radiometric properties (Harris, 2003). The importance of cloud dynamic properties for PV applications is due to the fact that cloud motion is the main reason for PV power fluctuations whereas the radiometric properties of clouds, including light scattering and optical properties, govern the interactions of solar irradiance with water droplets creating the clouds. Kokhanovsky (2004) provides a comprehensive review of cloud optical properties. Cloud detection and classification methods utilize either ground-based measurements or satellite images. Tapakis and Charalambides (2013) extensively review cloud detection and classification methods and equipment utilized in the literature. In addition to the mentioned cloud detection techniques, various studies have been conducted to model the cloud coverage. Models introduced by Cai and Aliprantis (2013), Morf (2011) and Jones (1992) are example of these models.

Several irradiance models in the literature consider cloud coverage and sunshine duration for irradiance estimation under cloudy sky conditions. See for example (Schüepp, 1966; Ehnberg and Bollen, 2005; Biga and Rosa, 1979; Biga and Rosa 1980; Morf, 1998; Morf, 2013; Badescu, 2002a). Such models generate time-series of global solar irradiance on horizontal surfaces with respect to the geographical location of the application sites. The achieved sequences of solar irradiance on horizontal surfaces should then be converted to irradiance incident on inclined PV module surfaces for output power estimation purposes (Padovan and Del Col, 2010; Nijmeh and Mamlook, 2000; Reindl et al., 1990b).

In parallel, non-identical solar irradiance received by different PV panels in a PV array, which is mostly caused by cloud passages, is known as one of the most challenging issues during estimation and analysis of PV power generation. Since cloud shadows dramatically decrease PV power generation, precise estimation and development of an appropriate model for cloud shadows and the resulting irradiance profiles on PV arrays would ease estimation of power generation or selection of proper strategies to combat the negative effects. During the past years, numerous research studies have been conducted to model partial shading effects on PV power generation. Examples of these studies are provided by Villalva et al. (2009), Ishaque et al. (2011a, 2011b, 2011c), Wang and Hsu (2010, 2011). However, most of the models consider shadow patterns on PV arrays that are generated without consideration of a real cloud coverage and its characteristics during their analyses. On the other hand, most of solar radiation models consider the total cloud coverage existing in the sky, as a whole, which does not provide the opportunity for generation of shadow patterns on PV arrays based on the existing cloud shape and its distribution in the sky.

Currently most of solar radiation forecasting methods rely on two main approaches being Numerical Weather Prediction (NWP) and forecasting methods based on real-time measurements of satellites or ground-based instruments (Yang et al., 2014). However, the mentioned ground-based measurement equipment are typically point sensors which do not provide spatial irradiance information (Chow et al., 2011). Satellite-based data outperform data generated by NWP models in determining the exact position of the clouds while NWP forecasts are found to outperform satellite forecasts for longer forecast horizon times (Perez et al., 2010). However, as previously mentioned, these models are presently unable to predict the exact position of clouds and their effects on solar radiation over a specific location of interest. On the other hand, satellite based forecasts are not optimal for very short-term and high resolution forecasts due to sparse update cycles, coarse spatial resolution and long lasting data transfer and process times. Therefore, by taking the above into consideration, development of a better short-term measurement-based forecast with high spatial and temporal resolutions is needed (Yang et al., 2014). Sky imagers are relatively more economical and reliable passive devices that also can be benefited for unattended operations (Allmen and Kegelmeyer, 1996). They provide various features, making them desirable for cloud studies. They provide possibility of visual measurement of the whole sky dome providing high temporal and spatial resolution. A charge coupled device (CCD) camera, a fisheye lens, an environmental housing and a CCD sensor and application dependent solar occultor are the typical components of a sky imager (Chow et al., 2011). Sky images have been used in various research studies to retrieve atmospheric properties such as aerosol optical depth, cloud optical depth, cloud coverage, cloud type and Cloud Base Height (CBH) (Heinle et al., 2010; Huo and Lu, 2009,2010; Kassianov et al., 2005; Long et al., 2006; Pfister et al., 2003; Seiz et al., 2007). Moreover, Nguyen and Kleissl (2014) have used sky images for determination of cloud base height (CBH) to overcome the low temporal resolution and high cost drawbacks of the existing CBH measurement technologies such as radiosonde, ceilometer, Droppler LIDAR and cloud radar. Sky imagers have also been utilized in (Yang et al., 2014) for solar irradiance forecasting and Chow et al. (2011) have deployed sky imager data for intra-hour, sub-kilometer cloud forecasting and solar irradiance nowcasting purpose.

Nguyen et al. (2016) propose a method which utilizes sky imager data to generate irradiance profiles with high spatial and temporal resolution on different geographically distributed PV systems. The study determines irradiance profiles on five different PV sites in San Diego, CA, USA. The structure of the utilized method in the mentioned study can briefly be summarized as follows; Sky images taken every 30 s. by a fisheye lens sky camera are processed using a cloud detection algorithm to determine cloudy and clear pixels of the images and hence determine the location of clouds within the image. Each image covers a circular region in the sky where the radius of the coverage area depends on the cloud base height, obtained utilizing a specific cloud base height calculation method. The images are then mapped into 2D sky grids. Ray tracing method is then utilized to generate cloud shadow maps on the desired PV application areas and hence, to determine if any individual PV generator in the application area is shadowed by the clouds. Cloud conditions are classified under three different cloud categories namely being; no cloud (clear-sky), thin clouds (partly cloudy) and thick clouds (overcast sky) conditions. These cloud classes are then utilized to obtain irradiance profiles. For this purpose, a histogram of the measured irradiance values is formed. The measured irradiance values using a network of pyranometers are then normalized by the expected clear-sky irradiance values calculated based on a clear-sky model for the areas of interest to form clear-sky indices corresponding to the mentioned three cloudiness conditions. The horizontal irradiance incident on each PV panel is then calculated by multiplying the global horizontal clear-sky irradiance by the clear-sky index for the desired PV panel. The obtained irradiance values are then converted to irradiance values incident on inclined solar panel surfaces. However, limitation of the existing cloud

coverage by the mentioned 3 categories can be considered as one of the main drawbacks of this method. Whereas in contrast, consideration of various cloud types and their specific light transmission coefficients, discussed throughout the further parts of the paper, allows for a more realistic analysis of effects of the existing clouds during generation of irradiance profiles. Another weak aspect of the method introduced in (Nguyen et al., 2016) is the dependency on pyranometer measurements to form the irradiance histograms and obtain clear-sky indices, which makes the model sensor dependent. Unavailability of pyranometer measurements for each area of interest due to lack of equipment and/or irregular data recordings may cause undesired obstacles against use of the mentioned method for some locations. The mentioned disadvantage is overcome in this paper by calculation of the irradiance values using an irradiance estimation model, as discussed in the further parts, which enables calculation of solar irradiance under cloudy sky conditions. Hence, the model is not dependent on pyranometer measurements and is applicable to almost any desired geographical location. The mentioned two factors may be considered as the main added values by this work to the study by Nguyen et al. (2016).

In a recent study, Lohmann et al. (2017) have used a fractal cloud model in order to simulate clear-sky index increment correlations under mixed sky conditions. They have utilized an extensive set of sky camera and satellite images along with data from two pyranometer networks and CBH estimations from a ceilometer. The mentioned data are utilized for estimation of cloud edge fractal dimensions under partly cloudy sky conditions, generation of cloud shadow patterns on the ground and evaluation of suitability of the generated artificial fractal cloud shapes for modeling of the previously mentioned autocorrelation structures. For this purpose, firstly, measured clear-sky index time-series, K_o, are calculated using pyranometer measurements and a clear-sky irradiance model for each individual pyranometer. Red-Blue Ratio (RBR) values together with CBH estimations, as discussed also in further parts of this study, are utilized for cloud detection in sky camera images and determination of the area covered on the ground. Cloud index maps and cloud motion vectors are also obtained based on quarter-hourly satellite images. Cloud shadow maps are obtained by generation of fractal cloud images and then virtually moving them in the direction of the wind over a set of virtual pyranometer networks where cloud speeds are derived from satellite data. Finally, the modeled cloud index values are converted to clear-sky index time-series using an empirical relationship. However, comparison results present both differences and similarities between the modeled and measured clear-sky index values. In one hand, it is shown that the modeled field statistics are similar to the measured values and the variable characters of the mean of the modeled and measured sensors are in a very good agreement. On the other hand, incompatibility of the large-scale satellite observations with the utilized empirical relationship in order to convert cloud index values to clear-sky index time-series is provided to be the main reason for the mentioned differences. Results of the study by Lohmann et al. (2017), showing that satellite observations are not suitable for short-term forecasts, once again approves the previous discussions of this paper. Also it is provided that satellite approximations of cloud edge dimensions are higher than sky imager data and the authors concluded that sky imagers are more suitable for cloud analyses, where the mentioned conclusion also supports the previous discussions of this paper. A drawback of the model utilized by Lohmann et al. (2017), similar to the one utilized in (Nguyen et al., 2016), is that different cloud types are all combined within one category without consideration of the light interaction characteristics of each specific cloud type. This issue caused a higher dispersion range of the observation-derived spatial autocorrelation structures of clear-sky index values compared with the modeled ones, around the medians. The utilized fractal cloud model does not include light interaction characteristics of different cloud classes that cause it being not necessarily applicable to different geographical locations than those analyzed in the paper. Another drawback of the work by Lohmann et al. (2017) is its high dependency on instrumental observations (e.g. pyranometer and ceilometer measurements, satellite and sky camera images) which makes its application difficult where the mentioned data are not readily accessible due to lack of equipment and/or irregular or incompatible data recordings. As previously discussed and in order to overcome the mentioned issue, this paper proposes a global model with minimum requirements to instrument measured data which is applicable to any desired geographical location, by considering different cloud types and their effects on the received solar irradiance.

As mentioned earlier, this paper proposes a modeling approach which mainly focuses on generation of spatially dispersed irradiance profiles on desired PV application areas. The mentioned profiles are generated based on cloud shadow patterns induced on the area by the existing real clouds in the sky. The method presents the opportunity to obtain instantaneous site-specific Spatially Dispersed Irradiance Profiles (SDIPs) considering the instant position of the Sun in the sky with respect to each individual observation point, existing cloud patterns and their light transmission characteristics. Therefore, since the method provides instantaneous irradiance values incident on the surface of each solar panel within the PV plant based on the existing cloud coverage in the sky, it could be thought of as a prerequisite for PV system performance investigation models by providing the required solar irradiance data for the mentioned investigations. Utilization of the proposed model offers the possibility for creation of unique, site-specific irradiance profiles under any type or amount of cloudiness based on real cloud shadow patterns for desired geographical locations at any given desired time instant. Also utilization of the proposed model together with consecutive local sky images provides the opportunity to obtain irradiance time-series for desired observation points during a day. The highlighted feature makes the model useful to be utilized for realistic and precise analysis of PV power generation and its fluctuations and also for selection of proper improving strategies under cloudy sky conditions.

The remaining parts of the paper are organized as follows; Different data parameters utilized throughout the paper are explained in Section 2 while Section 3 presents the proposed modeling approach to generate SDIPs on PV fleets with respect to existing real-time cloud pattern and its interactions with solar irradiance. Results obtained with the proposed modeling approach are discussed through Section 4. Appendices A and B present details of the utilized model for estimation of daily global irradiance time-series on a horizontal surface and the conversion procedure for irradiance sequences on horizontal surface to irradiance incident on inclined PV module surface, respectively.

2. Data

This part of the paper includes various data utilized throughout the paper. The data consist of measured solar irradiance, solar irradiance values derived from satellite observations, sky images and observed cloud coverage for desired geographical locations.

Since irradiance measurements incident on an inclined surface were not available for Berlin, Germany, where the main focus area of this paper is, the irradiance data measured using a pyranometer for Famagusta, North Cyprus (Latitude: 35°8′18″, Longitude: 33°55′45″) are utilized in Appendix B for validation purposes. Per-minute irradiance measurements on an inclined surface in Famagusta, North Cyprus (Latitude: 35°8′18″, Longitude: 33°55′45″) are conducted using a 45° inclined irradiance sensor (pyranometer). These data are used in order to verify the accuracy and effectiveness of the selected clear-sky model and the conversion method of the horizontal irradiance to irradiance incident on inclined surfaces.

However, as previously stated and since not all of the required parameters are recorded and readily available for Famagusta city, it is preferred to apply the general model on Berlin, Germany (Latitude: 52°33′56″, Longitude: 13°18′39″) as a well-known location with easy access to the required data. Therefore, measured per-minute horizontal irradiance data for Lindenberg, Germany (Latitude: 52°12′36″, Longitude: 14°7′19″) is utilized as another source of data in the paper. The mentioned irradiance measurements are retrieved from WRMC-BSRN (World Radiation Monitoring Center – Baseline Surface Radiation

Network) website (WRMC-BSRN, 2016). These data are used for verification purposes as described in Section 4.1.

Hourly mean global irradiance values for an observation point in Berlin, Germany (Latitude: 52°33′56″, Longitude: 13°18′39″) along with its four surrounding geographical locations are retrieved from METEOSAT observations data set provided by the Satellite Application Facility on Climate Monitoring (CMSAF) with 0.03 × 0.03 degrees spatial resolution (Posselt et al., 2011). The mentioned irradiance observations are used for verification purposes as described in Section 4.2.4.

Sky images form another source of data utilized in this paper in order to obtain cloud patterns over application areas. Local sky images are taken with 1-min. time resolution both in Lindenberg and Berlin, Germany, by a commercial camera providing 720 × 576 RGB images. These local sky images are assumed as two dimensional cloud maps projected on latitude-longitude from whole sky images, as detailed in Section 3.

Observed cloud coverage for Lindenberg, Germany (Latitude: 52°12′36″, Longitude: 14°7′19″) provided by Behrens (2016) is another source of data which is utilized in this paper during model verification procedure, as described in Section 4.1. Table 1 provides brief information regarding different data utilized in the paper along with the location and purpose of utilization of the data.

3. Generation of Spatially Dispersed Irradiance Profile (SDIP) based on existing cloud patterns

Following the earlier discussions, a detailed knowledge of the incident irradiance on inclined PV module surfaces is of paramount importance for PV system design and management purposes. Such values can readily be obtained using irradiance models under absence of clouds since they do not vary over the extent of PV array. However, under cloudy sky conditions, presence of clouds, their shapes, distribution and light scattering characteristics cause significant variations in the incident irradiance on PV module surfaces distributed within an array. As the power generation in PV modules is directly affected by the incident irradiance, effects of non-identical irradiance values caused by the mentioned variations give rise to significant fluctuations in PV power generation. Thus, realistic estimations of the incident non-identical irradiance values present the opportunity for precise analysis and consideration of appropriate coping strategies in PV arrays. Generation of such reliable estimations requires realistic site-specific cloud shadow patterns to be integrated into irradiance models. A modeling approach for generation of site-specific spatially dispersed irradiance profiles on PV arrays which utilizes the Sun's position in the sky along with the distribution and characteristics of the existing cloud coverage is proposed in this paper. The proposed model in this paper utilizes clear-sky irradiance components along with the existing local cloud coverage and its light interaction characteristics to generate the irradiance profiles. The Morf (2013) model, as described in Appendix A, is utilized to generate clear-sky direct, diffuse and global irradiance values as well as the cloud transmission factor, $\bar{\tau}$, which are then utilized by the proposed model to generate SDIPs. The Morf (2013) model is selected due to its simplicity and compatibility with the goals of this paper. The mentioned model, in general, assumes the incident global horizontal irradiance as a combination of the beam irradiance, the diffuse irradiance coming from the cloudy part of the sky and the diffuse irradiance from the clear-sky.

The model proposed in this paper basically considers the instant position of the Sun in the sky with respect to each observation point, as well as the existing cloud type and their light transmittance characteristics. The Sun's disk is viewed by each observer as the base of a cone with opening angle of 0.5° (Duffie and Beckman, 2006). For each PV module, the cut of the cone by the cloud layer forms a circle when $\hat{\theta}_Z = 0°$. These circles then transform to ellipses in parallel with the variations of solar zenith angle during a day and each PV module receives the beam irradiance through the mentioned ellipses. In fact, the Sun's disk may only be partly obscured by the existing clouds at a given time instant. Thus, the beam irradiance is only affected by the cloud cover which is enclosed by the ellipse, not the total cloud cover existing in the sky. On the other hand, the diffuse irradiance received from the cloudy part of the sky remains unchanged as well as the diffuse irradiance incident from the clear-sky portion. As the position of the Sun in the sky varies continuously, the determinative task is now to obtain the most appropriate ellipse associated with each observer at each time instant. Determination of the mentioned ellipses is discussed in detail in Section 3.1.5.

Once the proper ellipse for each observer at each time instant is obtained, the incident irradiance value is achieved using Eq. (1) which is a modified version of the Morf (2013) model provided by Eq. (A.1). The incoming beam irradiance is divided into two components; the beam irradiance directly coming from the clear-sky portion and the attenuated beam irradiance from the cloud covered portion of the sky enclosed by the mentioned ellipses. The magnitude of the attenuation of the beam irradiance depends on the cloud transmittance, τ_c, which varies based on the cloud type. For each individual observation point, the instantaneous global irradiance falling on a horizontal surface is determined as;

$$G_g(t) = [((1-cc_\varepsilon(t))\cdot G_b(t)) + cc_\varepsilon(t)\cdot\tau_c\cdot G_b(t)] + (1-cc(t))\cdot G_d(t) + cc(t)\cdot\bar{\tau}\cdot G_o(t) \quad (1)$$

As discussed earlier, Nguyen et al. (2016) in their model categorize the existing cloud conditions into three different classes: no cloud (clear-sky), thin and thick cloud and use this categorization to convert cloud shadow maps into irradiance profiles. This is achieved by calculation of the clear-sky indices corresponding to each cloud condition by utilizing a histogram of measured global irradiance values provided by pyranometers and modeled values of clear-sky global irradiance. Instead of the method proposed in (Nguyen et al., 2016), this paper obtains the incident global irradiance at each observation point through an irradiance model, providing the opportunity to separately obtain each irradiance component (beam, diffuse and ground-reflected) and reducing the dependency on irradiance sensors or pyranometers, as the mentioned devices may not be available for each application area. Since higher number and more detailed cloud classes are considered, utilization of transmission coefficients for different cloud types in this paper also provides possibility to increase the accuracy during analysis of the interactions of solar irradiance with the existing clouds.

Different steps of the proposed modeling method in this paper are

Table 1
Summary of the data utilized in the paper.

Data Type	Location	Purpose of Utilization
Measured Global Solar Irradiance Time-Series	Famagusta, North Cyprus	Verification of the selected clear-sky irradiance model and the conversion method of horizontal irradiance to irradiance incident on inclined panel surface (Appendix B)
	Lindenberg, Germany	Verification of the model proposed to generate spatially dispersed irradiance profiles (Section 4.1)
Hourly Mean Global Solar Irradiance Values Derived from Satellite Observations	Berlin, Germany	Verification of the capability of the proposed model to reflect the variable characteristic of the incident irradiance at different observation points (Section 4.2.4)
Sky Images	Lindenberg and Berlin, Germany	Generation of cloud patterns over the application areas (Section 3 and Section 4)

explained in a flow chart as shown in Fig. 1 for easier follow up of the flow of the contents. The developed model is provided as a global model which is applicable to either online or historical sky images or cloud maps of any spatial resolution containing any class of clouds regardless of their base heights in the sky.

3.1. Simulation procedure

This part of the paper provides details on the simulation of each single step of the proposed modeling method, as shown in Fig. 1, which finally leads to generation of spatially dispersed irradiance profiles for desired application areas. Several research studies have proposed models or estimations for cloud coverage and/or shadow patterns. However, it is believed that the existing local shadow pattern over a geographical area at each time instant can best be represented by the existing real clouds in the sky at the corresponding instant of time. Nguyen et al. (2016) proposes cloud shadow maps on application areas that are generated using images taken by total sky imagers (TSI). It is provided that the fisheye nature of the sky imagers causes the spatial resolution of different areas of shadow maps being dependent on their distance from the center of the sky image. For this purpose, a geometric transformation with details provided in (Yang et al., 2014) similar to the Pseudo-Cartesian transformation introduced by Allmen and Kegelmeyer (1996) is utilized to obtain a two dimensional latitude-longitude grid representing the "cloud map" centered at the sky imager position above the application area. The proposed approach in this paper utilizes real-time captured local sky images, as described in Section 2, to obtain instantaneous shadow patterns over the application areas. The mentioned sky images are assumed as two dimensional latitude-longitude cloud maps obtained from whole sky images over the application areas. The Sun's position in the sky at each desired time instant is calculated and the Sun is virtually located on the mentioned sky images. This approach provides possibility for simulation of interactions of solar irradiance and clouds, under any type of cloud distribution and for any desired time instant.

3.1.1. Cloud decision

This part specifically provides information regarding the method utilized to classify the cloudy or clear pixels of the sky image. Once the two dimensional sky images are obtained, the first task is to identify cloudy and clear parts of the sky in the mentioned images. An image processing method similar to the one which is widely utilized in cloud cover estimation studies is utilized to decide if each pixel of the sky image is cloudy or not. This method relies on the concept of the ratio of the scattered red light to the blue light which was firstly developed at the Scripps Institution of Oceanography (Johnson et al., 1989; Johnson et al., 1991; Shields et al., 2007). In general, the amount of the scattered blue light is higher compared to the red light under clear-sky conditions while clouds scatter more red light in contrast. Hence, the method considers the differences between the scattered blue and red lights and examines the Red/Blue Ratio (RBR) for each pixel. A threshold value based on the atmospheric conditions and the capturing equipment is set and pixels with RBR values exceeding this threshold are assumed as "cloudy" pixels.

3.1.2. Cloud pattern

Cloud patterns are generated following the cloud decision that is made as a result of the method provided in Section 3.1.1 by assignment of 1's and 0's to cloudy and clear pixels, respectively. In order to maintain uniformity and facilitate application of the model to sky images with different resolutions, the obtained cloud pattern image is resized to an $m \times m$ image to assist further analyses. It should be noticed that as well as the cloud maps, the resulting cloud patterns are also 2D latitude-longitude images. The image size, (m), may arbitrarily be chosen according to the application requirements. There always exists a tradeoff between the higher accuracies achieved with higher image sizes against increases in computational time and memory usage.

3.1.3. Cloud transmittance

As discussed earlier, the beam irradiance is affected by the cloud transmittance, τ_c. Cloud transmittance is a parameter governing the interactions of solar irradiance with clouds and its magnitude depends on different cloud types. Cloud transmittance in this paper is calculated using the method introduced by Jewell and Ramakumar (1987) using Eqs. (2), (3) based on a list of cloud transmission coefficients, x' and y', as given in Table 2. Cloud types are manually evaluated from the utilized sky images based on their shape in accordance with the classification provided in the International Cloud Atlas (1987).

$$\tau_c = (AM \times y') + x' \tag{2}$$

$$Airmass = AM = \frac{35}{(1224\cos^2\theta_Z + 1)^{1/2}} \tag{3}$$

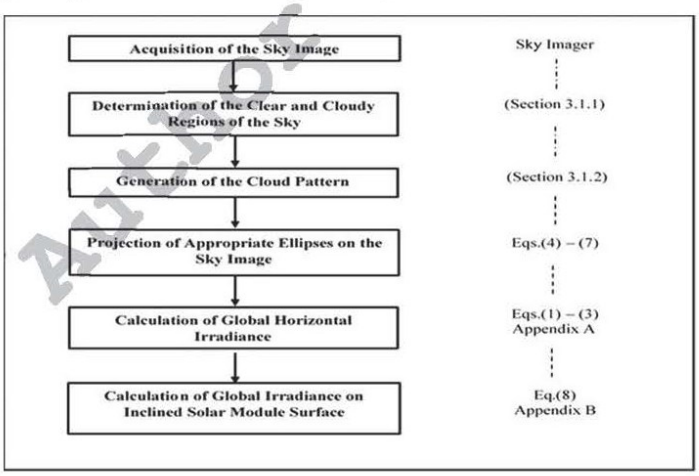

Fig. 1. Flow chart of different steps of the proposed modeling method.

Table 2
List of cloud transmittance coefficients.

Cloud Type	x'	y'
Fog	0.163	0.005
Stratus Nimbostratus	0.268	0.101
Stratocumulus	0.366	0.015
Cumulus	0.366	0.015
Cumulonimbus	0.236	0.015
Altostratus	0.413	0.001
Altocumulus	0.546	0.024
Cirrostratus	0.905	0.064
Cirrus	0.872	0.018

3.1.4. Cloud base height

As discussed in Section 3.1.3, cloud types and base heights in this paper are manually evaluated based on their shapes according to the cloud classification introduced in the International Cloud Atlas (1987). The mentioned cloud base heights are used to obtain the ground area covered by the utilized sky images. As an example, the minimum and maximum base height values, as provided in Table 3, are utilized to approximately calculate the lower and upper limits of the ground area that may be covered by each cloud type in Fig. 8. Information regarding the considered cloud types, their corresponding classes and height ranges are summarized in Table 3. It should be noticed that Table 3 only includes information regarding cloud types that are utilized during analyses of this paper. These cloud types are manually selected as representatives of low, middle and high level cloud classes defined by the International Cloud Atlas (1987) while each mentioned class may also include some other cloud types. Some examples of the mentioned cloud types are provided in Table 2.

3.1.5. Determination of appropriate ellipses

The next step is to determine appropriate ellipses for each individual solar module within the array or each "*array observer*" on the cloud layer, through which the beam irradiance is received by the observer. This is accomplished by considering the virtually located instantaneous positions of the Sun in the local sky images during a day, from sunrise to sunset. PV modules within the PV power plant are assumed to be south oriented in the northern hemisphere. The geographical extent of the PV array is then considered as an $k \times l$ area on the ground with $0 < k \leq m$, $0 < l \leq m$. A size of 100 ($m = k = l = 100$) is utilized in this paper so that the cloudy and clear parts of sky as well as the areas of PV array subject to the resulting irradiance profiles are assumed to be represented as percentage areas. Approximate values for the actual ground coordinates of the PV array covered by the utilized sky image vary according to the cloud base height and are discussed throughout the rest of the paper. Eqs. (4)–(7) are utilized to determine the corresponding ellipse for each array observer and project it on the cloud layer at each time instant. Fig. 2 shows the position of the Sun in the sky with respect to a solar panel on the ground at two different time instant and the resulting circles/ellipses through which the solar panel receives the beam irradiance. As previously mentioned, each solar panel within the PV power plant sees the Sun's disk as the base of a cone with opening angle of 0.5° and receives the beam irradiance through circles when these cones cut the cloud layer exactly at solar noon ($\theta_Z = 0°$). The mentioned circles then transform to ellipses in parallel with the movement of the Sun in the sky and variations of the solar zenith angle towards sunset or sunrise during a day (Morf, 2013). Thus, the beam irradiance received by each observer is affected by the cloud coverage falling within the mentioned circles/ellipses. This fact is the motivation to develop a model to determine the most appropriate ellipse (in terms of the ellipse thickness and coordinates of the ellipse center) at each time instant for each individual observer and to detect the cloud coverage within the ellipse as the factor affecting the magnitude of the received beam irradiance by each observer.

Obviously the position and thickness of ellipses, through which the beam irradiance is received, depend on the instantaneous positions of the Sun in the sky. Since the position of the Sun in the sky is defined by two different angles being solar zenith angle and solar azimuth angle, the thickness and location of these ellipses are also assumed to be controlled by and adjusted on the mentioned two angles. As discussed earlier, changes in ellipse thickness are considered proportional to the changes of the solar zenith angle considering at the same time the opening angle of the cone, (0.5°), which forms the ellipse by cutting the cloud layer, as provided by Eq. (4). Thus, at solar noon ($\theta_Z = 0°$) the thickness of the ellipse has its maximum value and the major axis of the ellipse takes the smallest value forming the closest ellipse to a circle while the thinnest ellipse is formed when the solar zenith angle takes its maximum value towards sunset or sunrise. At the same time, the minor axis of the ellipse is geometrically defined based on the major axis as demonstrated by Eq. (5). Here also the instantaneous positions of the ellipse centers on the utilized sky image should be determined for adequate location of the ellipses on the image. For this purpose, changes of the position of the ellipse center along the x-axis are considered to be proportional to the Sun's movement in the sky from east to west during a day which is defined by solar azimuth angle, as provided by Eq. (6). Hence, the ellipse center is assumed to be located at the center (directly above each PV panel) at solar noon ($\alpha = 0°$) and at the outmost positions at sunrise and sunset. Movement of the ellipse center along y-axis is considered to be proportional to the solar zenith angle as demonstrated by Eq. (7). In this way, generation of the thickest ellipses located exactly above each PV module at solar noon is made possible while the ellipses get thinner and further towards sunrise and sunset proportional to the Sun's movement in the sky.

$$D_x(t) = 2\lfloor((\theta_z(t) + 0.25)/(90°)) \times m\rfloor \tag{4}$$

$$D_y(t) = 2D_x(t)\sqrt{(1-e^2)} \tag{5}$$

$$C_x(t) = \begin{cases} [\alpha(t)/\alpha(t_{sunrise})] \times m, & t < 12\ LST \\ [\alpha(t)/\alpha(t_{sunset})] \times m, & t \geqslant 12\ LST \end{cases} \tag{6}$$

$$C_y(t) = [\theta_z(t)/90°] \times m \tag{7}$$

$C_x(t)$ and $C_y(t)$ represent the coordinates of the ellipse center projected on the cloud layer, for each observer. The ellipse centers locate on east and west sides of each observer before and after solar noon, respectively.

3.1.6. Modeling of solar irradiance

Once the most appropriate ellipse for each observer is determined and projected on the utilized local sky image at each time instant, the cloudy and clear pixels of the portion of the sky image enclosed by the mentioned ellipse are determined as discussed in Section 3.1.1. The ellipse enclosed cloud cover (EECC) is then identified by dividing the number of cloudy pixels by the total pixel number enclosed within the ellipse. The horizontal irradiance received at each observation point is then obtained through Eqs. (1)–(3) and Table 2. A procedure similar to the one in Appendix B is followed to convert the obtained horizontal irradiance into irradiance incident on inclined surfaces as;

$$G_{b\beta}(t) = [(1-cc_e(t))G_{b\beta}(t) + cc_e(t)\tau_c G_{b\beta}(t)] + (1-cc(t))G_{d\beta}(t) + cc(t)\bar{\tau}R_d G_o(t) + \rho R_r G_g(t) \tag{8}$$

Table 3
Information regarding the utilized cloud types.

Cloud type	Cloud class	Cloud height (ft)
Cumulus	Low Clouds	2000–3000
Stratocumulus	Low Clouds	2000–6500
Altocumulus	Middle Clouds	6500–18000
Cirrus	High Clouds	16500–45000

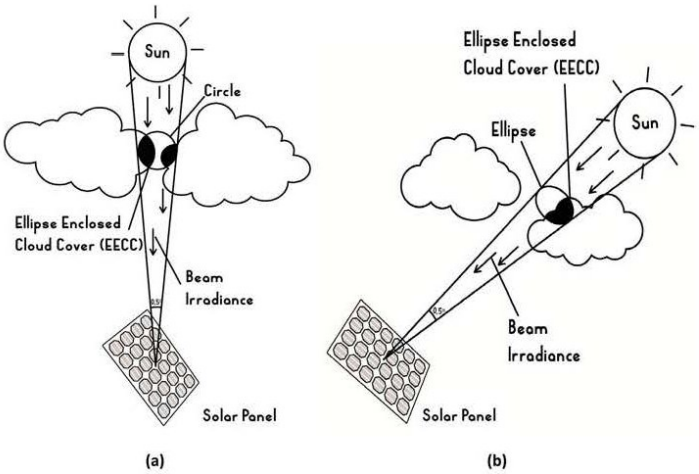

Fig. 2. Position of the Sun in the sky and the resulting circle/ellipse with respect to a ground-mounted solar panel at (a) solar noon, (b) a time instant towards the sunset or sunrise.

3.1.7. Ground coverage area

As mentioned in Section 3.1.4, cloud base height plays a key role for precise determination of the area covered by each utilized local sky image on the ground. However, lack of precise data regarding cloud base height, which may be due to unavailability of proper equipment, etc., may cause errors in calculation of the exact area covered by the utilized sky images on the ground. In order to overcome this issue and make the model applicable to any sky image, even when precise cloud base height information data are not available, the area on the ground covered by the sky image, and hence the resulting irradiance profile, are presented by percentage values instead of exact ground coordinates in meters, etc. For example, the whole area on the ground covered by each sky image is presented as 100% area instead of exact coordinates in meters, which may not be accurate in cases where precise cloud base height data are not available. As it was previously mentioned in Section 3.1.2, cloud patterns in this paper are resized to an $m \times m$ image in order to maintain uniformity and the resulting irradiance profiles on the ground are presented by percentage values in a $k \times l$ 2D latitude-longitude grid as discussed previously in Section 3.1.5. In this way, regardless of the cloud type and its height in the sky, the model presented in this paper can be applied to any sky image containing any class of clouds with different heights in the sky, even in cases when precise cloud base height values are not readily available. In addition to the above mentioned presentation of the ground area covered by irradiance profiles, the method introduced by Chow et al. (2011) is also used in further parts of the paper. The mentioned method is utilized in order to approximately calculate the coordinates of the ground area covered by each utilized sky image by considering the min. and max. cloud base height values defined for each cloud type according to Table 3. Chow et al. (2011) define the coordinates of the ground area covered by each sky image as a function of the cloud base height from the ground level as;

$$\begin{Bmatrix} x \\ y \end{Bmatrix} = \Delta H \tan\theta_p \begin{Bmatrix} \sin\alpha_p \\ \cos\alpha_p \end{Bmatrix} \tag{9}$$

where, ΔH represents the cloud base height from the ground level, θ_P and α_P represent the pixel zenith and azimuth angles in the sky image, respectively. Obviously, according to Eq. (9), higher clouds result in wider ground areas covered by the sky image.

4. Results and discussion

The proposed approach provides the opportunity to obtain irradiance profiles on PV arrays based on the existing real cloud patterns and their characteristics and hence provides the possibility for accurate analysis of the effects of the incident non-identical irradiance values caused by cloud passages. This part of the paper includes validation of the developed model along with some examples and results of application of the model. The model is successfully verified using measured irradiance data and presented high accuracy in modeling irradiance variability during the validation time period.

4.1. Model verification

The proposed model for generation of SDIPs on PV arrays based on local real sky images is validated using the Variability Index (VI) metric, defined as a measure of irradiance variability over a specified time period, as proposed by Stein et al. (2012) and also utilized by Nguyen et al. (2016). The metric is defined as;

$$VI = \frac{\sum_{t=2}^{n} \sqrt{(G(t)-G(t-1))^2 + \Delta t^2}}{\sum_{t=2}^{n} \sqrt{(G_o(t)-G_o(t-1))^2 + \Delta t^2}} \tag{10}$$

The proposed model in this paper is presented as a global model which is capable of irradiance estimation for different geographical locations, where appropriate input data are available. Thus, it is assumed that once the model is validated it can generate reliable irradiance profiles for desired application areas. Therefore, although the model itself is applied and sample results are provided for Berlin, Germany, measured irradiance data provided by WRMC-BSRN for Lindenberg Station (Latitude: 52°12′36″, Longitude: 14°7′19″), as the closest station providing the required data, are utilized for model validation. Modeled VI values are validated against the measured VI data for Lindenberg, Germany. This is accomplished by calculating the VI metric values for measured and modeled daily global horizontal irradiance sequences with 1 min. resolution for a time period including a total number of 117 days from April to August, while the days for which measured data are not provided by the weather station are excluded. This time period is chosen for validation purposes due to the highly variable cloudiness amounts reported by the weather station at the

mentioned geographical location. Distribution of the cloud coverage during the validation time period is presented as a histogram in Fig. 3. Daily VI values calculated using both measured and simulated 1-min. global horizontal irradiance (GHI) data for the array observer located at the center of the obtained irradiance profile are compared during the mentioned time period. For this purpose, the global irradiance sequences between 07:00 – 19:00 at the mentioned geographical location are simulated utilizing a set of local sky images, as described in Section 2, providing the same average cloudiness for each day as the observed values during the validation time period provided in (Behrens, 2016). Clear-sky global irradiance values are calculated according to Appendix A. As previously mentioned, calculations of the VI metric are performed for the center point of the simulated irradiance profiles as the reference point since the irradiance measurements reported by the weather station are also measured using a single pyranometer located at the center point of the ground area covered by the local sky image at the measurement station. Cumulus cloud, as a common cloud type at the geographical location and time period of interest, is considered as the cloud type during the simulations. The comparison results of the measured and the modeled VI values present statistics of mean bias error (MBE) of 0.16, root mean square error (RMSE) of 2.39, correlation coefficient of 0.94 and mean absolute error (MAE) of 1.91.

The autocorrelation function and irradiance increments are two other measures that are utilized for validation purposes in this paper. The mentioned two factors are used in order to analyze both the simulated and ground-measured irradiance time-series and prove their statistical closeness to each other. An irradiance increment, ΔG, as defined by Eq. (11) (Lohmann et al., 2017), is considered as the difference between irradiance values at two different time instants;

$$\Delta G_\tau = G(t+\tau) - G(t) \tag{11}$$

The lag-1 autocorrelation function, as proposed by Skartveit and Olseth (1992), and the magnitude of consecutive irradiance increments ($\tau = 1min.$) are calculated for both the ground-measured and simulated irradiance time-series for Lindenberg, Germany, for the above-mentioned validation time period. Fig. 4 shows the comparison results between the measured and modeled lag-1 autocorrelation coefficients and probability of irradiance increments during the validation time period. The results approve a good conformity between the measured and modeled irradiance time-series during the validation period in terms of autocorrelation coefficients and irradiance increments. It is observed that both the autocorrelation coefficients and irradiance increments, as well as the variability index, vary together with the variations of the amount of cloud cover in the sky. While the extremely overcast and clear days are represented by the lowest values of VI, lowest irradiance increments and highest values of autocorrelation coefficients, it is observed that magnitude of irradiance increments increase and autocorrelation coefficient values decrease together with increasing values of VI as a result of variations in the amount of cloud coverage. Expectedly better results, although slightly, could be obtained if precise information regarding the cloud type and its distribution at the measurement station during the verification time period were available.

Moreover, measured irradiance data gathered from an extensive set of adequately positioned ground-mounted pyranometers within the application area of the model would definitely enrich the validation of the proposed SDIPs in this paper. Such data would create the opportunity for point-to-point validation of the generated spatial irradiance time-series for different observation points within the application area of the proposed model as well as a comprehensive analysis of correlation structures between irradiance time-series at the mentioned observation points. However, unavailability of such data is considered as a limitation in this paper. In the absence of the above-mentioned set of measured irradiance data from multiple ground-mounted irradiance sensors, analyses and model validation in this paper are conducted based on the readily available single-point measured irradiance time-series for Lindenberg, Germany, in terms of VI, autocorrelation coefficients and irradiance increments. Taking the mentioned limitations and constraints into consideration, a comprehensive analysis on the spatial properties and correlation structures as well as the point-to-point comparison between the measured and modeled irradiance time-series for different observation points within the application area of the model can be considered as a future work in light of the measured irradiance time-series obtained from a set of ground-mounted pyranometers positioned within the model's application area.

4.2. Examples of application of the model

Examples of different applications of the developed model are provided and discussed in this part of the paper. The model has firstly been utilized to generate daily irradiance sequences for observers with different locations within the ground coverage area of a specific unchanged cloud map during a day. It is observed that despite the unchanged cloud conditions, different irradiance sequences are obtained at different locations as a result of movement of the Sun in the sky during the day. The model's capability for generation of instantaneous irradiance profiles under different cloud coverage and types is also presented, where different cloud distributions, types and their light interaction characteristics yield different irradiance profiles for the same instant of time. Finally, the model is utilized along with a set of 1-min. captured local sky images to generate daily irradiance sequences for different locations within the ground coverage area of the sky images, where comparison results provide significant differences between the obtained irradiance sequences as a result of the geographical location of the observer as well as the cloud distribution in the sky.

4.2.1. Daily irradiance sequences for different array observers with unchanged cloud coverage

This part of the paper presents daily irradiance sequences obtained

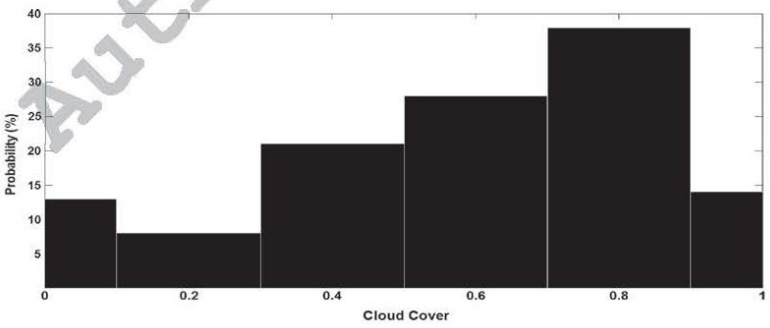

Fig. 3. Distribution of cloud coverage during validation period.

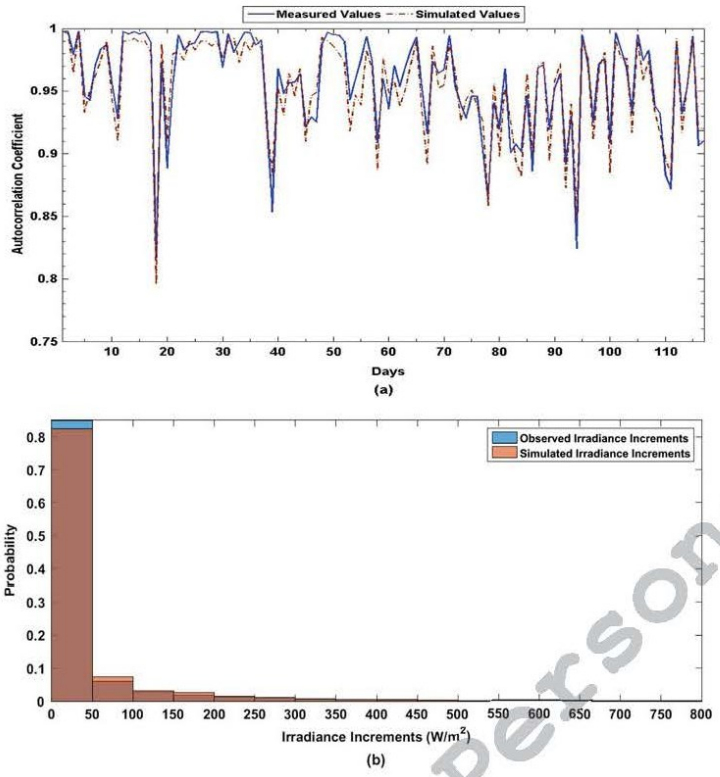

Fig. 4. Comparison between (a) lag-1 autocorrelation coefficients and (b) probability of irradiance increments of the measured and modeled irradiance time-series for Lindenberg, Germany.

with the proposed model for different array observers while the cloud coverage is assumed to be identical during the day. Thus, the model's capability to simulate shadow patterns and daily irradiance sequences as a result of variations of the Sun's position in the sky (while the cloud coverage remains unchanged) is presented.

Fig. 5 shows a sample of a whole sky image, a two dimensional cloud map and the obtained cloud pattern. The whole sky image is reconstructed from the two dimensional sky image (or cloud map) based on the earlier discussions.

Cumulus cloud is considered as the cloud type. The cloud pattern is kept unchanged and the achieved irradiance profiles with the pattern at different time instants during a typical day in July for Berlin, Germany are presented in Fig. 6. The idea here is to highlight the impacts of the Sun's movement in the sky, which is virtually located on the image at the desired time instants, on irradiance profiles received on the ground, under identical cloud distribution during a day.

The achieved different profiles of EECC for array observers clearly demonstrate the influences of the Sun's movement in the sky during a day. Although the total cloud coverage and its shape remain unchanged, observers at different areas of the array experience irradiance attenuations caused by the existing cloud as a result of the movement of the Sun in the sky during the day. The magnitude of the attenuation of the beam irradiance is directly dependent on the EECC, $(cc_e(t))$.

Daily global irradiance sequences achieved with the cloud pattern of Fig. 5 for observers at three different locations are presented in Fig. 7. The irradiance sequences demonstrate the effects of the variations in the Sun's

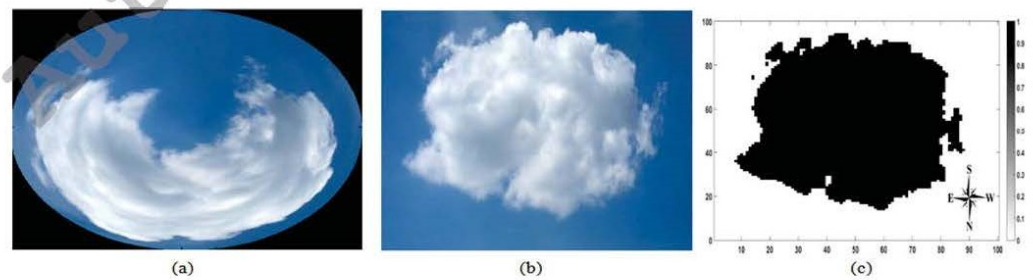

Fig. 5. (a) All-sky image, (b) cloud map and (c) the obtained cloud pattern with a Cumulus cloud, cc = 45%, m = 100.

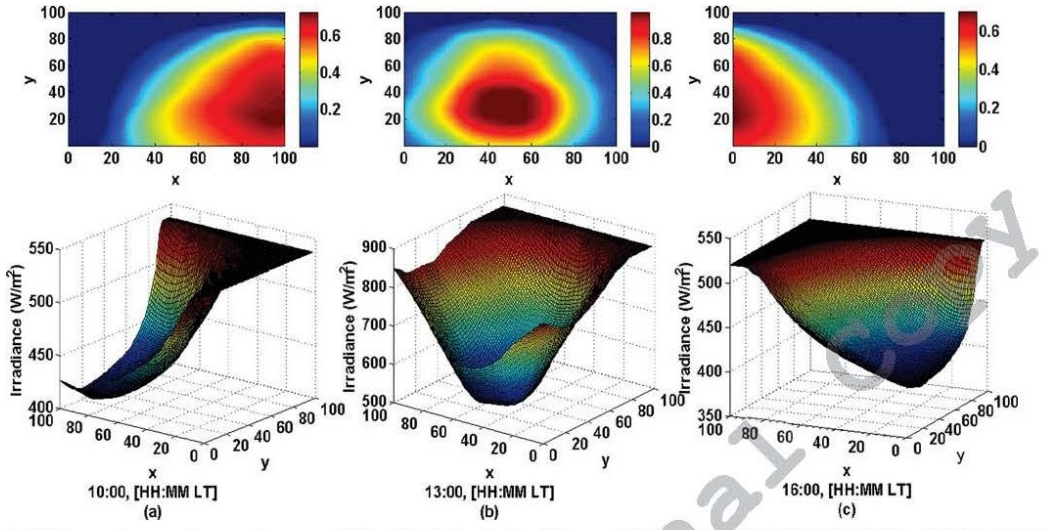

Fig. 6. EECC for array observers and corresponding generated SDIP on 45° inclined south oriented PV array at (a) 10:00, [HH:MM LT], (b) 13:00, [HH:MM LT] and (c) 16:00, [HH:MM LT] for Berlin, Germany (Latitude: 52°33′56″, Longitude: 13°18′39″) in July. ($k = l = m = 100$).

position in the sky during the day. Obviously, the observer located at the east side of the array is affected by the incident non-identical irradiance values before solar noon while the observers at the center and the west sides experience the irradiance degradation at later hours, respectively.

As previously discussed, higher clouds in the sky result in wider ground coverage areas. Cumulus clouds are low level clouds usually existing at maximum 1000 m above the ground. On the other hand, coordinate transformation for zenith angles near the horizon is not valid. Therefore, consideration of the upper limit of cloud base height for Cumulus cloud and $\theta_P < 65°$ yield a maximum ground coverage area of approximately 4 km^2, with the sky imager being located at the center. Hence, the coordinates of the mentioned observers in Fig. 7 corresponds to the points approximately located at a = (500 m,500 m), b = (1000 m,1000 m) and c = (1500 m,500 m), respectively.

4.2.2. Instantaneous irradiance profiles based on different cloud distribution and characteristics

Capability of the model to generate and simulate instantaneous irradiance profiles on PV array surfaces according to various cloud distributions and classes is presented in this part of the paper. As mentioned in the earlier parts of the paper, in addition to the cloud pattern, the light transmission characteristics of the clouds should also be considered during analyses of the effects of non-identical irradiance levels. The proposed model considers the influences of different cloud types along with their distribution in the sky in order to achieve more accurate results. Fig. 8 presents irradiance profiles generated with four different cloud types and distributions. The range of the area that each sky image may cover on the ground, according to the existing cloud type and its minimum and maximum height in the sky as mentioned in Table 3, is also provided. The time instant of the simulations is kept constant to provide the opportunity of comparison between the results.

In addition to the major dependency of the obtained irradiance profiles on the cloud distributions, the magnitude of irradiance degradation, specially the beam component, varies according to the type of the existing clouds. According to the results, the Cirrus cloud presents the smallest influence on the incident irradiance values and the

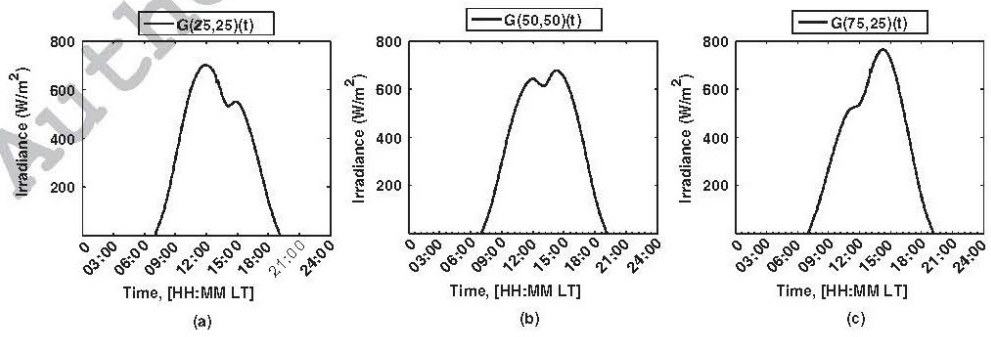

Fig. 7. Daily global irradiance on 45° inclined PV module surface for three different array observers with unchanged cloud coverage for Berlin, Germany (Latitude: 52°33′56″, Longitude: 13°18′39″) in July, cc = 45%.

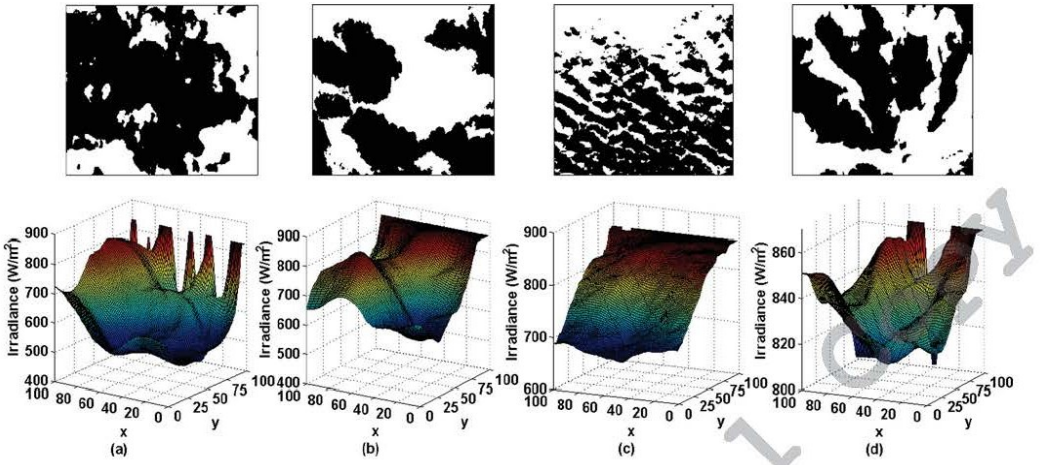

Fig. 8. Sky image and SDIP at 13:00, [HH:MM LT] for an arbitrary (a) Stratocumulus cloud (μ_G = 608.6 W/m^2, R_G = 347.6 W/m^2), Ground Coverage Area (GC) ≅ 1.5–18.5 km^2, (b) Cumulus cloud (μ_G = 730.8 W/m^2, R_G = 293 W/m^2), GC ≅ 1.5–4 km^2, (c) Altocumulus cloud (μ_G = 787.4 W/m^2, R_G = 189.5 W/m^2), GC ≅ 18.5–140 km^2, and (d) Cirrus cloud (μ_G = 832.6 W/m^2, R_G = 61 W/m^2), GC ≅ 115–860 km^2, on 45° inclined PV module surface for Berlin, Germany (Latitude: 52°33′56″, Longitude: 13°18′39″) in July. ($k = l = m = 100$).

irradiance profiles show similar dispersion characteristics under Stratocumulus and Cumulus clouds.

4.2.3. Daily irradiance sequences for different array observers based on variable cloud coverage

This part of the study intends to present the model's capability to simulate daily irradiance sequences on the surface of solar modules with different geographical locations on the ground, based on variable cloud coverage and the Sun's position in the sky during a day. Sample sequences of daily global irradiance for different observation points under partly cloudy sky are simulated based on the presented approach. A set of captured local sky images with 1 min. time resolution from 07:00 to 19:00, as described in Section 2, is utilized for this purpose. Fig. 9 presents the total cloud coverage for the mentioned set of sky images along with a sample of EECC for a selected observation point, retrieved from the above mentioned set of sky images using the proposed method. Cumulus cloud is selected to represent the cloud type for simulations due to its convenience with the image database. The simulated irradiance sequences at five different points located on the diagonals of the array are presented in Fig. 10.

As determined in Section 4.2.1, the maximum ground area covered by the mentioned sky images is approximately 4 km^2 and the observation points are located at ground coordinates of (500 m,1500 m), (1500 m,500 m), (1000 m,1000 m), (500 m,500 m) and

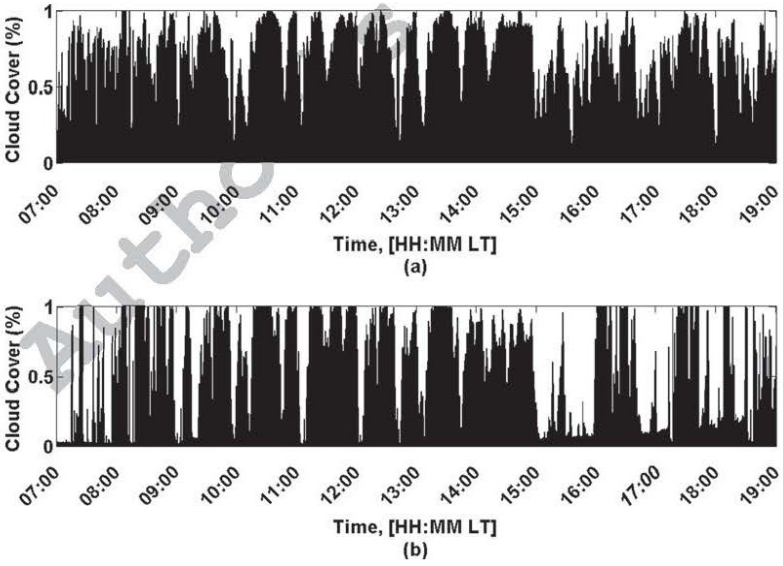

Fig. 9. (a) Total cloud cover, $cc(t)$ and (b) $cc_k(t)$ for $(x,y) = (50,50)$ retrieved from sky image set, Δt = 60 sec.

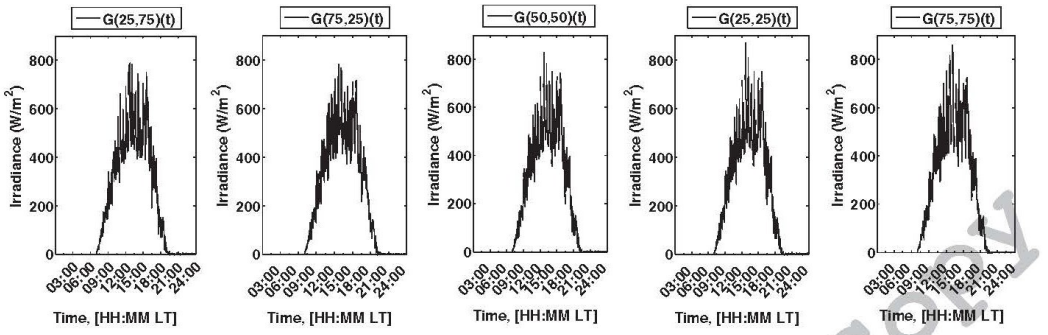

Fig. 10. Simulated daily global irradiance sequences on 45° tilted PV module surfaces located at five different locations within the array for Berlin, Germany (Latitude: 52°33′56″, Longitude: 13°18′39″) in July. $\Delta t = 60$ sec.

(1500 m,1500 m), respectively. The obtained irradiance sequences obviously exhibit the influences of cloud distribution on the irradiance values received by array observers. Same clouds during the day have created non-identical irradiance sequences at different locations within the array. Instant fluctuations of the irradiance sequences are directly dependent on the EECC for each observer, as well as the fluctuations in the diffuse irradiance from cloudy sky portion. Since the location of the ellipses on the cloud layer varies with respect to the geographical location of the observers at each time instant, EECC differs from point to point with respect to the cloud distribution in the sky.

4.2.4. Variable characteristic of irradiance sequences at different locations

It is expected that the daily irradiance sequences received at different observation points within an application area differ from each other as a result of the distribution of clouds in the sky. This part of the study is allocated to a comparison between the daily irradiance sequences as well as examination of the model's capability to reflect the variable characteristic of the daily irradiance sequences incident on different observation points within a PV array. For a better illustration of the influence of the cloud distribution on the incident irradiance values, scatter graphs are used to compare the modeled daily irradiance sequences for five different array observers. The comparison results are presented in Fig. 11. The irradiance sequences are simulated using the previously described local sky image set, defined in Section 4.2.3., and the same cloud type. In order to facilitate the comparison, the observers are particularly selected on the diagonals of the application area covering the area from north to south and east to west. It is observed that though the irradiance sequences incident on geographically closer observers present less amount of dispersion, daily irradiance sequences received by different array observers are not identical during the day. The results demonstrate the variable characteristic of the daily irradiance sequences received by different PV array observers during a day. Obviously, the mentioned non-identical irradiance sequences, as well as the dispersion range of the incident instantaneous irradiance values, are caused by the existing cloud coverage and its distribution in the sky.

Instantaneous irradiance values received by the observation points show relatively high dispersion as a direct result of the existing irradiance profile. The range of the mentioned dispersion also differs from point to point since the EECC for each observer varies according to the observer's geographical location. The selected observation points are assumed to be representatives of the whole application area. Similar to the presented results, non-identical daily irradiance sequences have also been obtained for the rest of array observers during the simulations. It is assumed that the relatively less amount of variation in the daily irradiance sequences in some cases is a result of relative closeness of the corresponding observation points to each other.

Differences between the instantaneous irradiance values received by different observers within the application area are caused by the attenuating effect of the EECC corresponding to the individual observers on the beam irradiance component.

Satellite-observed irradiance values are utilized in order to verify the model's capability to simulate the daily irradiance sequences for different observation points within an application area and reflect their variable characteristic. For this purpose, the ground coordinates of the observation points utilized in Fig. 11 are used to virtually locate them on the ground within the application area. A sample day in July with the same cloud coverage as the one defined in Section 4.2.3 and utilized in Fig. 11 is selected and the hourly mean irradiance values for each observation point, as specified in Section 2, are derived from satellite observations. The scatter plots provided in Fig. 12 present comparison results between the mentioned hourly mean irradiance values for different observation points within the application area. The comparison results obviously show that the observed hourly mean irradiance values differ from point to point during the day. The dispersion range of the hourly mean irradiance values, as expected, are relatively less than those of the instantaneous values. However, the comparison results clearly show the dispersed characteristics of the received irradiance values by different observation points during a day and confirm the results obtained by the model. Obviously, the incident irradiance values and their dispersion range are directly affected by the existing cloud coverage and its distribution in the sky. Different cloud distributions during a day may cause different results and dispersion ranges for different observation points, even for days with the same amount of cloudiness.

5. Conclusion

This paper proposes a modeling approach to generate Spatially Dispersed Irradiance Profiles (SDIPs) on the surface of inclined PV panels assembled within a PV power plant based on the existing cloud coverage and its light transmission characteristics. Real sky images are utilized to identify the existing cloud coverage, its distribution and light transmission characteristics. Different cloud classes are considered for analysis purposes in the paper where the cloud types and their heights in the sky are evaluated based on the classification provided in the International Cloud Atlas (1987). The limits of the application area of the PV power plant is assumed to be defined by the ground coverage area of the utilized sky images. The minimum and maximum cloud base height values for each cloud type are utilized to obtain the approximate coordinates of the ground coverage area (the application area) of each utilized sky image. The diffuse and ground reflected components of solar irradiance are assumed to be affected by the existing total cloud coverage in the sky and hence are identical for each individual observer within the application area. However, the beam irradiance component is received by each observer through cones with 0.5°

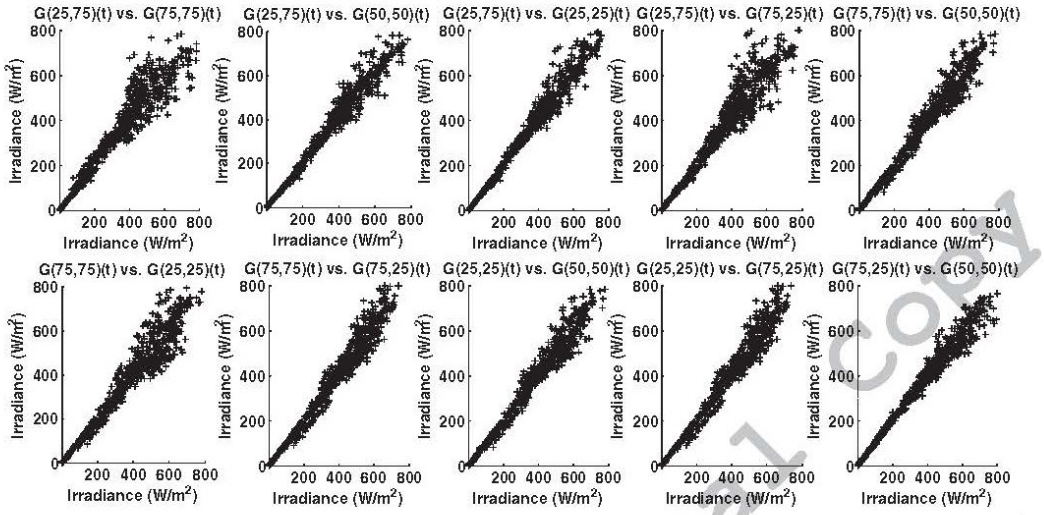

Fig. 11. Scatter plots of daily irradiance sequences on the surface of 45° inclined PV modules for different observation points within the PV array for Berlin, Germany (Latitude: 52°33′56″, Longitude: 13°18′39″) in July, $\Delta t = 60$ sec.

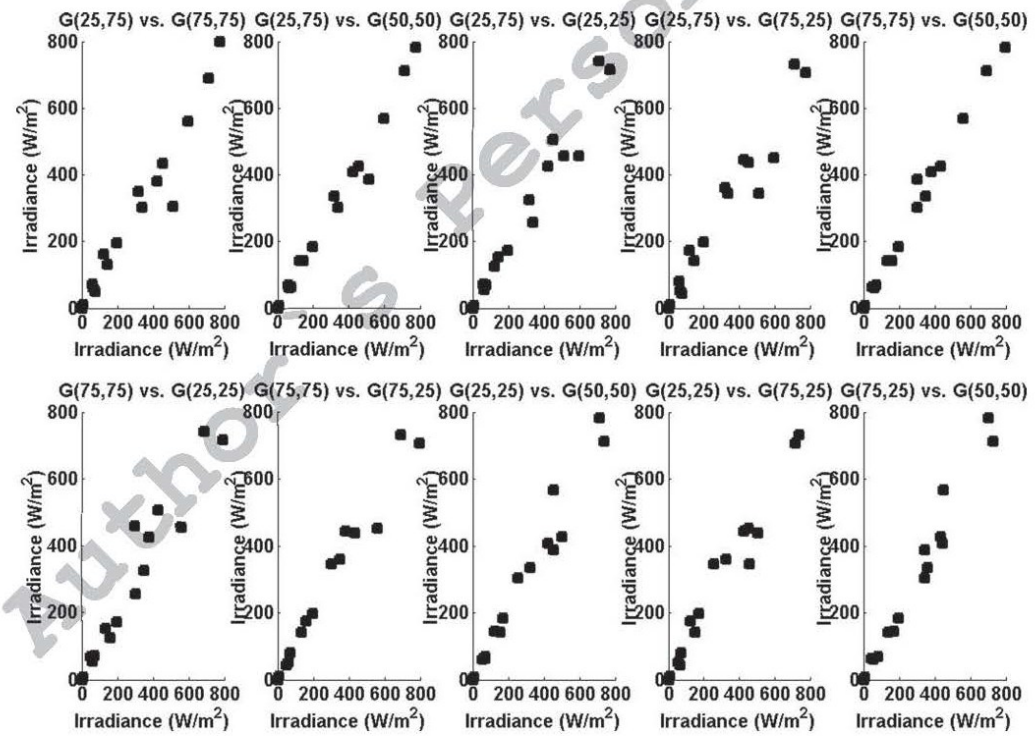

Fig. 12. Scatter plots of the observed hourly mean irradiance values for different observation points within the PV array for Berlin, Germany (Latitude: 52°33′56″, Longitude: 13°18′39″) in July.

opening angles. Consequently, it is assumed that the incident beam irradiance is not affected by the total sky cloud coverage. The beam component is only affected by the portions enclosed by ellipses formed when the cones are cut by the cloud layer. From this point of view the cloud shape and distribution earn extra significance because observers, according to their geographical location within the application area, receive the beam irradiance at each time instant through different ellipses containing different amounts of clouds. The shape of the mentioned ellipses also vary in parallel with the movement of the Sun in the sky. The ellipses get narrower during a day with increasing solar zenith angle values and transform to a circle exactly at solar noon. The proposed model firstly obtains the incident irradiance on inclined module surfaces under clear-sky conditions for each observer within the area of the PV array. It is then followed by consideration of the most appropriate ellipse for each individual observer at each time instant and generation of Spatially Dispersed Irradiance Profiles on horizontal surface by taking into account the attenuating effect of the ellipse enclosed cloud coverage on the beam irradiance received by each observer through the ellipses. The obtained horizontal irradiance profiles are then converted into irradiance profiles on inclined PV panel surfaces. It is shown that the incident instantaneous irradiance values received by different observers are widely dispersed and vary from point to point based on the cloud type and distributions. Relatively wide dispersion range of the instantaneous irradiance values received by different array observers is a result of the attenuating effects of cloud coverage enclosed by the corresponding different ellipses on the beam irradiance and clearly highlights the significance of utilization of such a modeling approach to investigate the effects of the incident non-identical irradiance values on PV arrays. Influences of cloud coverage and its distribution are reflected on daily irradiance sequences, derived for different array observers, as instantaneous fluctuations. The differences between the mentioned daily irradiance sequences also approve the significance of site-specific irradiance profiles based on the existing clouds for desired analyses of PV systems.

Appendix A. Solar irradiance on horizontal surface

Calculation of the incident irradiance on a horizontal surface is the first building block of the proposed model. To serve the purpose of the study, the utilized irradiance model should consider the cloud coverage and sunshine duration to model time-series of solar irradiance on horizontal surfaces. Due to its simplicity and eligibility to the goals of the study, the model proposed by Morf (2013) is chosen. The general lines of the mentioned model are briefly presented here. Detailed information regarding calculation of different parameters utilized by this model, such as $\overline{\tau}$, $\overline{K_o}$ and $\overline{D_o}$, can be found in (Morf, 2013).

A.1. Model structure

The model obtains time-series of global solar irradiance on a horizontal surface using Ångström-Prescott regression. The original model has firstly been developed by Schüepp (1966) and then refined by Biga and Rosa (1980). The model obtains global irradiance on a horizontal surface at a given time instant using the following pair of equations[1];

$$G(t) = SIF(t)G_b(t) + (1-cc(t))G_d(t) + cc(t)\overline{\tau}G_o \tag{A.1}$$

$$G_o(t) = G_d(t) + G_b \tag{A.2}$$

The terms on the right hand side of Eq. (A.1) respectively stand for;

a. The beam irradiance received from the clear part of the sky. $SIF(t)$ (Stochastic Insolation Function) takes the values of 0 or 1 corresponding to the cases that the Sun is covered by the clouds or it is shining, respectively.
b. The diffuse irradiance incident from the clear part of the sky.
c. The diffuse irradiance received from the cloudy part of the sky.

According to Eq. (A.2), the clear-sky global irradiance on a horizontal surface is composed of two main components; the beam and the diffuse irradiances. The irradiance above the clouds is assumed to be equivalent to clear-sky irradiance.

A.1.1. The clear-sky model

According to Eq. (A.2) a clear-sky model should be able to determine the clear-sky global irradiance on horizontal surfaces. The model of Biga and Rosa (1980) is considered for the mentioned purpose due to its convenience with the Berland formula (Kondratyev, 1969) which has been reported to outperform the other popular clear-sky models (Lanetz et al., 2007). The clear-sky model is utilized to determine appropriate expressions for $G_d(t)$ and $G_b(t)$. The clear-sky beam, diffuse and global irradiance values on a horizontal surface are obtained as;

$$G_b(t) = G_0(t)exp\frac{-\alpha}{cos\theta_z(t)} \tag{A.3}$$

$$G_d(t) = c(G_0(t) - G_b(t)) = G_0(t)c\left(1-exp\frac{-\alpha}{cos\theta_z(t)}\right) \tag{A.4}$$

$$G_o(t) = G_0(t)\left(c + (1-c)exp\frac{-\alpha}{cos\theta_z(t)}\right) \tag{A.5}$$

$c = \frac{(a+b)\cdot\overline{D_o}}{1-(a+b)(1-\overline{D_o})} = \frac{\overline{K_d}}{1-\overline{K_b}}$ is an adjustment constant and α is set to a value that ensures the following equation;

$$\frac{\overline{H_b}}{H_0} = (a+b)(1-\overline{D_o}) = \frac{1}{H_0}\int_{SR}^{SS} G_0(t)exp\frac{-\alpha}{cos\theta_z(t)}dt \tag{A.6}$$

[1] The expectations of beam, $(\overline{G_b(t)})$, diffuse, $(\overline{G_d(t)})$ and global irradiance, $(\overline{G_o(t)})$, on a horizontal surface at a given hour, (t), are used by Morf (2013) since variations in the clear-sky irradiance during an hour are very little.

Appendix B. Solar irradiance on inclined surface

In order to be utilized in power generation analyses in PV systems, the global irradiance on horizontal surface should be converted to irradiance on inclined PV module surface. The conversion procedure is presented together with a sample of the results and the model's reliability is verified using measured global irradiance data throughout this part of the paper.

B.1. Model structure

Global irradiance on an inclined surface, for cloudy and clear-sky conditions, is determined as;

$$G_\beta(t) = SIF(t)G_{b\beta}(t) + (1-cc(t))G_{d\beta}(t) + cc(t)\bar{\tau}R_d G_o(t) + \rho R_r G(t) \quad (B.1)$$

$$G_{o\beta}(t) = G_{b\beta}(t) + G_{d\beta}(t) + G_{r\beta}(t) \quad (B.2)$$

B.1.1. The beam irradiance

The clear-sky beam irradiance, $G_{b\beta}(t)$, is obtained by multiplying the beam component of the global irradiance on horizontal surface by the ratio between the beam irradiance on inclined plane and the beam irradiance on horizontal plane, R_b, as;

$$G_{b\beta}(t) = G_b(t)R_b = G_b(t)\frac{\cos\theta_S(t)}{\cos\theta_Z(t)} \quad (B.3)$$

The incidence angle of the solar irradiance on an inclined surface, θ_S, and the solar zenith angle, θ_Z, are obtained as;

$$\cos\theta_S = \sin\delta\sin\varphi\cos\beta - \sin\delta\cos\varphi\sin\beta\cos\alpha + \cos\delta\cos\varphi\cos\beta\cos\omega + \cos\delta\sin\varphi\sin\beta\cos\alpha\cos\omega + \cos\delta\sin\alpha\sin\omega\sin\beta$$

($South$: $\alpha = 0°$) (B.4)

$$\cos\theta_Z = \sin\delta\sin\varphi + \cos\delta\cos\varphi\cos\omega = \sin\gamma_S \quad (B.5)$$

B.1.2. The diffuse irradiance

The models developed for estimation of diffuse irradiance on inclined surfaces are categorized under two groups; Isotropic and Anisotropic models. The isotropic models (Badescu, 2002b; Koronakis, 1986) consider a uniform distribution for diffuse sky radiation over the sky dome while anisotropic models (Reindl et al., 1990b; Skartveit and Olseth, 1986; Steven and Unsworth, 1980; Hay, 1979; Temps and Coulson, 1977) consider anisotropic diffuse sky radiation for circumsolar region (the region near the solar disk) and isotropic distribution of diffuse radiation for the other regions of the sky. The disadvantage of isotropic models against their simplicity is the underestimation of the diffuse irradiance on surfaces which are tilted towards the equator. The anisotropic model presented by Reindl et al. (1990b) is utilized in this paper to obtain the diffuse irradiance on inclined module surfaces. The model defines the ratio between the diffuse irradiance on inclined surface and the diffuse irradiance on horizontal surface, R_d, as;

$$R_d = \frac{\overline{H_b}}{H_0}R_b + \left(1-\frac{\overline{H_b}}{H_0}\right)[(1+\cos\beta)/2][1+\sqrt{\overline{H_b}/\overline{H_a}}\,\sin^3(\beta/2)] \quad (B.6)$$

$$G_{d\beta}(t) = G_d(t)R_d \quad (B.7)$$

B.1.3. The ground reflected irradiance

Due to the low reflectivity of the ground, the ground-reflected irradiance has a small effect on PV module surfaces. Most of the models assume the ground to be horizontal and isotropically reflecting the solar irradiance. Hence, the ground-reflected irradiance is defined as;

$$G_{r\beta} = G_o(t)\rho R_r = G_o(t)\rho\frac{1-\cos\beta}{2} \quad (B.8)$$

The value of ρ varies with the ground type and it is commonly utilized as $\rho = 0.2$ for the cases where the exact value is unknown (Lorenzo, 2003).

B.2. Sample Sequence of global solar irradiance on inclined surface

The accuracy of the model is initially examined using measured irradiance data during a typical clear November day on a 45° inclined module surface in Famagusta, North Cyprus (Latitude: 35°8′18″, Longitude: 33°55′45″), where the experiment was conducted. The irradiance on a horizontal surface is first derived through Eqs. (A.3)–(A.5) and then converted to irradiance on inclined surface by Eqs. (B.2)-(B.8). The measured and simulated global irradiance values are compared through Fig. B.1. A threshold of $50W/m^2$ is applied and irradiance values lower than this threshold are omitted to avoid data uncertainty effects as suggested by Padovan and Del Col (2010). The figure also presents the results obtained with four different anisotropic diffuse irradiance estimation models. Details regarding the mentioned models are provided in Table B.1. Performance metrics (Appendix C) regarding the mentioned methods are provided in Table B.2.

According to the results, in one hand, the models introduced by Steven and Unsworth (1980) and Temps and Coulson (1977) generally overestimate the irradiance values while providing slightly better estimation performance for high zenith angles. On the other hand, the models recommended by Reindl et al. (1990b), Hay (1979), and Skartveit and Olseth (1986) show almost the same estimation performance providing the best estimations for low zenith angles. The relatively low estimation error achieved by the model presented by Reindl et al. (1990b) is within acceptable limits which confirms the reliability of the mentioned model for further analysis.

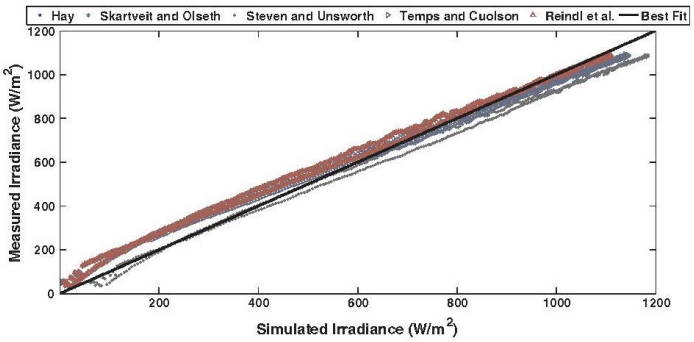

Fig. B.1. Measured vs. simulated global irradiance on 45° inclined surface for a typical clear day in November in Famagusta, North Cyprus (Latitude: 35°8′18″, Longitude: 33°55′45″). $\Delta t = 60$ sec.

Table B.1
List of the compared anisotropic diffuse irradiance models.

Reference	Model Type	R_d
Reindl et al. (1990b)	Anisotropic	$\frac{H_b}{H_0}R_b + \left(1-\frac{H_b}{H_0}\right)[(1+\cos\beta)/2][1+\sqrt{H_b/H_o}\sin^3(\beta/2)]$
Skartveit and Olseth (1986)	Anisotropic	$\frac{H_b}{H_0}R_b + \Omega^1\cos\beta + \left(1-\frac{H_b}{H_0}-\Omega\right)[1+\cos\beta]/2$
Steven and Unsworth (1980)	Anisotropic	$0.51R_b + ([1+\cos\beta]/2) - 1.74/1.26\pi \times [\sin\beta - (\beta \times \pi/180)\cos\beta - \pi\sin^2(\beta/2)]$
Hay (1979)	Anisotropic	$\frac{H_b}{H_0}R_b + \left(1-\frac{H_b}{H_0}\right)[1+\cos\beta]/2$

[1]: $\Omega = max\left\{0,(0.3-2)\frac{H_b}{H_0}\right\}$.

Table B.2
Mean Absolute Error (MAE), Root Mean Square Error (RMSE), Mean Absolute Percentage Error (MAPE) and Root Mean Square Percentage Error (RMSPE) for five anisotropic diffuse irradiance model.

Model	MAE (W/m^2)	RMSE (W/m^2)	MAPE (%)	RMSPE (%)
Hay (1979)	33.0062	43.1067	10.2670	18.7669
Reindl et al. (1990b)	32.4287	42.1637	9.9690	18.1157
Skartveit and Olseth (1986)	33.3397	43.7528	10.3217	18.6814
Steven and Unsworth (1980)	53.2710	62.6140	8.1557	13.7442
Temps and Coulson (1977)	40.7762	45.1770	10.0820	17.2402

Appendix C

The performance of estimation systems can be examined using different metrics. The metrics utilized in this paper to analyze and compare the performance of different solar irradiance models are given as;

$$Mean\ Absolute\ Error\ (MAE) = \frac{1}{n}\sum_{n}^{i=1} M_i - E_i \tag{C.1}$$

$$Root\ Mean\ Square\ Error\ (RMSE) = \sqrt{\frac{1}{n}\sum_{n}^{i=1}(M_i - E_i)^2} \tag{C.2}$$

$$Mean\ Absolute\ Percentage\ Error\ (MAPE) = \frac{1}{n}\left(\sum_{n}^{i=1}\frac{M_i - E_i}{M_i} \times 100\right) \tag{C.3}$$

$$Root\ Mean\ Square\ Percentage\ Error\ (RMSPE) = \sqrt{\frac{1}{n}\sum_{n}^{i=1}\left(\frac{M_i - E_i}{M_i} \times 100\right)^2} \tag{C.4}$$

M_i: ith value of the measured data, E_i: ith value of the estimated data.

Reference

Allmen, M.C., Kegelmeyer, W.P., 1996. The computation of cloud-base height from paired whole-sky imaging cameras. J. Atmos. Ocean. Technol. 13, 97–113.

ASHRAE, 1999. ASHRAE Handbook. HVAC publications, Atalanta.

Badescu, V., 2002a. A new kind of cloudy sky model to compute instantaneous values of diffuse and global solar irradiance. Theor. Appl. Climatol. 72, 127–136.

Badescu, V., 2002b. 3D isotropic approximation for solar diffuse irradiance on tilted surfaces. Renew. Energy 26, 221–223.

Behrens, K., 2016. Expanded measurements from station Lindenberg (2007–07). doi:10.1594/PANGAEA.859609.

Biga, A.J., Rosa, R., 1980. Estimating solar irradiation sums from sunshine and cloudiness observations. Sol. Energy 25, 265–272.

Biga, A.J., Rosa, R., 1979. Contribution to the study of the solar radiation climate of Lisbon. Sol. Energy 23, 61–67.

Cai, C., Aliprantis, D.C., 2013. Cumulus cloud shadow model for analysis of power systems with photovoltaics. IEEE Trans. Power Syst. 28, 4496–4506. http://dx.doi.org/10.1109/TPWRS.2013.2278685.

Chow, C.W., Urquhart, B., Lave, M., Dominguez, A., Kleissl, J., Shields, J., Washom, B., 2011. Intra-hour forecasting with a total sky imager at the UC San Diego solar testbed. Sol. Energy 85, 2881–2893.

Davies, J.A., McKay, D.C., 1989. Evaluation of selected models for estimating solar radiation on horizontal surfaces. Sol. Energy 43, 153–168.

Duffie, J.A., Beckman, W.A., 2006. Solar Engineering of Thermal Processes. Wiley, Hoboken, New Jersey.

Ehnberg, J.S.G., Bollen, M.H.J., 2005. Simulation of global solar radiation based on cloud observations. Sol. Energy 78, 157–162. http://dx.doi.org/10.1016/j.solener.2004.08.016.

Erbs, D.G., Klein, S.A., Duffie, J.A., 1982. Eastimation of the diffuse radiation fraction for hourly, daily and monthly-average global radiation. Sol. Energy 28, 293–302.

Gueymard, C., 1993. Mathematically integrable parametrization of clear-sky beam and global irradiances and its use in daily irradiation applications. Sol. Energy 50, 385–397.

Gueymard, C.A., 2012. Clear-sky irradiance predictions for solar resource mapping and large-scale applications: Improved validation methodology and detailed performance analysis of 18 broadband radiative models. Sol. Energy 86, 2145–2169.

Harris, M.J., 2003. Real-time cloud simulation and rendering. ACM SIGGRAPH 2005 Courses - SIGGRAPH '05 222. doi:10.1145/1198555.1198792.

Hay, J.E., 1979. Calculation of monthly mean solar radiation for horizontal and inclined surfaces. Sol. Energy 23, 301–330.

Heinle, a., Macke, a., Srivastav, a., 2010. Automatic cloud classification of whole sky images. Atmos. Meas. Tech. 3, 557–567. http://dx.doi.org/10.5194/amt-3-557-2010.

Huo, J., Lu, D., 2010. Preliminary retrieval of aerosol optical depth from allsky images. Adv. Atmos. Sci. 27, 421–426.

Huo, J., Lu, D., 2009. Cloud determination of all-sky images under low visibility conditions. J. Atmos. Ocean. Technol. 26, 2172–2180.

International Cloud Atlas, 1987. World Meteorological Organization.

Iqbal, 1983. An Introduction to Solar Radiation. Academic press, Toronto.

Ishaque, K., Salam, Z., Syafaruddin, 2011a. A comprehensive MATLAB Simulink PV system simulator with partial shading capability based on two-diode model. Sol. Energy 85, 2217–2227. http://dx.doi.org/10.1016/j.solener.2011.06.008.

Ishaque, K., Salam, Z., Taheri, H., 2011b. Simple, fast and accurate two-diode model for photovoltaic modules. Sol. Energy Mater. Sol. Cells 95, 586–594. http://dx.doi.org/10.1016/j.solmat.2010.09.023.

Ishaque, K., Salam, Z., Taheri, H., Syafaruddin, 2011c. Modeling and simulation of photovoltaic (PV) system during partial shading based on a two-diode model. Simul. Model. Pract. Theory 19, 1613–1626. http://dx.doi.org/10.1016/j.simpat.2011.04.005.

Jewell, W., Ramakumar, R., 1987. The effect of moving clouds on electric utilities with dispersed photovoltaic generation. IEEE Trans. Energy Convers. EC-2, 570–576.

Johnson, R., Hering, W., Shields, J., 1989. Automated visibility and cloud cover measurements with a solid-state imaging system.

Johnson, R.W., Shields, J.E., Koehler, T.L., 1991. Analysis & Interpretation of Simultaneous Multi-station Whole Sky Imagery.

Jones, P.A., 1992. Cloud-cover distributions and correlations. J. Appl. Meteorol. 31, 732–741.

Kassianov, E., Long, C., Christy, J., 2005. Cloud base-height estimation frompaired ground-based hemispherical observations. J. Appl. Meteorol. 44, 1221–1233.

Kokhanovsky, A., 2004. Optical properties of terrestrial clouds. Earth-Sci. Rev. 64, 189–241. http://dx.doi.org/10.1016/S0012-8252(03)00042-4.

Kondratyev, K., 1969. Radiation in the Atmosphere. Academic Press, New York.

Koronakis, P.S., 1986. On the choice of the angle of tilt for south facing solar collectors in the Athens basin area. Sol. Energy 36, 217–225.

Lanetz, A., Lyubanski, V., Setter, I., Krlheli, B., Evseev, E.G., Kudish, A.I., 2007. Intercomparison of different models for estimating clear sky solar global radiation for the Negev region in Israel. Energy Convers. Manag. 48, 259–268.

Liu, B.Y.h., Jordan, R.C., 1960. The inter-relationship and characteristic distribution of direct, diffue and total solar radiation. Sol. Energy 4, 1–19.

Lohmann, G.M., Hammer, A., Monahan, A.H., Schmidt, T., Heinemann, D., 2017. Simulating clear-sky index increment correlations under mixed sky conditions using a fractal cloud model. Sol. Energy 150, 255–264. http://dx.doi.org/10.1016/j.solener.2017.04.048.

Long, C., Sabburg, J., Calbo, J., Pages, D., 2006. Retrieving cloud characterisitcs from ground-based daytime color all-sky images. J. Atmos. Ocean. Technol. 23.

Lorenzo, E., 2003. Energy Collected and Delivered by PV Modules. In: Luque, A., Hegedus, S. (Eds.), Handbook of Photovoltaic Science and Engineering. John Wiley & Sons Ltd., West Sussex, pp. 905–970.

Louche, A., Notton, G., Poggi, P., Simonnot, G., 1991. Correlations for direct normal and global horizontal irradiations on a French Mediterranean site. Sol. Energy 46, 261–266.

Morf, H., 2013. A stochastic solar irradiance model adjusted on the Ångström-Prescott regression. Sol. Energy 87, 1–21. http://dx.doi.org/10.1016/j.solener.2012.10.005.

Morf, H., 2011. The Stochastic two-state cloud cover model STSCCM. Sol. Energy 85, 985–999. http://dx.doi.org/10.1016/j.solener.2011.02.015.

Morf, H., 1998. The stochastic two-state irradiance model (STSIM). Sol. Energy 62, 101–112.

Nguyen, A., Velay, M., Schoene, J., Zheglov, V., Kurts, B., Murray, K., Torre, B., Kleissl, J., 2016. High PV penetration impacts on five local distribution networks using high resolution solar resource assessment with sky imager and quasi-steady state distribution system simulations. Sol. Energy 132, 221–235.

Nguyen, D., Kleissl, J., 2014. Stereographic methods for cloud base height determination using two sky imagers. Sol. Energy 107, 495–509.

Nijmeh, S., Mamlook, R., 2000. Testing of two models for computing global solar radiation on tilted surfaces. Renew. Energy 20, 75–81. http://dx.doi.org/10.1016/S0960-1481(99)00091-9.

Padovan, A., Del Col, D., 2010. Measurement and modeling of solar irradiance components on horizontal and tilted planes. Sol. Energy 84, 2068–2084. http://dx.doi.org/10.1016/j.solener.2010.09.009.

Perez, R., Kivalov, S., Schlemmer, J., Hemker Jr., K., Renne, D., Hoff, T.E., 2010. Validation of short and medium term operational solar radiation forecasts in US. 2Solar. Energy 84, 2161–2172.

Pfister, G., McKenzie, R., Liley, J., Thomas, A., 2003. Cloud coverage based on all-sky imaging and its impact on surface solar irradiance. J. Appl. Meteorol. 42.

Posselt, R., Müller, R., Stöckli, R., Trentmann, J., 2011. CM SAF Surface Radiation MVIRI Data Set 1.0 - Monthly Means / Daily Means / Hourly Means. doi:DOI:10.5676/EUM_SAF_CM/RAD_MVIRI/V001.

Reindl, D.T., Beckman, W.A., Duffie, J.A., 1990a. Diffuse fraction corrections. Sol. Energy 45, 1–7.

Reindl, D.T., Beckman, W.A., Duffie, J.A., 1990b. Evaluation of hourly tilted surface radiation models. Sol. Energy 45, 9–17.

Schüepp, W., 1966. Direct and scaterred radiation reaching the earth, as influenced by atmospheric, geographical and astronomical factors. In: Robinson, N. (Ed.), Solar Radiation. Elsevier, Amesterdam, pp. 111–160.

Seiz, G., Shields, J., Feister, U., Baltsavias, E., Gruen, A., 2007. Cloud mapping with ground-based photogrammetric cameras. Int. J. Remote Sens. 28, 2001–2032.

Shields, J.E., Burden, A.R., Johnson, R.W., Hodgkiss, W.S., Shields, J., Karr, M., Burden, A., Johnson, R., 2007. Continuing Support of Cloud Free Line of Sight Determination Including Whole Sky Imaging of Clouds Final Report for ONR Contract.

Skartveit, A., Olseth, J.A., 1992. The probability density and autocorrelation of short-term global and beam irradiance. Sol. Energy 49, 477–487. http://dx.doi.org/10.1016/0038-092X(92)90155-4.

Skartveit, A., Olseth, J.A., 1987. A model for diffuse fraction of hourly global radiation. Sol. Energy 38, 271–274.

Skartveit, A., Olseth, J.A., 1986. Modelling slope irradiance at high latitudes. Sol. Energy 36, 333–344.

Stein, J., Hansen, C., Reno, M., 2012. The variability index: a new and novel metric for quantifying irradiance and PV output variability. World Renew. Energy Ellipsis 1–7.

Steven, M.D., Unsworth, M.H., 1980. The angular distribution and interception of diffuse solar radiation below overcast skies. Q. J. R. Meteorol. Soc. 106, 57–61.

Tapakis, R., Charalambides, A.G., 2013. Equipment and methodologies for cloud detection and classification: a review. Sol. Energy 95, 392–430. http://dx.doi.org/10.1016/j.solener.2012.11.015.

Temps, R.C., Coulson, K.L., 1977. Solar radiation incident upon slopes of different orientations. Sol. Energy 19, 179–184.

Villalva, M.G., Gazoli, J.R., Filho, E.R., 2009. Comprehensive approach to modeling and simulation of photovoltaic arrays. IEEE Trans. Power Electron. 24. http://dx.doi.org/10.1109/TPEL.2009.2013862.

Wang, Y.-J., Hsu, P.-C., 2010. Analytical modelling of partial shading and different orientation of photovoltaic modules. IET Renew. Power Gener. 4, 272. http://dx.doi.org/10.1049/iet-rpg.2009.0157.

Wang, Y.J., Hsu, P.C., 2011. An investigation on partial shading of PV modules with different connection configurations of PV cells. Energy 36, 3069–3078. http://dx.doi.org/10.1016/j.energy.2011.02.052.

Wong, L.T., Chow, W.K., 2001. Solar radiation model. Appl. Energy 69, 191–224. http://dx.doi.org/10.1016/S0306-2619(01)00012-5.

WRMC-BSRN [WWW Document], 2016. URL http://bsrn.awi.de/ (accessed 5.20.16).

Yang, H., Kurtz, B., Nguyen, D., Urquhart, B., Chow, C.W., Ghonima, M., Kleissl, J., 2014. Solar irradiance forecasting using a ground-based sky imager developed at UC San Diego. Sol. Energy 103, 502–524.

Appendix C: Adaptive Photovoltaic Array Reconfiguration Based on Real Cloud Patterns to Mitigate Effects of Non-Uniform Spatial Irradiance Profiles

Moein Jazayeri, Kian Jazayeri, Sener Uysal, "Adaptive photovoltaic array reconfiguration based on real cloud patterns to mitigate effects of non-uniform spatial irradiance profiles", Elsevier Solar Energy Journal, vol. 155, 2017.

ABSTRACT

This paper proposes a simple and dynamic reconfiguration algorithm for photovoltaic (PV) arrays in order to mitigate negative effects of non-uniform spatial irradiance profiles on PV power production. Spatially dispersed irradiance profiles incident on inclined PV module surfaces at each application site are generated based on real sky images. Models of PV modules are constructed in MATLAB/Simulink based on one-diode mathematical model of a PV cell. The proposed dynamic reconfiguration algorithm operates based on irradiance equalization principle aiming for creation of balanced-irradiance series-connected rows of PV modules. The proposed algorithm utilizes an irradiance threshold to obtain near-optimal configurations in terms of irradiance equalization and number of switching actions under any type of non-uniform spatial irradiance profile. The algorithm provides no limits on the number of PV modules within the array. The reconfiguration algorithm is examined with different irradiance profiles and significant improvements, almost equivalent to the ideal case corresponding to equal irradiance for all panels, are achieved for each shading pattern. The advantages of the algorithm are simplicity and providing significant improvements in array's power generation alongside with reduced number of switching actions.

Solar Energy 155 (2017) 506–516

Contents lists available at ScienceDirect

Solar Energy

journal homepage: www.elsevier.com/locate/solener

Adaptive photovoltaic array reconfiguration based on real cloud patterns to mitigate effects of non-uniform spatial irradiance profiles

Moein Jazayeri *, Kian Jazayeri, Sener Uysal

Electrical and Electronic Engineering Department, Eastern Mediterranean University, Famagusta, Via Mersin 10, Turkey

ARTICLE INFO

Article history:
Received 23 July 2016
Received in revised form 5 May 2017
Accepted 19 June 2017

Keywords:
PV array reconfiguration
Irradiance profile
Irradiance equalization
Irradiance estimation
Spatial irradiance profile
Reconfigurable PV system
Solar energy

ABSTRACT

This paper proposes a simple and dynamic reconfiguration algorithm for photovoltaic (PV) arrays in order to mitigate negative effects of non-uniform spatial irradiance profiles on PV power production. Spatially dispersed irradiance profiles incident on inclined PV module surfaces at each application site are generated based on real sky images. Models of PV modules are constructed in MATLAB/Simulink based on one-diode mathematical model of a PV cell. The proposed dynamic reconfiguration algorithm operates based on irradiance equalization principle aiming for creation of balanced-irradiance series-connected rows of PV modules. The proposed algorithm utilizes an irradiance threshold to obtain near-optimal configurations in terms of irradiance equalization and number of switching actions under any type of non-uniform spatial irradiance profile. The algorithm provides no limits on the number of PV modules within the array. The reconfiguration algorithm is examined with different irradiance profiles and significant improvements, almost equivalent to the ideal case corresponding to equal irradiance for all panels, are achieved for each shading pattern. The advantages of the algorithm are simplicity and providing significant improvements in array's power generation alongside with reduced number of switching actions.

1. Introduction

Solar energy due to its clean and renewable nature outperforms many conventional energy resources and its application areas have significantly been growing during the recent years. The non-linear nature and dependency of this energy source to the incident solar irradiance is one of its main disadvantages. Non-uniform irradiance levels incident on the surface of photovoltaic (PV) modules within a PV power plant, mostly caused by passing clouds, reduce their performance. Therefore, proper management and operation of PV systems requires reliable knowledge of solar irradiance values at the application areas. Large-scale centralized PV power plants or distributed PV generators on wide geographical areas are examples of such systems and applications with precise and site-specific high resolution irradiance data requirement. However unavailability or incompatibility of data provided by measurement stations with the analysis requirements (unavailability of data for desired application areas or incompatibility of the resolution of data with the analysis purposes) and other limitations associated with the mentioned stations and equipment cause problems from PV analyses point of view.

The mentioned problems have motivated research studies to develop models for estimation of solar radiation and several models are proposed to estimate clear-sky radiation as well as radiation under cloudy sky to be utilized for PV analyses purposes. Irradiance data generated by irradiance estimation models forms the required input data for PV analyses purposes. Thus, an adequate irradiance model from PV research point of view should be able to consider interactions of sunlight with clouds and take into account cloud properties to provide reliable irradiance data for desired application areas. Such a model should be capable of generating high resolution spatial irradiance data incident on PV module surfaces within a PV array. Reliable analyses of PV system performance become possible once the required high resolution spatial irradiance data for the desired PV application areas is obtained by the mentioned irradiance models and/or measurement equipment.

Mathematical modeling of PV systems has been widely considered for investigation of system performance under variable environmental conditions. One-diode and two-diode mathematical models of a solar cell have been widely utilized for the mentioned purpose (Liu and Dougal, 2004; Villalva et al., 2009; Ishaque et al., 2011a, 2011b). These models generally estimate PV system characteristics utilizing datasheet parameters provided by PV manufacturers along with environmental parameters such as solar irradiance and temperature.

* Corresponding author.
E-mail addresses: moein.jazayeri@cc.emu.edu.tr (M. Jazayeri), kian.jazayeri@cc.emu.edu.tr (K. Jazayeri), sener.uysal@emu.edu.tr (S. Uysal).

http://dx.doi.org/10.1016/j.solener.2017.06.052
0038-092X/

Nomenclature

cc	cloud cover [%]
LT	local time
N_{PV}	number of PV modules in the array
N_{SW}	number of switching actions
I_{ph}	photo-current [A]
I_S	diode saturation current [A]
n	diode ideality factor
R_S	series resistance [Ohms]
R_{SH}	shunt resistance [Ohms]
$\overline{G}_i$	average irradiance of the ith row [W/m^2]
G_{ij}	incident irradiance on the jth PV module of the ith row [W/m^2]
$\overline{G}$	array's average irradiance [W/m^2]
ΔG	irradiance threshold [W/m^2]
l	number of PV modules in a row
P_{NR}	array's non-reconfigured maximum power [W]
$P_{OPT.}$	array's maximum power under ideal conditions [W]

Taking proper precautions and application of efficient strategies to mitigate the negative effects of non-uniform spatial irradiance profiles are significantly important for PV system planning and management. Utilization of bypass diodes or different PV array architectures are examples of such strategies (Silvestre et al., 2009; Carannante et al., 2009). Series-Parallel (SP), Bridge-Link (BL) and Total-Cross-Tied (TCT) are the most widely utilized array configurations while the TCT topology provides higher efficiency in reducing losses caused by non-uniform spatial irradiance profiles (Ramaprabha and Mathur, 2012; Kaushika and Gautam, 2003).

Dynamic reconfiguration of PV module interconnections within a PV array is another leading-edge research area. Velasco-Quesada et al. (2009) proposes an optimization algorithm based on irradiance equalization index, aiming for creation of series connected rows of parallel connected PV modules with average irradiances equivalent to the array's average irradiance. The algorithm examines all possible array configurations and selects the most proper configuration. The reconfiguration of PV modules is considered as a mixed integer quadratic programming problem in (Shams El-Dein et al., 2013) with capability of utilization with non-equal module number per row. Wilson et al. (2013) propose an iterative and hierarchical sorting algorithm based on irradiance equalization method in order to achieve near-optimal configuration considering number of switching actions, N_{SW}. Connection of an adaptive bank of modules to a fixed part of the PV array through a switching matrix, based on a model-based control algorithm is considered in (Nguyen and Lehman, 2008). Alahmad et al. (2012) propose a flexible switch array matrix topology for real-time power generation improvement.

The irradiance value incident on the surface of each individual PV module should be known for reliable analysis of the effects of non-uniform spatial irradiance profiles on PV power production. This paper utilizes a modeling technique which generates spatially dispersed irradiance profiles incident on PV module surfaces at the application sites. The model utilizes real sky images and accounts for light interaction properties of different cloud types to generate irradiance profiles based on the existing cloud patterns and their sunlight interaction properties. A simple reconfiguration algorithm which is based on irradiance equalization method is proposed to reduce losses caused by non-uniform spatial irradiance profiles on PV systems. The algorithm aims for providing near-optimal array reconfiguration in terms of irradiance equalization and N_{SW}. The contributions of this paper are mainly to the utilization of site-specific irradiance profiles based on existing cloud distributions for analyses of the effects of non-uniform spatial irradiance profiles and the dynamic and simple reconfiguration algorithm which offers no limits on the number of PV modules included within the array and shading profiles alongside with the significant improvements in power generation. This paper addresses the need to a simple dynamic reconfiguration algorithm to mitigate negative effects of non-uniform spatial irradiance profiles induced on the extent of PV plants, mainly caused by the existing clouds. The innovation of this work is the design of an algorithm capable of dynamic reconfiguration of the interconnections of PV modules within a PV plant according to the spatially dispersed irradiance profiles incident on the PV plant area at any instance. The algorithm, which operates based on irradiance equalization principle, provides near optimal PV array configurations in order to generate approximately the maximum possible power under non-uniform spatial irradiance profiles at any instance. The algorithm also considers reduction of number of switching actions in order to preserve the lifetime of switching devices. For this purpose, unnecessary switching actions which do not provide significant contribution to power generation are eliminated. In this way, yielding approximately maximum possible power generation alongside with minimum reconfiguration and switching numbers are ensured under non-uniform spatial irradiance profiles.

The remaining parts of the paper are organized as follows. The model utilized for generation of Spatially Dispersed Irradiance Profiles (SDIPs) for the application sites is briefly presented in Section 2. Section 3 provides a brief review on mathematical modeling of PV systems and different PV array architectures and presents the proposed PV array reconfiguration algorithm and its application through a dynamic switching matrix.

2. Model of spatially dispersed irradiance profile

Significant analysis of the effects of non-uniform spatial irradiance profiles on PV arrays requires high resolution spatial irradiance data incident on PV module surfaces. This study utilizes a modeling technique developed to generate Spatially Dispersed Irradiance Profiles (SDIPs) at the application sites based on existing clouds and their properties. The model deploys 2D latitude-longitude sky images serving as cloud coverage drivers and processes them to generate SDIPs. The utilized sky images are 720×576 RGB images taken by a commercial camera on per-minute time basis. Sky images are particularly selected to represent samples of different sky conditions (from partly cloudy sky conditions with different cloud coverages up to overcast sky). The criterion for selection has been representation of different cloudiness amounts and cloud distributions. The provided irradiance profiles are generated based on 4 independent samples of sky images. The model is explained here with its general lines while detailed information regarding the model can be found in our previous study. Fig. 1 briefly presents different steps of the model. The irradiance model considers different cloud types and their sunlight interaction characteristics (cloud transmittivity) to generate irradiance profiles incident on PV arrays. Cumulus cloud is utilized in this paper as a common cloud type that is also consistent with the utilized sky images. The ground coverage area of each irradiance profile depends on Cloud Base Height (CBH) values as defined by Chow et al. (2011). As the precise coordinates of the ground coverage area of irradiance profiles (e.g. in meters) may

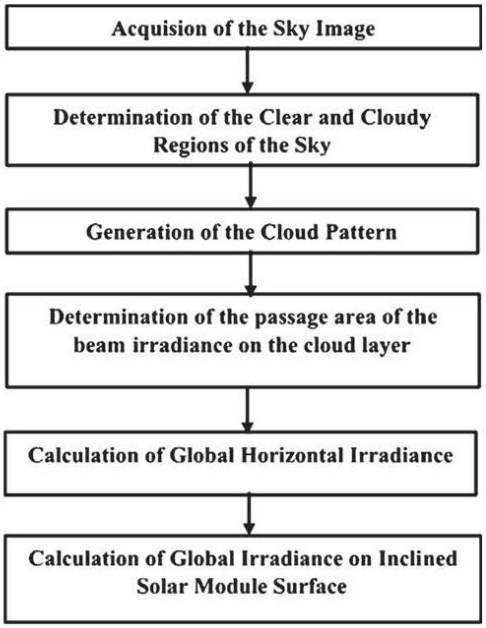

Fig. 1. Flow chart of the model for generation of SDIPs.

not be accurately calculated due to lack of information regarding precise values of the cloud base heights, the coverage areas of irradiance profiles as well as the location of PV modules within the mentioned profiles in this paper are represented as percentage values. The intention here is to present the effectiveness of the proposed reconfiguration algorithm regardless of the distance between PV modules in different geographical distributions. However, due to the fish eye nature of the sky camera lenses, spatial resolution of the irradiance profiles on the surface of PV plants depends on the distance of each pixel to the center of the sky image. This resolution varies between the pixels at the center to pixels at the edges of the sky image and changes depending on two main factors being CBH and resolution of the sky image (Nguyen and Kleissl, 2014). Hence, the required high spatial resolutions for applications with closely located PV modules can also be achieved with the proposed model by utilizing sufficiently high resolution sky images and considering also the existing CBH values.

Samples of generated SDIPs are presented in Fig. 2 and referred to as shading scenarios in the next parts of the paper. As it is discussed in the next parts of the study, the 1st shading scenario representing overcast sky conditions is not found appropriate for the proposed reconfiguration operation. The proposed array reconfiguration algorithm provides improved power generation under the 2nd, 3rd and 4th shading scenarios.

3. Photovoltaic array reconfiguration

As previously discussed, the one-diode mathematical model of a solar cell is utilized for PV modeling in this paper due to its simplicity and reliable performance and results. PV modules are modeled as a number of series and/or parallel connected PV cells and PV arrays are made as combinations of specific numbers of PV modules with different architectures. The equivalent electrical circuit of a solar cell based on one-diode mathematical model of a solar cell is presented in Fig. 3. According to this model the relationship between the cell's current and voltage is expressed as;

$$I - I_{ph} - I_s\left(\exp\frac{q(V+R_sI)}{nkT} - 1\right) - \frac{(V+R_sI)}{R_{sh}} \quad (1)$$

According to Eq. (1), I_{ph}, I_s, n, R_s and R_{sh} should be known to obtain the cell's current value depending on the voltage values according to the one-diode mathematical model.

Considering the direct relationship between the incident solar irradiance and power generation in PV modules, power generation in PV arrays consisting of large numbers of PV modules is highly affected by variation of the incident irradiance values. Power production of the array is limited by the modules receiving less amount of solar irradiance and generating less power accordingly. Obviously variation of power production in PV arrays, particularly in parallel with extension of their size, is directly proportional to the range of variation of solar irradiance values incident on PV module surfaces. The amount of degradation of power generation also depends on different interconnection types between PV modules within a PV array. The mentioned interconnection types help to increase power generation under non-uniform irradiance profiles. For this purpose, several architectures of PV arrays are recommended to mitigate the negative effects of non-uniform spatial irradiance profiles on power generation. Series-Parallel (SP), Bridge-Link (BL) and Total-Cross-Tied (TCT) are the most widely utilized PV array architectures. SP interconnection is formed by parallel connection of series-connected module strings. TCT interconnection is the most complex array architecture with PV modules connected in series and parallel with each other at the same time. Number of switching elements are increased in this architecture. The number of switching elements in BL configuration is reduced to half with respect to TCT configuration. Fig. 4 presents samples of different PV array architectures.

As discussed earlier, reconfiguration of PV module interconnections, in order to reduce negative effects of non-uniform spatial irradiance profiles, has been considered in several research studies. However, complex structures and/or limitations associated with the algorithms are the main disadvantages of the proposed reconfiguration algorithms. This study proposes a simple and adaptive dynamic reconfiguration algorithm applicable for PV arrays with large number of PV modules.

3.1. Method

The working principle of the proposed reconfiguration algorithm relies on the Irradiance Equalization method introduced by Velasco-Quesada et al. (2009). The concept of Irradiance Equalization basically aims to form series connected rows of parallel connected PV modules in a manner that yields balanced average row irradiance values in a TCT configuration. This implies that PV modules with either different or similar irradiance levels, depending on the existing irradiance profile, are connected in parallel in such a manner that results in forming rows with average irradiance values similar or close enough to each other to prevent limitation of power production by less current generating rows. This is made possible by relocating PV modules with different irradiance levels within the array until the desired balanced-irradiance rows are achieved. Thus, the mentioned approach ensures that none of the series connected rows inside the TCT architecture provides higher current generation and therefore limits the current produced by the other rows in a series connection. This method improves power generation under any type of non-uniform spatial irradiance profile. Obviously the ideal case is when the array's average irradiance

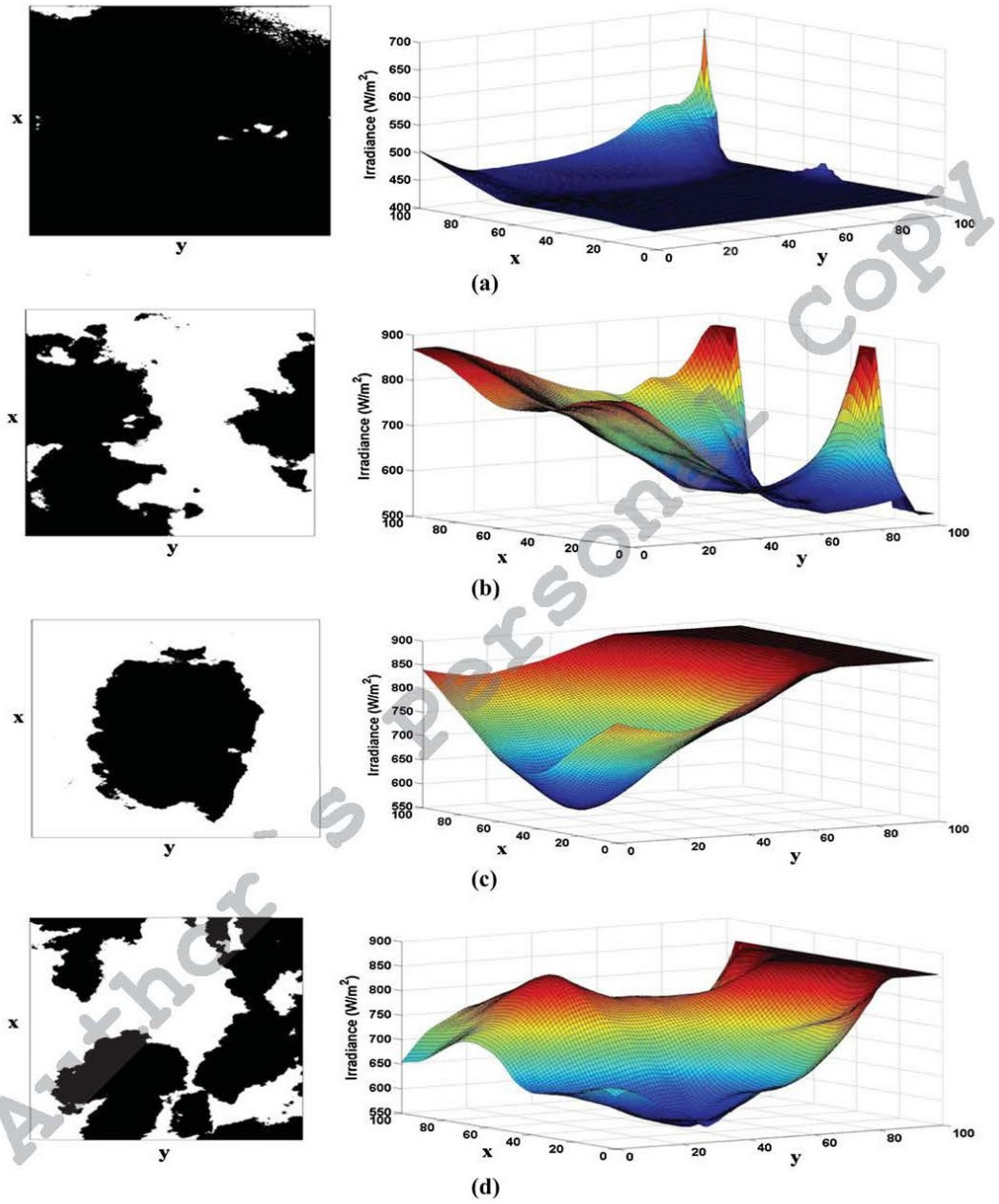

Fig. 2. Cloud patterns and SDIPs (shading scenarios) generated by the irradiance model at 13:00 Local Time (LT) considering Cumulus clouds, (a) Shading scenario 1, cc − 96%, (b) Shading Scenario 2, partly cloudy sky, cc − 44%, (c) Shading scenario 3, cc − 34%, (d) Shading scenario 4, cc − 50%, for Berlin, Germany (Latitude: 52°33′56″ N, Longitude: 13°18′39″ E) in July. 'x' and 'y' denote sides of the application area on the ground shown as percentage values.

and the average irradiance on each row are exactly equal. Hence, accurate knowledge of the incident irradiance on each individual module surface plays a key role from this point of view. The allocation of PV modules within different rows of the array is made possible using a flexible Switching Matrix controlled by the Reconfiguration Algorithm. The flowchart of the proposed reconfigura-

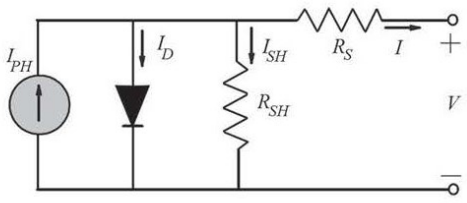

Fig. 3. Equivalent electrical circuit of a solar cell based on one-diode mathematical model.

tion system for PV arrays is presented in Fig. 5. The data acquisition task involves gathering of the irradiance data incident on each PV module surface. The ideal way to achieve this in a PV plant is to utilize one pyranometer for each individual PV module. However, feasibility considerations, instrumental limitations, etc. prevent realization of the mentioned scenario. Alternatively, estimation of irradiance values based on measurements of module voltage, current and temperature is proposed in several studies (Nguyen and Lehman, 2008; Patnaik et al., 2012). This significant task is carried out in this paper utilizing the previously defined shading scenarios. On the other hand, the previously mentioned models of PV modules are utilized for the analyses.

3.1.1. Reconfiguration algorithm

As mentioned earlier, the module relocation basically considers the irradiance equalization criteria. Average irradiance incident on parallel connected PV modules in a row, $\overline{G}_i$, is expressed as;

$$\overline{G}_i - \frac{\sum_{j=1}^{l} G_{ij}}{l} \tag{2}$$

As it was previously discussed, the goal of Irradiance Equalization is to form balanced-irradiance rows of parallel connected PV modules in a TCT interconnection. The goal here is to avoid current limitation effect of the rows producing less current in a series connection within the array. Therefore, according to Eq. (2), this goal is achieved when equal $\overline{G}_i$'s are obtained for different rows of the array architecture as a result of the array reconfiguration. In this way all series connected rows produce the same current and hence the array's power generation is not affected or limited by less current generating rows.

3.1.1.1. Working principle. As discussed earlier, the ideal case from Irradiance Equalization point of view is when the average irradiance incident on parallel connected PV modules of each individual row is equal to the average irradiance value incident on the surface of all PV modules within the array ($\overline{G}_i = \overline{G}$). Since reaching this goal under real world conditions may not always be possible due to highly variable spatial distribution of the incident irradiance values, forcing the algorithm to find the ideal configuration may put it in an infinite loop. To overcome this problem, the proposed algorithm in this paper aims for finding the near-optimal array configuration which yields reduction of the reconfigured row numbers, decreases the iterations of the algorithm and increases the algorithm's operation speed. Thus, the algorithm prevents unnecessary row reconfigurations which do not provide significant improvement on array's output power production. As mentioned in the previous discussions, the goal of the algorithm is to find the near-optimal array configuration in terms of irradiance equalization by forming rows with average irradiance levels falling within a tolerable interval of the arrays average irradiance value. For this purpose, an irradiance threshold, (ΔG), is set which is in fact a tolerance shown against current limitation effects of rows generating smaller current values. For example $\Delta G = 0.05G$ implies 50 W/m^2 reconfiguration tolerance under STC. The algorithm determines the rows to be reconfigured if $(\overline{G}_i > \overline{G} + \Delta G)$ or $(\overline{G}_i < \overline{G} + \Delta G)$. Although the average row irradiance values may not be exactly equal to each other in the proposed near-optimal array configuration, they remain within a tolerable difference limit. Therefore by application of this algorithm, the current values generated by all rows remain within tolerable limits and rows with less irradiance levels do not provide significant effects on array's power generation or the limiting effects of those rows remain within tolerable limits while the number of iterations of the algorithm and the

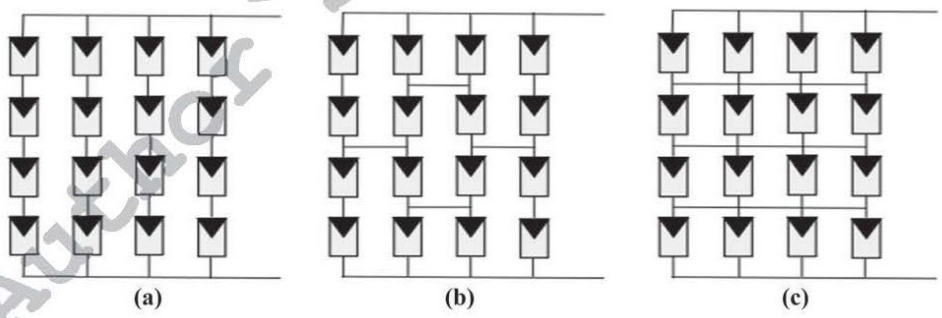

Fig. 4. PV array configurations: (a) 4 × 4 Series-Parallel (SP), (b) 4 × 4 Bridge-Link (BL), (c) 4 × 4 Total-Cross-Tied (TCT).

Fig. 5. PV array reconfiguration system flowchart.

required row reconfigurations are reduced. Here an important point is that the mentioned irradiance threshold, (ΔG), should accurately be chosen according to the conditions and requirements of the application. Obviously, in one hand, a low threshold causes higher number of module reconfigurations and consequently, increases the necessary switching actions to be further executed by the switching matrix as described in Section 3.1.2. On the other hand, proper selection of the threshold value prevents reconfigurations that do not provide significant effect on array's power generation and resultantly, avoids unnecessary switching actions by the switching matrix and saves switching equipment lifetime. For example, determination of $\Delta G = 100\ W/m^2$ prevents reconfiguration of the rows with average irradiances within 0—100 W/m^2 range below or above the array's average irradiance. Therefore the switching matrix does not execute any switching action for PV modules in the mentioned non-reconfigured rows. It should be noticed that since the spatial irradiance data forms the input of the proposed reconfiguration algorithm, switching actions are done as the last step by the switching matrix once the reconfiguration algorithm converges and the new reconfigured PV module positions are determined within the array as a result of application of the algorithm. In fact each switching action corresponds to a PV module reconfiguration determined by the reconfiguration algorithm. The algorithm firstly removes the non-configured rows for which the average row irradiance falls within the tolerable limits (irradiance threshold) of the array's average irradiance value. The algorithm then forms a new matrix including the rows to be reconfigured. Elements of this matrix are PV modules connected in rows with average row irradiance values falling out of the tolerable limits of the array's average irradiance value. PV modules of the new matrix, according to the incident irradiance on their surface, are then sorted column-wise in ascending order which implies that the first element of each column contains the remaining unsorted PV module having the lowest irradiance. This sorted matrix is then divided into two sub-matrices of size $k \times l/2$. While the elements of the first sub-matrix remain unchanged, the elements of the second sub-matrix are sorted in descending order assigning the remaining highest unsorted irradiance value to the first element of each column of the second sub-matrix. The sub-matrices are concatenated in the next step and the reconfigured PV module matrix is created after integration of the non-reconfigured rows to the new matrix. Working principle of the algorithm can be somehow thought of as a queue. Each time, the remaining PV modules to be reconfigured having the highest and the lowest irradiance levels in the queue are assigned consecutively to the elements of each row of the matrix. This method ensures formation of balanced-irradiance reconfigured rows which also complies with the goals of irradiance equalization. Taking into account that average irradiance of the non-reconfigured rows already falls within the tolerable interval, ΔG, the goals of irradiance equalization are achieved in terms of obtaining optimal array configuration. Since the order of the parallel connected PV modules in a row does not affect the current production, there is no need to specifically determine the location of each module in a row.

A sample diagram of the reconfiguration algorithm for a 4×4 array with $G_1 < G_2 < \ldots < G_{16}$ is presented in Fig. 6. The irradiance values incident on each PV module are shown and the effect of module relocation on average row irradiance values is demonstrated in the figure.

As shown in the figure, the 2nd and 3rd rows in the provided example are not reconfigured by the algorithm since their average irradiance values lie within the tolerable limits ($\Delta G \cong 40\ W/m^2$) of the array's average irradiance value ($\overline{G} = 801.56\ W/m^2$). These rows are extracted and replaced by the algorithm as shown in Fig. 6(a) and (e), respectively. The average irradiance values of the 1st and 4th rows exceed the specified threshold value and these rows are reconfigured as shown in Fig. 6(b)–(d). It is shown that the average irradiance values of the reconfigured rows lie within the tolerable limits of the array's average irradiance as a result of the array reconfiguration. It is also worth mentioning that the reconfiguration algorithm preserves the row numbers yielding the initial voltage of series connected rows in order to meet the application requirements.

3.1.1.2. Reduction of switching actions. This part of the study contains information of the way the unnecessary switching actions are avoided by the proposed algorithm in order to save the lifetimes of the switching devices. As it was previously mentioned, the input of the proposed reconfiguration algorithm is the spatial irradiance data, provided as different shading scenarios described in Section 2. The switching actions corresponding to module reconfigurations are performed as the last step by the switching matrix in order to place the reconfigured PV modules at their new locations within the array once the reconfiguration algorithm converges and the resulting new reconfigured PV module positions are determined. As the result of application of the reconfiguration algorithm and during the irradiance sorting procedure, the location of some PV modules may be changed by other modules having the same irradiance values from different rows of the array. In fact such reconfigurations do not affect the average row irradiance values and only change the position of PV modules with the same irradiance level within the array, requiring unnecessary switching actions to be performed by the switching matrix. At this stage, once the algorithm converges and before performing the switching actions, the algorithm tries to reduce the number of reconfigurations by searching for module reconfigurations (if any) which actually change the locations of modules having the same irradiance levels within a specific row or between different rows. As mentioned before, such reconfigurations are unnecessary since they do not affect average row irradiances and hence do not have any impact on array's power generation. This way, the reconfiguration algorithm reduces the number of module reconfigurations and thus the number of switching actions to be performed by the switching matrix through elimination of the unnecessary reconfigurations. Obviously the number of switching actions depends on the size of the array and the existing spatial irradiance profile.

3.1.2. Switching matrix

The switching matrix indicates the necessary switching actions in order to execute the reconfiguration plan formed by the reconfiguration algorithm. A switching action, corresponding to a PV module reconfiguration, is the action performed to disconnect a PV module from its initial non-reconfigured row position and connect it to its new position within the reconfigured PV array which is determined as a result of application of the reconfiguration algorithm. This action is performed by switching devices and switching control mechanism. This part of the study presents brief explanations regarding the structure and control method of the switching matrix performing the desired array reconfiguration.

3.1.2.1. Matrix structure. The structure of the switching matrix is explained briefly in this part. A sample of the switching matrix configuration is provided in Fig. 7. The matrix structure is based on utilization of electrical buses and provides the capability of parallel interconnection of each PV module to each row. The flexible dynamic interconnections are made possible by using $2 \times N_{PV}$ single-pole k-throw switches (Velasco-Quesada et al., 2009).

3.1.2.2. Matrix control. The controlling method of the switching matrix is presented in this part. The input to the matrix control

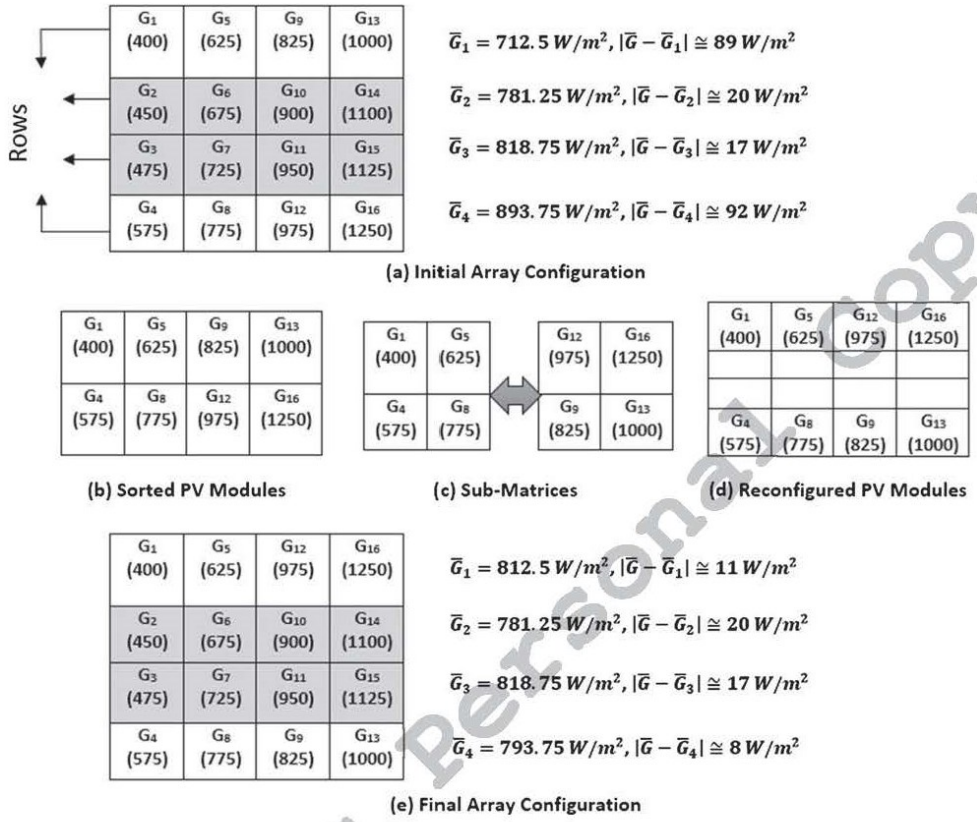

Fig. 6. Sample diagram of the reconfiguration algorithm for a 4 × 4 PV array ($G_1 < G_2 < \ldots < G_{16}$) where $\bar{G} = 801.56$ W/m², $\Delta G = 0.05\bar{G} \cong 40$ W/m².

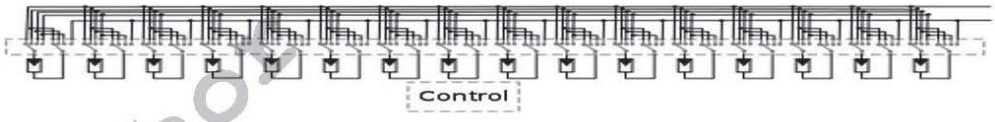

Fig. 7. Switching matrix structure.

Table 1
P_{NR}, $P_{OPT.}$, P_{max} (kW) and N_{SW} associated with different irradiance thresholds for shading scenarios.

ΔG	2nd Shading Scenario (P_{NR} = 3.695, $P_{OPT.}$ = 3.871, $P_{OPT.}/P_{NR}$ = 1.047)			3rd Shading Scenario (P_{NR} = 4.449, $P_{OPT.}$ = 4.731, $P_{OPT.}/P_{NR}$ = 1.063)			4th Shading Scenario (P_{NR} = 4.286, $P_{OPT.}$ = 4.406, $P_{OPT.}/P_{NR}$ = 1.027)		
	N_{SW}	P_{max}	P_{max}/P_{NR}	N_{SW}	P_{max}	P_{max}/P_{NR}	N_{SW}	P_{max}	P_{max}/P_{NR}
$0.1\bar{G}$	17	3.740	1.012	42	4.689	1.053	9	4.286	1
$0.075\bar{G}$	54	3.805	1.029	47	4.696	1.055	9	4.286	1
$0.05\bar{G}$	68	3.860	1.044	57	4.724	1.061	66	4.396	1.025
$0.025\bar{G}$	83	3.868	1.046	57	4.724	1.061	76	4.404	1.027

algorithm is the reconfiguration plan produced by the reconfiguration algorithm. The matrix control algorithm then sends the required switching instructions (or triggering signals) to the aforementioned switches in order to execute the reconfigured new array interconnections determined by the reconfiguration algorithm.

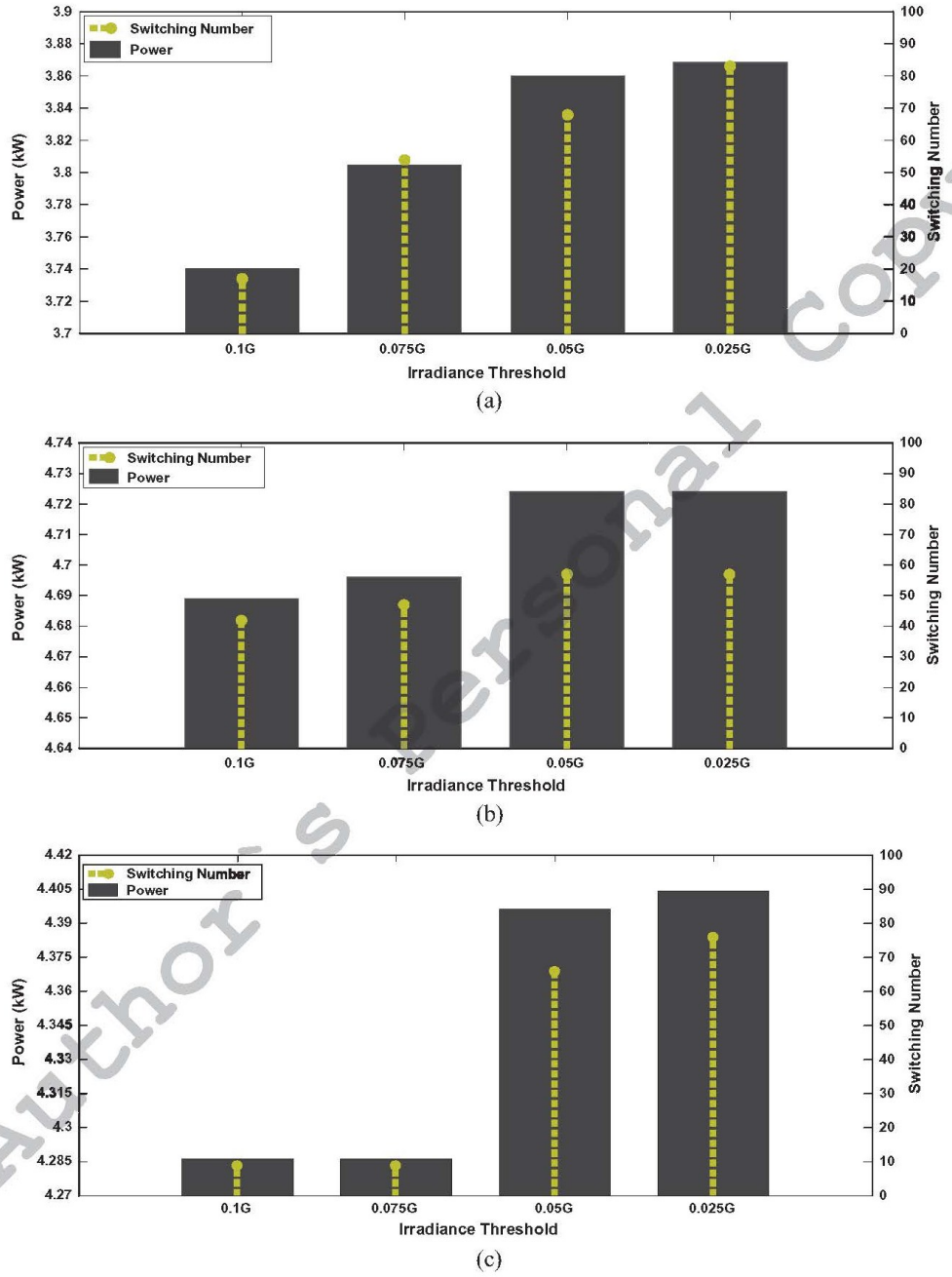

Fig. 8. Changes in PV array's output power and switching numbers in parallel with irradiance threshold ΔG, for (a) the 2nd shading scenario, (b) the 3rd shading scenario, (c) the 4th shading scenario.

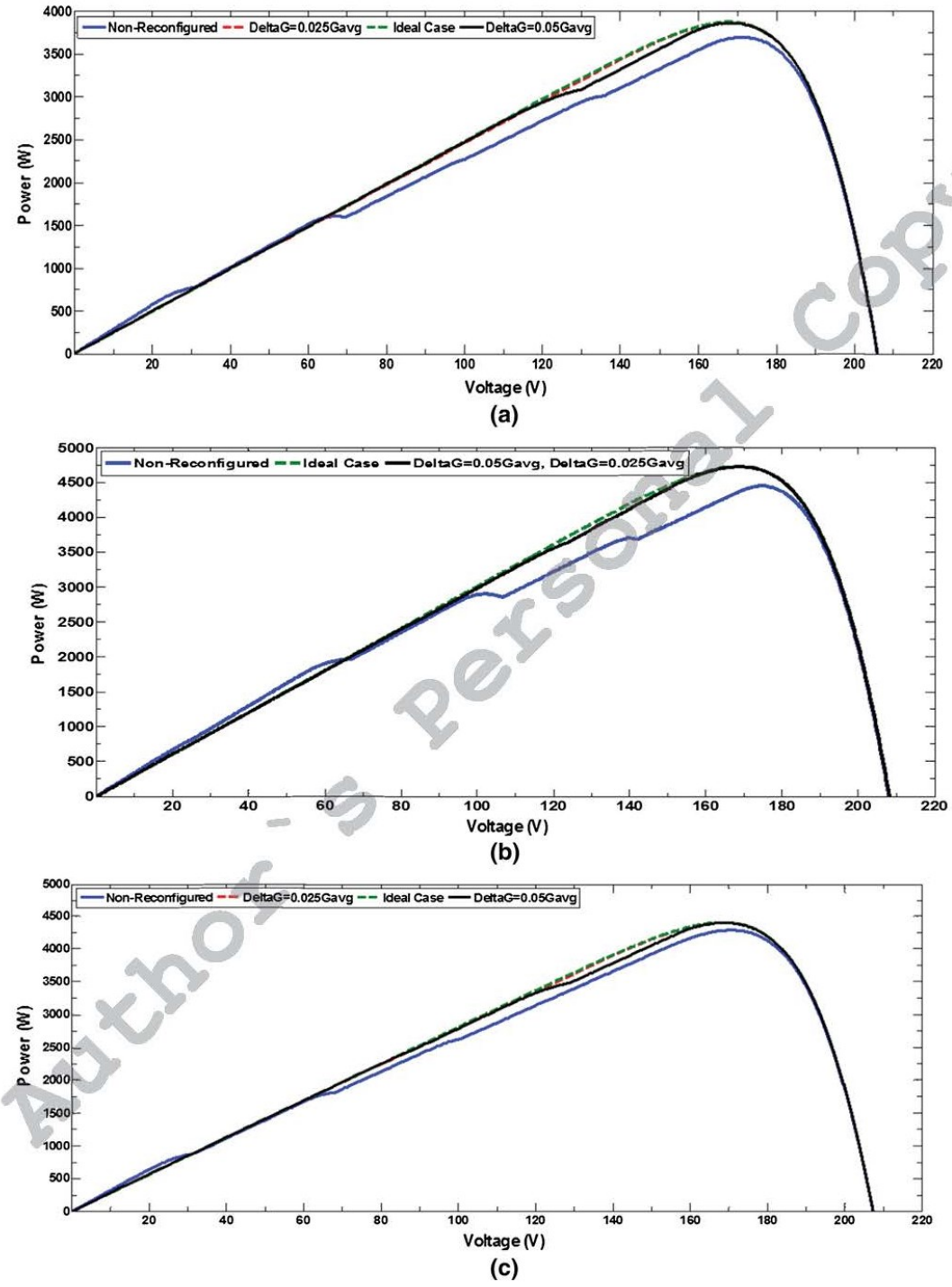

Fig. 9. Array P-V characteristic curves before and after reconfiguration, for (a) the 2nd shading scenario, (b) the 3rd shading scenario, (c) the 4th shading scenario.

3.2. Results and discussion

The system is simulated in MATLAB/Simulink, utilizing 100 Solarex MSX60 (P_{max} = 60 W, V_{oc} = 21.1 V, I_{sc} = 3.8 A) type PV modules in a 10 × 10 PV array. PV modules are assumed to be located with equal distances implying that one PV module is located per each 10% area of the array as discussed in Section 2. Different ΔG values are examined and the results are compared. It is empirically observed that for all shading scenarios $\Delta G > 0.1\overline{G}$ provides almost no contribution to the maximum power point (P_{max}) value. Therefore totally four different values between 0 and $0.1\overline{G}$ are examined utilizing equivalent increments. According to the observations, $\Delta G > 0.075\overline{G}$ and $\Delta G < 0.025\overline{G}$ also do not provide significant contribution to P_{max} contrary to the associated relatively low and high number of switching actions performed by the switching matrix to form the reconfigured PV array, respectively, for the 4th and 3rd shading scenarios. Under the 2nd shading scenario, the existing irradiance profile causes significant contributions to P_{max} to be achieved with $\Delta G = 0.1\overline{G}$. At the same time, due to the almost uniform illumination, reconfiguration of PV modules under overcast sky (1st shading scenario) is not applicable. For a better comparison, Table 1 provides information regarding P_{NR}, $P_{OPT.}$, number of switching actions performed by the switching matrix to form the reconfigured array (N_{SW}), and obtained P_{max} values after reconfiguration, associated with each irradiance threshold for the mentioned shading scenarios. The non-reconfigured PV array performances under the 2nd, 3rd and 4th shading scenarios are considered as the reference cases for which the array's output power values before reconfiguration are shown by P_{NR} in the table. Also the optimum output power production, in terms of irradiance equalization, for each case is provided as $P_{OPT.}$. The table presents the obtained maximum output power values together with the number of switching actions after reconfiguration considering various ΔG values. The results show that the reconfiguration algorithm has been able to improve power generation by 4.7%, 6.1% and 2.7% respectively under the 2nd, 3rd and 4th shading scenarios, considering $\Delta G = 0.025\overline{G}$. Changes in PV array's power generation and the number of switching actions alongside with ΔG for different shading scenarios are presented in Fig. 8.

The results show that almost for all shading scenarios in this paper, $\Delta G = 0.05\overline{G}$ would be a proper selection in terms of the reconfiguration numbers and contribution to P_{max}. Obviously the threshold value and improvements in power generation strongly depend on the existing spatial irradiance profile based on the existing cloud patterns and their sunlight interaction characteristics.

Fig. 9 presents array P-V characteristic curves for different shading scenarios, before and after reconfiguration. The contribution of array reconfiguration to power generation is obvious for shading scenarios where the reconfiguration is applicable. Also the smoothing effect of ΔG on the characteristic curves worths mentioning. It is shown that smaller threshold values result in smoother characteristic curves and higher P_{max}, to the cost of higher reconfiguration numbers. Characteristic curves for the ideal case are also provided for each shading scenario. Obviously there is almost no difference between P_{max} values obtained by the proposed method and the ideal case for each shading scenario.

It should also be taken into consideration that analyses in this paper are carried out and presented only for a single time step and a single geographical location. The sample results are provided as representatives for the model's performance and its ability to improve power generation under non-uniform spatial irradiance profiles. However, the model is applicable to any geographical location and irradiance profile, whilst the performance of the model depends on the incident irradiance profiles. The model is expected to provide better performances as the range of irradiance variations within an existing irradiance profile increases.

As previously discussed, the total number of switches required for development of the proposed reconfiguration system is $2 \times N_{PV}$. However it should be taken into consideration that all the switches may not necessarily perform at the same time during reconfiguration of PV array under an existing spatial irradiance profile. This also preserves the lifetime of the switching devices. According to the results provided in Table 1, it is obvious that the total number of switching actions, (N_{SW}), corresponding to PV module reconfigurations during dynamic reconfiguration of PV array totally depends on the existing spatial irradiance profile and the selected irradiance threshold, ΔG. The number of module reconfigurations and therefore switching actions increase according to the P_{OPT}/P_{NR} ratio while smaller irradiance thresholds also lead to increases in module reconfiguration and the number of switching actions during dynamic reconfiguration of PV array, resultantly. As an example it is observed that although there are a total number of 200 switches utilized in the array, only 83 of the switches have performed to apply the reconfiguration under the 2nd shading scenario with $\Delta G = 0.025\overline{G}$.

4. Conclusion

Various solutions have been introduced to cope with factors limiting the use of solar energy resources such as electrical mismatches, variable weather conditions, etc. Obviously the ideal case to prevent mismatch losses is to form PV arrays by connecting electrically identical PV modules in different configurations. However, all PV modules included in a PV array may not have identical electrical characteristics due to differences in materials and variabilities of manufacturing processes. Variable electrical characteristics between PV modules caused by the mentioned differences and variabilities is referred to as module mismatch. In this case, the optimal operating point of the PV modules may differ from one to another in a PV array, yielding reductions in array's power production. Thus, under module mismatch conditions, the practical maximum output power of a PV array is always less than the sum of the maximum output powers of PV modules forming the array. Utilization of appropriately rated by-pass diodes and blocking diodes are examples of measures taken to cope with mismatch losses in PV arrays. Dynamic reconfiguration of PV arrays is also one of the leading edge research areas to mitigate negative effects of non-uniform irradiance profiles incident on PV application areas. Various reconfiguration strategies and control algorithms are developed for this purpose. While improvements in power generation is the most significant common advantage of all developed strategies, each individual strategy has ceratin specific drawbacks and limitations. Adaptive Bank strategy utilizing bubble-sort model-based control algorithm is one of the mentioned strategies where the main disadvantage of this method is the need for a fixed adaptive bank of solar cells which potentially increases the number of required cells, switching devices and complexity of the connections. Elastic Photovoltaic Structure (EPVS), Solar Irradiance Level Categories and Rough Set Theory are other examples of reconfiguration algorithms developed to be applicable to SP array architecture. Non-conformity with TCT interconnection, high number of required switching devices and complexity of the control algorithms form the main disadvantages of the mentioned methods. Irradiance Equalization as a widely utilized strategy has been deployed together with various control algorithms such as Deterministic Random Search Algorithm and Best-Worst Sorting for TCT interconnection. Here also the complexity of the control algorithms and the required high number of switching devices form the main disadvantages of these methods. Taking the complexity of the

system into consideration, from both hardware and software points of view, the proposed strategy in this paper is sensitive to the size of the application and best fits large scale rooftop, Building Integrated Photovoltaic Systems (BIPV) and ground mounted PV plants rather than small scale residential PV applications. Obviously, implementation of a reconfigurable PV system comes with additional costs (wiring, switching devices, etc.) for PV developers. Therefore a tradeoff between extra costs and the expected improvements in power generation will always exist. However, the mentioned costs may be reduced by means of taking appropriate measures such as utilization of proper system topologies, switching devices and control algorithms which minimize the required switching devices and switching numbers. The utilized DC/AC conversion devices (inverters) and Maximum Power Point Tracking (MPPT) algorithms controlling them also may negatively affect power generation of PV arrays under non-uniform irradiance profiles. MPPT algorithms may consider a local Maximum Power Point (MPP) as the array's absolute MPP. Also the utilized inverter number and their configurations may significantly affect the array's power generation. Smart MPPT strategies and proper selection of the conversion groups (e.g. Central-inverter, string-inverter, multi-string inverter and micro-inverter architecture) are examples of the measures to be taken to reduce the negative effects through power conversion procedure.

This paper firstly utilizes a modeling approach to generate irradiance profiles on PV arrays based on real sky images as cloud coverage drivers. The generated irradiance profiles vary in parallel to the variations of the existing cloud coverage in the sky. The study then proposes a PV array reconfiguration algorithm which seeks to find near-optimal array configurations and provides a simple structure based on irradiance equalization approach. This is accomplished by utilizing an irradiance threshold where smaller thresholds provide smoother curves contrary to higher reconfiguration numbers. The algorithm also considers minimization of the number of switching actions by eliminating the unnecessary reconfigurations and therefore saves the lifetimes of switching devices. Reconfiguration of modules is made possible through a flexible dynamic switching matrix allowing for parallel interconnection of each module to any row of the array. Application of the proposed reconfiguration method results in significant improvements in array's power generation. Although magnitude of the improvements totally depends on the existing spatial irradiance profile, the proposed algorithm has successfully managed to improve array's power generation as much as it would be possible under ideal conditions, for each shading scenario. The system's performance results are presented and analyzed for a single time step and a single geographical location, however the system can obviously be utilized to improve power generation for any geographical location with any irradiance profile. It should be taken into consideration that high resolution spatial irradiance data is needed to implement the proposed reconfiguration methodology where PV modules are closely located within the PV application area. The system's performance increases in parallel with the increases in the range of variation of irradiance levels available within an existing irradiance profile. Also it should be noticed that PV modules in this paper are assumed to have identical electrical characteristics and therefore array level losses such as module mismatch and wiring resistance are not considered. The advantages of the proposed algorithm are high performance, dynamic and simple structure, relatively low number of the required switching actions and switching devices, conformity with TCT array topology and applicability to arrays consisting of large numbers of PV modules.

References

Alahmad, M., Chaaban, M.A., Lau, S.K., Shi, J., Neal, J., 2012. An adaptive utility interactive photovoltaic system based on a flexible switch matrix to optimize performance in real-time. Sol. Energy 86, 951–963.

Carannante, C., Fraddanno, C., Pagano, M., Piegari, L., 2009. Experimental performance of MPPT algorithm for photovoltaic sources subject to inhomogeneous insolation. IEEE Trans. Ind. Electron. 56, 4374–4380.

Chow, C.W., Urquhart, B., Lave, M., Dominguez, A., Kleissl, J., Shields, J., Washom, B., 2011. Intra-hour forecasting with a total sky imager at the UC San Diego solar testbed. Sol. Energy 85, 2881–2893.

Ishaque, K., Salam, Z., Syafaruddin, 2011a. A comprehensive MATLAB Simulink PV system simulator with partial shading capability based on two-diode model. Sol. Energy 85, 2217–2227. http://dx.doi.org/10.1016/j.solener.2011.06.008.

Ishaque, K., Salam, Z., Taheri, H., Syafaruddin, 2011b. Modeling and simulation of photovoltaic (PV) system during partial shading based on a two-diode model. Simul. Model. Pract. Theory 19, 1613–1626. http://dx.doi.org/10.1016/j.simpat.2011.04.005.

Kaushika, N.D., Gautam, N.K., 2003. Energy yield simulations of interconnected solar PV arrays. IEEE Trans. Energy Convers. 18, 127–134. http://dx.doi.org/10.1109/TEC.2002.805204.

Liu, S., Dougal, R.A., 2004. Dynamic multiphysics model for solar array. IEEE Trans. Energy Convers. 17, 285–294.

Nguyen, D., Kleissl, J., 2014. Stereographic methods for cloud base height determination using two sky imagers. Sol. Energy 107, 495–509.

Nguyen, D., Lehman, B., 2008. An adaptive solar photovoltaic array using model-based reconfiguration algorithm. IEEE Trans. Ind. Electron. 55, 2644–2654. http://dx.doi.org/10.1109/TIE.2008.924169.

Patnaik, B., Mohod, J.D., Duttagupta, S.D., 2012. Distributed multi-sensor network for real time monitoring of illumination states for a reconfigurable solar photovoltaic array. In: 2012 1st International Symposium on (Physics and Technology of Sensors (ISPTS), Pune, India, pp. 106–109.

Ramaprabha, R., Mathur, B.L., 2012. A comprehensive review and analysis of solar photovoltaic array configurations under partial shaded conditions. Int. J. Photoenergy 2012. http://dx.doi.org/10.1155/2012/120214.

Shams El-Dein, M.Z., Kazerani, M., Salama, M.M.A., 2013. Optimal photovoltaic array reconfiguration to reduce partial shading losses. IEEE Trans. Sustain. Energy 4, 145–153. http://dx.doi.org/10.1109/TSTE.2012.2208128.

Silvestre, S., Boronat, A., Chouder, A., 2009. Study of bypass diodes configuration on PV modules. Appl. Energy 86, 1632–1640.

Velasco-Quesada, G., Guinjoan-Gispert, F., Piqué-López, R., Román-Lumbreras, M., Conesa-Roca, A., 2009. Electrical PV array reconfiguration strategy for energy extraction improvement in grid-connected PV systems. IEEE Trans. Ind. Electron. 56, 4319–4331. http://dx.doi.org/10.1109/TIE.2009.2024664.

Villalva, M.G., Gazoli, J.R., Filho, E.R., 2009. Comprehensive approach to modeling and simulation of photovoltaic arrays. IEEE Trans. Power Electron. 24, 1198–1208. http://dx.doi.org/10.1109/tpel.2009.2013862.

Wilson, P., Storey, J., Bagnall, D., 2013. Improved optimization strategy for irradiance equalization in dynamic photovoltaic arrays. IEEE Trans. Power Electron. 28, 2946–2956.

Appendix D: Comparative Analysis of Levenberg-Marquardt and Bayesian Regularization Backpropagation Algorithms in Photovoltaic Power Estimation Using Artificial Neural Network

Kian Jazayeri, Moein Jazayeri, Sener Uysal, "Comparative analysis of levenberg-marquardt and bayesian regularization backpropagation algorithms in photovoltaic power estimation using artificial neural network", in *Proceedings - Lecture Notes in Computer Science (including subseries Lecture Notes in Artificial Intelligence and Lecture Notes in Bioinformatics*), vol. 9728, New York City, NY, USA 2016.

Abstract. This paper presents a comparative analysis of Levenberg-Marquardt (LM) and Bayesian Regularization (BR) backpropagation algorithms in development of different Artificial Neural Networks (ANNs) to estimate the output power of a Photovoltaic (PV) module. The proposed ANNs undergo training, validation and testing phases on 10000+ combinations of data including the real-time measurements of irradiance level (W/m^2) and PV output power (W) as well as the calculations of the Sun's position in the sky and the PV module surface temperature (°C). The overall performance of the LM and the BR algorithms are analyzed during the development phases of the ANNs, and also the results of implementation of each ANN in different time intervals with different input types are compared. The comparative study presents the trade-offs of utilizing LM and BR algorithms in order to develop the best ANN architecture for PV output power estimation.

Comparative Analysis of Levenberg-Marquardt and Bayesian Regularization Backpropagation algorithms in Photovoltaic Power Estimation Using Artificial Neural Network

Kian Jazayeri, Moein Jazayeri, Sener Uysal

Eastern Mediterranean University, Department of Electrical and Electronic Engineering, Famagusta, Via Mersin 10, Turkey
kian.jazayeri@cc.emu.edu.tr
moein.jazayeri@cc.emu.edu.tr
sener.uysal@emu.edu.tr

Abstract. This paper presents a comparative analysis of Levenberg-Marquardt (LM) and Bayesian Regularization (BR) backpropagation algorithms in development of different Artificial Neural Networks (ANNs) to estimate the output power of a Photovoltaic (PV) module. The proposed ANNs undergo training, validation and testing phases on 10000+ combinations of data including the real-time measurements of irradiance level (W/m^2) and PV output power (W) as well as the calculations of the Sun's position in the sky and the PV module surface temperature (°C). The overall performance of the LM and the BR algorithms are analyzed during the development phases of the ANNs, and also the results of implementation of each ANN in different time intervals with different input types are compared. The comparative study presents the trade-offs of utilizing LM and BR algorithms in order to develop the best ANN architecture for PV output power estimation.

1 Introduction

Solar energy is a renewable and sustainable resource that emerges to meet the energy requirements of today's modern world. The solar energy is converted to direct current (DC) electricity by the Photovoltaic (PV) effect. PV cells are connected to form a PV module (solar panel), which can be connected to other PV modules to construct PV arrays and systems. The importance of developing handling techniques of PV systems is highlighted considering the growing world energy demands and the limitations and threats associated with the traditional energy resources. Artificial Intelligence (AI) techniques are deployed in various applications as an alternative to conventional techniques due to their capabilities in solving complicated practical problems. Artificial Neural Network (ANN) is one of the most popular branches of AI. ANNs are mathematical models that imitate the behavior of biological Neural Systems. An ANN, which is a collection of interconnected computation units, is able to generalize outputs for new inputs after being trained on patterns of training data. ANNs are deployed in many practical applications due to their fault tolerance, flexibility and robustness in

handling noisy data. Some of the ANN application examples in PV systems are given as follows.

Estimation of the daily solar radiation using ANNs is proposed by Elizondo et Al. [1] and Williams and Zazueta [2]. Golabl solar radiation prediction using ANN is suggested by Alawi and Hinai [3] and monthly mean daily values of global solar radiation on horizontal surfaces are modeled by Mohandes et al. [4] using Radial Basis Function (RBF) networks. An ANN based total solar radiation time-series simulation model is offered by Mihalakakou et al. [5] and RBF networks are used for estimating total daily solar radiation by Mellit et al. [6].

The right choice of network types and algorithms is essential in order to attain desirable modeling, estimation and prediction outputs using ANNs. Different ANN architectures are employed for PV power estimation purposes by Lo Brano et al [7]. The ambient temperature, solar irradiance and wind speed data are provided to the ANNs in the mentioned study to estimate the output power of two PV test modules. The authors conclude that the Multi-layer Perceptron (MLP) architecture provides the best performance in terms of the estimation error. A similar study is carried out by Saberian et al. [8] and the minimum temperature, maximum temperature, mean temperature and solar irradiance data are fed to different ANN topologies in order to estimate the output power of a PV module. The authors indicate that the feed-forward MLP with backpropagation training algorithm provides the best performance in PV module power estimation. A comparison of Levenberg-Marquardt (LM) and Bayesian Regularization (BR) backpropagation algorithms for efficient localization in wireless sensor network is presented by Payal et al. [9], a comparison of BR and Cross-Validated Early-Stopping (CVES) backpropagation algorithms for streamflow forecasting is carried out by Wang et al. [8] and a comparative study of backpropagation algorithms in ANN based identification of power system is proposed by Tiwari et al. [11].

In this study, well-detailed and highly accurate data is acquired using appropriate and highly-sensitive measurement equipment to be described in section 2. However no matter how well-detailed and straight-forward-looking the inputs be, the PV power generation relationships are non-linear and cannot be expressed by simple analytical or physical approaches. Especially the effect of the PV module surface temperature highly complicate the relation between the solar irradiance and the PV output power as the PV power generation tendency decreases with increasing PV module surface temperature, which is caused by increasing irradiance. In other words, the solar irradiance has a very complex effect (compliant and opposite effects at the same time) on the PV power generation which cannot be expressed by simple equations or analytical models. The need for using a qualified machine learning technique for PV module output power estimation is highlighted by taking the above into consideration. The scope of this study is to give insight of the competency of the well-known MLP approach with eligible backpropagation algorithm in PV power estimation applications in existence of sufficient inputs. A comparative analysis of LM and BR backpropagation training algorithms in estimation of PV module output power using MLP approach is proposed and the trade-offs of utilizing each algorithm is represented in terms of training error, time, speed, etc. Finally the performances of applying different ANNs trained by LM and BR algorithms for PV power estimation in several ANN implementation intervals with different input types are analyzed.

2 Data Collection

It is aimed to provide the calculated values of the Sun's position in the sky, the angle of incidence and the PV module surface temperature as well as the irradiance level measurements to the Artificial Neural Networks (ANNs) as the input data, and the measurements of the PV module output power as the target data, during the training, testing and validation phases. The only preprocessing applied to the mentioned data is the normalization process which is described in the following sub-sections. Nov. 1st to Nov. 25th, 2015 is selected as the data acquisition interval due to the highly variable meteorological conditions during daylight hours in this period in Cyprus Island where the experiments took place. The ANNs receive highly variable training and testing data in this relatively short time interval. The noise is negligible due to the sensitivity of the measurement equipment utilized for this study. The acquired data for development of the ANNs is described comprehensively in this section.

2.1 The Sun's Position Data

The Sun's position in the sky is defined by the solar altitude and the solar azimuth angles [12]. The solar altitude angle indicates the Sun's elevation from Earth's surface and is expressed as:

$$\gamma_s = \sin^{-1}(\sin\varphi\sin\delta + \cos\varphi\cos\delta\cos\omega) \quad (1)$$

$$\delta = \sin^{-1}\left\{0.3987\sin\left(j^{`}80.2° + 1.92\left(\sin\left(j^{`}\text{-}2.80°\right)\right)\right)\right\} \quad (2)$$

$$j^{`} = j \times (360/365.25) \quad (3)$$

$$\omega = 15(LST - 12) \quad (4)$$

Where,
φ : latitude of the observation point
δ : solar declination angle
j : Julian day number
ω : hour angle

Because of the irregularity of Earth's orbit as well as human adjustments (time zones and daylight saving application), Local Solar Time (LST) is slightly different than Local Time (LT) and is represented as:

$$LST = LT + \frac{TC}{60} \quad (5)$$

$$TC = 4(Longitude - LSTM) + EoT \quad (6)$$

$$EoT = 9.87\sin(2B) - 7.53\cos(B) - 1.5\sin(B) \tag{7}$$

$$B = \frac{360}{365}(j - 81) \tag{8}$$

$$LSTM = 15° . \Delta T_{GMT} \tag{9}$$

Where,

TC : Time correction factor
EoT : Equation of time
$LSTM$: Local standard time meridian
ΔT_{GMT} : The difference of local time from Greenwich Mean Time

The solar azimuth angle indicates the Sun's deviation from the north axis and is expressed by:

$$\begin{cases} \alpha_s = 180 - \cos^{-1}(\cos \alpha_s) & \text{If } \sin \alpha_s < 0 \\ \alpha_s = 180 + \cos^{-1}(\cos \alpha_s) & \text{If } \sin \alpha_s > 0 \end{cases} \tag{10}$$

Where,

$$\cos \alpha_s = (\sin \varphi \sin \gamma_s - \sin \delta) / \cos \varphi \cos \gamma_s \tag{11}$$

$$\sin \alpha_s = \cos \alpha_s \sin \omega / \cos \gamma_s \tag{12}$$

The mentioned values are normalized between 0 and 1, yielding data close to 1 for the values that have the most impact on the PV module output power and data close to 0 vice versa. The normalized values of the solar altitude and the solar azimuth angles calculated in minutely basis during daylight time interval on Nov. 16th, 2015, as a typical data acquisition period, are shown in Fig. 1.

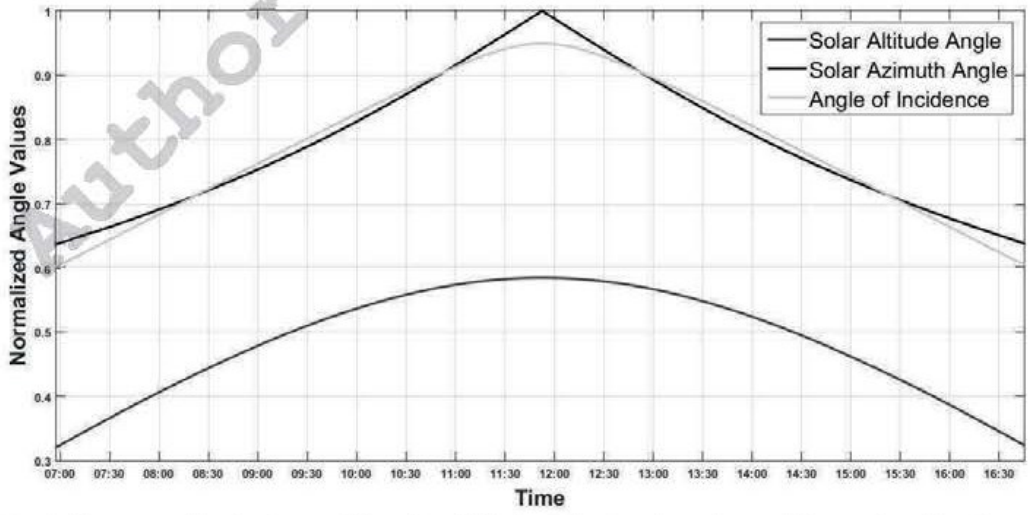

Fig. 1. The normalized values of the solar altitude and azimuth angles and the angle of incidence, calculated on Nov. 16th, 2015.

2.2 The Angle of Incidence

The angle of incidence is the angle between the Sun's beams and a vector perpendicular to the surface of a solar panel and is represented as:

$$\theta=\cos^{-1}\begin{bmatrix}\cos(\beta)\cos(Z_s)+\\ \sin(\beta)\sin(Z_s)\cos(\alpha_s-\alpha_m)\end{bmatrix} \quad (13)$$

$$Z_s = 90 - \gamma_s \quad (14)$$

Where,

β : Tilt angle of the solar panel (45° in this case)
Z_s : Zenith sngle of the Sun
α : Module azimuth angle (in this case: south = 180°)

The normalized values of the angle of incidence, calculated minutely on Nov. 16th, 2015, are shown in Fig. 1. The normalized value takes on 1 when the Sun's beams are perpendicularly received on the solar panel surface and as the Sun's beams deviate from the perpendicular axis, the normalized value decreases down to 0.

2.3 Irradiance Level

The density of the solar radiation power received on a given surface is defined as the irradiace and is measured in Watts per meter square. In this study a south oriented, 45° tilted pyranometer is used for field measurements. The measured irradiance values are normalized between 0 and 1. The normalized irradiance values measured minutely on Nov. 16th, 2015 as a typical data acquisition period are shown in Fig. 2.

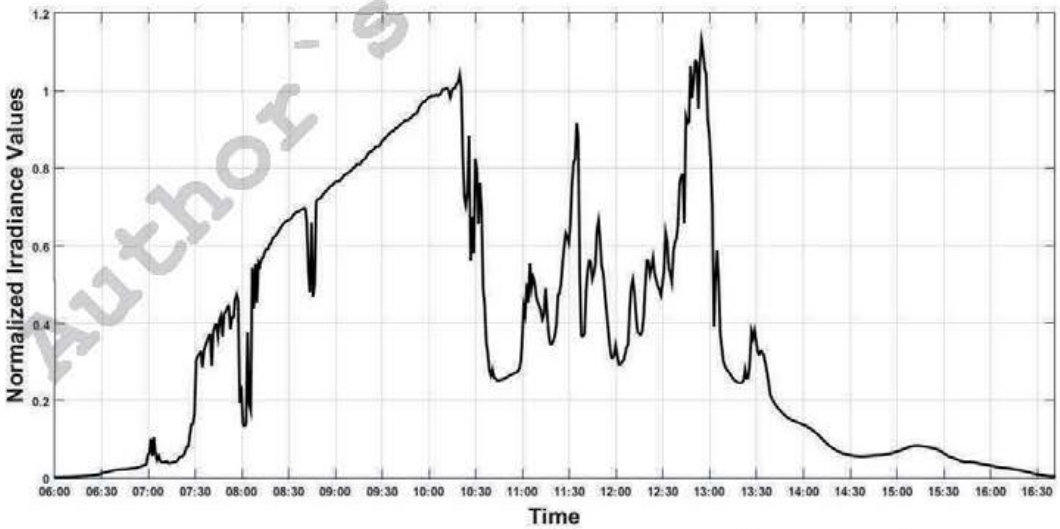

Fig. 2. The normalized irradiance values, measured in (W/m^2) on Nov. 16th, 2015.

2.4 PV Module Surface Temperature

The PV Module Surface Temperature has a reverse impact on the PV module performance efficiency since the PV power generation tendency is reduced as the surface temperature increases. According to [13], the PV module surface temperature can be calculated as a function of *NOCT* and the ambient temperature using the following equation:

$$T = T_{ambient} + ((NOCT - 20°C)(E_{tot}/800\ Wm^{-2})) \quad (15)$$

Where,
T = PV Module surface temperature
$T_{ambient}$ = Ambient temperature
$NOCT$ = Nominal operating cell temperature
E_{tot} = Irradiance level (W/m^2)

The minutely temperature ($T_{ambient}$) values in (°C) obtained from the Larnaca International Airport (LCLK) weather station and the measurements of irradiance levels are used for PV module surface temperature calculations. The calculated values are normalized between 0 and 1, yielding values close to 1 for the lower surface temperatures and values close to 0 conversely. The normalized values of the PV module temperature calculated minutely on Nov. 16th, 2015 are shown in Fig. 3.

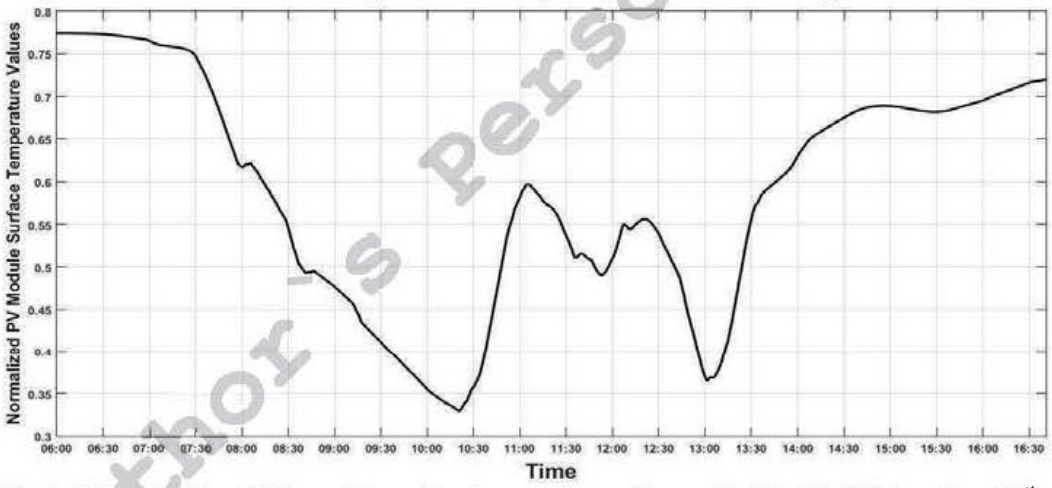

Fig. 3. The normalized PV module surface temperature values, calculated in (°C) on Nov. 16th, 2015.

2.5 Photovoltaic Module Output Power

A south oriented, 45° tilted monocrystalline silicon solar panel (P_{max}: 40 W, V_{OC}: 21.6 V, I_{SC}: 2.56 A) located at 35° 8′ 51″ N, 33° 53′ 58″ E, with 1 meters elevation from the sea level is used for the field measurement purposes. The output power of the PV module directly feeding a constant resistive DC load, is measured (mW) minute by minute and logged after being normalized between 0 and 1. The normalized values of the PV module output power measured in minutely basis on Nov. 16th, 2015, is shown in Fig. 4.

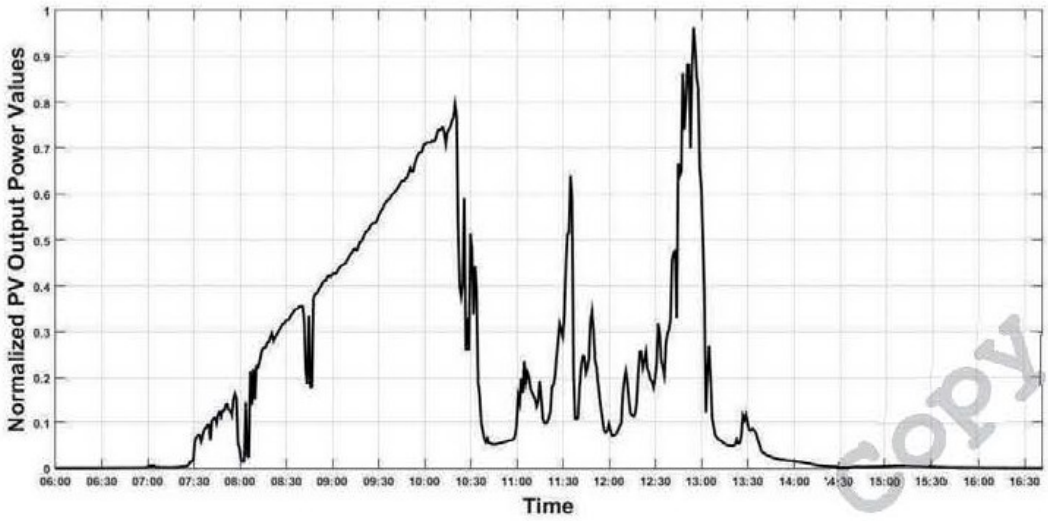

Fig. 4. The normalized PV output power values, measured in (mW) on November 16th, 2015.

3 Development of Artificial Neural Network (ANN) Architectures

It is intended to develop Artificial Neural Networks (ANNs) that are capable of deriving the appropriate relations defining the output power of a PV module, after being trained and tested on the data collected during the acquisition period. In this section, the comprehensive analysis of the training, testing and validation phases of the ANNs with Levenberg-Marquardt (LM) and Bayesian Regularization (BR) backpropagation algorithms are presented. As described in detail in the data collection part, the inputs to the proposed ANNs are the normalized values of the solar altitude angle, the solar azimuth angle, the angle of incidence, the irradiance level and the PV module surface temperature and the output of the ANN is the PV module output power which is reconstructed from the normalized value. The developed ANNs are three-layer fully connected feed-forward networks with Tan-Sigmoid activation function in hidden layer and linear activation function in output layer. The number of hidden neurons are decided such that the network maintains the required accuracy while the computation time and memory does not exceed certain limits. It is observed the estimation accuracy of the ANN does not show significant improvement for more than 10 neuron sized hidden layers, while the computation time and memory allocation raise significantly with larger hidden layers. Therefore the number of hidden neurons are set to 10. The mentioned ANN architecture is illustrated in Fig. 5. Random small values are assigned to the network weights at the beginning of the training process and the training inputs are fed to the network through the input layer. The training data propagate through the network to reach the output layer. At this point the training error is calculated by comparing the estimated output and the target output which is presented to the network to supervise the learning process. The error is back-propagated in the network to adjust the weights. The training error threshold is set such that the network is kept from being either under-fitted or over-fitted. An under-fitted ANN lacks accuracy in estimation while an over-fitted ANN fails in generalization for new inputs.

Backpropagation is used to obtain the first and the second derivatives of the error function $E(w)$ with respect to the network weight vector, $w=[w_1\ w_2 \dots w_N]^T$.

First derivative of the error function with respect to the weight vector is called the Gradient of $E(w)$ and is expressed by Eq. 16. Second derivative of $E(w)$ is the Hessian of $E(w)$ given in Eq.17. The Levenberg–Marquardt (LM) algorithm developed by Kenneth Levenberg and Donald Marquardt is suitable for ANNs dealing with moderate-sized problems. Wilamowski and Yu [12] introduce the approximation to Hessian matrix indicated in Eq. 18. The update rule of the LM algorithm is presented as Eq. 19. Further mathematical details regarding the LM backpropagation algorithm can be investigated in [14], [15] and [16].

The BR backpropagation algorithm provides robust estimation for noisy and difficult inputs in the existence of sufficient amount of training data. The algorithm works effectively by eliminating network weights that do not have much impact on the problem solution and shows better performance in avoiding the local minima difficulties. Cross validation is not necessary in BR algorithm, which avoids part of training data from being reserved for validation purposes. Also BR algorithm prevents the ANN from over-training and over-fitting problems. Comprehensive details about BR backpropagation algorithm can be found in [17] and [18].

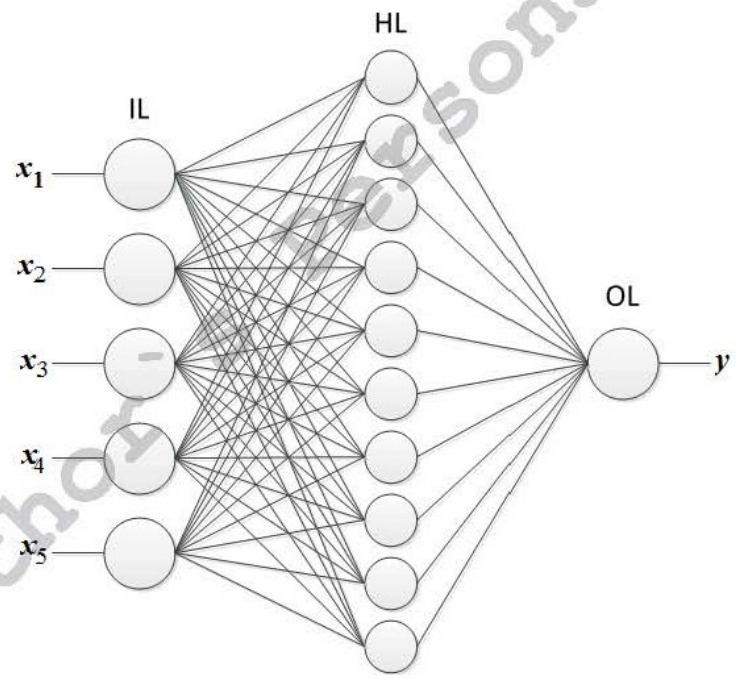

Fig. 5. The proposed ANN architecture (x_1: normalized solar altitude angle, x_2: normalized solar azimuth angle, x_3: normalized angle of incidence, x_4: normalized irradiance, x_5: normalized PV module surface temperature, y: normalized PV module output power, IL: Input Layer, HL: Hidden Layer, OL: Output Layer).

$$\nabla E(w) = \frac{d}{dw}E(w) = \begin{bmatrix} \frac{\partial E}{\partial w_1} \\ \frac{\partial E}{\partial w_2} \\ \cdots \\ \frac{\partial E}{\partial w_N} \end{bmatrix} \tag{16}$$

$$H = \nabla\nabla E(w) = \frac{d^2}{dw^2}E(w) = \begin{bmatrix} \frac{\partial^2 E}{\partial w_1^2} & \frac{\partial^2 E}{\partial w_1 \partial w_2} & \cdots & \frac{\partial^2 E}{\partial w_1 \partial w_N} \\ \frac{\partial^2 E}{\partial w_2 \partial w_1} & \frac{\partial^2 E}{\partial w_2^2} & \cdots & \frac{\partial^2 E}{\partial w_2 \partial w_N} \\ \cdots & \cdots & \cdots & \cdots \\ \frac{\partial^2 E}{\partial w_N \partial w_1} & \frac{\partial^2 E}{\partial w_N \partial w_2} & \cdots & \frac{\partial^2 E}{\partial w_N^2} \end{bmatrix} \tag{17}$$

$$H = J^T J + \mu I \tag{18}$$

$$w_{k+1} = w_k - (J_k^T J_k + \mu I)^{-1} J_k e_k \tag{19}$$

Where,
J : Jacobian matrix (matrix of first derivatives with respect to weight vector)
μ : Combination coefficient
and,
I : Identity matrix.

The training, testing and validation processes of the ANNs are performed on 10695 combinations of data, each combination containing 5 inputs and 1 target output. The normalized values of the solar altitude and azimuth angles, angle of incidence, irradiance and PV module surface temperature are fed to the network through the input layer. The inputs pass through the hidden layer consisting of 10 hidden neurons each having a Tan-Sigmoid transfer function and reach the output layer which contains one neuron with linear transfer function. The estimated output which is in range of 0 to 1 is compared to the learning target output and the error is back-propagated through the network. After several epoch of backpropagation and weight adjustment the training goal is achieved and the network becomes ready to generalize new outputs for unseen inputs.

As mentioned earlier, it is aimed to develop ANNs which are neither under-fitted nor over-fitted. A loose training goal results in a weak network that is not capable of making precise estimations while a very tight training goal will force the network to adjust its weights in order to achieve outputs almost similar to learning targets. Such an over-fitted network provides very accurate results for training inputs but lacks in making generalizations for new and unseen inputs. The Minimum Gradient is set to 1.0e-10 for both ANNs as the training goal in order to achieve accuracy and generalization capabilities at the same time.

In order to create the first ANN, 70% (7487 paths) of the mentioned data collection is allotted to the training process in which the inputs and the output are presented to the ANN and the weight adjustments between the neurons are done based on the LM back-propagation algorithm. Another 15% (1604 paths) of the collected data is presented to the ANN as the validation data to determine the generalization abilities of the network. The rest 15% (1604 paths) of the collected data is given to the network during the testing process, which is carried out independently from the training and validation processes and gives a measure of the network performance. In the testing process, output targets are not presented to the network in order to measure the estimation and generalization abilities of the ANN. The training stops when the validation process show no more generalization.

The same procedure is repeated for construction of the second ANN with BR training backpropagation algorithm. 85% (9091 paths) and 15% (1604 paths) of the collected data is presented to this ANN during the training and testing phases respectively. As mentioned before, validation is unnecessary in the BR algorithm which allows further 1604 paths to be added to the training data. The training stops at a pre-set limit of 1000 epochs.

The regression plots and the performance metrics of the ANNs for the training, validation and testing processes are given in Fig.6 and Table.1 respectively. The performance details of the LM and the BR backpropagation algorithms during the training, testing and validation processes are given in Table. 1 and the Mean Absolute Error (MAE) and the Mean Absolute Percentage Error (MAPE) [1] between the estimated and the measured PV module output power values for ANN implementations from Nov. 26th to Dec 7th, 2015 are given in Table. 2.

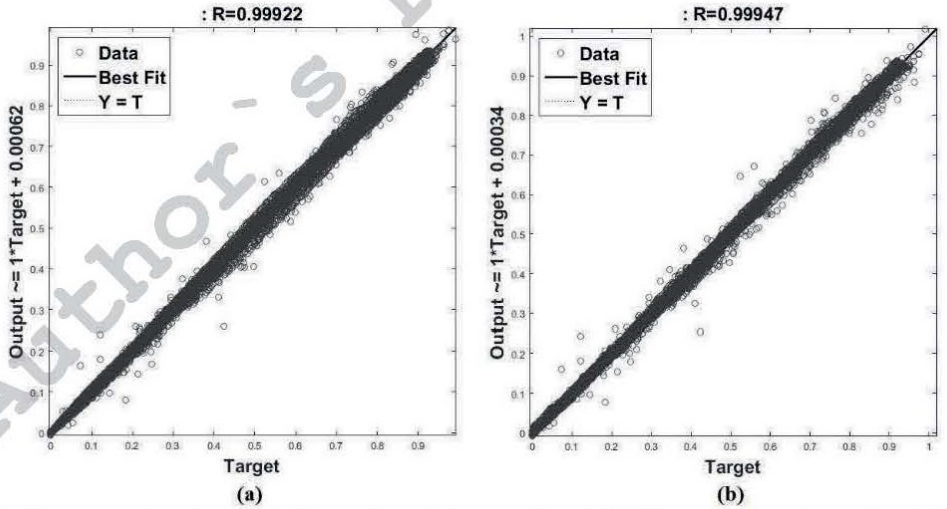

Fig. 6. The regression plots of (a) Levenberg-Marquardt and (b) Bayesian Regularization training backpropagation algorithms.

[1] The noisy data is filtered out in order to maintain reasonable and robust (MAPE) values.

Table 1. Performance metrics of the Levenberg-Marquardt (LM) and the Bayesian Regularization (BR) training backpropagation algorithms.

Performance Metrics	Levenberg-Marquardt (LM) Algorithm	Bayesian Regularization (BR) Algorithm
Best Training Performance	1.2549e-04	1.0211e-04
Best Validation Performance	1.3365e-04	Not applied in BR
Best Testing Performance	1.0787e-04	1.0418e-04
No. of Training Epochs	162	1000
Best Training Epoch	154	1000
Minimum Gradient	6.2957e-06	1.2496e-08
Training Time (in Seconds)	16.27	114.53

Table 2. The Mean Absolute Error (MAE) and the Mean Absolute Percentage Error (MAPE) between the estimated and the measured PV module output power values for different ANN implementation periods.

ANN Implementation Period	Mean Absolute Error(LM) (mW)	Mean Absolute Error(BR) (mW)	Mean Absolute Percentage Error (LM)	Mean Absolute Percentage Error (BR)
November 26th, 2015	1.45	1.42	7.05%	5.87%
November 27th, 2015	1.12	0.94	5.62%	5.43%
November 28th, 2015	1.58	1.04	5.74%	4.54%
November 29th, 2015	1.82	1.29	9.74%	6.28%
December 2nd, 2015	1.7	0.93	7.33%	4.77%
December 7th, 2015	2.16	0.71	3.18%	2.06%

4 Implementation of the Developed Artificial Neural Networks (ANNs)

The ANNs created during the development processes described in section-3 are implemented in a period from Nov. 26th, 2015 to Dec. 7th, 2015. During this period the performances of the ANNs for estimation of PV module output power in different meteorological situations varying from highly fluctuating partly cloudy to smooth clear sky conditions are monitored. In order to better express the performance of each ANN, a scatter graph of the measured vs. the estimated PV module output power values for

each ANN implementation in three different weather conditions on Nov. 26th, Nov. 28th and Dec. 7th, 2015 are given in Fig. 7. As it is obvious from the figures, the ANN trained by the Bayesian Regularization (BR) backpropagation algorithm shows a better performance than the ANN trained by the Levenberg-Marquardt (LM) backpropagation algorithm especially in higher output values. This performance difference was expected since the BR algorithm is known to work well with noisy and difficult data as described in section-3. Although the estimation performance improvements of the BR algorithm may appear to be relatively small for a single PV module application, the improvement becomes definitely significant when the application is extended to broader PV arrays after taking developmental considerations. On the other hand, the higher performance of the BR algorithm comes with a cost. As it is obvious from Table. 2, the training time of the BR algorithm is significantly higher than that of the LM algorithm. The training time of the BR algorithm increases more and more by setting the maximum epoch number to higher limits in order to maintain lower training error. The BR algorithm may not be deployed in time-constrained situations. The PV module output power estimated by the ANN with BR algorithm vs. the measured PV module output power for Nov. 26th, Nov. 28th and Dec. 7th, 2015 are plotted in Fig. 8.

5 Conclusions

The performances of Artificial Neural Networks (ANNs) developed by the Levenberg-Marquardt (LM) and the Bayesian Regularization (BR) training backpropagation algorithms for PV module power estimation are analyzed in this paper. The results show that the BR algorithm provides a better performance than the LM algorithm in PV power estimation, to the cost of higher computation time. The average Mean Absolute Error (MAE) and the Mean Absolute Percentage Error (MAPE) between the estimated and the measured PV module output power values for ANN implementation period from Nov. 26th to Dec. 7th, 2015 are 1.64 (mW) and 6.44% respectively for the LM algorithm, which are reduced to 1.05 (mW) and 4.83% by the BR algorithm. The estimation improvement of BR algorithm is highlighted by the fact that the proposed PV power estimation algorithm can be extended to broader PV fleets after taking necessary developmental considerations. On the other hand the training time of the LM algorithm is 16.27 (s), which is increased to 114.53 (s) by the BR algorithm. The training time of the BR algorithm further increases in order to maintain higher accuracy. Consequently it can be concluded that the BR training backpropagation algorithm presents better performance in ANN based PV power estimation purposes and is the right choice where high accuracy is required but this algorithm is significantly time-consuming and may not be utilized where the training speed is of major concern. The LM algorithm is the proper choice in time-constrained situations.

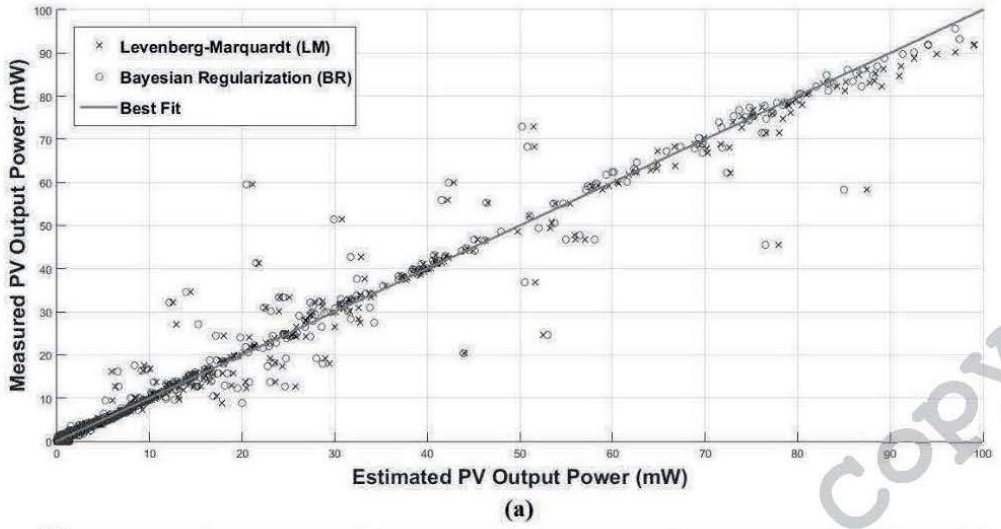

(a)

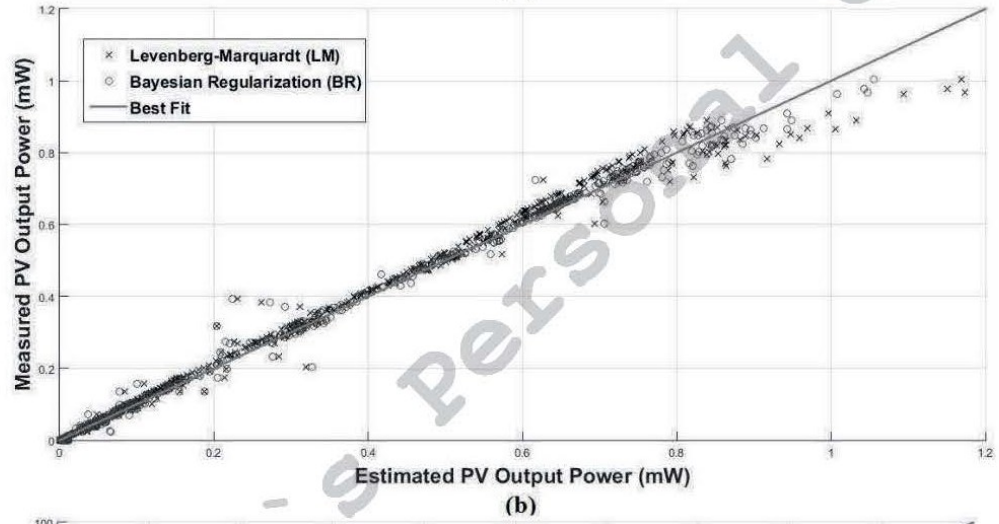

(b)

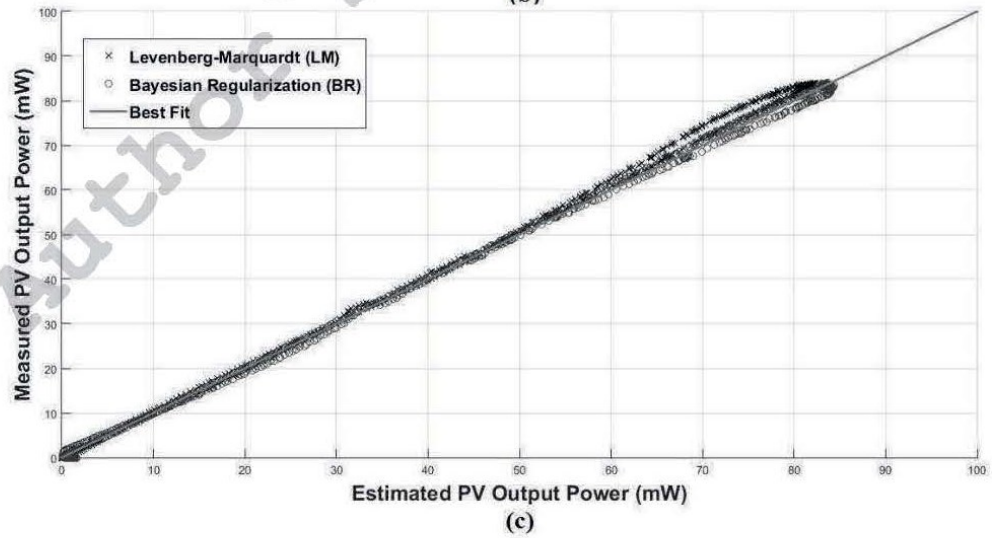

(c)

Fig. 7. The measured vs. the estimated PV module output values for ANNs implemented by the LM and the BR algorithms on (a) November 26th, 2015, (b) November 28th, 2015 and (c) December 7th, 2015.

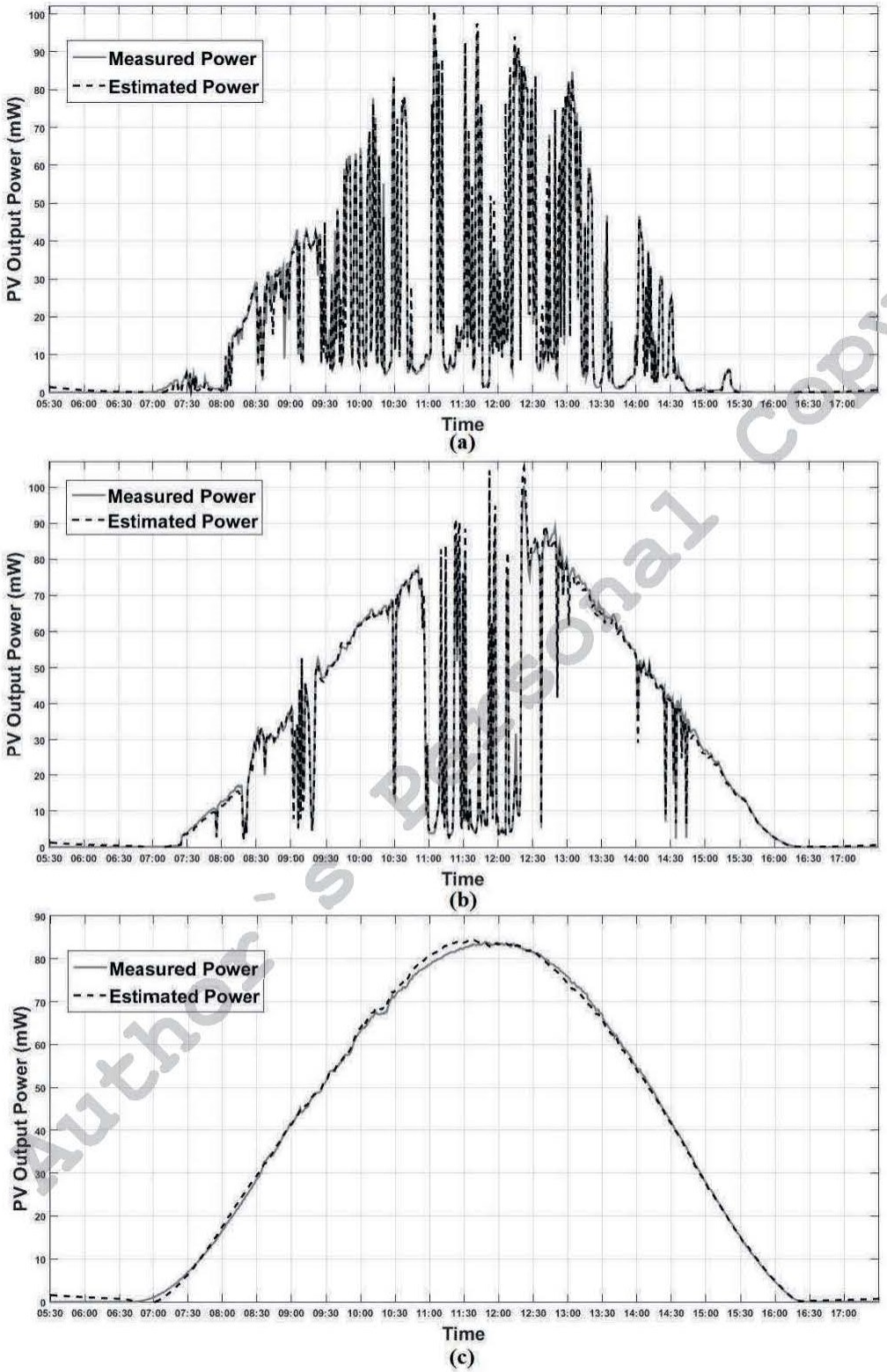

Fig. 8. The measured vs. the estimated PV module output power values for ANN implemented by the BR algorithm on (a) November 26th, 2015, (b) November 28th, 2015 and (c) December 7th, 2015.

References

1. Elizondo D., Hoogenboom G., Mcclendon R.: Development of a Neural Network Model to Predict Daily Solar Radiation. Agric For. Met., Vol. 71, (1994) 115-132
2. Williams D. and Zazueta F.: Solar Radiation Estimation via Neural Network. In Sixth International Conference on Computers in Agriculture, ASAE, Cancun, Mexico (1994) 140-146
3. Alawi S. and Hinai H.: An ANN-Based Approach for Predicting Global Radiation in Locations with No Direct Measurement Instrumentation. Renew. Energy, Vol. 14, (1998) 199-204
4. Mohandes M., Balghonaim A., Kassas M., Rehman S., Halawani T.: Use of Radial Basis Functions for Estimating Monthly Mean Daily Solar Radiation. Sol. Energy, Vol. 68 (2), (2000) 161-168
5. Mihalakakou G., Santamouris M., Asimakopoulos D.: The Total Solar Radiation Time Series Simulation in Athens, Using Neural Network. Theor. Appl. Climatol, Vol. 66, (2000) 185-197
6. Mellit A., Benghanem M., Hadj Arab A., Guessoum A.: Modeling of Global Solar Radiation Data from Sunshine Duration and Temperature Using the Radial Basis Function Networks, In the IASTED, Grindelwald, Switzerland (2004)
7. Lo Brano, V., Ciulla, G., Di Falco, M.: Artificial Neural Networks to Predict the Power Output of a PV Panel. Int. J. Photoenergy, Vol. 2014, (2014) 1-12
8. Saberian, A., Hizam, H., Radzi, M., Kadir, M., Mirzaei, M.: Modelling and Prediction of Photovoltaic Power Output Using Artificial Neural Networks, Int. J. Photoenergy, Vol. 2014, (2014) 1-10
9. Payal A., Rai C., Reddy B.: Comparative Analysis of Bayesian Regularization and Levenberg-Marquardt Training Algorithmfor Localization in Wireless Sensor Network, In 15th International Conference on Advanced Communication Technology (ICACT), PyeongChang, South Korea, (2013) 191-194
10. Wang W., Gelder P., Vrijling J.: Comparing Bayesian Regularization and Cross-Validated Early-Stopping for Streamflow Forecasting with ANN Models, In 2nd International Symposium on Methodology in Hydrology, Nanjing, China, (2005) 216-221
11. Tiwari S., Naresh R., Jha R.: Comparative Study of Backpropagation Algorithms in Neural Network Based Identification of Power System. Int. J. of Comput. Sci. and Inform. Tech., Vol 5(4), (2013) 93-107
12. Scharmer K., and Greif J.: The European Solar Radiation Atlas, Vol.1: Fundamentals and Maps, Paris, France: Les Presses de l`Ecole des Mines, (2000) 23-42
13. Luque A. and Hegedus S.: Handbook of Photovoltaics Science and Engineering, West Sussex, UK: Wiley, (2003) 906-912
14. Wilamowski B. and Yu H.: Improved Computation for Levenberg-Marquardt Training. IEEE Trans. on Neural Networks, Vol. 21, (2010) 930-937
15. Levenberg K.: A method for the solution of certain problems in least-squares, Quart. Appl. Math., Vol. 2, (1944) 164-168
16. Marquardt D.: An Algorithm for least-Squares Estimation of Non-Linear Parameters. J. of the Soc. For Ind. and Appl. Math., Vol. 11, (1963) 431-441
17. MacKay D.: Bayesian Interpolation. Neural Computation, Vol. 4(3), (1992), 448-472.
18. Buntine W. and Weigend A.: Bayesian Backpropagation. Complex Systems, Vol. 5, (1991) 603-643

Appendix E: A Comparative Study on Different Photovoltaic Array Topologies under Partial Shading Conditions

Moein Jazayeri, Sener Uysal, Kian Jazayeri, "A comparative study on different photovoltaic array topologies under partial shading conditions", in *Proceedings - IEEE PES T&D Conference and Exposition*, Chicago, IL, USA, 2014.

***Abstract*—This paper mainly analyzes the performance of different photovoltaic array configurations under various shading patterns. A Matlab/Simulink based simulation model of a PV module is utilized as the smallest building block of the mentioned topologies. The model is validated using the datasheet parameters of the `SOLAREX MSX-60` PV module. The performance and output characteristics of `Series-Parallel`, `Total-Cross-Tied` and `Bridge-Link` array topologies are analyzed and compared using a 6x6 PV array under 6 different shading scenarios. The effects of bypass diodes during partial shading conditions are considered and the analysis results are presented and compared with and without bypass diodes. The mentioned shading scenarios are defined in such a way to simulate the passage of a cloud in different patterns. The results show that all the mentioned topologies have similar performances under identical illuminations while the `Total-Cross-Tied` (TCT) configuration, despite the high complexity of the system, outperforms both `Series-Parallel` (SP) and `Bridge-Link` (BL) structures under partial shading conditions. `Bridge-Link` and `Series-Parallel` configurations stand on the 2nd and 3rd performance stages respectively while a Series-Parallel connection presents the least system complexity. The analyses and results provide detailed information on the characteristics of different array topologies which can be utilized by system designers to estimate the power yield and choose the most appropriate system configuration with respect to the existing environmental conditions to improve the overall efficiency.**

***Keywords*—array configuration, bridge-link, module characteristics, series-parallel simulink, solar cell, solar energy, solar module, total-cross-tied,**

A Comparative Study on Different Photovoltaic Array Topologies under Partial Shading Conditions

Moein Jazayeri, Sener Uysal, *Member, IEEE,* Kian Jazayeri

Electrical and Electronic Engineering Department, Eastern Mediterranean University

Famagusta, North Cyprus, via Mersin 10 Turkey

moein.jazayeri@cc.emu.edu.tr

sener.uysal@emu.edu.tr

kian.jazayeri@cc.emu.edu.tr

***Abstract*—This paper mainly analyzes the performance of different photovoltaic array configurations under various shading patterns. A Matlab/Simulink based simulation model of a PV module is utilized as the smallest building block of the mentioned topologies. The model is validated using the datasheet parameters of the `SOLAREX MSX-60` PV module. The performance and output characteristics of `Series-Parallel`, `Total-Cross-Tied` and `Bridge-Link` array topologies are analyzed and compared using a 6x6 PV array under 6 different shading scenarios. The effects of bypass diodes during partial shading conditions are considered and the analysis results are presented and compared with and without bypass diodes. The mentioned shading scenarios are defined in such a way to simulate the passage of a cloud in different patterns. The results show that all the mentioned topologies have similar performances under identical illuminations while the `Total-Cross-Tied` (TCT) configuration, despite the high complexity of the system, outperforms both `Series-Parallel` (SP) and `Bridge-Link` (BL) structures under partial shading conditions. `Bridge-Link` and `Series-Parallel` configurations stand on the 2nd and 3rd performance stages respectively while a Series-Parallel connection presents the least system complexity. The analyses and results provide detailed information on the characteristics of different array topologies which can be utilized by system designers to estimate the power yield and choose the most appropriate system configuration with respect to the existing environmental conditions to improve the overall efficiency.**

Keywords—array configuration, bridge-link, module characteristics, series-parallel simulink, solar cell, solar energy, solar module, total-cross-tied,

I. INTRODUCTION

The infinite, renewable, clean and noiseless nature of the solar energy makes it one of the most preferred sources of renewable energies which is increasingly finding application areas in today`s human life. However, despite of the mentioned advantages, this clean energy source has some disadvantages which should be overcome for an efficient use. Relatively high production costs of PV panels, unavailability of economically efficient energy storage devices and high dependency of energy production on the environmental conditions are some of the main disadvantages. As one of the main factors, the amount of energy produced by solar panels strongly depends on the incident solar irradiance on the panel surface. The amount of energy production is subjected to variations as the received solar irradiance is not constant at any time instance. This variation may be caused by the variations of the position of the sun in the sky during a day or shading effects caused by passing clouds, neighboring houses, etc. Partial or full shading of solar modules caused by any reason has a direct effect on their output power. When it is extended to large-scale PV plants, these kinds of effects may cause big amounts of economic losses and reduce the overall efficiency of the systems. Therefore, estimation of the power yield under different environmental conditions and finding methods to overcome the negative effects of the mentioned conditions and finally improving the efficiency of the PV generation systems has been considered by many researchers during the recent years.

Estimation of power yield under various shading conditions and developing methods to prevent power losses or decrease the negative effects of shading are the most important two stages which should be taken into consideration to improve the system efficiency.

Mathematical modeling of solar cells has been one of the most preferred methods to investigate the characteristics of PV systems under different environmental conditions. Solar cells are the smallest building blocks of any PV generation system and hence a cell based analysis can be extended to the desired system applications.

Various models have been proposed by researchers to investigate the characteristics of solar cells. Single-Diode model [1-2], R_s-model [3-4], R_P-model [5-6] and two-diode models [7-9] of a solar cell have been the most widely utilized models to investigate the behaviors of a solar cell. The one-diode model of a solar cell is the simplest model which has been utilized by many researchers and also forms the basis of the analyses in this study.

As it was mentioned earlier, the second stage to improve the efficiency of a system is to find methods to decrease the negative effects of the environmental factors. Appropriate design of PV array configurations has shown significant improvements on the overall system performance. In this manner, `Series-Parallel`, `Total-Cross-Tied` and `Bridge-Link` configurations are the most preferred array topologies [10-12].

The characteristics of PV arrays with the mentioned configurations are analyzed and compared under 6 different shading scenarios. Each of the mentioned scenarios represents

978-1-4799-3656-4/14/$31.00 ©2014 IEEE

a passing cloud with different characteristics. A Matlab/Simulink based simulation model of a solar cell is utilized to construct each of the mentioned array configurations. Also the use of bypass diodes is considered in order to take the effects of partial shading on arrays performances into account.

II. MODELING OF THE PV ARRAY

Output characteristics of PV arrays with Series-Parallel, Total-Cross-Tied and Bridge-Link configurations are analyzed and compared in this paper. The mentioned arrays consist of 36 PV modules in a 6x6 array configuration and the one-diode mathematical model of a solar cell is utilized to simulate each module. This model is used due to its simplicity and wide application area. The equivalent electrical circuit of the one-diode model of a solar cell is illustrated in Fig. 1. As it is obvious from the figure, the model consists of a current source, a diode, a parallel resistance expressing the leakage current and a series resistance representing the internal resistance of a solar cell.

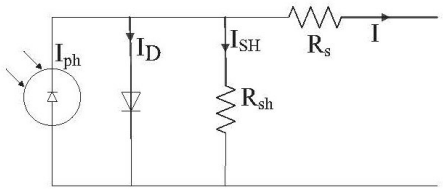

Fig. 1. Equivalent One-Diode Circuit of a Solar Cell

The one-diode model of a solar cell defines the voltage – current relationship of the cell using the following equation,

$$I = I_{ph} - I_S\left(exp\frac{q(V + R_S I)}{nkT} - 1\right) - \frac{(V + R_S I)}{R_{SH}} \quad (1)$$

Where;

I_{ph} : Photocurrent (A)

I_S : Diode Saturation Current (A)

q : Electron Charge ($1.60217646 \times 10^{-19}$ C)

n : Diode Ideality Factor

k : Boltzmann Constant ($1.3806503 \times 10^{-23}$ J/K)

T : Temperature of the p-n Junction (K)

R_S : Series Resistance (Ω)

R_{SH} : Shunt Resistance (Ω)

The open-circuit voltage, (V_{oc}), short-circuit current, (I_{sc}), maximum power point, (P_{max}), current and voltage at the maximum power point, (V_{mp}) and (I_{mp}), are generally provided in the manufacturer's datasheet under Standard Test Conditions (STC). According to (1), I_{ph}, I_S, n, R_s and R_{sh} are the 5 unknown parameters to be determined by the simulation model.

A Matlab/Simulink based simulation model of a solar module forms the basis for the analyses of this paper. The model is validated using datasheet parameters of SOLAREX MSX-60 solar panel. The simulated I-V and P-V curves, under STC, are illustrated in Fig. 2 and the numerical results are tabulated and compared in Table I. The characteristic curves and provided numerical data clearly show that the simulation model has the capability for accurate modeling of the module characteristics. The structures of the simulation models for the mentioned three topologies are presented in Fig. 3. The block diagram of each individual module is shown in Fig. 4 where the inputs to each individual module are datasheet parameter values along with the temperature, irradiance and number of series and parallel connected cells in the module.

TABLE I. SOLAREX MSX-60 MODULE SIMULATED PARAMETERS

Parameter	Simulated Value	Datasheet Value
P_{max}	60 W	60 W
V_{oc}	20.93 V	21.1 V
I_{sc}	3.8 A	3.8 A
V_{mp}	17.09 V	17.1 V
I_{mp}	3.51 A	3.5 A

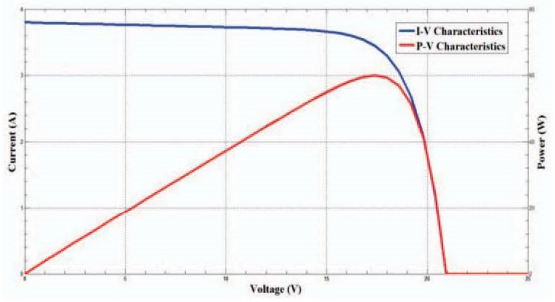

Fig. 2. Simulated I-V and P-V Curves for SOLAREX MSX-60 Panel

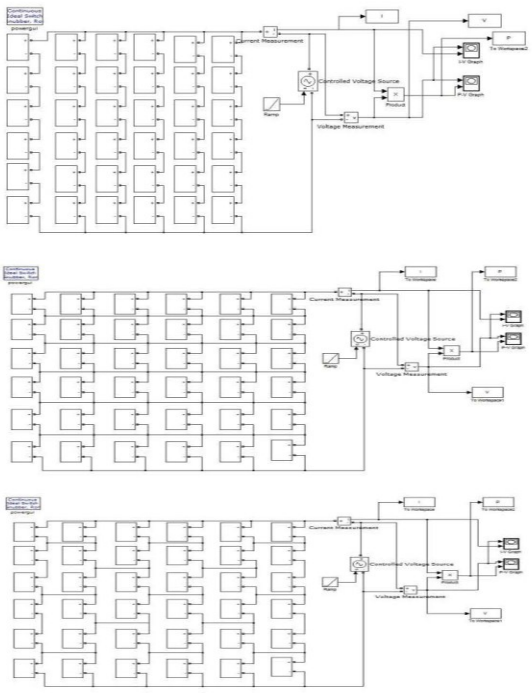

Fig. 3. PV array simulation model for a)Series-Parallel b)Total-Cross-Tied c) Bridge-Link configurations

It is obvious that Total-Cross-Tied and Bridge-Link configurations include some additional connections with respect to the Series-Parallel case. In a Series-Parallel structure, the series connected module strings are connected in parallel to form a Series-Parallel configuration. The Total-Cross-Tied configuration, as the most complex structure type, connects each individual module in series and parallel with the other one at the same time. The number of connections is reduced to half of the TCT configuration in a Bridge-Link structure. The simulated I-V and P-V characteristics for the mentioned topologies under identical illumination conditions are illustrated in Fig. 5.

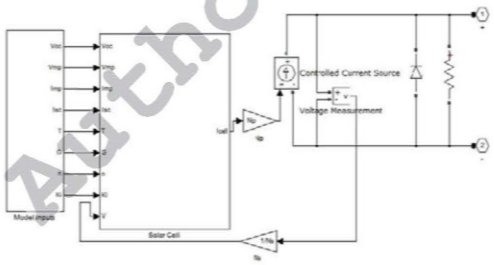

Fig. 4. Block diagrams of a solar cell simulation model

III. MODELING OF PARTIAL SHADING EFFECST

The main focus of this paper is to analyze and investigate the performance of different array topologies under variable shading scenarios. Six different shading patterns, as shown in Fig. 6 are defined to represent the passage of a cloud over the PV array. Each pattern consists of three different irradiance levels, namely 200 W/m^2, 600 W/m^2 and 1000 W/m^2 to represent the most darkness cloud center, more clear cloud edge and full illumination conditions, respectively. The mentioned shading scenarios can be described as follows,

- 1st Shading Scenario: The cloud center is located over the corner of the PV array and covers 4 modules while there are 12 modules illuminated with 600 W/m^2 and 16 modules fully illuminated with 1000 W/m^2.
- 2nd Shading Scenario: The cloud enters the array from the bottom. The cloud center covers two rows (12 modules) while two rows are partially shaded with 600 W/m^2 and the remaining two rows are fully illuminated.
- 3rd Shading Scenario: The cloud enters from the left side of the array. The cloud center covers two columns (12 modules) while two columns are illuminated with 600 W/m^2 and the remaining two columns are fully illuminated.
- 4th Shading Scenario: The cloud enters from top of the array, The first two rows (12 modules) are covered by the cloud center, two rows are illuminated with 600 W/m^2 and the remainnig two rows are fully illuminated with 1000 W/m^2.
- 5th Shading Scenario: The cloud center covers 4 modules at the middle of the array while 12 modules are illuminated with 600 W/m^2 and 20 modules are fully illuminated with 1000 W/m^2.

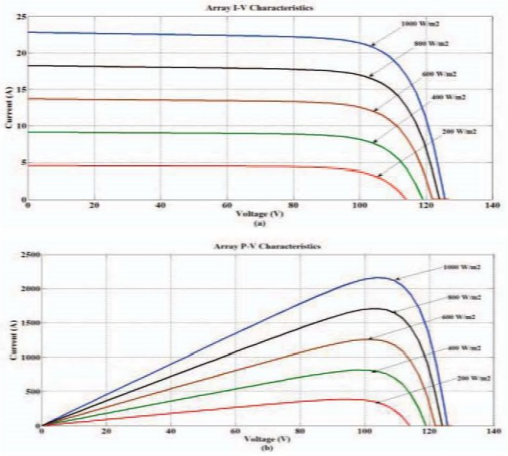

Fig. 5. Simulated array a) I-V and b) P-V characteristiscs under identical illumination

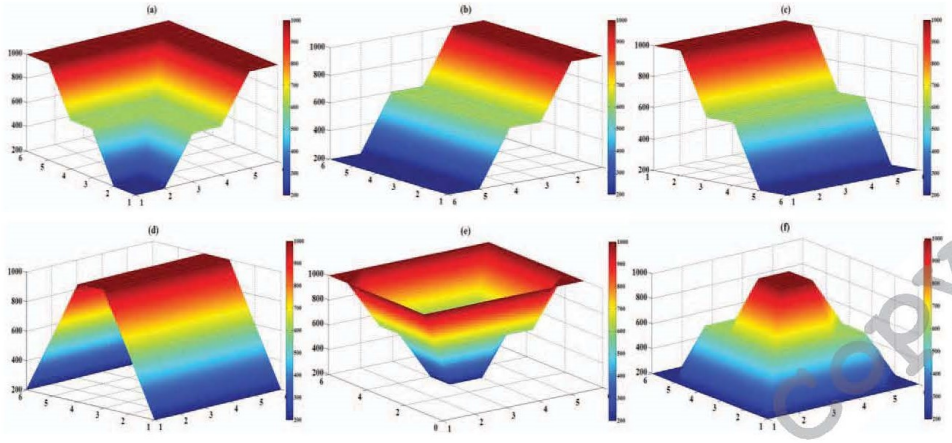

Fig. 6. Different array shading scenarios

- 6th Shading Scenario: The 4 modules at the center of the array are fully illuminated while 12 surrounding modules are illuminated with 600 W/m^2 and the outer 20 modules are fully illuminated with 1000 W/m^2.

IV. Simulation Results

The output characteristics of the mentioned three array topologies under identical illumination are illustrated in Fig. 5. The results show that all the mentioned configurations have similar output characteristics under identical illumination. The P-V characteristics of the mentioned array topologies under 6 predefined partial shading patterns are illustrated in Fig. 7. The characteristics are obtained considering the effects of bypass diodes. According to the results, the mentioned topologies represent similar characteristics in the presence of the same number of modules receiving the same values of solar irradiance (Scenarios No.2,3&4). At the same it is observed that in the 3rd scenario the bypass diodes have not affected the P-V characteristics due to the presence of complete columns illuminated with identical solar irradiance values. The effects of the bypass diodes are clearly visible in the P-V curves of the array under the 1st, 5th and 6th shading scenarios. These effects are caused by modules with different irradiance values in the same column of the array. It is also observed that the Total-Cross-Tied topology outperforms the Series-Parallel and Bridge-Link configurations under the mentioned shading scenarios. It is obvious that the Bridge-Link configuration has the second higher performance after the TCT topology. The disadvatnge of the TCT topology with respect to the Series-Parallel configuration is the high number of switching devices and complex wiring while the number of connections in the Bridge-Link topology has been reduced to the half of the TCT design. A comparison of the P_{max} values of the three topologies, with and without bypass diodes, under the mentioned shading scenarios is presented in Fig. 8.

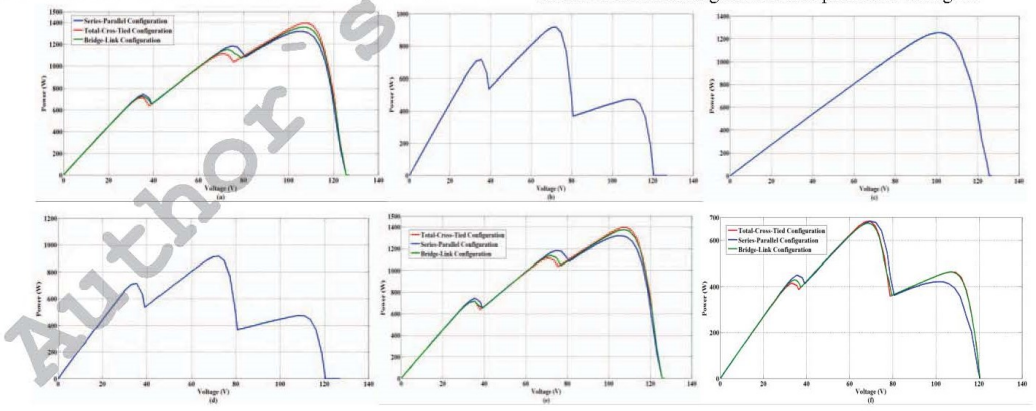

Fig. 7. Array P-V characteristics under a) 1st shading scenario, b) 2nd shading scenario, c) 3rd shading scenario, d) 4th shading scenario, e) 5th shading scenario, f) 6th shading scenario

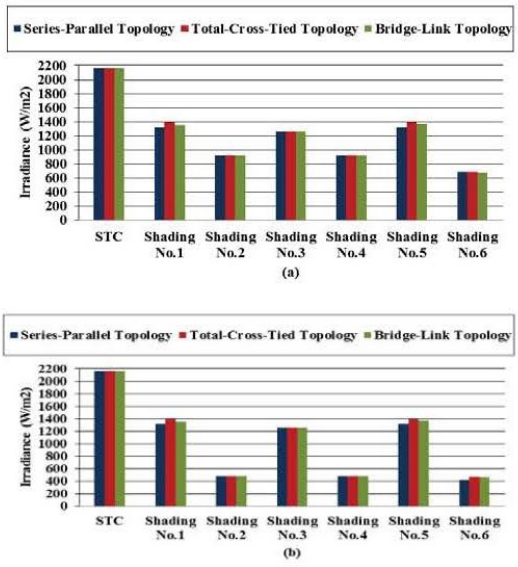

Fig. 8. P-V characteristics for three different array topologies a) with bypass diodes b) without bypass diodes

The graphics clearly highlight the effects of application of bypass diodes. It is observed that bypass diodes have a great improvement, specially in the 2nd, 4th and 6th shading scenarios where application of bypass diodes have increasing effects in the P_{max} values up to 93.41% and 61.60% under the 2nd (the same as the 4th) and the 6th shading scenarios. According to the results the Total-Cross-Tied and Bridge-Link configurations have improved the amount of P_{max} by 5.84% and 2.8% compared with the Series-Parallel topology under the 1st and 5th shading scenarios, respectively. It is also observed that, in the absence of bypass diodes, the amount of P_{max} has been increased by 10% and 9% in TCT and BL topologies respectively. The P_{max} values of the mentioned topologies under the 2nd, 3rd and 4th shading scenarios are almost similar due to the existence of the same number of identically illuminated modules.

According to the results, the TCT configuration has presented the best performance under non-identical partial shading conditions and it can be estimated that, beside its design complexities, it will be advantageous in the presence of more complex shading patterns under real environmental conditions.

V. Conclusions

Different system topologies are utilized in PV generation plants to improve the overall system efficiency. Series-Parallel, Total-Cross-Tied and Bridge-Link configurations are the most widely used PV array topologies in order to reduce the negative effects of partial shadings mostly caused by passing clouds. A Matlab/SIMULINK based simulation model of a solar module has been utilized to analyze and compare the performances of each configuration type in a 6x6 sized PV array. Six different shading scenarios are defined to present a cloud passage and also the use of bypass diodes is considered and the results are analyzed with and without the mentioned bypass diodes.

The results indicate that the TCT configuration outperforms the other two system topologies under all partial shading conditions. The mentioned topology has been able to increase the array`s P_{max} value up to 5.84% with bypass diodes and up to 10% without application of bypass diodes. The amount of improvement obtained using a Bridge-Link topology has been 2.8% and 9% respectively with and without application of bypass diodes. It is also observed that all the mentioned system topologies have similar performances under identical illumination conditions.

The results provide useful and reliable information on the performance of array topologies under changing shading conditions and can be utilized during system design to improve the overall efficiency of the PV system.

References

[1] Y.T. Tan, D.S. Kirchen and N. Jenkins, "A model of PV generation suitable for stability analysis," *IEEE Trans. Energy Convers.*, vol.19, no.4, pp.748-755, Dec. 2004.

[2] A. Kajihara and A.T. Harakawa, "Model of photovoltaic cell circuits under partial shading," *Proc. IEEE Int. Conf. Ind. Technol. (ICIT)*, Hong Kong, 2005, pp.866-870.

[3] W. Xiao, W.G. Dunford and A. Capel, "A novel modeling method for photovoltaic cells", *Proc. IEEE 35th Annu. Power Electron. Spec. Conf. (PESC)*, Vol.3, 2004, pp.1950-1956

[4] N. Celik and N. Acikgoz, "Modeling and experimental verification of the operating current of mono-crystalline photovoltaic modules using four- and five-parameter models," *Appl. Energy J.*, vol.84, no.1, 2007, pp.1-15

[5] C. Carrero, J. Amador and S. Arnaltes, "A single procedure for helping PV designers to select silicon PV module and evaluate the loss resistances," *Renewable Energy J.*, vol.32, no.15, 2007, pp.2579-2589

[6] M.G. Villalva, J.R. Gazoli and E.R. Filho, "Comprehensive approach to modeling and simulation of photovoltaic arrays," *IEEE Trans. Power Electron.*, vol.24, no.5, pp.1198-1208, May. 2009.

[7] J.A. Gow and C.D. Manning, "Development of a photovoltaic array model for use in power-electronics simulation studies," *IEE Proc. Elect. Power Appl.*, vol.146, no.2, pp.193-200, 1999.

[8] J.A. Gow and C.D. Manning, "Development of a photovoltaic array model for use in simulation studies of solar energy conversion systems," *Proc. 6th Int. Conf. Power Electron. Variable Speed Drives.*, 1996, pp.69-74

[9] S. Chowdhury, G. A. Taylor, S. P. Chowdhury, A. K. Saha and Y. H. Song, "Modelling, simulation and performance analysis of a PV array in an embedded environment," *Proc. 42nd Int. Univ. Power Eng. Conf. (UPEC)*, 2007, pp.781-785

[10] R.Ramaprabha and B.L.Mathur, "A comprehensive review and analysis of solar photovoltaic array configurations under partial shaded conditions," *Intl. J. Photoenergy*, vol.2012, 2012, pp.1-16

[11] D.Picault, B.Raison, S.Bacha, J.De la Casa and J.Aguilera, "Forecasting photovoltaic array power production subject to mismatch losses," *Solar Energy*, vol.84, 2010, pp.1301-1309

[12] D.Picault, B.Raison, S.Bacha, J.Aguilera and J. De La Casa, "Changing photovoltaic array interconnections to reduce mismatch losses: a case study", Proc. EEEIC 2010, Prague, Czech Republic, 2010

Appendix F: Evaluation of Maximum Power Point Tracking Techniques in PV Systems Using MATLAB/Simulink

Moein Jazayeri, Sener Uysal, Kian Jazayeri, "Evaluation of Maximum Power Point Tracking Techniques in PV Systems Using MATLAB/Simulink", in *Proceedings - Sixth Annual IEEE Green Technologies Conference*, Corpus Christi, TX, USA, 2014.

***Abstract*— This paper mainly focuses on the performance evaluation of "Perturb&Observe" and "Incremental Conductance" algorithms as the most commonly utilized two Maximum Power Point Tracking (MPPT) techniques for photovoltaic systems. Matlab/SIMULINK platform is used to model and simulate the entire system. The simulation model of a PV module is constructed based on the one-diode mathematical model of a solar cell and the model is validated using the manufacturer`s datasheet parameters for a commercially available PV module. A boost type DC/DC converter topology is utilized and modeled and simulation models for "P&O" and "IncCond" algorithms are constructed. According to the results, both of the algorithms have shown almost similar performances under identical test conditions. Despite its relatively high complexity, the IncCond algorithm has been slightly more efficient and has reached to the MPP in a shorter time period, while most probably the simple structure of the P&O algorithm has caused it to be the most preferred MPPT algorithm. The paper provides reliable information on the performance and characteristics of the mentioned two MPPT techniques which can be used by system designers to improve the overall efficiency and reduce the cost of PV system applications.**

Keywords- DC/DC converter, boost converter, incremental conductance, MPPT, perturb&observe, PV module, solar energy, solar cell.

2014 Sixth Annual IEEE Green Technologies Conference

Evaluation of Maximum Power Point Tracking Techniques in PV Systems using MATLAB/Simulink

Moein Jazayeri, Sener Uysal, *Member, IEEE*, Kian Jazayeri
Electrical and Electronic Engineering Department
Eastern Mediterranean University
Famagusta, North Cyprus, via Mersin 10 Turkey
moein.jazayeri@cc.emu.edu.tr
sener.uysal@emu.edu.tr
kian.jazayeri@cc.emu.edu.tr

***Abstract*— This paper mainly focuses on the performance evaluation of "Perturb&Observe" and "Incremental Conductance" algorithms as the most commonly utilized two Maximum Power Point Tracking (MPPT) techniques for photovoltaic systems. Matlab/SIMULINK platform is used to model and simulate the entire system. The simulation model of a PV module is constructed based on the one-diode mathematical model of a solar cell and the model is validated using the manufacturer`s datasheet parameters for a commercially available PV module. A boost type DC/DC converter topology is utilized and modeled and simulation models for "P&O" and "IncCond" algorithms are constructed. According to the results, both of the algorithms have shown almost similar performances under identical test conditions. Despite its relatively high complexity, the IncCond algorithm has been slightly more efficient and has reached to the MPP in a shorter time period, while most probably the simple structure of the P&O algorithm has caused it to be the most preferred MPPT algorithm. The paper provides reliable information on the performance and characteristics of the mentioned two MPPT techniques which can be used by system designers to improve the overall efficiency and reduce the cost of PV system applications.**

Keywords- DC/DC converter, boost converter, incremental conductance, MPPT, perturb&observe, PV module, solar energy, solar cell.

I. INTRODUCTION

Solar cells first entered human`s life in 1883 [1] and the clean nature of this huge energy source in parallel with the noiseless operation and long lifetime of the systems have all been forming the reasons for investments in this field. However, despite the mentioned advantages, there are still some disadvantages which form barriers for a wide use of this clean and sustainable energy source. Relatively high production and installation costs, leakage of economically efficient energy storage devices and relatively low energy production efficiency are all the disadvantages that should be overcome for a wide and efficient use of this energy source. Fortunately, due to the mass production techniques in the recent years, the cost trend has become downward and the researches show that PV energy is becoming cost competitive and will be available for a wider use in the near future.

In general, the energy production in PV modules, regardless their manufacturing technology, energy conversion efficiency, etc., highly depends on the environmental conditions. The fluctuations in the amount of received solar irradiance, mostly caused by passing clouds, dramatically affect the module characteristics and change the amount of electrical current production by the module. The mentioned variations in the amount of electrical power generated by PV systems cause their efficiencies to be reduced and therefore larger systems are required to produce the desired amounts of electrical power. Taking the mentioned negative effects into the consideration, development and application of appropriate methods to enhance the energy production by the systems earns a great importance for an efficient use of solar energy generation systems. MPPT as one of the mentioned methods has been subjected to many research projects and various techniques have been proposed by researchers [2-4]. Despite the differences in their performance and working principles, the common purpose of the mentioned techniques is to extract the maximum power from PV modules under variable environmental conditions by operating them at their maximum power point.

Perturb and Observe (P&O) methods are most widely preferred MPPT techniques due to their simplicity and effectiveness. The algorithm basically compares the PV power before and after perturbation of the control parameter and decides on the next perturbation. However, the fixed perturbation step size in the conventional P&O method causes these methods to suffer from oscillations around MPP. Larger perturbation steps increase oscillations while smaller perturbation steps decrease the MPPT speed. Utilization of variable perturbation steps have proposed by many researchers [5,6] to reduce the oscillation problem and hence improve the MPPT efficiency. Also various approaches have been introduced to handle the oscillation problem around the MPP [7-9] while smoother steady-state conditions are obtained in [10].

Also utilization of artificial intelligence approaches such as fuzzy logic controller [11] and neural networks [12] has been considered by many researchers. The mentioned

978-1-4799-3934-3/14 $31.00 © 2014 IEEE
DOI 10.1109/GREENTECH.2014.21

methods have also shown high performances while extensive computation requirements are the main disadvantages of these techniques. As an example, dealing with the fuzzification, rule base storage, inference mechanism and difuzzification operations is the main disadvantage of FLC while the requirement of neural network based techniques to large amount of training data is known to be their main handicap [7]. Unlike the modified or adaptive P&O techniques, the mentioned disadvantages cause artificial intelligence approaches to be inappropriate for use in low-power applications [13].

DC/DC converters are the means by which in many MPPT applications the maximum power point tracker maintains the module at its maximum power point voltage, (V_{mp}), to extract the maximum power. Buck, Boost and Buck-Boost converters are mostly used in photovoltaic MPPT systems [14].

The maximum power available from the panels varies with respect to the amount of the received solar irradiance on the panel surface. Therefore, the power yield from the panels should be estimated or calculated for an appropriate system design. Mathematical modeling of solar panels is a method which is widely utilized by researchers to estimate the power yield of the modules. Various numbers of models have been proposed to estimate the module characteristics under different environmental conditions. Single-Diode model [15,16], R_s-model [17,18], R_P-model [19,20] and two-diode models [21,22] of a solar cell have mostly been utilized by researchers.

This paper evaluates the performance of P&O and IncCond MPPT algorithms as the two most commonly used techniques. The one-diode mathematical model of a solar cell is used to simulate the characteristics of the PV module due to its simplicity and a boost type DC/DC converter is utilized where the main criteria on the selection of this topology has been the suitability of this converter for grid connected applications.

II. MAXIMUM POWER POINT TRACKING

As previously mentioned, development of methods for efficiency improvement has been considered by many researchers and various numbers of MPPT techniques have been proposed. The common working principle of these techniques is that all of them improve the system efficiency by operating the PV system at its maximum power point (P_{max}). P&O and IncCond have the greatest application area among the mentioned methods. The operation principle of these two techniques is briefly presented in this part of the study.

A. Perturb & Observe Method

Perturb&Observe method is one of the "Hill-Climbing" MPPT techniques. This technique tracks the module's maximum power point with respect to the sign of dP/dV. The sign of dP/dV on module's P-V curve is illustrated in Fig. 1. As it is obvious from the figure, dP/dV>0 for operating points on the left side of the maximum power point and dP/dV<0 for the operating points on the right side. The algorithm perturbs the voltage by a constant value and observes the variations in dP/dV. If dP/dV>0, the perturbation is in a correct direction and it continues to reach the maximum power point. If dP/dV<0, it means that the operation point is getting far from the maximum power point and hence the next perturbation will be in the reverse direction. The procedure continues until the maximum power point is reached, meaning that the module operates at V_{mp} point. This method is most probably the most preferred MPPT technique in the literature due to its simplicity and high tracking efficiency while oscillations around the maximum power point and low tracking efficiency under rapidly changing solar irradiance conditions are the most well-known disadvantages of this technique [2]. The reported efficiency for this technique in the literature has been over 90%. The flowchart of the P&O algorithm is shown in Fig. 2.

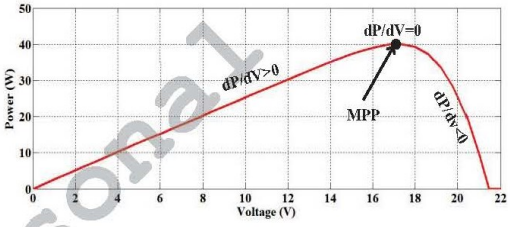

Figure 1. Sign of dP/dV on module P-V characteristics curve

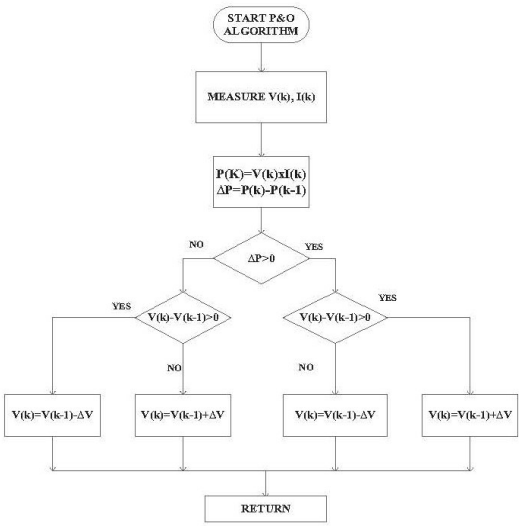

Figure 2. Flowchart of the P&O MPPT algorithm

B. Incremental Conductance Method

The Incremental Conductance method is another Hill-Climbing method which is introduced as an improvement to the P&O algorithm. This algorithm tracks the maximum power point by comparing the module's instantaneous I-V characteristics and its incremental conductances (dI/dV) using the following equations,

$$\frac{dP}{dV} = \frac{d(VI)}{dV} = V\frac{dI}{dV} + I \tag{1}$$

$$\left.\frac{dP}{dV}\right|_{\substack{I=I_{mp}\\V=V_{mp}}} = 0 \Rightarrow \left.\frac{dI}{dV}\right|_{\substack{I=I_{mp}\\V=V_{mp}}} = -\frac{I_{mp}}{V_{mp}} \tag{2}$$

This algorithm has the ability to determine the distance to the maximum power point and hence stop the perturbation and tracking procedure after reaching the MPP [23].

Because of the mentioned property this algorithm theoretically reduces the oscillations around the MPP. Practically it is observed that still oscillations exist around the MPP as (2) is not always completely achieved. Though higher accuracies are reported with respect to the P&O algorithm [3], this algorithm still has low tracking efficiency under fast changing environmental conditions. The flowchart of the IncCond algorithm is illustrated in Fig. 3.

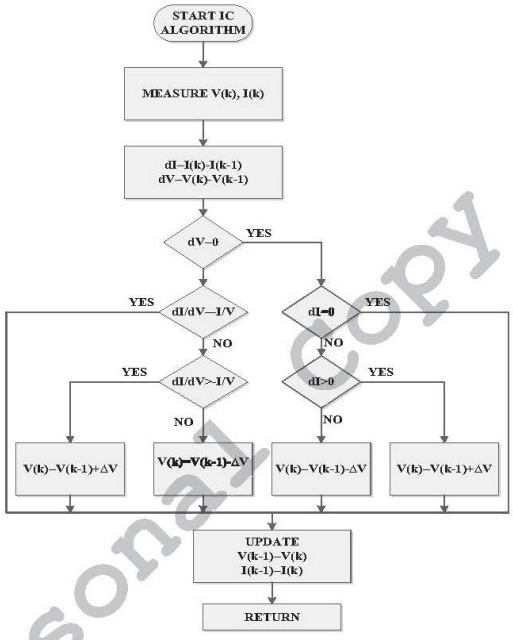

Figure 3. Flowchart of the Incremental Conductance MPPT algorithm

III. Modeling of System Components

Different components of the constructed simulation model for MPPT algorithm performance evaluation are described in this part of the study. A general overview of the simulation model is illustrated in Fig. 4. As it is seen from the figure, the PV module, MPPT algorithm, PWM generator and DC/DC converter are the main components of the system.

A. Modeling of the PV Module

The one-diode mathematical model of a solar cell is used to simulate the PV module. The model is preferred due to its simplicity and wide application area. The equivalent electrical circuit of the one-diode model of a solar cell is presented in Fig. 5. The one-diode model of a solar cell defines the voltage – current relationship of the cell using the following equation,

$$I = I_{ph} - I_s\left(\exp\frac{q(V + R_S I)}{nkT} - 1\right) - \frac{(V + R_S I)}{R_{SH}} \tag{3}$$

Where;

I_{ph} : Photocurrent (A)
I_S : Diode Saturation Current (A)
n : Diode Ideality Factor
k : Boltzmann Constant ($1.3806503 \times 10^{-23}$ J/K)
T : Temperature of the p-n Junction (K)
R_S : Series Resistance (Ω)
R_{SH} : Shunt Resistance (Ω)

The open-circuit voltage, (V_{oc}), short-circuit current, (I_{sc}), maximum power point, (P_{max}), current and voltage at the maximum power point, (V_{mp}) and (I_{mp}), are generally provided in the manufacturer's datasheet under Standard Test Conditions (STC). According to (1), I_{ph}, I_S, n, R_s and R_{sh} are the 5 unknown parameters to be determined by the simulation model.

The PV module is simulated in Matlab/SIMULINK platform. The simulation model is validated using datasheet parameters of a commercially available PV module. The simulated module I-V and P-V curves, under STC, are illustrated in Fig. 6 and the numerical results are tabulated and compared in Table I.

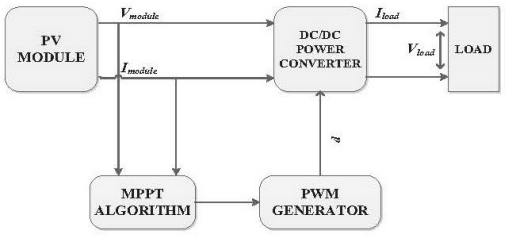

Figure 4. A general overview of the simulation model

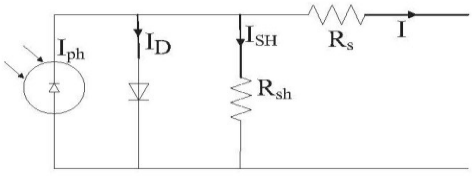

Figure 5. Equivalent One-Diode circuit of a solar cell

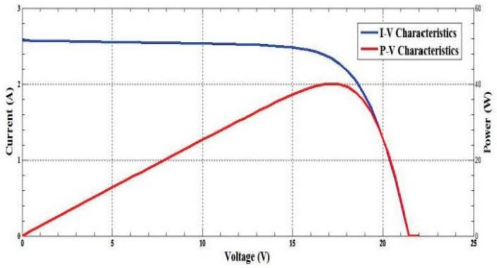

Figure 6. Simulated I-V and P-V characteristics of the PV module

The characteristic curves and provided numerical data clearly show that the simulation model is capable of an accurate modeling of the module characteristics. A comparison between the simulation results and the module datasheet values show that the simulated curves are in a good agreement with the real-world module characteristic data provided by the manufacturer. The inputs to the model are datasheet parameter values along with the temperature, irradiance and number of series and parallel connected cells in the module.

TABLE I. PV MODULE SIMULATED PARAMETERS

Parameter	Simulated Value	Datasheet Value
P_{max}	40	40
V_{oc}	21.4	21.6
I_{sc}	2.57	2.57
V_{mp}	17.27	17.3
I_{mp}	2.31	2.31

B. *Modeling of MPPT Algorithm*

The simulation models of the P&O and IncCond MPPT algorithms are constructed based on the flowcharts of the mentioned algorithms as illustrated in Fig. 2 and Fig. 3, respectively. The simulation models are presented in Fig. 7 and Fig. 8, respectively.

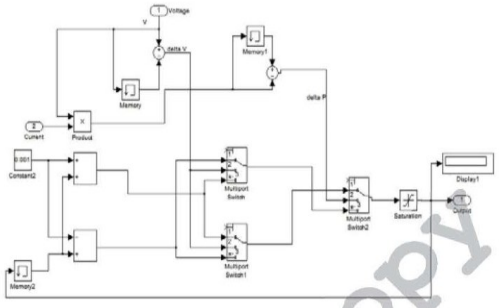

Figure 7. Simulation model of the P&O MPPT algorithm

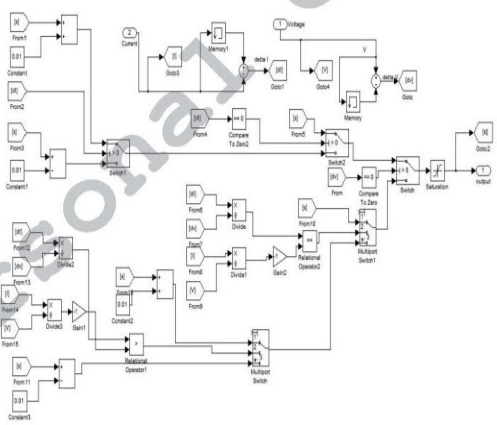

Figure 8. Simulation model of the IncCond MPPT algorithm

C. *Modeling of DC/DC Converter*

The boost converter topology is utilized in this paper due to its grid connection suitability. The electrical circuit diagram of a simple boost converter is presented in Fig. 9. As it is clear from the figure, this converter topology consists of an inductor, a switch, a capacitor and a diode.

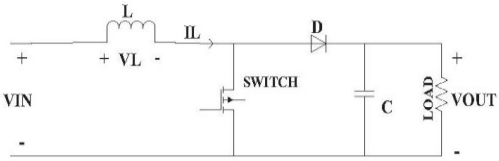

Figure 9. Circuit diagram of a boost DC/DC converter

The boost converter has two operation modes. The 1st mode begins when the switch is turned on ($t = T_{on}$). During this mode the rising input current flows through the inductor and switch and the energy is stored in the inductor. The 2nd mode begins when the switch is turned off ($t = T_{off}$). The current flows through the inductor, diode, capacitor and the load. The inductor current falls until the beginning of the next cycle and the energy is transferred to the load. The relationship between the input and output voltage values can be described by the following equation,

$$V_{out} = \frac{1}{(1-D)} \times V_{in} \quad (4)$$

Where,
D : Duty Cycle

IV. Simulation Results

The system simulation results, with both P&O and IncCond MPPT algorithms, are presented and discussed during this part of the paper. In order to highlight the importance and improving effects of MPPT application, the mentioned results are compared with the results obtained from the system simulation without any maximum power point tracker. The simulation model executed for 0.1 second under STC (G = 1000 W/m^2, Ambient Temperature = 25°C). A general overview of the constructed simulation model for the entire system is presented in Fig. 10.

According to the results, both of the algorithms have delivered almost the same amount of power to the load while the output power of the Incremental Conductance algorithm has been slightly higher than the P&O algorithm. The simulated system output power values are presented in Fig. 11.

The results also show that the output power of the IncCond algorithm has reached the maximum value in a shorter time period compared with the P&O algorithm. The results clearly highlight the importance and improving role of the MPPT application. It is obvious that the power delivered to the load is less than 10 W without application of MPPT while after MPPT application this value is higher than 35 W.

The results regarding the efficiencies of the MPPT algorithms are also presented in Fig. 11. Several approaches have been introduced to calculate and evaluate the efficiency of the MPPT algorithms. The efficiency evaluation and comparison in this paper is performed according to the following equation,

$$\eta = \frac{P_{out}}{P_{real}} \quad (5)$$

Where,
P_{real} : The available maximum power under the test conditions

According to the results, the recorded efficiency for both of the algorithms is greater than 90% which is quite satisfactory. At the same time it is observed that the efficiency of the IncCond algorithm is slightly greater than P&O algorithm and has reached to the maximum value in a shorter time period. The consistency between the similar MPPT simulation results and the real-time measured module outputs under identical solar insolation conditions is also confirmed in literature [2]. Table II contains detailed numerical results regarding different parameters of the system.

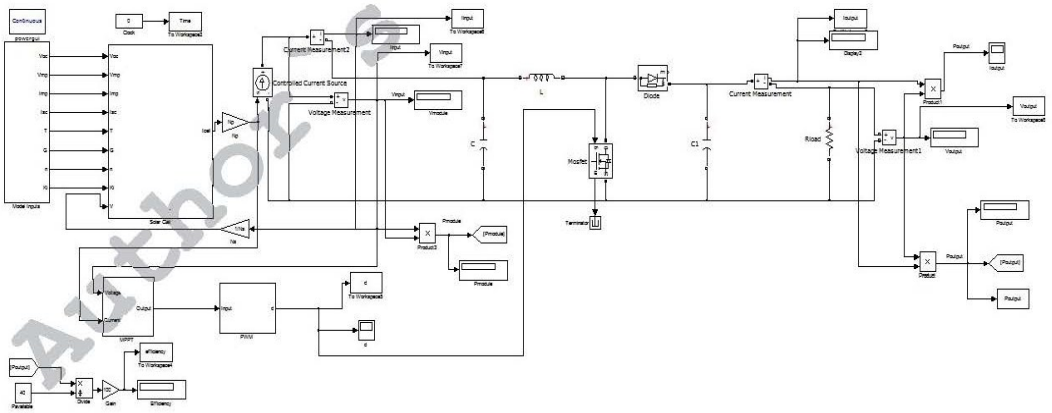

Figure 10. General overview of the system simulation model

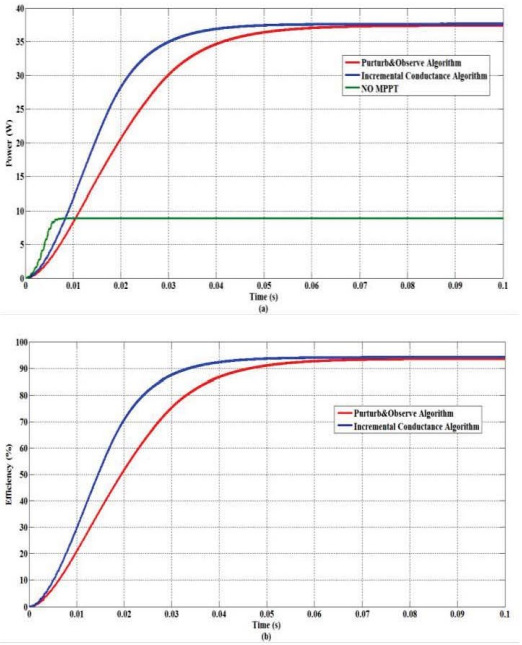

Figure 11. a) System output power with and without MPPT, b) Efficiency of MPPT algorithms

According to the results, the operation point of the module with P&O algorithm locates at the left side of the MPP while the IncCond algorithm operates the module at the right side of the MPP. Also it is observed that the operation point is near the open-circuit without application of maximum power point trackers. It is observed that MPPT algorithms have improved the overall efficiency of the system by more than 70%.

TABLE II. NUMERICAL SIMULATION RESULTS

Parameter	P&O Algorithm	IncCond Algorithm	NO MPPT
V_{in} (V)	15.8	18.16	21.03
V_{out} (V)	43.21	43.34	21.03
I_{in} (A)	2.46	2.14	0.42
I_{out} (A)	0.86	0.86	0.42
P_{max} (W)	37.24	37.60	8.84
η (%)	93.56	94.47	22.22

Considering the results together with the advantages and drawbacks of P&O and IncCond techniques, a tracking system which simultaneously tracks the MPP of the modules using both P&O and IncCond techniques may be suggested as a practical solution. The MPPT system may monitor and compare the outputs of the mentioned techniques and chose the most appropriate MPPT technique according to the existing environmental conditions and application/load requirements. Hence more efficient/reliable control may be provided to take the advantage of each individual MPPT technique under existing environmental conditions/application requirements.

V. CONCLUSIONS

The P&O algorithm is the simplest MPPT algorithm while the IncCond algorithm, proposed as an improvement to the P&O algorithm, has a relatively more complex structure. The simulation results presented in this paper show that both of the algorithms have almost the same efficiencies (η>90%) under identical illumination conditions. According to the results, the IncCond algorithm has shown a slightly better performance in tracking the maximum power point of the module. It is also observed that the output power of the IncCond algorithm reaches to the maximum point in a shorter time period compared with the P&O algorithm. The simple structure and its high tracking efficiency make the P&O algorithm to be the most preferred and utilized maximum power point tracker for PV systems. The results clearly highlight the improving role of the MPPT in PV systems where application of maximum power point trackers has increased the total system output power by more than 70%. The simulation results provide useful information which can be used by system planners for power yield and performance estimation of PV energy generation systems.

REFERENCES

[1] A. Luque and S. Hegedus, Handbook of Photovoltaics Science and Engineering, West Sussex, UK: Wiley, 2003, pp.905-933.

[2] D. Sera, "Real-time Modelling, Diagnostics and Optimised MPPT for Residential PV systems," Ph.D. dissertation, Dept. Elect. Eng., Aalborg Univ., Denmark, 2009.

[3] D. P. Hohm and M. E. Ropp, "Comparative Study of Maximum Power Point Tracking Algorithms," Prog. Photovolt: Res. Appl., vol. 11, Nov. 2002, pp.47-62, doi: 10.1002/pip.459.

[4] A. A. J. A. Nabulsi, "Efficiency Optimization of a Standalone Solar Energy System Using Fuzzy Based MPPT," Master's Thesis, Colg. Eng., American Univ., Sharjah, UAE, 2012.

[5] A. K. Abdelsalam, A. M. Massoud, S. Ahmed, and P. N. Enjeti, "High-Performance Adaptive Perturb and Observe MPPT Technique for Photovoltaic-Based Microgrids," IEEE Trans. Power Electron., vol. 26, no. 4, Apr. 2011, pp. 1010–1021, doi: 10.1109/TPEL.2011.2106221

[6] N. Femia, G. Petrone, G. Spagnuolo, and M. Vitelli, "Optimization of Perturb and Observe Maximum Power Point Tracking Method," IEEE Trans. Power Electron.., vol. 20, no. 4, Jul. 2005, pp. 963–973, doi: 10.1109/TPEL.2005.850975.

[7] K. Ishaque, Z. Salam, M. Amjad and S. Mekhilef, "An Improved Particle Swarm Optimization (PSO)-Based MPPT for PV with

Reduced Steady-State Oscillation," IEEE Trans. Power Electron., vol.27, no.8, Aug. 2012, pp.3627-3638, doi: 10.1109/TPEL.2012.2185713.

[8] Q. Zhang, C. Hu, L. Chen, A. Amirahmadi, N. Kutkut, Z.J. Shen and I. Bataresh, "A Center Point Iteration MPPT Method with Application on the Frequency-Modulated LLC Microinverter," IEEE Trans. Power Electron., vol.29, no.3, Mar. 2014, pp.1262-1274, doi: 10.1109/TPEL.2013.2262806.

[9] A.A. Nabulsi and R. Dhaouadi, "Efficiency Optimization of a DSP-Based Standalone PV System using Fuzzy Logic and Dual-MPPT Control," IEEE Trans. Ind. Informat., vol.8, no.3, Aug. 2012, pp.573-584, doi: 10.1109/TII.2012.2192282.

[10] W. Xiao, W.G. Dunford, P. R. Palmer and A. Capel, "Application of Centered Differentiation and Steepest Descent to Maximum Power Point Tracking," IEEE Trans. Ind Electron., vol.54, no.5, Oct. 2007, pp.2539-2549, doi: 10.1109/TIE.2007.899922.

[11] B. N. Alajmi, K. H. Ahmed, S. J. Finney, and B. W. Williams, "Fuzzy-Logic-Control Approach of a Aodified Hill-Climbing Method for Maximum Power Point in Microgrid Standalone Photovoltaic System," IEEE Trans. Power Electron., vol. 26, no. 4, Apr. 2011, pp. 1022 1030, doi:10.1109/TPEL.2010.2090903.

[12] A. K. Rai, N. D. Kaushika, B. Singh, and N. Agarwal, "Simulation Model of ANN Based Maximum Power Point Tracking Controller for Solar PV System," Solar Energy Mater. Solar Cells, vol. 95, Feb. 2011, pp. 773 778, doi: 10.1016/j.solmat.2010.10.022.

[13] H. Kim, Y. Min, C. Jeong, K. Kim, C. Kim and S. Kim, "A 1-mW Solar-Energy-Harvesting Circuit using an Adaptive MPPT with a SAR and a Counter," IEEE Trans. Circuits Syst. II, Exp. Briefs., vol.60, no.6, June 2013, pp.331-335, doi: 10.1109/TCSII.2013.2258262.

[14] R. F. Coelho, F. M. Concer and D. C. Martins, "Analytical and Experimental Analysis of DC-DC Converters in Photovoltaic Maximum Power Point Tracking Applications," Proc. IECON 2010, IEEE Press., Nov. 2010, pp.2778-2783, doi: 10.1109/IECON.2010.5675090.

[15] Y.T. Tan, D.S. Kirchen and N. Jenkins, "A Model of PV Generation Suitable for Stability Analysis," IEEE Trans. Energy Convers., vol.19, no.4, Dec. 2004, pp.748-755, doi: 10.1109/TEC.2004.827707.

[16] A. Kajihara and A.T. Harakawa, "Model of Photovoltaic Cell Circuits under Partial Shading," Proc. IEEE Int. Conf. Ind. Technol. (ICIT 05), IEEE Press., Dec. 2005, pp.866-870, doi: 10.1109//ICIT.2005.1600757.

[17] W. Xiao, W.G. Dunford and A. Capel, "A Novel Modeling Method for Photovoltaic Cells", Proc. IEEE 35th Annu. Power Electron. Spec. Conf. (PESC 04), vol.3, IEEE Press., Jun. 2004, pp.1950-1956, doi: 10.1109/PESC.2004.1355416.

[18] N. Celik and N. Acikgoz, "Modeling and Experimental Verification of the Operating Current of Mono-Crystalline Photovoltaic Modules using Four- and Five-Parameter Models," Appl. Energy J., vol.84, no.1, Jan. 2007, pp.1-15, doi: 10.1016/j.apenergy.2006.04.007.

[19] S. Liu and R.A. Dougal, "Dynamic Multiphysics Model for Solar Array," IEEE Trans. Energy Convers., vol.17, no.2, Jun. 2004, pp.285-294, doi: 10.1109/TEC.2002.1009482.

[20] M.G. Villalva, J.R. Gazoli and E.R. Filho, "Comprehensive Approach to Modeling and Simulation of Photovoltaic Arrays," IEEE Trans. Power Electron., vol.24, no.5, May 2009, pp.1198-1208, doi: 10.1109/TPEL.2009.2013862.

[21] J.A. Gow and C.D. Manning, "Development of a Photovoltaic Array Model for Use in Power-Electronics Simulation Studies," Proc. IEE Elect.. Power Appl., vol.146, no.2, IEEE Press., Mar. 1999, pp.193-200, doi: 10.1049/ip-epa:19990116.

[22] J.A. Gow and C.D. Manning, "Development of a Photovoltaic Array Model for Use in Simulation Studies of Solar Energy Conversion Systems," Proc. 6th Int. Conf. Power Electron. Variable Speed Drives, IEEE Press., Sept. 1996, pp.69-74, doi: 10.1049/cp:19960890.

[23] D. Holm and M. Ropp, "Comparative Study of Maximum Power Point Tracking Algorithms Using an Experimental, Programmable, Maximum Power Point Tracking Test Bed," Proc. 28th IEEE Photovoltaic Specialists Conf., IEEE Press., Sept. 2000, pp.1699-170, doi: 10.1109/PVSC.2000.9162320.

Appendix G: MATLAB/Simulink Based Simulation of Solar Incidence Angle and the Sun's Position in the Sky with Respect to Observation Points on the Earth

Kian Jazayeri, Sener Uysal, Moein Jazayeri, "MATLAB/simulink based simulation of solar incidence angle and the sun's position in the sky with respect to observation points on the Earth", in *Proceedings of 2013 International Conference on Renewable Energy Research and Applications, ICRERA*, Madrid, Spain, 2013.

Abstract— **This paper proposes a simulation model for calculation of the sun`s position in the sky and the incidence angle of sunlight beams on the surface of solar modules with any tilt angle, located at any geographical location on the Earth`s surface. The electrical power generated by a solar panel directly depends on the amount of the received solar irradiance on panel surface where the received irradiance is directly proportional to the sun's position in the sky. Therefore, it is of great importance for solar energy researchers and system designers to have a precise knowledge about the movement and position of the sun in the sky with respect to any specific observation point on the earth. A simple and practical simulation model of the sun's position in the sky is designed using MATLAB/Simulink platform. The model simulates the sun`s position in the sky and solar angle of incidence based on the latitude and longitude of the observation point, solar module`s azimuth and tilt angle values, the Julian day number and the local clock time. The proposed model provides the possibility of instantaneous or continuous determination and tracking of the sun's position in the sky for any geographical location on earth and can be considered as a helpful tool for sun tracking and other system planning purposes.**

Keywords*— *photovoltaic, photovoltaic simulation, solar altitude, solar angle of incidence, solar azimuth, solar energy, sun`s position in the sky, sun tracking,

MATLAB/Simulink Based Simulation of Solar Incidence Angle and the Sun`s Position in the Sky with Respect to Observation Points on the Earth

Kian Jazayeri, Sener Uysal, *Member, IEEE,* Moein Jazayeri

Electrical and Electronic Engineering Department., Eastern Mediterranean University
Famagusta, North Cyprus, via Mersin 10 Turkey
kian.jazayeri@cc.emu.edu.tr
sener.uysal@emu.edu.tr
moein.jazayeri@cc.emu.edu.tr

Abstract— **This paper proposes a simulation model for calculation of the sun`s position in the sky and the incidence angle of sunlight beams on the surface of solar modules with any tilt angle, located at any geographical location on the Earth`s surface. The electrical power generated by a solar panel directly depends on the amount of the received solar irradiance on panel surface where the received irradiance is directly proportional to the sun's position in the sky. Therefore, it is of great importance for solar energy researchers and system designers to have a precise knowledge about the movement and position of the sun in the sky with respect to any specific observation point on the earth. A simple and practical simulation model of the sun's position in the sky is designed using MATLAB/Simulink platform. The model simulates the sun`s position in the sky and solar angle of incidence based on the latitude and longitude of the observation point, solar module`s azimuth and tilt angle values, the Julian day number and the local clock time. The proposed model provides the possibility of instantaneous or continuous determination and tracking of the sun's position in the sky for any geographical location on earth and can be considered as a helpful tool for sun tracking and other system planning purposes.**

Keywords— photovoltaic, photovoltaic simulation, solar altitude, solar angle of incidence, solar azimuth, solar energy, sun`s position in the sky, sun tracking,

I. INTRODUCTION

The alternative clean and sustainable energy resources have been the subject of many scientific researches in the recent decades with respect to the limitations and threats associated with the traditional energy resources. The solar energy is one of the most competitive and rapidly growing energy resources that emerge to meet the modern world's energy requirements without causing any damage to the planet earth. The importance of this energy source can better be realized considering that the amount of energy generated by the sun in just one hour can satisfy the world energy requirements for one year [1].

The amount of power generated by solar panels is determined by the amount of the energy carried by the sun`s radiation that is received on the panel surface. The solar irradiance incidence on any given point on the earth is directly proportional to the sun's position in the sky with respect to the specified observation point. Due to the mentioned dependency of the power generation to the received insolation by solar panels, the amount of power generation by a solar panel during any specific day is not constant and shows variations in parallel with changing position of the sun in the sky. The mentioned variations cause the overall system efficiencies to be reduced and the cost of energy production to be increased. Therefore it is of major significance to put effort on developing techniques of determination and tracking of the sun's position in the sky and the matter has been considered in many research projects [2-6]. Determination of the sun`s position in the sky is also considered in [7] from solar radiation data processing point of view. However the study does not contain information on determination of solar angle of incidence.

This paper specifically focuses on designing a simple and practical simulation model for calculation of the sun`s position in the sky together with the values of the solar angle of incidence using MATLAB/Simulink. The model is also capable of calculation of the incidence angle of the sunlight beams on panel surfaces. The values of the latitude and longitude of the observation point, solar panel's azimuth and tilt angle, Julian day number and the local clock time are the inputs of the model and the model calculates the sun's position in the sky and solar incidence angle values for a specified time instant or interval. Detailed information on calculating the sun's position in the sky is reviewed in the next parts of the study and then followed by the designing procedure of the proposed simulation model and the obtained simulation results for specified sample dates.

II. SUN'S POSITION IN THE SKY

As described in [8], the sun's position in the sky is determined by two different factors, namely being the Solar Altitude Angle, the Solar Azimuth Angle and the Solar Angle of Incidence determined the angles between a perpendicular line on panel surface and the incoming sunlight rays. The mentioned parameters are used by the proposed simulation model to calculate the position of the sun in the sky for any specified geographical location and time interval.

978-1-4799-1464-7/13/$31.00 ©2013 IEEE

A. Solar Altitude Angle

The solar altitude angle, (γ_s), represents the sun's elevation from the Earth's surface and is expressed by (1), as follows,

$$\gamma_s = \sin^{-1}(\sin\varphi\sin\delta + \cos\varphi\cos\delta\cos\omega) \quad (1)$$

$$\delta = \sin^{-1}\left\{0.3987\sin\left(j'80.2°+1.92\left(\sin\left(j'-2.80°\right)\right)\right)\right\} \quad (2)$$

$$\omega = 15(t-12) \quad (3)$$

Where,

φ : The latitude of the observation point
δ : The solar declination angle (Degrees)
ω : The solar hour angle (Degrees)
t : Decimal hours on the 24 hour clock

The solar altitude angle value increases during morning hours and reaches its peak at solar noon which corresponds to the sun's highest elevation in the sky with respect to any observation point on the ground.

B. Solar Azimuth Angle

The solar azimuth angle, (α_s), represents the sun's deviation from the North axis and is expressed by (4), as follows,

$$\begin{cases} \alpha_s = 180 - \cos^{-1}(\cos\alpha_s) & \text{If } \sin\alpha_s < 0 \\ \alpha_s = 180 + \cos^{-1}(\cos\alpha_s) & \text{If } \sin\alpha_s > 0 \end{cases} \quad (4)$$

Where,

$$\cos\alpha_s = (\sin\varphi\sin\gamma_s - \sin\delta)/\cos\varphi\cos\gamma_s \quad (5)$$

$$\sin\alpha_s = \cos\alpha_s\sin\omega/\cos\gamma_s \quad (6)$$

For an observation point located in northern hemisphere, the solar azimuth angle reaches 180° at solar noon which represents the sun's least deviation from the south oriented solar panels.

C. Solar Incidence Angle

The solar incidence angle, (θ), which is represented by (7), is the angle between the sun's radiations and a vector perpendicular to the surface of a solar panel on the earth.

$$\theta = \cos^{-1}\left[\begin{matrix}\cos(\beta)\cos(Z_s) + \\ \sin(\beta)\sin(Z_s)\cos(\alpha_s - \alpha_m)\end{matrix}\right] \quad (7)$$

Where,

β : Tilt angle of the solar panel (45° In this case)
Z_s : Zenith Angle of the Sun (Degrees)
α_m : Module azimuth angle (In this case: South = 180°)

and,

$$Z_s = 90 - \gamma_s \quad (8)$$

For a specified observation point on the earth, the value of the solar incidence angle decreases during morning hours and takes on its minimum at solar noon which indicates that the sun's radiations are received with lowest deviation from a perpendicular vector on a solar panel surface at the specified point.

III. Modeling of the System Components

The desing procedure of the proposed simulation model is described in this part of the study. A mask implementation of the simulation model constructed in MATLAB/Simulink environment is shown in Fig. 1. As it is obvioud from the figure, the model accepts the values of the latitude and the longitude of the observation point, the Julian day number and the panel tilt and azimuth angles along with the time settings as inputs. The sun's position in the sky is then calculated and simulated based on mathematical descriptions through the model sub-systems.The model contains five main sub-systems that are designed for calculations of the hour angle, the declination angle, the solar altitude angle, the solar azimuth angle and the solar angle of incidence. The local clock time instant or interval which is set in the time settings of the model is processed to turn out as the desirable solar time instant or incremental solar time interval.

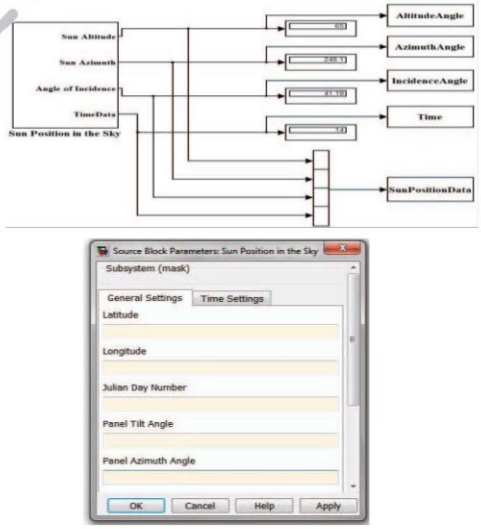

Fig. 1. A mask implementation of the simulation model of the sun's position in the sky

A. *Simulation of Hour Angle*

The structure of the sub-system used for simulation of the hour angle is illustrated in Fig. 2. As it is obvious from the figure, the inputs to the model are the local time, the longitude of the observation point, the time difference from GMT, the Julian day number and the daylight saving time. The simulation model first converts the input Local Time to Local Solar Time, through the Time Subsystem, and then calculates the hour angle based on (3).

1) Calculation of the Local Solar Time (LSTM) : The local time of an observation point on the earth's surface is determined by the longitude of the point. But the sun's movement in the sky is independent of any geographical divisions on the earth and is only specified by the solar time [9]. In instance, the sun's highest elevation in the sky which exactly corresponds to the solar noon may not necessarily be observed at the exact noon in different observation points on the earth. The reason is the difference between the local solar time and the local clock time of the observation points.

The proposed simulation model converts the local clock time of any observation point on the earth's surface to the Local Solar Time which is the time format used for determination of the sun's position in the sky. The structure of the simulation model utilized to convert the Local Time (LT) to the Local Solar Time (LST) is shown in Fig. 3. The local solar time is calculated based on the following equations,

$$LST = LT + \frac{TC}{60} \quad (9)$$

$$TC = 4 \times (LSTM - Longitude) + EOT \quad (10)$$

$$EOT = 9.87\sin(2B) - 7.53\cos(B) - 1.5\sin(B) \quad (11)$$

$$B = \frac{360}{365}(d - 81) \quad (12)$$

$$LSTM = 15^{\circ}.\Delta T_{GMT} \quad (13)$$

Where,

LST : Local Solar Time

LT : Local Time

TC : Time Correction Factor

LSTM : Local Solar Time Meridian

EOT : Equation of Time

ΔT_{GMT} : Difference from Greenwich MeanTtime

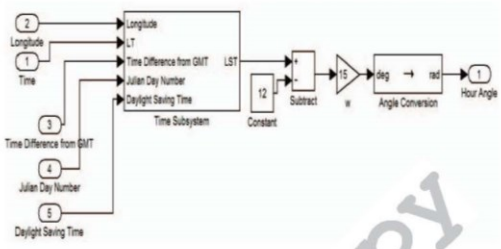

Fig. 2. The structur of the hour angle simulation sub-system

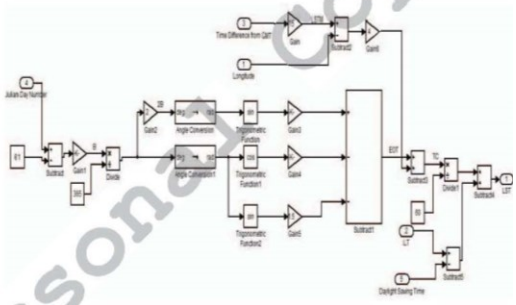

Fig. 3. The structur of the LT-LST conversion sub-system

B. *Simulation of Declination Angle*

The structure of the simulation model utilized to calculate the declination angle is illustrated in Fig. 4. The model accepts the Julian day number as input and returns the declination angle for the specified day in degrees based on (2).

C. *Simulation of the Solar Altitude Angle*

The solar altitude angle is calculated using the values of the hour angle and the solar declination angle which were calculated in the previous sub-systems together with the latitude of the observation point. the simulation model calculates the value of the solar altitude angle based on (1). The structure of the utilized sub-system for calculation of the solar altitude angle is illustrated in Fig. 5.

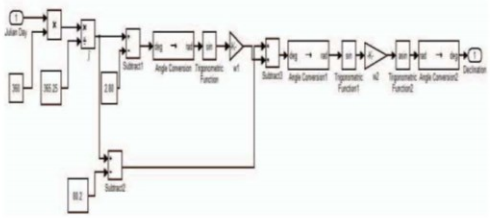

Fig. 4. The structur of the declination angle simulation sub-system

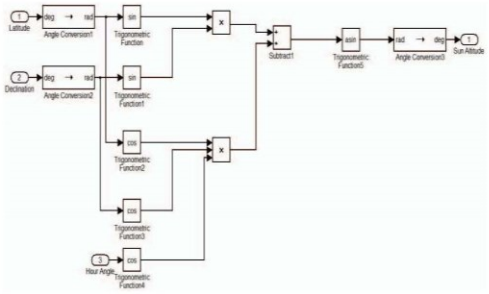

Fig. 5. The structur of the the solar altitude angle sub-system

D. Simulation of the Solar Azimuth Angle

The sub-system which is used to simulate the solar azimuth angle takes the values of the hour angle and the solar declination angle from the corresponding sub-systems along with the latitude and the altitude of the observation point to calculate the solar azimuth angle based on (4)-(6). The structure of the mentioned sub-system is shown in Fig. 6.

E. Simulation of the Solar Angle of Incidence

The solar angel of incidence is calculated based on (7), using the latitude of the observation point and the panel tilt and azimuth angle values together with the solar azimuth angle value which was calculated in the corresponding sub-system. The structure of the sub-system utilized for the simulation of the solar angle of incidence is shown in Fig. 7. A general overview of the entire proposed simulation model is shown in Fig. 8.

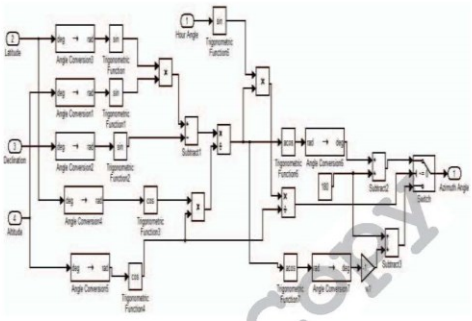

Fig. 6. The structur of the the solar azimuth angle sub-system

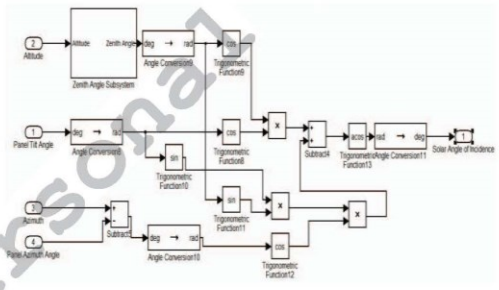

Fig. 7. The structur of the the solar angle of incidence simulation sub-system

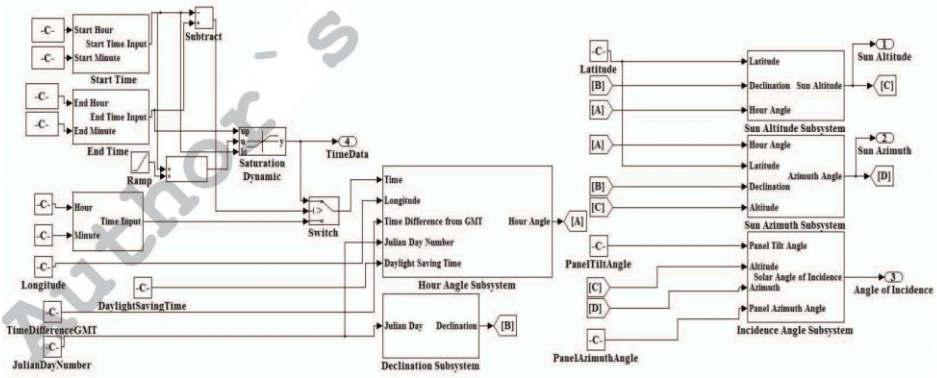

Fig. 8. A general overview of the proposed simulation model

IV. Simulation Results

The simulation results of the solar altitude, azimuth and incidence angles for January 1st, April 1st, July 1st and October 1st corresponding to Julian day numbers 1, 91, 182 and 274, respectively are shown in Fig. 9.

As it is obvious from the figures, for each sample day, highest value of the solar altitude angle occurs at solar noon (12:00 LST). It is also obvious that the sun is due South at the same time instant. (Solar Azimuth Angle = 180°). This is exactly the time at which the lowest value of the solar incidence angle happens, meaning that the sunlight beams hit the panel surface with the closest angle to 90°.

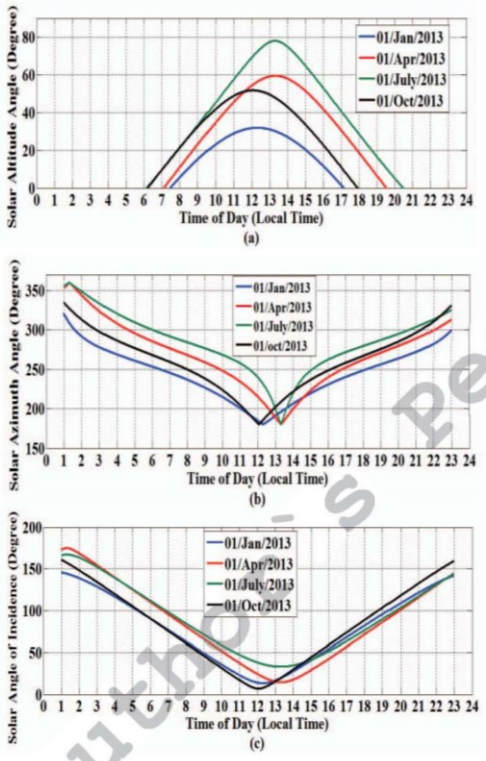

Fig. 9. Simulation results for a)Solar Altitude Angle, b)Solar Azimuth angle, c)Solar Angle of Incidence

V. Conclusions

Estimation of solar panel output power carries a great importance considering the rapid growth of the solar power utilization. The amount of power produced by a solar panel is directly proportional to the amount of solar irradiance falling on the panel surface which is subjected to variations with respect to the movement of the sun in the sky. Hence tracking and determination of the sun's position in the sky has been the subject of many research projects.

A comprehensive and practical simulation model of the sun's position in the sky is proposed in this paper. The simulation model is constructed in MATLAB/Simulink platform and is capable of calculating the sun's position in the sky and the solar angle of incidence for any specified time instant and geographical location on the earth's surface. The calculation and simulations are based on the values of latitude and longitude of the observation point, solar panel's azimuth and tilt angle, Julian day number and the local clock time. The results show that, at solar noon, the sun is due South with the highest altitude in the sky, for observation points in the northern hemisphere. This is exactly the time at which the sunlight beams hit the module surface with the closest angle to 90° and cause the module to produce the maximum output power. The simulation model provides the researchers and system designers with reliable and precise information on the sun's position in the sky.

References

[1] P.A. Lynn, *Electricity from Sunlight : An Introduction to Photovoltaics*, West Sussex, UK: Wiley, 2010, pp.1-23.

[2] E. Hossain, R. Muhida and A. Ali, "Efficiency Improvement of Solar Cell Using Compound Parabolic Concentrator and Sun Tracking System", in *IEEE-EPEC*, Canada, 2008, pp.1-8.

[3] R. Tejwani and C.S. Solanki, "360°C Sun Tracking with Automated Cleaning System for Solar PV Modules", in *IEEE-PVSC*, Hawaii, USA, 2010, pp.2895-2898.

[4] Zhou Yan and Zhu Jiaxing, "Application of Fuzzy Logic Control Application in a Microcontroller-Based Sun Tracking System", in *IEEE-ICIE*, BeiDai, China, 2010, pp.161-164.

[5] A. Ponniran, A. Hashim and H.A. Munir, "A Design of Single Axis Sun Tracking System", in *IEEE-PEOCO*, Selangor, Malaysia, 2011, pp.107-110.

[6] G. Chicco, J. Schlabbach and F. Spertino, "Performance of Grid-Connected Photovoltaic Systems in Fixed and Sun-Tracking Configurations", in *IEEE - Power Tech*, Lausanne, 2007, pp.677-682.

[7] C. Shen, Y. He, Y. Liu, W. Tao, "Modelling and simulation of solar radiation data processing with Simulink," *Simulation Modelling Practice and Theory*, vol.16, 2008, pp.721-735.

[8] K. Scharmer and J. Greif, *The European Solar Radiation Atlas Vol.1: Fundamentals and Maps*, Paris, France: Les Presses de l'Ecole des Mines, 2000, pp. 23-42.

[9] A. Luque and S. Hegedus, Handbook of Photovoltaics Science and Engineering, West Sussex, UK : Wiley, 2003, pp.905-933.

Appendix H: Experimental Analysis of Effects of Connection Type on PV System Performance

Moein Jazayeri, Sener Uysal, Kian Jazayeri, Seyda Yapici, "Experimental analysis of effects of connection type on PV system performance" in *Proceedings of 2013 International Conference on Renewable Energy Research and Applications, ICRERA*, Madrid, Spain, 2013.

Abstract — **This paper mainly focuses on experimental performance analysis of solar modules under different irradiance values. Also effects of interconnection types and bypass diode application on module output characteristics under variable shading patterns are analyzed. The mentioned analyses are based on and supported by real-time measurement data and the results confirm the direct relationship between the power generation by solar modules and the incident solar irradiance. According to the results, although higher voltage values are obtained, series strings of solar cells/modules, without bypass diodes, show a higher sensitivity to shading effects and string output power is subjected to higher amounts of reduction compared with the parallel connection conditions. On the other hand, parallel connected solar cells/modules provide higher values of generated current amounts while the output voltages are equivalent to that of each individual cell/module. Experimental results also show that application of bypass diodes in series connected module strings has a great improving effect on power production by the string. The significance of the results arises during design and planning procedures of solar energy systems, where detailed knowledge of system characteristics under different shading patterns creates the opportunity to take the required measures and obtain optimum system performance.**

Keywords— I-V characteristics, photovoltaic cell interconnection, photovoltaic power generation, P-V characteristics, solar energy, solar modules

Experimental Analysis of Effects of Connection Type on PV System Performance

Moein Jazayeri, Sener Uysal, *Member, IEEE,* Kian Jazayeri and Seyda Yapici
Electrical and Electronic Engineering Department, Eastern Mediterranean University
Famagusta, North Cyprus, via Mersin 10 Turkey
moein.jazayeri@cc.emu.edu.tr
sener.uysal@emu.edu.tr
kian.jazayeri@cc.emu.edu.tr
seyda.ypc@gmail.com

Abstract — **This paper mainly focuses on experimental performance analysis of solar modules under different irradiance values. Also effects of interconnection types and bypass diode application on module output characteristics under variable shading patterns are analyzed. The mentioned analyses are based on and supported by real-time measurement data and the results confirm the direct relationship between the power generation by solar modules and the incident solar irradiance. According to the results, although higher voltage values are obtained, series strings of solar cells/modules, without bypass diodes, show a higher sensitivity to shading effects and string output power is subjected to higher amounts of reduction compared with the parallel connection conditions. On the other hand, parallel connected solar cells/modules provide higher values of generated current amounts while the output voltages are equivalent to that of each individual cell/module. Experimental results also show that application of bypass diodes in series connected module strings has a great improving effect on power production by the string. The significance of the results arises during design and planning procedures of solar energy systems, where detailed knowledge of system characteristics under different shading patterns creates the opportunity to take the required measures and obtain optimum system performance.**

Keywords— I-V characteristics, photovoltaic cell interconnection, photovoltaic power generation, P-V characteristics, solar energy, solar modules

I. Introduction

The rising energy requirements for almost all application areas and disadvantages of the conventional energy sources like pollution, limited amount, etc. in today's world have attracted the attentions to the renewable energy resources and meeting the energy requirements using solar energy as one of the mentioned renewable energy sources has been considered by many researchers during the recent years. However relatively high installation costs, lack of economically efficient energy storage devices and relatively low efficiencies have formed the disadvantages of this huge energy source.

However, for an efficient use of solar energy, having a precise knowledge of the amount of power yield of each individual photovoltaic generator under different conditions carries a great importance during system design procedures. The output characteristics of solar cells strongly depends on the changing environmental conditions (e.g. irradiance, temperature etc.) and the cell/module interconnection types in a solar module/array also affects the output characteristics of the module/array.

The I-V and P-V characteristics of solar cells/modules provide the most useful and reliable information regarding the operation of each cell/module under specific environmental condition and various models and approaches have been introduced by researchers to study and analyze the characteristics and behavior of solar cells under different environmental conditions.

In this paper the output characteristics of solar modules under changing illumination levels have been analyzed and the effects of different interconnection types on power generation by modules are investigated under various shading patterns. Also as a method of efficiency improvement, the effects of application of bypass diodes in solar energy systems is considered and analyzed. The mentioned analyses are based on and supported by real-time measurement data collected from a small-scale experimental test setup. The results demonstrate the relationships between the environmental conditions, system configuration and power generation by solar modules and can be extended to large-scale photovoltaic power plants.

The experimental results of the study provide reliable and useful information regarding the behavior of solar energy generator systems which can be considered for model validation and system design purposes for further research projects.

II. Solar Cell Characteristics

Output characteristics of solar cells/modules/arrays provide the most reliable and useful information during analyze and design procedures of the systems. Thus various approaches and methods have been utilized by researchers to investigate the mentioned characteristics. As an example, mathematical modeling of a solar cell is a common method used by many researchers to simulate and analyze the system characteristics. In this regard, the single-diode model, based on a linear independent current source in parallel to a diode [1-2] is the simplest model while R_s-models including a series connected resistance are introduced in [3-4]. The models referred to as R_p-models are improved versions of the single-diode model by adding a parallel connected resistance, (R_{sh}), to the models

978-1-4799-1464-7/13/$31.00 ©2013 IEEE

[5-7]. Two-diode model of solar cells also include an additional diode and is utilized by many researchers [8-10]. R_p-models or simply the one-diode model and the two-diode model as shown in Fig.1 are the most widely used models in the literature. Performances of these models also have been analyzed and compared by many researchers [11]. One-diode model of a solar cell has been used in many research studies due to its simplicity while the two-diode model is known to show a better accuracy at lower irradiance levels [12].

The output characteristics of a solar cell strongly depend on the environmental conditions (irradiance, temperature, etc.). The one-diode mathematical model of a solar cell defines the relationship between the cell`s output current and voltage using the following equation [13],

$$I = I_{ph} - I_S\left(exp\frac{q(V + R_S I)}{nkT} - 1\right) - \frac{(V + R_S I)}{R_{SH}} \quad (1)$$

Where;

I_{ph} : Photocurrent (A)
I_S : Diode Saturation Current (A)
q : Electron Charge ($1.60217646 \times 10^{-19}$ C)
n : Diode Ideality Factor
k : Boltzmann Constant ($1.3806503 \times 10^{-23}$ J/K)
T : Temperature of the p-n Junction (K)
R_S : Series Resistance (Ω)
R_{SH} : Shunt Resistance (Ω)

In (1), the photocurrent, I_{ph}, directly depends on the received solar irradiance and the diode saturation current, I_s, varies with ambient temperature and the diode ideality factor. The output characteristics of solar cells are generally represented as I-V and P-V curves. An identical solar cell I-V curve is illustrated in Fig. 2.

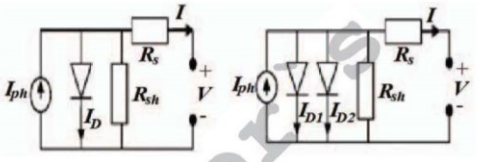

Fig. 1. a) One-Diode, b) Two-Diode model of a solar cell

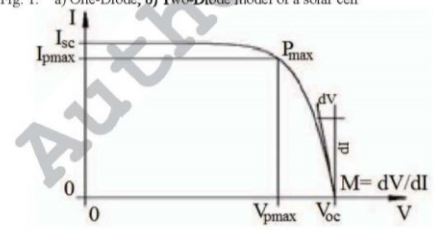

Fig. 2. Identical I-V curve of a solar cell

As it is obvious from the figure, while the output current varies between 0-I_{sc}, the voltage ranges between 0-V_{oc} in a solar cell/module. The characteristic curves and produced power amounts highly depend on solar insolation and temperature while the series and parallel resistance values as well as diode ideality factors have significant effects on the output characteristics.

III. Different Interconnection Types and Their Effects on Module Output Characteristics

As far as the values of output voltage and current of a single solar cell are not high enough to meet the desired application requirements, generally a number of cells are interconnected in series and/or parallel to form a solar module and obtain the desired voltage and current requirements. The modules are also connected in different combinations to form solar arrays. The effects of different interconnection types on array output characteristics have been analyzed by many researchers [14-17]. Therefore, for an efficient use, it is of a great importance to estimate/calculate the output characteristics of interconnected cells/modules with different interconnection types. Some of the most commonly used interconnection types for solar modules are shown in Fig. 3. It is clear that all of the mentioned configurations are extended combinations of series and parallel interconnections of solar cells/modules. Therefore studying the behavior of series and/or parallel connected solar modules, as the basic building blocks of bigger systems, helps for better understanding and analyses of large-scale power generation plant characteristics.

A. Series Connection of Solar Cells

The terminal voltage of a typical solar cell is not high enough (≈0.6 V) to meet the desired voltage requirements. Therefore a series connection of solar cells is preferred to produce the desired voltage values. The string output voltage, current and power values can be defined by the following equations,

$$V_{output} = \sum_{i=1}^{n} V_i \quad (2)$$

$$I_{output} = I_1 = I_2 = \cdots = I_j \quad (3)$$

$$P_{output} = V_{output} \times I_{output} = \sum_{i=1}^{n} V_i \times I_j \quad (4)$$

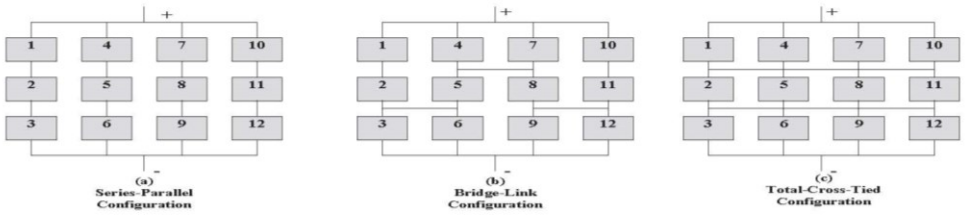

Fig. 3. Most common solar array configuration types

The advantage of a series connected cell string is the increased voltage values but the problem arises when one or more cells in a string are subjected to full or partial shading due to passing clouds, neighboring houses, etc. In the case of partial or full shading, the shaded cell/cells will not be able to produce the same amount of current and the string output current will be limited to the smallest current produced by the most shaded cell. The shaded cell/cells will be producing a negative power meaning that the power produced by the fully illuminated cells will be dissipated in shaded cell/cells and the total output power will be decreased.

B. Parallel Connection of Solar Cells

Different from the series strings, parallel connected solar cells/modules are preferred in the applications where there is a need to increase the amount of output current. The output voltage, current and power relationships in parallel connected solar modules can be defined by the following equations,

$$V_{output} = V_1 = V_2 = \cdots = V_i \quad (5)$$

$$I_{output} = \sum_{j=1}^{n} I_j \quad (6)$$

$$P_{output} = V_{output} \times I_{output} = \sum_{j=1}^{n} V_i \times I_j \quad (7)$$

The experimental test results show that parallel connected solar cells are not as sensitive to partial or full shading effects as the series connected cell strings. The amount of power loss due to partial or full shading effects in parallel connected modules is smaller than the mentioned amount in series connected strings.

IV. Analysis of Measured Module Output Characteristic Data

This part of the paper includes analyses of the collected real-time experimental measurement results. The mentioned analyses can be divided into 4 main groups as follows,

- Analysis of single module output characteristics under different irradiance levels
- Analysis of series connected module string output characteristics under different shading conditions
- Analysis of parallel connected module output characteristics under different shading conditions
- Analysis of effects of bypass diode application on string output power

The circuit diagram constructed for the mentioned measurements is shown in Fig. 4. It should be noticed that the measured data regarding each of the above mentioned analyses are collected in different days and so the analyses results are not related and should be considered individually.

A. Analysis of Single Module Characteristics under Different Irradiance levels

The I-V and P-V characteristics of a commercially available solar module are analyzed and compared under different irradiance levels. The module specifications are presented in Table I. The module is south aligned and tilted 45°, mounted at 17 m from sea level on top of the Electrical and Electronic Engineering Department, Eastern Mediterranean University (35° 8' 51" N, 33° 53' 58" E). The module I-V and P-V characteristics for different irradiance levels are shown in Fig. 5. The numerical results are also tabulated in Table II.

TABLE I. Specifications Of The Utilized Solar Module

Parameter	Value
P_{max}	40 W
V_{oc}	21.6 V
I_{sc}	2.57 A
V_{mp}	17.3 V
I_{mp}	2.31 A

According to the results, the module is not able to produce the same amount of current output when it is subjected to lower solar irradiance values.

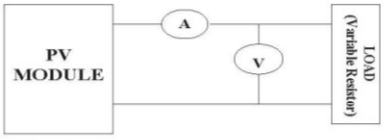

Fig. 4. Experimental measurement set-up

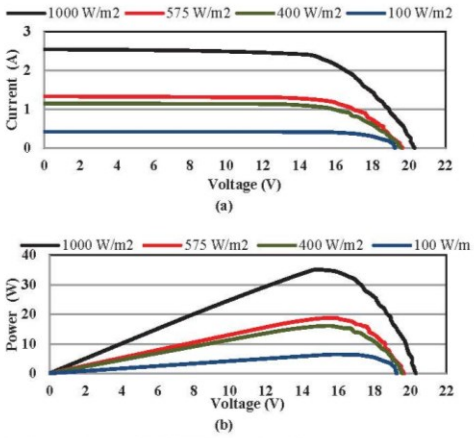

Fig. 5. Measured module a) I-V, b) P-V characteristics

The results show that the module short-circuit current, (I_{sc}), is subjected to a reduction of 47.63%, 54.72% and 83.47% in parallel with the reduction of the irradiance value to 575 W/m^2, 400 W/m^2 and 100 W/m^2 respectively. At the same time, the reduction amount of the maximum output power of the module, (P_{max}), has been 46.21%, 53.93% and 81.65% respectively for the same amounts of reduction in the irradiance levels. The measurement results clearly show that any change or reduction in the amount of irradiance immediately affects the module output characteristics. Therefore detailed and precise analysis of module behavior under different shading conditions earns a great importance from photovoltaic system design point of view.

TABLE II. SINGLE MODULE MEASUREMENT RESULTS

Irradiance (W/m^2)	1000	575	400	100
Maximum Power (P_{max})	34.88	18.76	16.06	6.40
Short-Circuit Current (I_{sc})	2.54	1.33	1.15	0.42
Open-Circuit Voltage (V_{oc})	20.3	19.65	19.55	19.24

B. Analysis of Series Connected Module String Characteristics under Different Shading Conditions

This part of the study includes the analysis of the results of experimental measurements made on a series connected solar module string output characteristics. The string consists of three identical commercially available solar modules as indicated in Table I.

The I-V and P-V characteristics of the string are obtained and compared for two different shading conditions as shown in Fig. 6. At the first stage all of the modules were subjected to identical irradiance and in the second case, one of the modules in the string was partially shaded and the remaining two modules were identically illuminated. The output characteristics of the string were measured for each case and the results are illustrated in Fig. 7.

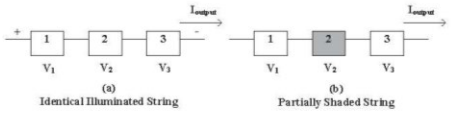

Fig. 6. Series connected string of solar modules

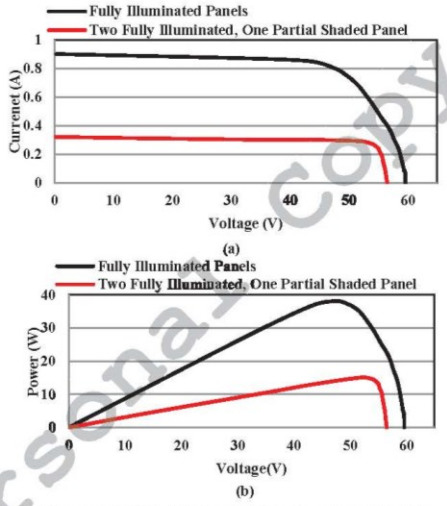

Fig. 7. Measured a) I-V, b) P-V characteristics of a series module string

According to the results, series connection of the modules has created the opportunity to obtain higher voltage values while the output current of the string is limited to the output current of each individual module. It is also obvious that partial shading of one module in a series string has limited the current output to the smallest current value produced by the shaded module while there is a small voltage drop in the string. The results show that partial shading of a single module in a series string including 3 identical modules has led to a 60.4% (23 W) reduction in the maximum output power. It is observed that existing of one fully shaded module in the string makes the string unable to deliver power to the load.

C. Analysis of Parallel Connected Module Output Characteristics under Different Shading Conditions

Three identical solar modules (as described in Table I.) were connected in parallel and their output characteristics were measured and compared. The measurements were conducted for two different shading conditions as shown in Fig. 8. For the first set of measurements all of the three panels were subjected to identical illumination and in the second case, one of the modules was fully shaded while the remaining two panels were identically illuminated. The results of the measurements are presented in Fig. 9.

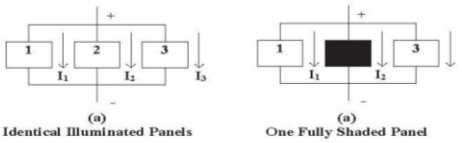

Fig. 8. Parallel connected solar panels

According to the results, in the case of parallel connected modules under identical irradiance values, the output voltage has been equivalent to the output voltage of each individual module. Also it is observed that the output current of parallel connected modules has been equivalent to the sum of output currents of parallel connected individual panels. In the case of parallel connection of one fully shaded module with two identically illuminated ones, the short-circuit current of the system has been decreased to almost 60% of the initial condition while there is no reduction in the open-circuit voltage value. It is also observed that fully shading of one module has caused a reduction of 31.7% (10.94 W) in the maximum output power of the system. The numerical measurement results obtained with series and parallel interconnections are presented and compared in Table III.

D. Analysis of Effects of Bypass Diode Application on String Power Output

As indicated by the experimental measurement results from the previous parts of the study, the received irradiance values and shading conditions have direct effects on the current produced by a series connected module string and hence the string output power is very sensitive to the shading effects.

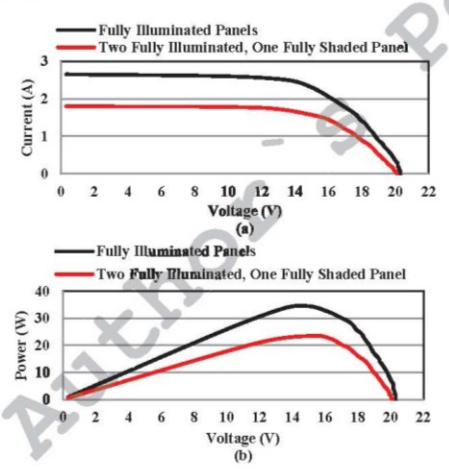

Fig. 9. Measured a) I-V, b) P-V characteristics of parallel connected panels

When modules of a series connected string are shaded, they are not able to produce the same current as the illuminated modules. Considering a series connection, the current produced by the illuminated modules has to pass through the shaded cells and hence forces them to work in the negative voltage region. This effect causes the shaded modules to dissipate power and work as a load which leads to reductions in the output power and hotspot problems. Many researchers have been working on methods to increase the efficiency and decrease the negative effects of shading on power production by solar systems. Application of bypass diodes is considered as one of the most common methods which is widely utilized in solar power generation applications. The bypass diodes connected to PV modules become forward biased when the module is shaded and the current of the illuminated modules is bypassed through these diodes. Bypass diodes lead to a small amount of voltage drop (≈0.6 V) in the bypassed modules and hence limit the reduction in the output power. In order to analyze the effects of bypass diodes on the output power of a series string, a bypass diode is connected in parallel to one of the modules in the string including three identical solar modules as indicated in Table I. The circuit diagram of the string is illustrated in Fig.10. The bypassed module was fully covered and the remaining two modules were identically illuminated. The experimental measurement results are presented in Fig. 11.

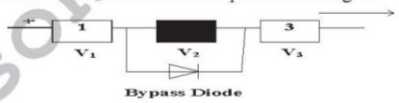

Fig. 10. Series connected panel string with bypass diode application

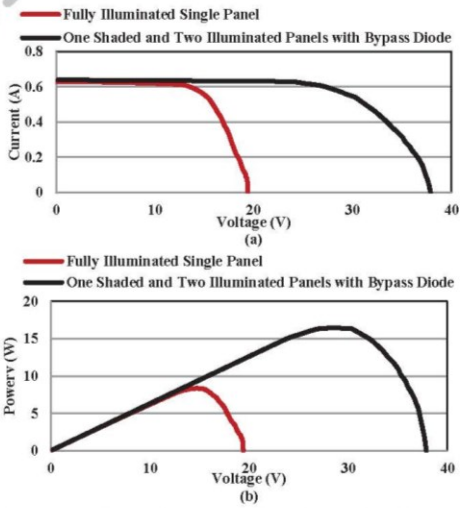

Fig. 11. Measured a) I-V, b) P-V characteristics of series string with bypass diodes

TABLE III. OUTPUT CHARACTERISTICS OF SERIES & PARALLEL CONNECTED MODULES

	Identical Illumination			Partial Shading			
	V_{oc}(V)	I_{sc} (A)	P_{max}	V_{oc}(V)	I_{sc} (A)	P_{max} (W)	Power Loss (%)
Series Connected Module String	59.6	0.9	38.08	56.5	0.32	15.8	60.4
Parallel Connected Modules	20.3	2.65	34.5	20.1	1.8	23.56	31.7

The measurement results clearly show that application of the bypass diode has caused the current produced by the illuminated modules to pass through the bypass diode which creates the opportunity to deliver power to the load while as discussed in the previous parts, the results obtained from similar measurements without bypass diodes illustrated that the string was not capable of delivering power to the load in the case of existence of a fully shaded panel in the string.

V. CONCLUSIONS

Solar modules are interconnected with different configurations to meet the desired application requirements. The results of the experimental analyses confirm the direct relationship between power generation in solar modules and the amount of received irradiance values. According to the experimental measurement results, it is observed that although higher voltage values are obtained, series connected module strings are more sensitive to the shading effects compared with the parallel connected modules. It is also observed that even partial shading of a module in a series string leads to higher reductions in generated power amounts compared to the parallel connection conditions. On the other hand, parallel connection of modules lead to higher amounts of current under identical illumination but in the case of partial or full shading of modules, the current output is subjected to reductions while the output voltage remains unchanged.

Application of bypass diodes is considered as one of the most effective methods to decrease or eliminate the effects of hotspot and shading on solar modules. The experimental results show that, in the case of existence of a fully shaded solar module in a series string, passage of current through the shaded module has been impossible and hence no power has been delivered to the load. On the other hand, application of a bypass diode connected in parallel with a fully shaded module in a series string influences the passage of the current produced by the other modules and hence causes the power to be delivered to the load. Taking the experimental results into the account, it is obvious that when extended to large scale solar power plants, selection of appropriate module configurations and application of bypass diodes play major roles in improving the solar generator system efficiency limitis.

ACKNOWLEDGMENT

We would like to express our sincere thanks to Prof.Dr.Aykut Hocanin, Assoc.Prof.Dr.Ugur Atikol and Assoc.Prof.Dr.Fuat Egelioglu for their kind support throughout this study.

REFERENCES

[1] Y.T. Tan, D.S. Kirchen and N. Jenkins, "A model of PV generation suitable for stability analysis," *IEEE Trans. Energy Convers.*, vol.19, no.4, pp.748-755, Dec. 2004.

[2] A. Kajihara and A.T. Harakawa, "Model of photovoltaic cell circuits under partial shading," *Proc. IEEE Int. Conf. Ind. Technol. (ICIT)*, Hong Kong, 2005, pp.866-870.

[3] W. Xiao, W.G. Dunford and A. Capel, "A novel modeling method for photovoltaic cells", *Proc. IEEE 35th Annu. Power Electron. Spec. Conf. (PESC)*, Vol.3, 2004, pp.1950-1956.

[4] N. Celik and N. Acikgoz, "Modeling and experimental verification of the operating current of mono-crystalline photovoltaic modules using four- and five-parameter models," *Appl. Energy J.*, vol.84, no.1, 2007, pp.1-15.

[5] D. Sera, R. Teodorescu and P. Rodriguez, "*PV Module Model Based on Datasheet Values*," in *IEEE-ISIE*, Vigo, Spain, 2007, pp. 2392-2396.

[6] C. Carrero, J. Amador and S. Arnaltes, "A single procedure for helping PV designers to select silicon PV module and evaluate the loss resistances,"*J. Renewable Energy*, vol.32, no.15, 2007, pp.2579-2589.

[7] M.G. Villalva, J.R. Gazoli and E.R. Filho, "Comprehensive approach to modeling and simulation of photovoltaic arrays,' *IEEE Trans. Power Electron.*, vol.24, no.5, pp.1198-1208, May. 2009.

[8] A. Hovinen, "*Fitting of the Solar Cell IV-curve to the Two Diode Model*," Physica Scripta, Vol.T54, pp.175-176, 1994.

[9] J.A. Gow and C.D. Manning, "Development of a photovoltaic array model for use in power-electronics simulation studies," *IEE Proc. Elect.. Power Appl.*, vol.146, no.2, pp.193-200, 1999.

[10] S. Chowdhury, G. A. Taylor, S. P. Chowdhury, A. K. Saha and Y. H. Song, "Modelling, simulation and performance analysis of a PV array in an embedded environment," *Proc. 42nd Int..Univ. Power Eng. Conf. (UPEC)*, 2007, pp.781-785.

[11] L. A. Kosyachenko, *Solar Cells-Silicon Wafer-Based Technologies*,Rijeka, Croatia:Intech, 2011, pp.201-228.

[12] K. Ishaque, Z. Salam and Syafaruddin, "A Comprehensive MATLAB Simulink PV System Simulator with Partial Shading Capability Based on Two-Diode Model", *Journal of Solar Energy (Elsevier)*, Vol.85, pp.2217-2227, 2011.

[13] R.L-Y. Sah., R.N. Noyce and W. Shockley, "*Carrier Generation and Recombination in P-N Junctions and P-N Junction Characteristics*," in *IEEE-IRE*, Vol.9, pp.1228-1243, Sept.1957.

[14] Ting-Chung Yu and Tang-Shiuan Chien, "*Analysis and Simulation of Characteristics and Maximumu Power Point Tracking for Photovoltaic Systems*", in *IEEE-PEDS 2009*, Taoyuan-Taiwan, Nov.2009, pp.1339-1344.

[15] E. Karatepe, M. Boztepe, M. Çolak, "Development of a Suitable Model for Characterizing Photovoltaic Arrays with Shaded Solar Cells," *Journal of Solar Energy (Elsevier)*, Vol.81, pp.977-992, 2007.

[16] A. D. Hansen, P. Sorensen, L. H. Hansen and H.Bindner, "Models for Stand-Alone PV System," Rios National Laboratory, Roskilde, Denmark, Rep. Riso-R-1219(EN)/SEC-R-1.

Appendix I: A Case Study on Solar Data Collection and Effects of the Sun's Position in the Sky on Solar Panel Output Characteristics in Northern Cyprus

Moein Jazayeri, Sener Uysal, Kian Jazayeri, "A case study on solar data collection and effects of the sun's position in the sky on solar panel output characteristics in Northern Cyprus", in *Proceedings of 2013 International Conference on Renewable Energy Research and Applications, ICRERA*, Madrid, Spain, 2013.

***Abstract*—This paper mainly focuses on methods of calculations of sun`s position in the sky and analyses of its effects on solar panel output characteristics collected during a case study. Methods for calculations of sun`s position in the sky and measurement of solar panel output characteristics are reviewed and then followed by a case study on an experimental data collection system in Northern Cyprus. During the case study, the collected ground measured data are analysed and the results are compared. The solar angle of incidence and the sun`s position in the sky are calculated and compared for different time intervals along with panel output characteristics. The short-term data sets belong to three sample days representing sunny, rainy and cloudy conditions in May-2012. The results highlight the effects of sun`s position in the sky and the incidence angles of sunlight, during different time intervals and dates, on module output characteristics. The results provide helpful information for researchers and system designers for system yield estimation purposes.**

Keywords*— *photovoltaics, solar angle of incidence, solar energy, solar data collection, solar radiation, sun`s position in the sky

A Case Study on Solar Data Collection and Effects of the Sun`s Position in the Sky On Solar Panel Output Characteristics in Northern Cyprus

Moein Jazayeri, Sener Uysal, *Member, IEEE*, Kian Jazayeri

Electrical and Electronic Engineering Department., Eastern Mediterranean University
Famagusta, North Cyprus, via Mersin 10 Turkey
moein.jazayeri@cc.emu.edu.tr
sener.uysal@emu.edu.tr
kian.jazayeri@cc.emu.edu.tr

***Abstract*—This paper mainly focuses on methods of calculations of sun`s position in the sky and analyses of its effects on solar panel output characteristics collected during a case study. Methods for calculations of sun`s position in the sky and measurement of solar panel output characteristics are reviewed and then followed by a case study on an experimental data collection system in Northern Cyprus. During the case study, the collected ground measured data are analysed and the results are compared. The solar angle of incidence and the sun`s position in the sky are calculated and compared for different time intervals along with panel output characteristics. The short-term data sets belong to three sample days representing sunny, rainy and cloudy conditions in May-2012. The results highlight the effects of sun`s position in the sky and the incidence angles of sunlight, during different time intervals and dates, on module output characteristics. The results provide helpful information for researchers and system designers for system yield estimation purposes.**

Keywords*— *photovoltaics, solar angle of incidence, solar energy, solar data collection, solar radiation, sun`s position in the sky

I. Introduction

The need for energy in today`s world is a well-known matter for almost all applications. Considering some disadvantages of traditional energy sources like limitations, high expenses and pollution caused by these sources, producing clean and unlimited energy is the subject of many of current researches in the field of renewable energy. Solar energy as one of the renewable energy sources has shown a rapid growth during the recent years. The amount of solar energy provided by the sun in just one hour can meet the energy requirements of the entire world for one year [1].

Producing energy without any moving parts, noiseless operation and low maintenance costs are some of the advantages of PV systems. Also as PV systems can be mounted in unused spaces on rooftops there is no need for additional space to mount PV systems for residential and medium scale applications. Additionally, PV technology provides the required power supply for remotely operated systems where traditional energy transmission and distribution is not feasible. Furthermore, solar panels are portable and can be placed or mounted anywhere depending on the required power supply. Beside these advantages, high energy production cost is the major disadvantage of PV energy at the moment. Together with high energy production costs, some materials used in the production procedure of PV modules or solar panels like arsenic, cadmium and even silicon could create health problems for workers.

Fortunately due to development of mass production techniques and facilities for PV module and components, the cost trend of PV systems has become downward and the researches show that PV produced electricity is becoming cost competitive and is able to match the conventional energy costs in near future.

The amount of output power generated by a solar energy system is directly related to the incoming solar irradiance and hence having a detailed and precise knowledge of the amount of available solar energy is one of the main requirements during the design and planning procedure of any solar energy related application. Calculation and/or estimation of the amount of incoming solar energy have been the subject of many researches in the literature. A few examples of such studies have been reviewed in [2-5]. The amount of incoming solar energy to the earth`s surface and as a result, the output power generated by solar systems directly depends on the position and the movement of the sun in the sky. In this paper the position of the sun in the sky is simulated as the main factor and its effects on solar panel output powers are analyzed.

II. Sun`s Position in the Sky

There is a need to calculate the position of the sun as it is seen from the earth when information about solar radiation for a specific time and location is required. The Latitude of the Observation Point, The Julian Day Number and The Time of the Day, which is represented as hour angle from solar noon, are the most important three factors used during calculations of the position of the sun in the sky. In this paper all the calculations regarding the Sun`s position in the sky are presented based on the method and equations described in [6].

The relation between the Julian day, j, and the i^{th} day of a month is described in Table I.

978-1-4799-1464-7/13/$31.00 ©2013 IEEE

TABLE I. RELATIONSHIP BETWEEN THE JULIAN DAY AND THE i^{TH} DAY OF A MONTH

Month	J for i^{th} day of the month	Leap Year
January	i	
February	31+i	
March	59+i	(+1)
April	90+i	(+1)
May	120+i	(+1)
June	151+i	(+1)
July	181+i	(+1)
August	212+i	(+1)
September	243+i	(+1)
October	273+i	(+1)
November	304+i	(+1)
December	334+i	(+1)

The time of the day or local solar time is represented by hour angle, ω, and is set to zero at solar noon (12:00) which is the time that the sun is exactly due south. The concept of solar time is based on the geographical location (longitude) of the observation point and is different from local clock time. The passage of every one hour represents a 15 degrees rotation. The hour angle, in degrees, is obtained using the following equation;

$$\omega = 15(t - 12) \quad (1)$$

A. Declination Angle

The declination angle, (δ), is defined as the angle between the Equatorial Plane and the line joining the center of the Earth's sphere to the center of the Solar disk [6]. The declination of the sun varies with time but a constant value for each day can be used as the rate of change for any specific day is very small. The declination angle can be defined for any specific time interval using just one parameter, the day number. The declination angle can be defined using the following equation;

$$\delta = \sin^{-1}\{0.3978\sin(\grave{j} - 80.2^0 + 1.92(\sin(\grave{j} - 2.80^0)))\} \quad (2)$$

Where $\grave{j} = j \times \left(\frac{360}{365.25}\right)$ is the Julian day number expressed as a day angle in degrees [5].

B. The Solar Altitude Angle

The solar altitude angle or the Sun's height, (γ_s), as described in [6], simply can be defined as;

$$\gamma_s = \sin^{-1}(\sin\varphi\sin\delta + \cos\varphi\cos\delta\cos\omega) \quad (3)$$

Where,

φ : The latitude of the observation point
δ : The solar declination angle in degrees
ω : The solar hour angle

C. The Solar Azimuth Angle

The solar Azimuth angle, (α_s), which is defined as the angle between the sun and the South axis ($0^\circ = South, 90^\circ = West$) is obtained using (4)-(7) as follows [6];

$$\cos\alpha_s = (\sin\varphi\sin\gamma_s - \sin\delta)/\cos\varphi\cos\gamma_s \quad (4)$$

$$\sin\alpha_s = \cos\alpha_s\sin\omega/\cos\gamma_s \quad (5)$$

If $\sin\alpha_s < 0$ $\quad \alpha_s = -\cos^{-1}(\cos\alpha_s)$ (6)

If $\sin\alpha_s > 0$ $\quad \alpha_s = \cos^{-1}(\cos\alpha_s)$ (7)

The position of the sun at a specific time of a day is shown in Fig. 1.

D. Solar Angle of Incidence

Solar angle of incidence, (θ_i), is defined as the angle between sunlight rays and a normal vector on the solar module, as shown in Fig. 2. The maximum output power of a solar panel directly depends on the cosine of the solar angle of incidence and hence the knowledge regarding this parameter earns a great importance during solar system design procedures. The Solar Angle of Incidence is defined using the following equation;

$$\theta_z = \cos^{-1}[\cos(\beta)\cos(Z_s) + \sin(\beta)\sin(Z_s)\cos(\alpha_s - \alpha_m)] \quad (8)$$

Where,

β : Tilt angle of the solar collector ($Horizontal = 0^\circ$)
Z_s : Zenith Angle of the Sun
α_m : Module azimuth angle ($North = 0^0, East = 90^\circ$)

and,

$$Z_s = 90^\circ - \gamma_s \quad (9)$$

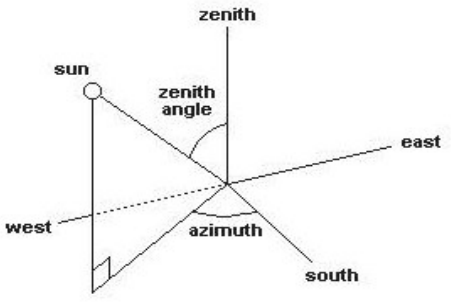

Fig. 1. The position of the sun at a specific time of a day

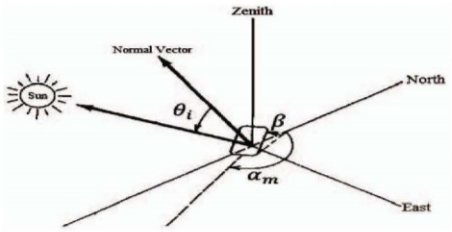

Fig. 2. Solar angle of incidence

III. Case Study : Ground Measurement of Solar Panel Output Data in Northern Cyprus and Experimental Analysis of Collected Data

In this part of the paper, the geographical characteristics, energy production and consumption profile of Northern Cyprus are explained in brief. This brief data is then followed by a short description of experimental system setup used for site measurements and data collection. The collected data is then analyzed and the results are discussed.

A. Geographical Characteristics, Energy Profile and Solar Energy Development in Northern Cyprus

Cyprus as the 3rd largest island in the Mediterranean is located at 33^0 east of Greenwich and 35^0 north of the equator. At the same time Cyprus is one of the best places for solar energy research and applications due to its geographical position. Cyprus has a Mediterranean climate with hot dry summers and mild winters [7].

1) *Energy Production and Consumption Profile in Northern Cyprus:* The energy consumption profile of Northern Cyprus is presented in Fig. 3. As it is clearly visible from the graphics the largest amount of energy, (32%), is used in houses. The most of the energy is consumed in houses for space and water heating applications.

Due to a forecast made by [8], the growth rate of PV energy production in Northern Cyprus is 20% in 2010 which is followed by 13% up to 2020, 6% up to 2030 and 3% up to 2040.

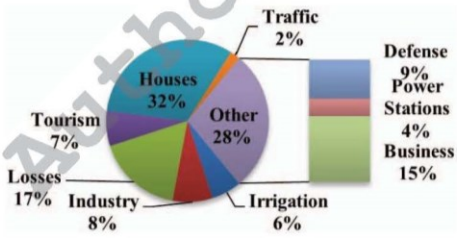

Fig. 3. Energy consumption profile in Northern Cyprus

B. Experimental Site Measurement and Data Collection System

The data used for analyses are measured and collected using a system consisting of software and hardware parts. The system which is constructed for data collection and measurements is somehow similar to the one introduced in [9].

The hardware part of the system consists of 6 commercially available crystalline silicon solar panels (P_{max} = 15 W, I_{sc} = 0.96 A, V_{oc} = 21.6 V) which are mounted at 17 m height from sea level on top of the Electrical and Electronic Eng. Dept. and an electronic circuit which is designed to transfer the collected solar data to a computer. The solar panels are aligned toward 6 different directions with a tilt angle of 45°. The main idea behind aligning solar panels in 6 different directions is to create the opportunity to follow, compare and analyze the effects of changes of sun`s position in the sky on the output characteristics of solar panels aligned in different directions.

The alignments used for solar panels are given in Table II. The angles are specified in degrees where "$0^{\circ} = South, 90^{\circ} = West$". The mentioned solar panels are shown in Fig. 4.

TABLE II. Angular Orientations of Solar Panels

Panel Alignment	Position
South	355^0
SouthEast	285^0
SouthWest	65^0
North	185^0
NorthEast	227^0
NorthWest	140^0

An electronic circuit, as shown in Fig. 5, is responsible of converting the analog input data collected from solar panels to digital and send them to a PC using serial port.

The terminals of each individual solar panel are connected in parallel to a constant valued power resistor, (load), to record the variation in panel output characteristics caused by changes in the sun`s position in the sky.

Measurements and data monitoring tasks are held using a visual basic based computer software. The software presents the opportunity for real-time monitoring of output voltage, current and power of each solar panel sent by the microcontroller and saves this data for further analyses.

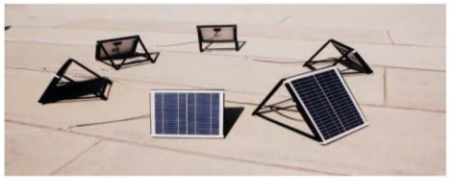

Fig. 4. Six solar panels in different alignements mounted at 17 m height from sea level on top of Electrical and Electronic Eng. Dept., Eastern Mediterranean University, used for ground measurement of solar data

C. Analysis of Collected Data

During this part of the study the collected ground measured solar panel output power data for three sample days are analyzed and the results are discussed and compared. The first set of data is collected on 08.05.2012 which is representing a sunny day. The second data set belongs to 16.05.2012 which is representing cloudy sky conditions and the last sample solar data set belongs to 21.05.2012 which is representing a day with heavy rain. The data are measured and logged every 15 min. along 24 hours. The main goal during the above mentioned analyses is to analyze the effects of movement of the sun in the sky during a full day on solar panel output characteristics and to show that the output power of each solar panel reaches to its maximum value as the incidence angle of sunlight beams reach to the closest value to 90°. The reason of selecting the instant output power of solar panels at every 15 min. is to create the opportunity of monitoring the fluctuations in output power due to changing environmental and atmospheric conditions. These kinds of effects can best be analyzed in cloudy days when panels are subjected to variable amounts of solar irradiance caused by passing clouds.

1) *Sun`s Position:* The Sun`s position and its movement in the sky is analyzed and simulated. The latitude of the observation point is $35^{\circ}8'22^{"}$. The Julian day numbers required for the calculations are obtained using Table I. Also declination angle, altitude angle and azimuth angles required for the calculations are calculated according to (1)-(7). As a result of the calculations, the sun`s position in the sky is obtained at different times for the specified three sample days. The sun`s positions for the 1st sample day is presented in Fig. 6, as an example. The mentioned data is presented in terms of sun`s altitude and azimuth angles in polar coordinates. Straight lines represent sun`s azimuth angle and the circles show sun`s elevation or altitude angles in degrees.

2) *Solar Angle of Incidence:* The solar angles of incidence are calculated according to (8) for all panel positions during each sample day. The results are presented in Fig. 7. All the graphics are based on Local Solar Time. It is obvious that for the 1st sample day (08/May/2012) the minimum incidence angle is reached at 12:00 (solar noon) for the South panel. This means that the incoming sun light is reaching the panel surface with the closest angle to perpendicular at this time. Analysis results show that panel output power increases as the incidence angle of the sunlight gets closer to 90°.

The minimum incidence angles on the South panel for the 2nd and 3rd sample days (16/May/2012) and (21/May/2012) are also obtained at 12:00. It is thought that cloud coverage and rain fall is preventing the panel to generate the maximum amount of output power when the minimum incidence angle values are obtained.

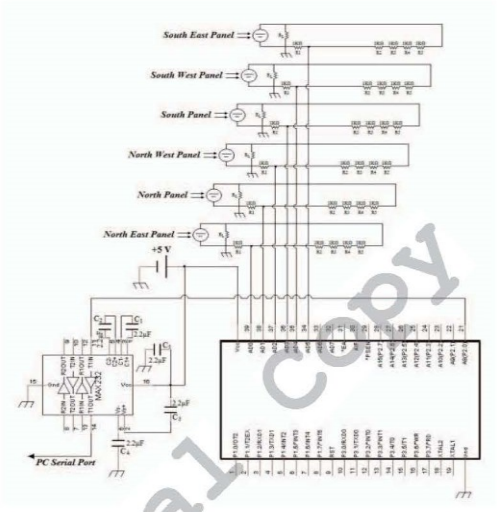

Fig. 5. The electronic circuit designed for data measurement, analog/digital data conversion and data transferring

As it is obvious from Fig. 6 and Fig. 7, the sun is due South at solar noon (12:00) and has the highest elevation or altitude in the sky at this time. Also the solar angle of incidence takes its smallest value at this time showing that the sunlight rays come on the module surface with the closest angle to normal at this time.

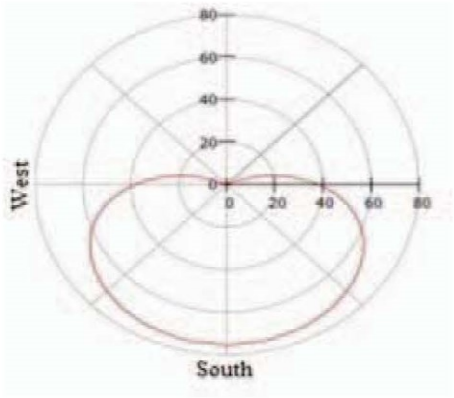

Fig. 6. Simulated sun`s position in the sky in a sunny day (08/May/2012)

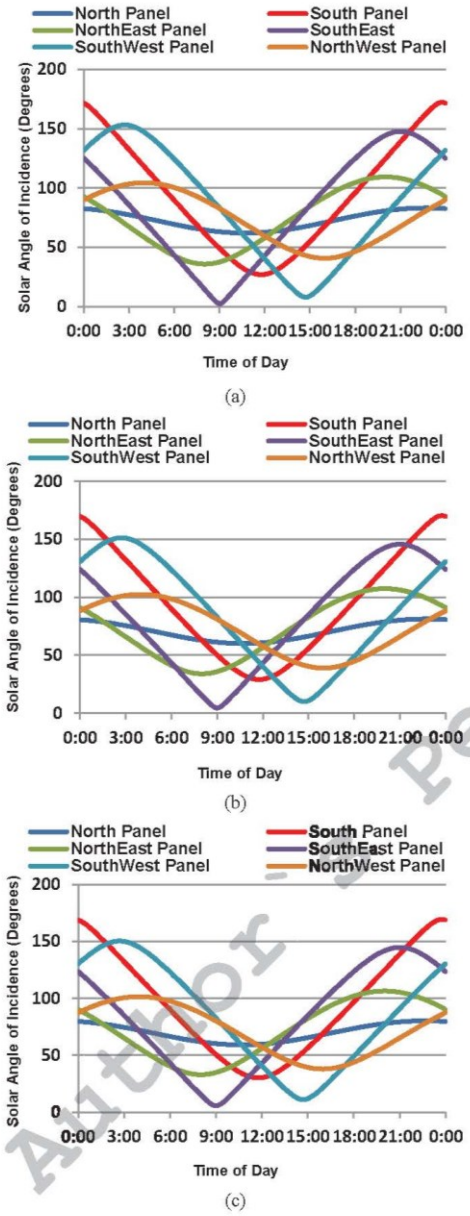

Fig. 7. Calculated solar angels of incidence, a) sunny day (08/May/2012), b) cloudy day (16/May/2012), c) rainy day (21/May/2012)

3) *Solar Panel Output Characteristics:* As a result of the analysis, it is obvious that the South panel has been producing the highest amount of power among the other panels for the first two sample days (Sunny and Cloudy conditions). The maximum value of power output for the 1st day for South panel is obtained at 13:15 pm (Local Time). Taking the differences between the local solar time and local time into the consideration, it is observed that this is the time when the incidence angle of sunlight beams has the closest value to normal and the sun has its maximum height in the sky. Hence it is confirmed that the maximum power output is obtained when the sunlight is hitting the panel surface with the closest angle to 90°. Also it is obvious that beside the lower values of output power obtained with the other modules, the maximum points are obtained at different time intervals. For North East and South East panels the maximum power outputs are obtained before 13:15 pm and for North West and South West modules this is happened after this time. The effects of sun's movements in the sky on panel output characteristics are clearly visible from the graphics. The output powers of all solar panels for the specified three sample days are compared in Fig. 8. It is clearly visible that the greatest amount of output power is generated by the South panel on the first two sample days. South East and South West panels are following this panel on 08/May/2012. The output power percentage generated by the South panel is decreased on 16/May/2012 compared to the previous day while the output power percentage of South East and North East panels is increased. This is continued on 21/May/2012 where the highest power output percentage belongs to the South East panel. The South panel has generated the second highest portion of power and the power produced by the North East panel has also been increased, compared to the first two days. Though the total amount of output power generated by the panels is decreased on the last two sample days, due to the effects of cloud coverage and heavy rain, the increasing rate of power production on North East and South East panels is a result of changes in the sun's movement in the sky. The contribution of each module to the total generated power is tabulated in Table III. It is observed that the least amount of power has been generated by the North module during the 1st and 3rd sample days and the Northwest panel during the 2nd sample day.

TABLE III. CONTRIBUTION OF MODULES TO THE TOTAL POWER GENERATION

Panel Alignment	08/05/2012	16/05/2012	21/05/2012
South	%28	%28	%18
SouthEast	%22	%25	%28
SouthWest	%19	%11	%11
North	%6	%11	%10
NorthEast	%12	%17	%21
NorthWest	%19	%8	%12

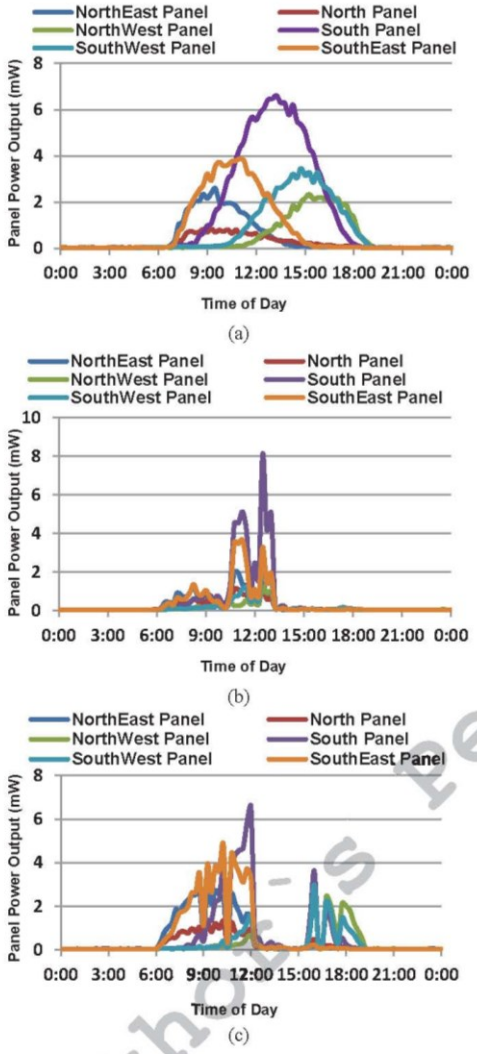

Fig. 8 Measured Module Output Powers, (a) Sunny Day (08/May/2012), (b) Cloudy Day (16/May/2012) , (c) Rainy Day (21/May/2012)

IV. Conclusions

The results of analyses of the collected data show that almost the highest amount of power has been generated by the modules which are aligned toward the South direction. The sunlight beams hit the panel surface of the South aligned panel with the closest angle to 90° and the sun has its maximum elevation in the sky at almost 12:00 (LST). It is observed that the panel generates the highest amount of power almost at the same time in a sunny day. The incidence angles present the closest value to the normal line at the same time for the other sample days but the cloud coverage and heavy rain cause the output power to be far from the maximum point. The shading effects caused by the cloud coverage cause rapid fluctuations in module power outputs. Also analyses of power generation ratios show that the movement of the sun in the sky has a direct effect on panel output powers. As the sun`s position is getting closer to the east on any specific day, the power generation ratios of the east panels starts to be increased while the other panels produce smaller amounts of power. As a general result, it is observed that the sun is due south at solar noon when the sun has the highest elevation in the sky and sunlight beams come to a South oriented solar panel with the closest angle to 90°. The analysis results show that a South oriented solar panel generates the maximum power at solar noon during a sunny day.

Acknowledgements

We would like to express our sincere appreciation to our dear friend Reza Abrishambaf for his helps and contributions throughout the preparation of data collection system setup and other various stages of this work.

References

[1] P.A. Lynn, *Electricity from Sunlight : An Introduction to Photovoltaics*, West Sussex, UK: Wiley, 2010, pp.1-23.

[2] M. Wittmann, H. Breitkreuz, M. Schroedter-Homscheidt and M. Eck, "Case Studies on the Use of Solar Irradiance Forecast for Optimized Operation Strategies of solar Thermal Power plants", *IEEE J. Sel. Topics Appl. Earth Observations and Remote Sensing*, Vol. 1, No. 1, pp.18-27, March 2008.

[3] E. Lorenz, J. Hurka, D. Heinemann and H.G. Beyer, "Irradiance Forecasting for the Power Prediction of Grid-Connected Photovoltaic Systems", *IEEE J. Sel. Topics Appl. Earth Observations and Remote Sensing*, Vol. 2, No.1, pp.2-10, March 2009.

[4] M. Suri, T. Huld, T. Cebecauer and E. Dunlop, "Geographic Aspects of Photovoltaics in Europe: Contribution of the PVGIS Website", *IEEE J. Sel. Topics Appl. Earth Observations and Remote Sensing*, Vol.1, No.1, pp.34-41, March 2008.

[5] G. Notton, C. Cristofari, M. Muselli, P. Poggi and N. Heraud, "Hourly Solar Irradiation Estimation: From Horizontal Measurements to Inclined Data", in *IEEE-ISEIM*, Corte-Ajaccio, France, 2006, pp.234-239.

[6] K. Schamer and J. Greif, *The European Solar Radiation Atlas Vol.1: Fundamentals and Maps*, Paris, France: Les Presses de l`Ecole des Mines, 2000, pp.23-42.

[7] J. Michaelides and P. Votsis, "Energy Analysis and Solar Energy Development in Cyprus", *J. Computing and Control Engineering Journal*, Vol.2, pp.211-215, 1991.

[8] *Concentrating Solar Power for the Mediterranean Region*, German Aerospace Center (DLR), Stutgart, Germany, 2005.

[9] J. Machacek, Z. Prochazka and J. Drapela, "System for Measuring and Collecting Data from Solar-Cell Systems", in *9th International Conference – Electrical Power Quality and Utilisation*, Barcelona, Spain, 2007, pp.1-4.

Appendix J: Experimental Analysis of Effects of Installation Alignment and Solar Insolation on Power Generation by Solar Panels

Moein Jazayeri, Sener Uysal, Kian Jazayeri, "Experimental analysis of effects of installation alignment and solar insolation on power generation by solar panels", in *Proceedings of the 3rd IEEE Global Humanitarian Technology Conference, GHTC 2013 (2013)*, San Jose, CA, USA, 2013.

***Abstract*— This paper mainly focuses on the effects of variations of solar irradiance on PV panel power outputs and considers the importance of choosing the right orientation for system installations. The analyses are based on real-time measured data collected during a 6-Month period (October/2012-March/2013) in Northern Cyprus. The mentioned data presents the months with the lowest solar insolation and the results clearly illustrate the direct relationship between the amounts of the solar irradiance and power generation by PV panels. The results can be utilized for effective use of PV systems, especially for rural areas and locations with relatively less amounts of available solar irradiance.**

Keywords*— *photovoltaics, solar energy, solar insolation, solar power generation, solar data collection, sun`s position in the sky

Experimental Analysis of Effects of Installation Alignment and Solar Insolation on Power Generation by Solar Panels

Moein Jazayeri, Sener Uysal, Kian Jazayeri

Electrical and Electronic Engineering Department, Eastern Mediterranean University

Famagusta, North Cyprus, via Mersin 10 Turkey

moein.jazayeri@cc.emu.edu.tr

sener.uysal@emu.edu.tr

kian.jazayeri@cc.emu.edu.tr

***Abstract*— This paper mainly focuses on the effects of variations of solar irradiance on PV panel power outputs and considers the importance of choosing the right orientation for system installations. The analyses are based on real-time measured data collected during a 6-Month period (October/2012-March/2013) in Northern Cyprus. The mentioned data presents the months with the lowest solar insolation and the results clearly illustrate the direct relationship between the amounts of the solar irradiance and power generation by PV panels. The results can be utilized for effective use of PV systems, especially for rural areas and locations with relatively less amounts of available solar irradiance.**

Keywords*— *photovoltaics, solar energy, solar insolation, solar power generation, solar data collection, sun`s position in the sky

I. INTRODUCTION

The rising energy demand for various applications in today`s world and the limitations and treats associated with the conventional energy sources, all draw the attentions to renewable energy resources. Research findings show that utilization of renewable sources can reduce the dependency on conventional energy resources by 70% by 2040 [1] while solar energy as a reliable, unlimited and clean source of energy is known to have the fastest growth rate among all other renewable energy sources [2]. Solar cells first entered human`s life in 1883 [3] and found various application areas in today`s energy sector. Just like any other source of energy, photovoltaic energy production also has some advantages and disadvantages. While infinity of the power source, low operation costs, energy production without any moving part, long life time of the modules, modularity and quick installation are some of the advantages of PV energy, high installation costs, lack of economically efficient energy storage and relatively low efficiency of energy conversion are some disadvantages which should be overcome for efficient use of this renewable power source. However, the cost trend of PV systems has become downward due to mass production techniques and facilities for modules and components. The annual capacity increasing rate of PV energy has been 58% during 2006-2011[2] and research findings show that PV energy is becoming cost competitive and will be able to replace conventional energy sources in near future.

Providing energy for off-grid devices and systems together with large-scale energy production as a substitute for conventional energy sources are the two main application areas of PV energy in Today`s world. Especially during energy planning for rural areas in developing countries, off-grid PV applications play great roles, considering that 1.4 billion people in the world do not have access to reliable energy [1]. Off-grid systems can meet electricity, heat and energy requirements in such rural areas while large-scale PV power plants contribute to the existing energy grids. Land-occupation and system efficiencies are two important concerns regarding both off-gird and grid-connected PV energy systems. According to research results, in geographical areas with high amounts of solar insolation, the area required for ground-mounted PV systems is less than conventional coal-fuel systems while large-scale PV power plants should carefully be located and installed to obtain optimum system performances [2]. According to research findings, replacement of the existing electricity grids with PV power plants can reduce emission of greenhouse gases, main contaminants, heavy metals and radioactive species at least by 89% [2]. The significance is better felt considering that according to the estimations made by the World Health Organization (WHO), 2.5 million women and children die each year from breathing the gases produced by conventional energy sources [1]. Technical and theoretical potentials of solar energy are compared with the other renewable energy sources in Table I. The statistics of Table I. clearly show that, solar energy is limitedly being utilized in today`s world though that it provides the greatest potentials among all other renewable energy sources. The mentioned utilization status of PV energy has been the reason for many research projects to be conducted in order to reduce the costs and improve higher energy conversion efficiencies.

Utilization of PV systems has been analyzed from various aspects in the literature. As an example, the effects of penetration of PV systems, as distributed generation technologies, on the voltage profile in low-voltage networks is analyzed in [4]. This paper uses the real-time measured PV panel output power data, collected during a 6-Month time period, for purposed analysis. The mentioned data sets belong to the period between October/2012 – March/2013 presenting the months with the lowest amounts of available solar

978-1-4799-2402-8/13/$31.00 ©2013 IEEE

insolation. The data sets are collected from 6 identical solar panels aligned toward 6 different directions. The obtained results highlight the importance and effects of selection of the most appropriate orientation for system installations on power generation by PV panels. The collected data are also compared with the calculated hourly solar irradiance values and the direct relationship between the amounts of available solar insolation and power production by solar panels is illustrated.

TABLE I. TECHNICAL AND THEORETICAL POTENTIALS OF RENEWABLE ENERGY SOURCES [1]

Resource	Current Use (EJ/Year)	Technical Potential (EJ/Year)	Theoretical Potential (EJ/Year)
Hydropower	9	50	147
Biomass	50	>276	2900
Solar Energy	0.1	>1575	3900000
Wind Energy	0.12	640	6000

II. SUN AS A SOURCE OF ENERGY

The amount of solar energy provided by the sun in just one hour can meet the energy requirements of the entire world for one year [5]. Such a huge potential of energy and the other advantages mentioned in the previous part of the paper makes the `Sun` an attractive source of energy. However, the limitations and other disadvantages corresponding to this energy source should be taken into the consideration for effective and optimum utilization of solar energy.

The amount of energy delivered from the sun to the Earth`s surface directly depends on the position of the sun with respect to observation points on the Earth. The amount of available solar insolation for different geographical locations is not constant and similar to each other. Latitudes of observation points, environmental conditions, shadows, etc. all affect the incoming solar irradiance. Thus, estimation or calculation of the available solar insolation is of prior importance for PV energy related application planning and design procedures. The mentioned importance is better felt in locations with lower amounts of sunlight, where an efficient use of the available solar irradiance plays a great role in meeting the energy requirements. Analysis of satellite image data, utilization of numerical weather prediction models, neural network based models, etc. are some of the techniques employed for prediction or calculation of the amount of available solar insolation and many research projects have been conducted on such methods and techniques [6]-[11].

The sun`s position in the sky with respect to observation points on the Earth`s surface can be defined using two main factors [13], as follows;

- *Sun`s Altitude Angle* ($\gamma_s$): The sun`s elevation in the sky.
- *The Solar Azimuth Angle* (α_s): The angle between the sun and the South axis ($0^\circ = South, 90^\circ = West$).

As indicated before, the amount of incoming solar irradiance to the Earth`s surface directly depends on the position of the sun in the sky. Thus, various sun tracking techniques have been developed and many valuable researches have been conducted for determination and tracking of the sun`s position in the sky [12]-[15].

The total amount of incoming solar radiation from the sun to the Earth`s surface is defined as `Global Radiation` and consists of three main components [3] as follows;

- *Direct or Beam Radiation:* Beam of sunlight that reaches the surface in a straight line from the sun without any reflection or scattering.
- *Diffuse Radiation:* The radiation scattered toward the receiver.
- *Albedo Radiation:* The radiation reflected from the ground.

In order to highlight the influences of geographical location on the amounts of the received solar irradiance, the monthly mean values of global solar irradiance on a horizontal surface for some different cities around the world are illustrated in Fig. 1. The comparisons are made based on 22-years averaged real-time measured data sets provided by `NASA Atmospheric Science Data Centre`. It is obvious from the figure that the geographical locations of observation and measurement stations have strong effects on the amount of the received solar insolation. The locations closer to the equator receive more energy from the sun while the cities in northern parts receive relatively smaller amounts of solar insolation.

III. METHODOLOGY

The utilized methodology for field data collection and measurements, calculation methods of hourly irradiance values and the methods of analyses of the measured data are briefly introduced during this part of the paper. The data sets belong to a 6-Month period collected between October/2012 – March/2013 in Famagusta, Northern Cyprus. The statistics of Fig. 1, clearly show that Famagusta, due to its geographical location, receives relatively high amounts of solar insolation during a year. The mentioned time period is chosen to represent the months with minimum incoming solar insolation amounts. Six identical crystalline silicon solar panels (P_{max} = 15 W, I_{sc} = 0.96 A, V_{oc} = 21.6 V) are utilized for data collection purposes. The panels are aligned toward six different directions (South, South East, South West, North, North East and North) with a tilt angle of 45°. The panels are mounted at 17 meters height from sea level on top of the Electrical and Electronic Eng. Dept., Eastern Mediterranean University (35° 8' 51" N, 33° 53' 58" E). The main idea is to track the effects of variations in the position of the sun in the sky on panel power outputs during a day and to determine the most appropriate orientations for PV system installations. An electronic circuit is utilized to transfer the measured power output data from the solar panels to a computer through serial port. The terminals of each panel are connected to a constant valued power resistor (load) to record and scale the variations in panel power outputs with respect to the variations in the incoming solar insolation as a function of the sun`s position in the sky.

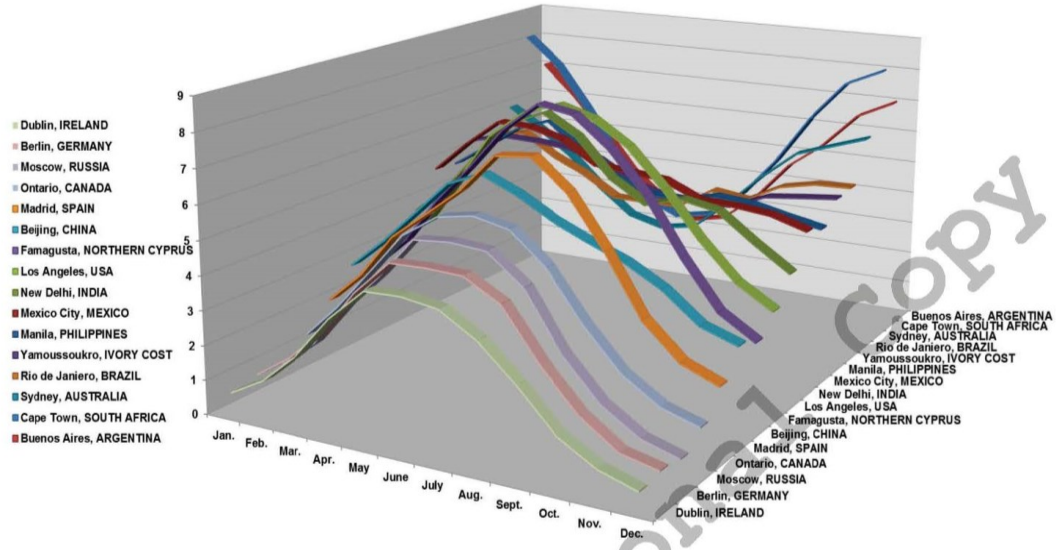

Fig. 1. Monthly Averaged Insolation on a Horizontal Surface (kWh/m^2/day) for Different World Cities

The mentioned data are averaged over a minute and logged with the rate of 60 samples per hour in order to obtain hourly mean values of power generation by each individual solar panel. The mentioned hourly mean values of panel output powers are calculated between 08:00 – 18:00 for each day during the mentioned time period. These data are then averaged over each month in order to obtain the monthly average values of mean hourly power generation by solar panels during the time period.

On the other hand, the hourly mean values of global irradiance incoming to the surface of solar modules with the mentioned tilt angle are calculated based on the monthly mean values of global irradiance on a horizontal surface for the observation point, as described in Fig. 1. The calculations are made based on the method introduced by [3]. The main goal is to highlight the direct relationship between the variations in the values of the incoming solar irradiance and the amounts of power generation by solar panels.

IV. Results And Experimental Analysis Of Collected Data

The real-time measured solar panel output power data sets and calculated hourly global solar irradiance values are analyzed and the relationship between the incoming solar insolation and power generation by solar modules is considered during this part of the paper.

It was mentioned before that the generated output power data from 6 identical solar panels are used to calculate the monthly average of mean hourly power generation ratios during the mentioned 6-months period. The results are illustrated in Fig. 2 for South and North oriented panels representing the maximum and minimum ratios of power generation during the time period, respectively. The results are illustrated as hourly mean values between 08:00 – 18:00 during each month.

Fig. 2 clearly shows that the ratio of power generation by the South oriented solar panel has been greater than the power generation ratio by the North oriented panel for each hour during the whole time period. The South oriented panel has been generating the highest power while the North oriented panel has the least amount of power generation among the mentioned 6 solar panels. According to the results of Fig. 2, both of the panels have generated their maximum amounts of power in October and March and the minimum power generation belongs to December. Also the power generation rate has reached to the maximum between 12:00 – 13:00 and the minimum power generation occurs after 16:00 during the time period.

The hourly mean values of power generation by solar panels are averaged during a day to obtain the daily average values of power generation by solar panels during each month and the results are presented in Fig. 3. The figure shows that the North, North East and North West oriented panels have generated very small amounts of power in a day during the mentioned time period.

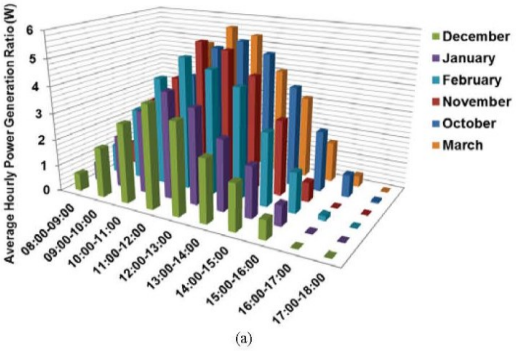

(a)

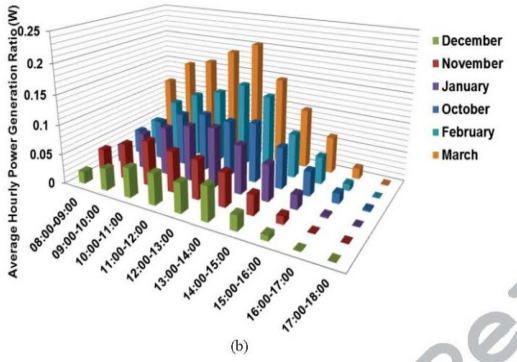

(b)

Fig. 2. Monthly Averag of Hourly Mean Values of Output Power Generated by a) South Oriented Panel, b) North Oriented Panel

The results of Fig. 3 show that the panels aligned toward the South orientations (South, South East and South West) have generated the most power during the mentioned time period. The South panel has generated the most amount of power during each month while South East and South West panels have followed this amount. At the same time, the power generated by the South East directed panel has been greater than the amount of generated power by the South West oriented panel during each month. Also Fig. 3 clearly shows that the power generation by the South oriented panel has been minimum during January and December and the maximum values obtained during October and March. It should be considered that January and December have the least amounts of incoming solar insolation and October and March represent the maximum amounts among the mentioned time period. This situation clearly illustrates the direct relationship between the amount of received solar insolation on panel surface and the amount of power generation by each individual solar panel.

In order to obtain the share of contributions of each solar panel in total power generation, the mean daily values of power generation by each individual solar panel have been averaged during the whole time period and the results are illustrated in Fig. 4.

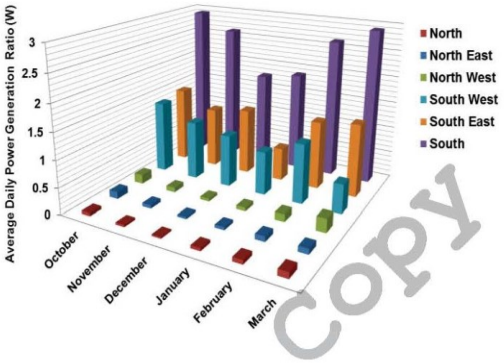

Fig. 3. Monthly Mean Values of Average Daily Power Generation Ratios By Solar Panels

Fig. 4 shows that the South oriented solar panel has the greatest contribution in power generation with %50. The South East and South West oriented panels have been following this amount by %24 and %20, respectively. At the same time, the North oriented panels (North, North East and North West) have presented the least contribution to power generation during the specified time period. The results are all confirming the direct relationship between the movement of the sun in the sky and power generation by solar panels. The importance of installation of PV systems in appropriate orientations for efficient and optimum utilization of the available solar insolation is clearly confirmed by the results. The results can be interpreted as a small representation of the situation of power generation by solar energy systems installed in different orientations. Also the results of Fig. 4 clearly show that variations in the orientation of solar modules can cause considerable variations in their power generation capabilities.

In order to highlight the relationship between the amounts of incoming solar insolation and power generation in solar panels, the data sets of Fig. 1 have been used to calculate the hourly mean values of global solar irradiance falling on solar panels during the time period. The calculations are made based on the method introduced by [3]. The calculation results are averaged over each month and the monthly average values of mean hourly solar irradiance on solar panels are obtained. The mentioned results are presented in Fig. 5 for the South oriented solar panel.

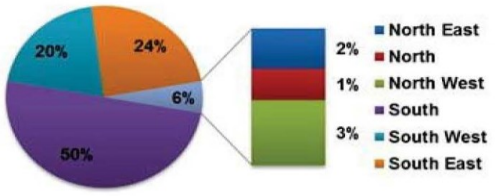

Fig. 4. Average Power Generation Ratio by Solar Panels During the Time Period

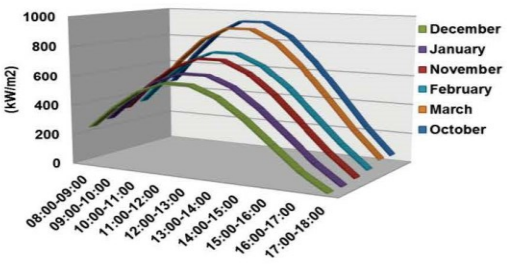

Fig. 5. Monthly Average Value of Mean Hourly Global Solar Irradiance Falling on South Oriented Solar Panel

The results of Fig. 5 show that the maximum amounts of mean hourly solar irradiance belong to October and March while the minimum values are obtained during December and January. Comparison of the mentioned results with the results of Fig. 3 shows that there is a direct relationship between the amounts of the received solar insolation on panel surface and the amounts of the generated power. The energy production of the South oriented panel has been maximum during October and March where according to the results of Fig. 2a, the maximum power generation in March and October has occurred between 12:00-13:00. Comparison of these results with the results obtained in Fig. 5, once again, approves the dependency of power generation by solar panels to the amount of the received solar insolation on their surface.

For a better comparison of the improvements obtained with an appropriate alignment, MATLAB/Simulink platform is utilized to simulate a series string including 17 SOLAREX MSX-60 type (P_{max} = 60 W, V_{oc} = 21.1 V, I_{sc} = 3.8 A) solar panels. The simulations are based on one-diode mathematical model of a solar cell [16],[17]. The theoretical MPP of the mentioned string of panels under STC is 1020 W which, as an example, can be used to meet the small-scale off-grid home lighting requirements in rural areas or during energy outage situations. The monthly average value of maximum mean hourly solar irradiance received by the string with the previously mentioned 6 different orientations is used for simulations and the string maximum power point values are recorded. The simulation results of string MPP values are presented in Fig. 6. The results clearly show that the highest value of maximum power produced by the string belongs to the South oriented string while the smallest value corresponds to the North oriented string during the time period. According to the results, even in December with the smallest amount of the received solar insolation, the maximum power generated by the South oriented string is almost 6 times greater than the maximum power produced by the North oriented string and this ratio is greater during the other months.

As indicated in the earlier parts of the paper, the land-use and system efficiency are two important concerns which should be considered for efficient use of PV systems. The simulation results confirm that an appropriate alignment of PV systems leads to significant improvements in power generation which leads to cost reduction and overall efficiency improvement.

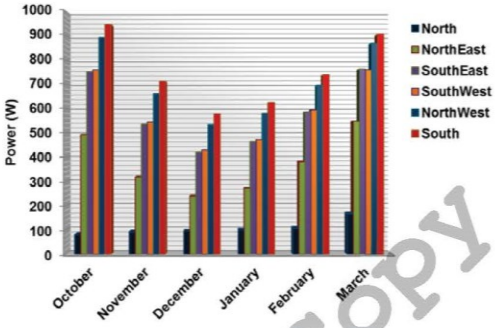

Fig. 6. Monthly Average Value of the Simulated Maximum Power Amounts Generated by Solar Panels in 6 Different Orientations

Higher power generation amount creates the opportunity of having more power with the same cost and land-use, which is highly considerable both in rural places of developing countries and areas with less insolation amounts.

V. Conclusions

Solar energy has found a greater share in meeting energy requirements in today`s world. Beside the disadvantages of this clean energy source, the advantages have made it one of the most important potential sources during energy planning procedures and the technological developments have increased its growth rate and popularity.

Though the sun is one of the most reliable clean energy sources, the amount of solar energy available on different geographical locations on the earth`s surface is not identical and similar to each other. The geographical location, environmental conditions, etc. all affect the incoming solar energy. Therefor having a detailed and precise knowledge regarding the available energy amounts carries a great importance for effective and optimum utilization of this clean energy source. The mentioned importance is better felt in countries and locations with relatively less amounts of solar energy where efficient use of the energy plays great role in energy management and meeting energy requirements.

The results of this study clearly highlight the direct relationship between the amount of incoming solar energy and the power generated by solar panels. The mentioned amount of energy directly depends on the sun`s movement in the sky. The system which is utilized for this study is designed to create the opportunity of tracking the effects of variations in the sun`s position in the sky on solar panel output powers.

According to the results, the South oriented solar panel is capable of generating the most amount of energy among panels aligned toward other orientations, even during the time period with relatively less amounts of incoming solar insolation. Also the results show that the North oriented solar panel has been generating the least energy amounts during the same time period as an opposite to the South oriented panel. Obtaining more power with the same number of solar panels leads to

reduction of energy generation cost and land-occupation. The results provide helpful information for selection of the most appropriate orientation for solar system installations in northern hemisphere while PV systems in the southern hemisphere or near the equator would need to be oriented toward the sun.

The results show that a South oriented solar panel has % 50 shares in power generation in a system including 6 identical solar panels with different orientations. According to the results, %94 of total energy production during a 6-month time period has been handled by South, South West and South East oriented panels and North oriented panels have presented very small contributions to energy production during the mentioned time period.

The results of this study can be assumed as a presentation for a big picture of solar energy systems which highlight the effects of installation orientations and dependencies of power generation by PV systems on the amounts of incoming solar irradiance and sun`s movement in the sky. The results can be considered for an efficient use of solar energy, especially for applications in rural areas or locations with relatively less amounts of sunshine. The results also illustrate that how can the selection of appropriate installation orientations improve the overall system efficiency and reduce the cost of energy production from sunlight.

REFERENCES

[1] B. Jeffries, K. Leun, B. Wesselink and K. Blok, "The energy report," WWF International, Switzerland, Tech. Rep., 2011.

[2] A. Archambault, "Solar PV atlas: solar power in harmony with nature," WWF International, Switzerland, Tech. Rep., 2012.

[3] A. Luque and S. Hegedus, *Handbook of Photovoltaics Science and Engineering*, West Sussex, UK : Wiley, 2003, pp.905-933.

[4] P. C. Chen, R. Salcedo, Q. Zhu, F. Leon, D. Czarkowski, Z. P. Jiang, V. Spitsa, Z. Zabar and R. E. Uosef, "Analysis of voltage profile problems due to the penetration of distributed generation in low-voltage secondary distribution networks,` *IEEE Trans. Power Del.*, vol.27, no.4, pp.2020-2028, Oct. 2012.

[5] P.A. Lynn, *Electricity from Sunlight : An Introduction to Photovoltaics*, West Sussex, UK: Wiley, 2010, pp.1-23.

[6] E.Lorenz, J.Hurka, D.Heinemann, and H.G. Beyer, "Irradiance forecasting for power prediction of grid-connected photovoltaic systems," *IEEE Journal of Selected Topics in Applied Earth Observations and Remote Sensing*, Vol.2, pp.2-10, March 2009.

[7] H. Bulut and O.Büyükalaca, "Simple model for the generation of daily global solar-radiation data in Turkey," *Journal of Applied Energy (Elsevier)*, Vol.84, pp.477-491, 2007.

[8] S.S. Chandel and R.K. Aggarwal, "Estimation of hourly solar radiation on horizontal and inclined surfaces in Western Himalayas," *Journal of Smart Grid and Renewable Energy*, Vol.2, pp.45-55, 2001.

[9] F.S. Tymvios, C.P. Jacovides, S.C. Michaelides, and C.Scouteli, "Comparative study of Angstrom's and artificial neural networks' methodologies in estimating global solar radiation," *Journal of Solar Energy (Elsevier)*, Vol.78, pp.752-762, 2005.

[10] N.Z. Al-Rawahi, Y.H. Zurigat, and N.A. Al-Azri, "Prediction of hourly solar radiation on horizontal and inclined surfaces for Muscat/Oman," *The Journal of Engineering Research*, Vol.8, pp.19-31, 2011.

[11] M.Wittmann, H.Breikreuz, M.Schroedter-Homscjeidt, and M.Eck, "Case studies on the use of solar irradiance forecast for optimized operation strategies of solar thermal power plants," *IEEE Journal of Selected Topics in Applied Earth Observations and Remote Sensing*, Vol.1, pp.18-27, March 2008.

[12] K. Scharner and J. Greif, *The European Solar Radiation Atlas Vol.1 : Fundamentals and Maps*, Paris, France: Les Presses de l`Ecole des Mines, 2000, pp.23-42.

[13] R. Tejwani and C.S. Solanki, "360°C Sun Tracking with Automated Cleaning System for Solar PV Modules", in *IEEE-PVSC*, Hawaii, USA, 2010, pp.2895-2898.

[14] A. Ponniran, A. Hashim and H.A. Munir, "A Design of Single Axis Sun Tracking System", in *IEEE-PEOCO*, Selangor, Malaysia, 2011, pp.107-110.

[15] G. Chicco, J. Schlabbach and F. Spertino, "Performance of Grid-Connected Photovoltaic Systems in Fixed and Sun-Tracking Configurations", in *IEEE - Power Tech*, Lausanne, 2007, pp.677-682.

[16] S. Liu and R.A. Dougal, "Dynamic multiphysics model for solar array," *IEEE Trans. Energy Convers.*, vol.17, no.2, pp.285-294, Jun. 2004.

[17] M.G. Villalva, J.R. Gazoli and E.R. Filho, "Comprehensive approach to modeling and simulation of photovoltaic arrays,` *IEEE Trans. Power Electron.*, vol.24, no.5, pp.1198-1208, May. 2009.

Appendix K: A Simple MATLAB/Simulink Simulation for PV Modules Based on One-Diode Model

Moein Jazayeri, Sener Uysal, Kian Jazayeri, "A simple MATLAB/Simulink simulation for PV modules based on one-diode model", in *Proceedings - High Capacity Optical Networks and Emerging/Enabling Technologies, HONET-CNS*, Famagusta, North Cyprus, 2013.

***Abstract*—This paper proposes a simple and practical simulation model for solar modules using MATLAB/Simulink. The model is based on a single-diode mathematical model of a solar cell and is capable of accurate modeling of I-V and P-V characteristics of a solar module. Model parameters are obtained from manufacturer`s datasheets and series and shunt resistances are calculated using a simple method based on open-circuit voltage, short-circuit current and irradiance values. The model is interfaced with SimPowerSystems toolbox. This feature makes the model capable of being used with power electronic devices and elements for advance analyses. The model is validated using measured I-V characteristics of a commercially available crystalline silicon solar module and the effects of environmental conditions (temperature and irradiance) as well as the effects of cell parameters like series and shunt resistances on module characteristics are investigated. The proposed model is capable of being used by solar energy researchers, system analysts and designers as a simple and helpful tool for advance analysis requirements.**

***Keywords*—solar energy, solar cell, solar module, module characteristics, simulink.**

A Simple Matlab/SIMULINK Simulation for PV Modules Based on One-Diode Model

Moein Jazayeri, Sener Uysal, Kian Jazayeri

Electrical and Electronic Engineering Department, Eastern Mediterranean University

Famagusta, North Cyprus, via Mersin 10 Turkey

moein.jazayeri@cc.emu.edu.tr

sener.uysal@emu.edu.tr

kian.jazayeri@cc.emu.edu.tr

Abstract—**This paper proposes a simple and practical simulation model for solar modules using MATLAB/Simulink. The model is based on a single-diode mathematical model of a solar cell and is capable of accurate modeling of I-V and P-V characteristics of a solar module. Model parameters are obtained from manufacturer`s datasheets and series and shunt resistances are calculated using a simple method based on open-circuit voltage, short-circuit current and irradiance values. The model is interfaced with SimPowerSystems toolbox. This feature makes the model capable of being used with power electronic devices and elements for advance analyses. The model is validated using measured I-V characteristics of a commercially available crystalline silicon solar module and the effects of environmental conditions (temperature and irradiance) as well as the effects of cell parameters like series and shunt resistances on module characteristics are investigated. The proposed model is capable of being used by solar energy researchers, system analysts and designers as a simple and helpful tool for advance analysis requirements.**

Keywords—solar energy, solar cell, solar module, module characteristics, simulink.

I. INTRODUCTION

The rising energy demand for various applications in today`s world and limited amount, pollution and other risks of conventional energy resources all point to the sun as a reliable, unlimited and clean resource of energy. Solar cells first entered human`s life in 1883 [1] and found various application areas in today`s energy sector. While infinity of the power source, low operation costs, energy production without any moving part, long life time of the modules, modularity and quick installation are some of the advantages, high installation costs, lack of economically efficient energy storage and relatively low efficiency of energy conversion form some disadvantages for this renewable power source. However the cost trend of PV systems has become downward due to mass production techniques and facilities for modules and components and researches show that PV energy is becoming cost competitive and will be able to replace the conventional energy sources in near future.

However having precise and detailed information regarding the behavior of solar generators (solar cells, solar modules, solar arrays, etc.) is a must for an efficient use of this clean and unlimited energy source, planning and design procedures of solar power generating systems.

Mathematical modeling of the electrical equivalent circuit of a solar cell, as the smallest building block of every solar energy system, is the most widely used method by researchers to characterize solar generator systems and investigate the behavior of the systems under various environmental conditions.

Various models have been proposed by researchers to investigate the characteristics of solar cells/modules. Among all, the simplest models are single-diode models based on a linear independent current source in parallel to a diode [2,3]. Improvements to the single-diode model have been made by adding a series connected resistance, (R_s), to the model. These models are referred to as R_s-models [4,5]. A more accurate model known as R_p-model, including a shunt resistance, (R_{sh}), also has been utilized by many researchers [6-8]. Two-diode model of a solar cell [9-12], including an additional diode, is a more detailed model being utilized in literature. Among all of the above mentioned models, R_p-model as the most improved version of the single-diode model has been preferred in a large number of applications due to its simplicity.

The R_p-model or simply the one-diode model comprises five unknown parameters to completely represent the I-V characteristics of a solar cell. These parameters are namely the photocurrent, (I_{ph}), the diode reverse saturation current, (I_S), series resistance, (R_s), shunt resistance, (R_p) and diode ideality factor (n). Once these parameters are determined, the model will be able to return the accurate characteristics of a solar cell.

This paper proposes a simple and practical MATLAB/Simulink based simulation model for solar modules based on single-diode model of a solar cell. Information regarding the open-circuit voltage, short-circuit current, voltage and current values at maximum power point and diode ideality factor are determined using the manufacturer`s datasheet. The values of series and shunt resistances are determined using a single mathematical approach based on open-circuit voltage and short-circuit current values. The model is interfaced with SimPowerSystem toolbox and is capable of being utilized in further advanced analyses.

978-1-4799-2569-8/13/$31.00 ©2013 IEEE

II. Mathematical Model of A Solar Cell

As it was mentioned previously, various mathematical models have been utilized to determine the characteristics of solar cells. In this paper, the improved R_p-model or simply the one-diode model of a solar cell is preferred due to its simplicity and wide application areas. The equivalent electrical circuit of the one-diode model of a solar cell is illustrated in Fig.1. The model consists of a linear current source, a diode, a parallel resistance expressing the leakage current and a series resistance representing the internal resistance of a solar cell.

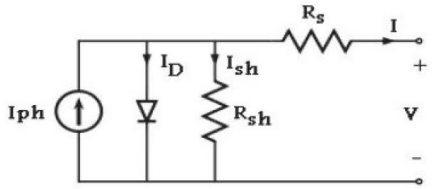

Fig. 1. Equivalent One-Diode Circuit of a Solar Cell

According to the one-diode model of a solar cell, the relationship between the cell`s current and voltage can be determined using the following equation,

$$I = I_{ph} - I_S\left(exp\frac{q(V + R_S I)}{nkT} - 1\right) - \frac{(V + R_S I)}{R_{SH}} \quad (1)$$

Where;

I_{ph} : Photocurrent (A)

I_S : Diode Saturation Current (A)

q : Electron Charge ($1.60217646 \times 10^{-19}$ C)

n : Diode Ideality Factor

k : Boltzmann Constant ($1.3806503 \times 10^{-23}$ J/K)

T : Temperature of the p-n Junction (K)

R_S : Series Resistance (Ω)

R_{SH} : Shunt Resistance (Ω)

Generally the values of the open-circuit voltage, (V_{oc}), short-circuit current, (I_{sc}), maximum power point, (P_{max}), current and voltage at the maximum power point, (V_{mp} and I_{mp}), are provided in the manufacturer`s datasheet under Standard Test Conditions (STC) (Irradiance = 1000 W/m^2, Temperature = 25°C, Air Mass = 1.5).

The aim of an accurate simulation model is to precisely calculate/estimate the above mentioned values under variable environmental conditions. To reach this goal, the simulation model should be capable of appropriate calculation/estimation of the parametrs affecting cell`s I-V characteristics. In the case of considering a one-diode model of a solar cell, there are five unkonwn parameters according to (1), namely being I_{ph}, I_S, n, R_s and R_{sh} to be calculated/estimated by the model.

III. Determination Of Cell Parameters

Considering the points highlighted in the previous part, the unknown parameters of (1) should be appropriately determined for an accurate simulation of the I-V characteristics of a solar cell. A description of the methodology utilized for determination of cell parameters is given during the following parts of the paper.

A. Determination of I_{ph}

The photocurrent, (I_{ph}), can simply be calculated according to the following equation as a function of irradiance and temperature values,

$$I_{ph} = [I_{sc} + k_i(T - T_{STC})]\frac{G}{G_{STC}} \quad (2)$$

Where;

I_{sc} : Short-Circuit Current (A)

k_i : Short-Circuit Current Coefficient

T : Working Temperature

T_{STC} : 25°C

G : Irradiance on the Surface of the Cell (Wh/m^2)

G_{STC} : 1000 Wh/m^2

The value of k_i is generally provided in the manufacturer`s datasheet.

B. Determination of Diode Saturation Current, (I_s) and Idelaity Factor (n)

The diode saturation current, (I_s), can be determined using the following formula considering the effects of variations in cell temperature [8],

$$I_s = I_{s,STC}\left(\frac{T_{STC}}{T}\right)^3 exp\left[\frac{qE_g}{nk}\left(\frac{1}{T_{STC}} - \frac{1}{T}\right)\right] \quad (3)$$

$$I_{s,STC} = \frac{I_{SC}}{exp(V_{oc}/nV_t) - 1} \quad (4)$$

Where;

E_g : The band gap energy of the semiconductor

V_t : Thermal voltage of the cell (V_t = kT/q)

E_g is defined by [13] using (5) and the diode ideality factor, (n), depends on cell`s manufacturing technology. Generally the ideality factor for a silicon cell varies in the range of n≈1-2.

$$E_g = 1.16 - 7.02 \times 10^{-4}\left(\frac{T^2}{T - 1108}\right) \quad (5)$$

C. Determination of Series and Shunt Resistances

Once the first three unknown parameters in (1) have been obtained according to the mentioned methodologies, the values of R_s and R_{sh} are required to complete the simulation model. Although in general it is assumed that $R_p >> R_s$, it should be considered that the simulation model should reflect the real characteristics of a solar module/array. Thus an accurate determination of the R_s and R_{sh} is required. Various methods have been proposed by many researchers to obtain the values of these unknown parameters. Extracting the values from I-V characteristics provided in manufacturer`s datasheet or analytical and iteration based calculation methods have been subjects of many researches in the literature [8,9]. However the unavailability of information on I-V characteristics, computational complexity, uncertainities, etc. are the main issues of utilizing these methods.

The values of R_s and R_{sh} are obtained using the methods introduced by [14] and [15] due to their simplicity and reliable results. According to [14] R_{sh} and R_s can be obtained using (6) and (7) and [15] defines (8) to take the effects of irradiance variations on the value of R_{sh} into account.

$$R_{sh} > 10\frac{V_{oc}}{I_{sc}} \tag{6}$$

$$R_s < 0.1\frac{V_{oc}}{I_{sc}} \tag{7}$$

$$\frac{R_{sh}}{R_{sh,STC}} = \frac{G}{G_{STC}} \tag{8}$$

IV. The Proposed Simulation Model

Considering the mentioned points, the focus of this paper is to propose a simple, practical and accurate simulation model for solar modules. The construction procedure of the simulation model has been described during the following parts of the paper.

A. Simulation Model of a Solar Module

The proposed simulation model of solar modules is based on the simulation of a solar cell as the smallest building block of every solar energy generator system. The simulation model of a single solar cell is constructed based on (1) – (8) in MATLAB/Simulink software environment. The mentioned platform is chosen due to its wide application area and popularity for almost all engineering branches.

A masked implementation of the proposed simulation model for a solar module is shown in Fig. 2. The model accepts the information provided in the manufacturer`s datasheet as I_{sc}, V_{oc}, V_{mp}, I_{mp} along with the temperature and irradiance information, number of series, (Ns), and parallel, (Np), connected solar cells in a module, diode ideality factor and short-circuit current coefficient, (k_i), as inputs and returns the module I-V and P-V characteristics as the output.

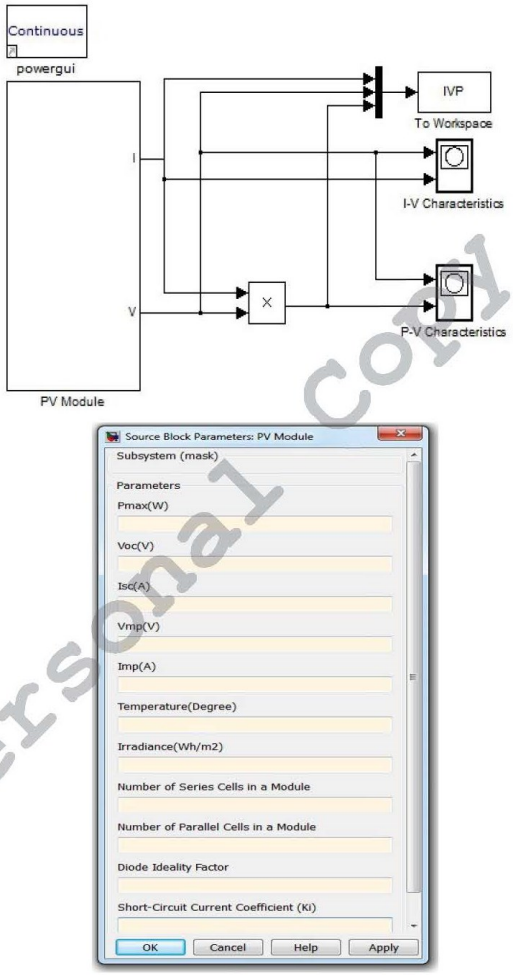

Fig. 2. Masked Implementation of the Solar Module Simulation Model

The blocks contained in the masked implementation are shown in Fig. 3. As it is obvious from the figure, the input parameters are included in a separate subsystem while the main construction block is a solar cell. The solar cell is simulated separately in a subsystem according to (1) – (8). The simulation model is designed for analyses of module behaviors under homogeneous irradiance conditions when the module is not subjected to any partial shading and the irradiance values received at any point on module surface are constant. Under the mentioned conditions the voltage across the terminals of the module is equivalent to the terminal voltage of one cell multiplied by the number of series connected cells in the module. Module`s current value is

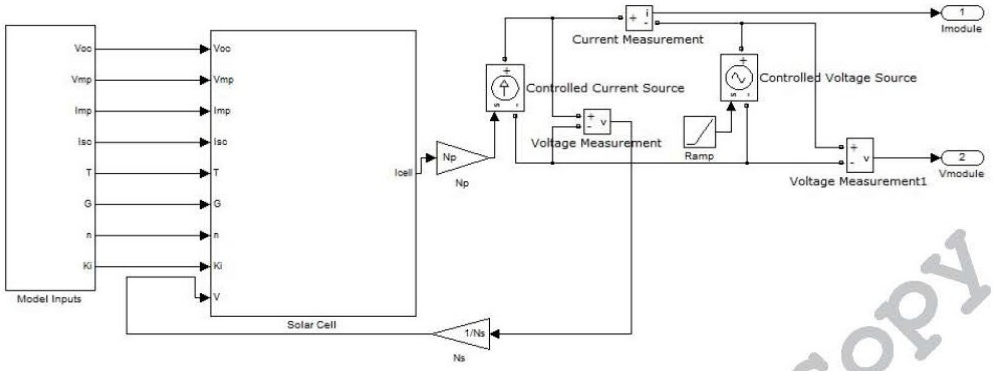

Fig. 3. Blocks of the Solar Module Simulation Model

equivalent to the current of one cell multiplied by the number of parallel connected cells in the module. Generally the open-circuit voltage of each individual solar cell is very small ($V_{cell} \approx 0.6$ Volts) and hence, considering the application requirements, a number of solar cells are internally connected in series and/or parallel combinations in a module to obtain the desired voltage and/or current values, respectively.

The simulation model is interfaced with SymPowerSystem Toolbox to create the possibility for advanced analyze purposes. The output current is connected to a controlled current source and the voltage across the terminals is sensed and externally fed back to the solar cell block. The module output current and voltage signals are considered to obtain the module I-V and P-V characteristics.

The internal architecture of the solar cell simulation block is shown in Fig. 4. The values of I_{ph}, I_s, R_{sh} and R_p are calculated in separate subsystems according to (2) – (8), respectively. The main loop returns the cell current value according to (1).

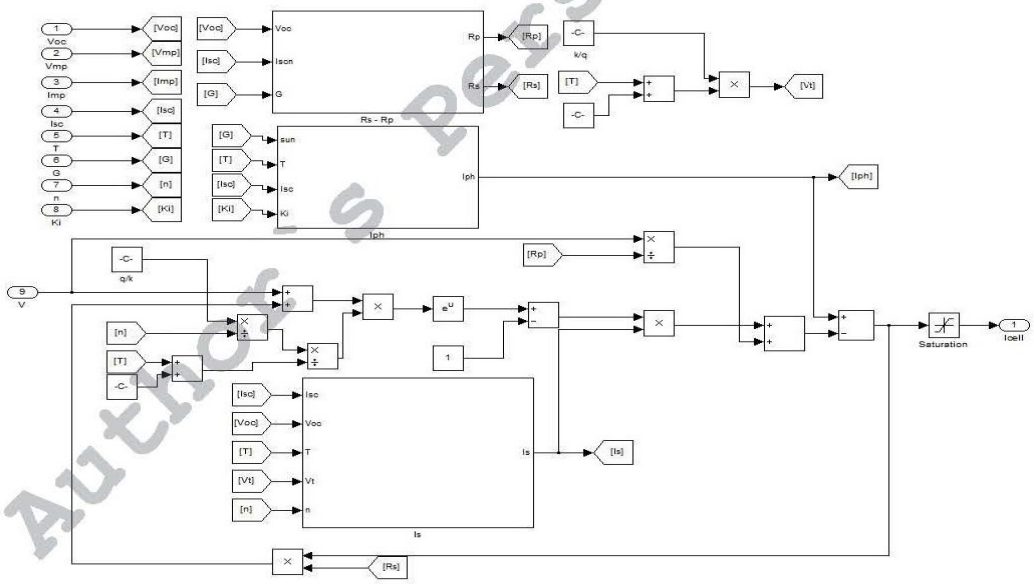

Fig. 4. Simulation Model of a Single Solar Cell

V. SIMULATION RESULTS

The proposed simulation model is designed to return the I-V and P-V characteristics of a solar module. The model is utilized to simulate the behavior of a commercially available crystalline silicon solar module with 36 series connected solar cells under STC and the simulation results are shown in Fig. 5. The parameters of the solar module provided by manufacturer are illustrated in Table I. As it is clearly visible from the figure, the terminal voltage of the module varies between 0-V_{oc} while the current value changes between I_{sc}-0 when the module`s operation point moves between short-circuit and open-circuit conditions, respectively. Under STC, the maximum voltage, ($V_{oc}$), is equal to the total open-circuit voltage values of individual series connected cells while the module`s maximum current, (I_{sc}), is equivalent to each individual cell`s I_{sc} in a series connection combination.

The model is validated using the measured I-V characteristics of the mentioned module. The results are compared and illustrated in Fig. 6. It is obvious that the model is capable of accurate simulation of the characteristics of the module and the measured and simulated values are in a very good agreement. The values of R_s and R_{sh} are chosen as 0.22 Ω and 126 Ω respectively corresponding to 0.027 V_{oc}/I_{sc} and 15 V_{oc}/I_{sc}.

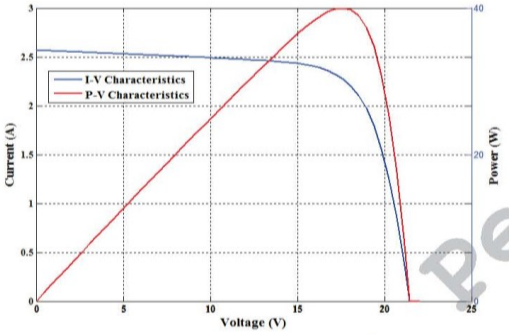

Fig. 5. Simulated I-V and P-V Characteristics of a Solar Module

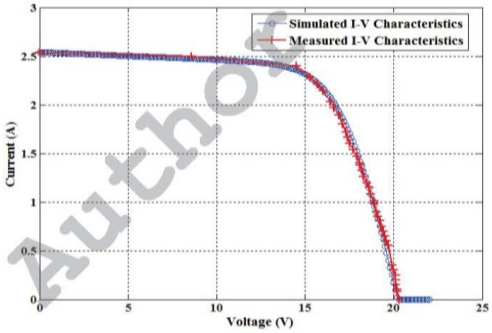

Fig. 6. Measured vs. Simulated I-V Characteristics of a Solar Module

TABLE I. SPECIFICATIONS OF THE SIMULATED MODULE

Parameter	Value
P_{max}	40 W
V_{oc}	21.6 V
I_{sc}	2.57 A
V_{mp}	17.3 V
I_{mp}	2.31 A
n	1.3
K_i	2 mA/°C

Parameters like cell`s working temperature, irradiance, diode ideality factor, series and shunt resistances have all significant effects on cell`s I-V and P-V characteristics. The effects of different factors on cell`s operation are analyzed during the following parts.

A. Temperature Effects

The effects of variations of working temperature on module`s I-V and P-V characteristics are illustrated in Fig. 7. It is observed that $V_{oc}$ is reduced when module`s working temperature is increased beyond 25°C in parallel with small increments in I_{sc}. As it is illustrated in P-V characterisitcs curve, increments in working temperature cause significant reductions in module`s power output and maximum power point.

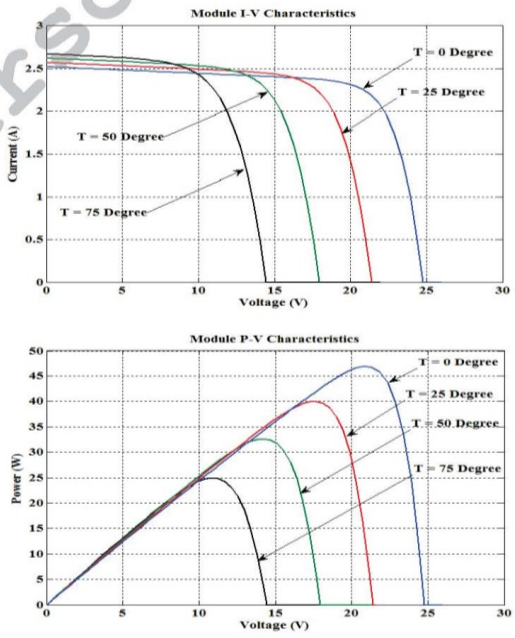

Fig. 7. Effects of Temperature Variations on Module I-V & P-V Characteristics

B. Irradiance Effects

The effects of variations of the amounts of the received solar irradiance on module`s I-V and P-V characteristics are shown in Fig. 8. The module output characteristics are simulated under five different irradiance levels, namely being 1000 Wh/m^2, 800 Wh/m^2, 600 Wh/m^2, 400 Wh/m^2 and 200 Wh/m^2. It is obvious that reductions in the amount of solar insolation received by the module have direct effects on module short-circuit current value while V_{oc} is also subjected to small reductions at the same time. It is observed that reductions in solar irradiance cause significant amounts of power loss by the module.

C. Effects of Series Resistance (R_s)

The value of R_s is very small and is neglected in some studies [2,3,16]. However, appropriate calculation/prediction of this parameter improves the accuracy of the simulation model. Fig. 9 illustrates the module`s I-V and P-V characteristics for 5 different values of R_s, namely being 0.168 Ω, 0.336 Ω, 0.504 Ω, 0.672 Ω and 0.840 Ω which correspond to 0.02 V_{oc}/I_{sc}, 0.04 V_{oc}/I_{sc}, 0.06 V_{oc}/I_{sc}, 0.08 V_{oc}/I_{sc} and 0.1 V_{oc}/I_{sc}, respectively. It is obvious that variations of R_s changes the slope of the characteristic curves near V_{oc} operating point and increments in the value causes reductions in power generated by the module.

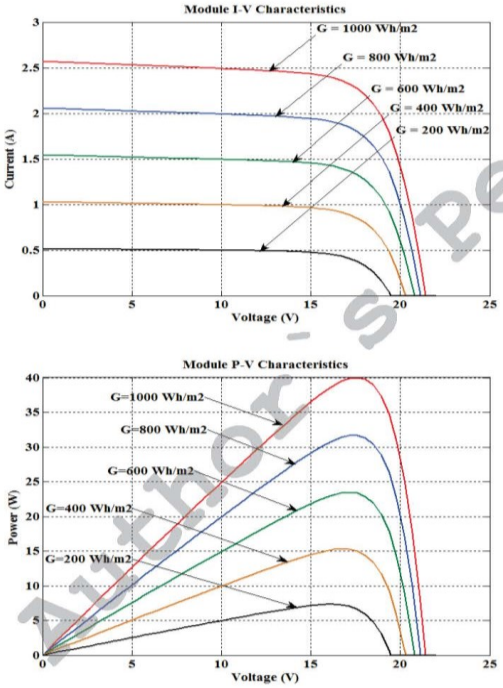

Fig. 8. Effects of Irradiance Variations on Module I-V & P-V Characteristics

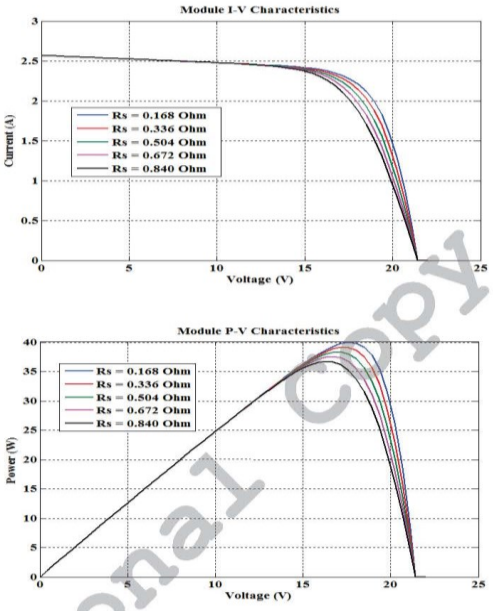

Fig. 9. Effects of Variations of R_s on Module I-V & P-V Characteristics

D. Effects of Shunt Resistance (R_{sh})

The value of the shunt resistance, (R_{sh}), is assumed to be very large compared to R_s. As it was mentioned previously, several methods have been introduced to predict/calculate this value. As an example, [14] defines the value of the R_{sh} by (6). The effects of variations in R_{sh} on module`s I-V and P-V characteristics are illustrated in Fig. 10. The curves are simulated for five different values of R_{sh} namely being 42 Ω, 84 Ω, 168 Ω, 504 Ω, which correspond to 5 V_{oc}/I_{sc} , 10 V_{oc}/I_{sc}, 20 V_{oc}/I_{sc} and 60 V_{oc}/I_{sc}, respectively. It is observed that variations in R_{sh} changes the slope of the characteristics curves near I_{sc} operatin point and increments in the value of R_{sh} increase the power generated by the module.

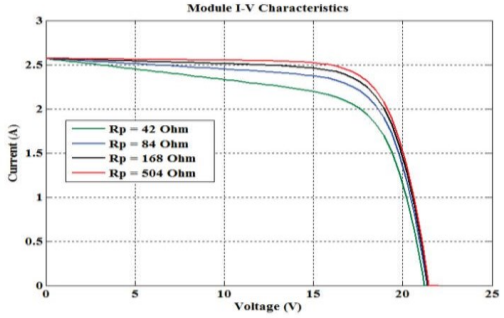

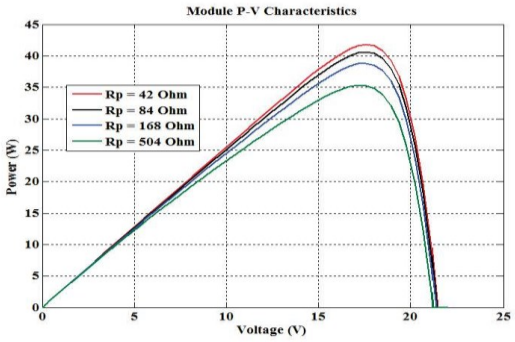

Fig. 10. Effects of Variations of R_{sh} on Module I-V & P-V Characteristics

VI. CONCLUSIONS

Solar energy generators show different behaviors under different environmental conditions. Having a precise and detailed knowledge of system characteristics under different conditions helps system designers and planners to improve the accuracy of predictions/calculations and as a result creates the possibility of optimal and efficient use of this clean and renewable energy resource.

An accurate and precise simulation of solar modules plays a major role in defining system characteristics under variable conditions. In general, the output characteristics of solar modules highly depends on their working temperature and the received solar irradiance as environmental factors as well as the parametric specifications of the module like the diode ideality factor, series and shunt resistance values. The mentioned factors should all be precisely specified for an accurate simulation of the output characteristics of a solar module.

The single-diode mathematical model of a solar cell is used to simulate the I-V and P-V characteristics of a solar module based on (1) – (8). The simulated I-V characteristics are validated using the measured values of a commercially available solar module and it is observed that the simulation results are in a very good agreement with the measurement results. The effects of different parameters on module output characteristics are analyzed and the dependencies of the module characteristics to each parameter are highlighted. It is observed that increments of working temperature of the module cause significant reductions in power generation by the module. It is also illustrated that the short-circuit current of the module is in a direct relationship with the amounts of received solar irradiance and any reduction in solar insolation causes I_{sc} to be reduced. It is also obtained that variations in the values of series and shunt resistances also affect the shape of the characteristic curves where variations of R_s and R_{sh} values cause variations in the slope of curves near V_{oc} and I_{sc} operating points, respectively. At the same time it is observed that increments in R_s cause reductions in power generation while the increments in R_{sh} directly affect the power generation and cause increments in power generation amount by the modules.

ACKNOWLEDGMENT

We would like to express our sincere thanks to Prof.Dr.Aykut Hocanin, Assoc.Prof.Dr.Ugur Atikol and Assoc.Prof.Dr.Fuat Egelioglu for their kind support throughout this study.

REFERENCES

[1] A. Luque and S. Hegedus, *Handbook of Photovoltaics Science and Engineering*, West Sussex, UK : Wiley, 2003, pp.905-933.

[2] Y.T. Tan, D.S. Kirchen and N. Jenkins, "A model of PV generation suitable for stability analysis," *IEEE Trans. Energy Convers.*, vol.19, no.4, pp.748-755, Dec. 2004.

[3] A. Kajihara and A.T. Harakawa, "Model of photovoltaic cell circuits under partial shading," *Proc. IEEE Int. Conf. Ind. Technol. (ICIT)*, Hong Kong, 2005, pp.866-870.

[4] W. Xiao, W.G. Dunford and A. Capel, "A novel modeling method for photovoltaic cells", *Proc. IEEE 35th Annu. Power Electron. Spec. Conf. (PESC)*, Vol.3, 2004, pp.1950-1956.

[5] N. Celik and N. Acikgoz, "Modeling and experimental verification of the operating current of mono-crystalline photovoltaic modules using four- and five-parameter models," *Appl. Energy*, vol.84, no.1, 2007, pp.1-15.

[6] C. Carrero, J. Amador and S. Arnaltes, "A single procedure for helping PV designers to select silicon PV module and evaluate the loss resistances," *Renewable Energy*, vol.32, no.15, 2007, pp.2579-2589.

[7] S. Liu and R.A. Dougal, "Dynamic multiphysics model for solar array," *IEEE Trans. Energy Convers.*, vol.17, no.2, pp.285-294, Jun. 2004.

[8] M.G. Villalva, J.R. Gazoli and E.R. Filho, "Comprehensive approach to modeling and simulation of photovoltaic arrays,` *IEEE Trans. Power Electron.*., vol.24, no.5, pp.1198-1208, May. 2009.

[9] C. Sah, R.N. Noyce and W. Shockley, "Carrier generation and recombination in p-n junctions and p-n junction characteristics," *Proc. IRE*, vol.45, no.9, 1957, pp.1228-1243.

[10] J.A. Gow and C.D. Manning, "Development of a photovoltaic array model for use in power-electronics simulation studies," *IEE Proc. Elect.. Power Appl.*, vol.146, no.2, pp.193-200, 1999.

[11] J.A. Gow and C.D. Manning, "Development of a photovoltaic array model for use in simulation studies of solar energy conversion systems," *Proc. 6th Int..Conf. Power Electron. Variable Speed Drives.*, 1996, pp.69-74.

[12] S. Chowdhury, G. A. Taylor, S. P. Chowdhury, A. K. Saha and Y. H. Song, "Modelling, simulation and performance analysis of a PV array in an embedded environment," *Proc. 42nd Int..Univ. Power Eng. Conf. (UPEC)*, 2007, pp.781-785.

[13] S.K Kim, J.H. Jeon, C.H. Cho, E.S. Kim and J.B. Ahn, "Modeling and simulation of a grid-connected PV generation system for electromagnetic transient analysis", *Solar Enery*, vol.83, pp664-678, 2009.

[14] H. Tian, F. Mancilla, K. Ellis, E. Muljadi and P. Jenkins, "A detailed performance model for photovoltaic systems," NREL, the U.S. Dept. Energy., Denver, NREL/JA-5500-54601, July 2012.

[15] W. Desoto, S. Klein and W. Beckman, "Improvement and validation of a model for photovoltaic array performance", *Solar Enery*, vol.80, pp.78-88, 2006.

[16] S. Nema, R.K. Nema and G. Agnihotri, "MATLAB/Simulink based study of photovoltaic cells / modules / array and their experimental verification", *Int. J. Energy and Environment*, vol.1, no.3, pp.487-500, 2010.

Appendix L: Determination of Power Losses in Solar Panels Using Artificial Neural Network

Kian Jazayeri, Sener Uysal, Moein Jazayeri, "Determination of Power Losses in Solar Panels Using Artificial Neural Network", in *Proceedings - IEEE AFRICON Conference*, Port Luis, Mauritius, 2013.

***Abstract*— The main purpose of this paper is on developing an intelligent system which provides real time monitoring and fault detection for solar panels. Utilizing artificial neural network technology, the solar panel fault detection system is capable of perceiving sun's position in the sky and estimating the corresponding output power of a solar panel based on the algorithms derived by the artificial neural network which has been trained on solar data at several time intervals. The system is capable of operating in any geographical location providing 24-hour monitoring and fault detection as well as future power estimations for solar panels.**

Keywords*—*artificial neural networks, fault detection, photovoltaic cells, photovoltaic systems, solar energy, solar power generation.

Determination of Power Losses in Solar Panels Using Artificial Neural Network

Kian Jazayeri, Sener Uysal, *Member, IEEE*, and Moein Jazayeri
Electrical and Electronic Engineering Department, Eastern Mediterranean University
Famagusta, North Cyprus, via Mersin 10 Turkey
kian.jazayeri@cc.emu.edu.tr
sener.uysal@emu.edu.tr
moein.jazayeri@cc.emu.edu.tr

Abstract— **The main purpose of this paper is on developing an intelligent system which provides real time monitoring and fault detection for solar panels. Utilizing artificial neural network technology, the solar panel fault detection system is capable of perceiving sun's position in the sky and estimating the corresponding output power of a solar panel based on the algorithms derived by the artificial neural network which has been trained on solar data at several time intervals. The system is capable of operating in any geographical location providing 24-hour monitoring and fault detection as well as future power estimations for solar panels.**

Keywords—artificial neural networks, fault detection, photovoltaic cells, photovoltaic systems, solar energy, solar power generation.

I. Introduction

It is of prior importance to put effort into developing techniques of gaining benefit from renewable energy resources. The term renewable refers to the sustainability of the energy resource. According to Lynn (2010), "The Sun's radiation beamed at us day by day, year by year, and century by century, is effectively free income to be used or ignored as we wish. This income is expected to flow for billions of years. Nothing is wasted or exhausted if we don't use it because it is there anyway" [1]. The free and sustainable solar energy will be available for human use through the next centuries without causing any environmental damage to the planet earth.

The performance estimation methods for solar panels and solar power stations have been the subject of many scientific works such as the irradiance forecast based PV power prediction methods introduced in [2] and the map-based simulation model discussed in [3].

As an alternative to such PV performance estimation methods, this paper focuses on developing an Artificial Neural Network (ANN) based fault detection system which is capable of calculating sun's position in the sky and estimating the corresponding solar panel output power.

In the following parts the details about collection and normalization of the solar data used to prepare the ANN training data sets will be given. When the ANN is implemented and trained, the solar data will also be used in execution of the fault detection system.

The solar panel fault detection system is developed using C programming language and the artificial neural network utilized in the system is implemented using the Fast Artificial Neural Network (FANN) library [4].

II. Sun's Position Data

As described in [5], the sun's position in the sky is expressed by three different angles which are the Solar Altitude Angle, the Solar Azimuth Angle and the Solar Angle of Incidence. These three values are fed as inputs to the ANN which will be utilized in the solar panel fault detection system. The methods of calculation and normalization of each of the angles in order to make them ready to be fed as inputs to the ANN are described in the following sections. All the sun's position data calculations are based on local solar time.

A. The Solar Altitude Angle

The Solar Altitude angle γ_s indicates sun's elevation from earth's surface and is calculated by (1):

$$\gamma_s = \sin^{-1}(\sin\varphi\sin\delta + \cos\varphi\cos\delta\cos\omega) \quad (1)$$

$$\delta = \sin^{-1}\left\{0.3987\sin\left(j^{\circ}80.2^{\circ}+1.92\left(\sin\left(j^{\circ}-2.80^{\circ}\right)\right)\right)\right\} \quad (2)$$

$$\omega = 15(t-12) \quad (3)$$

Where,

φ	: The latitude of the observation point
δ	: The solar declination angle (Degrees)
ω	: The solar hour angle (Degrees)
t	: Decimal hours on the 24 hour clock

It is observed that the solar altitude angle values range between -40 degrees to 90 degrees during a 24-hour period. The highest value of the solar altitude angle which optimally affects the performance of the solar panel is reached at 12:00 hrs and corresponds to the sun's highest elevation.

Before feeding the value as an input to the ANN it is normalized between 0 and 1. The value 0 refers to the value of the solar altitude angle that has the least effect on the performance of the solar panel. The value 1 refers to the angle value that has the most effect on panel's power output, which is 90 degrees and is reached at noon.

978-1-4673-5943-6/13/$31.00 ©2013 IEEE

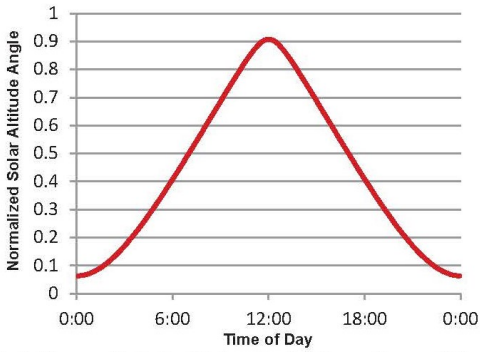

Fig. 1. The normalized solar altitude angle calculation results over a 24-hour period on July 1st, 2012

The normalization used to modify (1) is given in (4) and the result is given in (5), which represents $\gamma_{s,input}$ that is passed as the first input to the artificial neural network.

$$Normalized\ Value = \frac{Value - Minimum}{Max - Minimum} \tag{4}$$

$$\gamma_{s,input} = \frac{\gamma_s + 40}{130} \tag{5}$$

As discussed in [6] the factor j`=j×(360/365.25) indicates the effect of the Julian day number in the declination angle (δ) calculation.

Fig. 1, shows the results of per minute calculations of $\gamma_{s,input}$ for constant latitude and different time angles over a 24-hour period for Julian day number 182 which refers to July 1st. As it is obvious from the figure, $\gamma_{s,input}$ almost reaches its optimal value 1 which refers to 90 degrees for γ_S at 12:00 hrs on July 1st.

B. The Solar Azimuth Angle

The second value which is fed as input to the artificial neural network is the Solar Azimuth Angle. As described in [5] the solar azimuth angle indicates sun's deviation from north direction and is represented by (6):

$$\begin{cases} \alpha_s = 180 - \cos^{-1}(\cos\alpha_s) & \text{If } \sin\alpha_s < 0 \\ \alpha_s = 180 + \cos^{-1}(\cos\alpha_s) & \text{If } \sin\alpha_s > 0 \end{cases} \tag{6}$$

Where,

$$\cos\alpha_s = (\sin\varphi \sin\gamma_s - \sin\delta)/\cos\varphi\cos\gamma_s \tag{7}$$

$$\sin\alpha_s = \cos\alpha_s \sin\omega/\cos\gamma_s \tag{8}$$

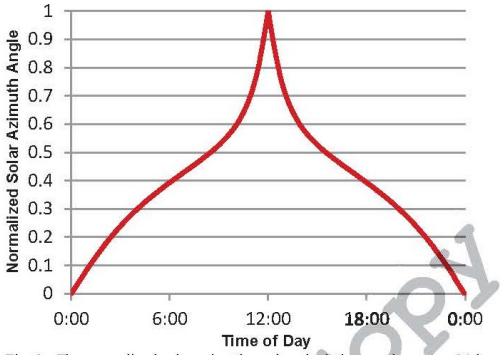

Fig. 2. The normalized solar azimuth angle calculation results over a 24-hour period on July 1st, 2012

The effect of time angle ω (3) makes sin α_s take on positive values from 12:00 to 00:00 hrs and negative values from 00:00 to 12:00 hrs, therefore (6) is modified in the data collection system to calculate the solar azimuth angle sin α_s for these two different periods of time.

The solar panel used for data collection is south oriented, therefore the values of the solar azimuth angle which represent the location of sun in south direction mostly affect the performance of the panel.

Since (6) represents sun's deviation from north direction, it takes on 0 and 180 degrees when sun is located in north and south directions respectively. Therefore, again using (4) we can normalize (6) in the form of (9) and (10):

For α_s<180,

$$\alpha_{s,input} = 1 - \frac{180 - \alpha_s}{180} \tag{9}$$

For α_s>180,

$$\alpha_{s,input} = 1 - \frac{\alpha_s - 180}{180} \tag{10}$$

Fig. 2, shows the results of per minute calculations of $\alpha_{s,input}$ over a 24-hour period for July 1st using (9) and (10). As it is obvious from the figure, $\alpha_{s,input}$ takes on its highest value 1 at 12:00 hrs which shows that the sun is located in south direction at noon. Since the solar panel is also headed in south direction, the value of $\alpha_{s,input}$ at noon refers to the situation in which the panel is located in front of sun and is expected to work with its maximum performance.

C. The Solar Incidence Angle

The third and last value to be passed as input to the ANN is the Solar Angle of Incidence (θ). The solar angle of incidence is the angle between the sun's radiations and a vector perpendicular to the solar panel's surface. When the sun's radiations are perpendicularly received on the solar

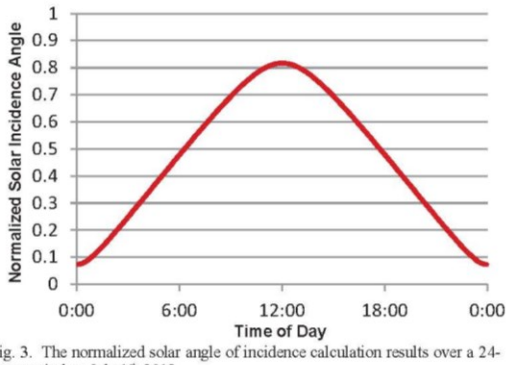

Fig. 3. The normalized solar angle of incidence calculation results over a 24-hour period on July 1st, 2012

panel's surface, θ takes on its optimal value 0 degree. Like the solar altitude and azimuth angles, the solar angle of incidence which is represented by (11) has a major role in solar panel output power estimations.

$$\theta=\cos^{-1}\left[\begin{matrix}\cos(\beta)\cos(Z_s)+\\ \sin(\beta)\sin(Z_s)\cos(\alpha_s-\alpha_m)\end{matrix}\right] \quad (11)$$

Where,

β : Tilt angle of the solar panel (45° in this case)
Z_s : Zenith Angle of the Sun (Degrees)
α_m : Module azimuth angle (in this case: South = 180°)

and,

$$Z_s = 90 - \gamma_s \quad (12)$$

Similar to the first two inputs ($\gamma_{s,input}$ and $\alpha_{s,input}$), it is desired to normalize the value of the solar angle of incidence between 0 and 1 before feeding it as the third input to the ANN. The normalized input value takes on 1 corresponding to 0° which is the optimal value of the angle of incidence and as this value moves towards 180°, the normalized input value decreases down to 0.

Again (4) is used to normalize (11) which results in (13):

$$\theta_{input} = 1 - \frac{\theta}{180} \quad (13)$$

Fig. 3, shows the results of per minute calculations of θ_{input} over a 24-hour period, again for the Julian day number 182 which refers to July 1st. As it is obvious from the figure, θ_{input} takes on its maximum value on 12:00 hrs which indicates that sun's radiations are perpendicularly received on the solar panel's surface at noon, and decreases down to its minimum value at midnight.

III. SOLAR PANEL OUTPUT POWER

The solar panel used to collect data for the fault detection system is a 50×60 cm^2 monocrystalline silicon panel (P_{max} : 40W, V_{OC} : 21.6 V, I_{SC} : 2.56 A) located at 17 meters above the sea level on the roof of the Electrical and Electronic Engineering Department, Eastern Mediterranean University at 35° 8' 51" N, 33° 53' 58" E. The panel is south oriented tilted 45 degrees.

The short circuit current, I_{SC}, is the maximum current that flows in a solar cell when its terminals are shorted with each other and the open circuit voltage, V_{OC}, is the maximum voltage generated across the terminals of a solar cell when they are kept open [7]. The output voltage and current values of a solar panel vary between 0-V_{OC} and 0-I_{SC} respectiveley under variable load and constant irradiance conditions. Here, a constant valued power resistor is connected to the terminals of the panel which provides the possibility of monitoring and measurement of the output power as a function of variable irradiance during daytime.

The output power is firstly used while the training data sets for the artificial neural network (ANN) are being prepared and then it is used to compare with the estimated output power after each execution of the ANN in the fault detection system (the details about training and execution of the ANN will be given in later parts). The corresponding time for solar panel output power measurements is the local time at the observation point.

An electronic circuit is constructed to measure the output power of the solar panel and transfer the data to a computer. The different parts of the solar panel output power measurement circuit consisting of (a) Microprocessor, (b) Max232, (c) Power Resistor and (d) Voltage Divider Circuit along with their connections are shown and labeled in Fig. 4.

The output power of the solar panel was firstly tracked and logged over a 24-hour period with a sample rate of 1 reading per minute. The system was designed to read the computer's serial port which was connected to the circuit in Fig. 4, log the data referred to the output power of the solar panel along with the time of reading the port and wait for 60 seconds.

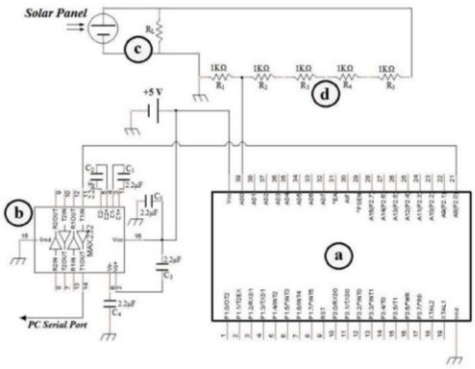

Fig. 4. The Circuit Used for Output Power Measurement of the Solar Panel

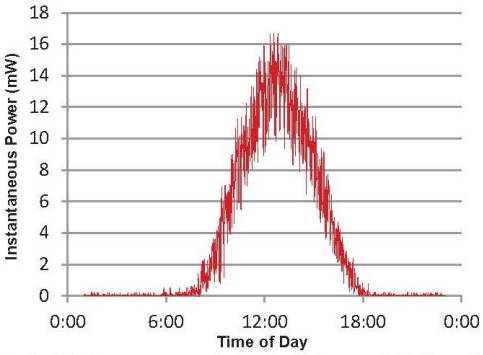

Fig. 5. Output power measured with 1 sample per minute for a 40W monocrystalline silicon solar panel over a 24-hour period on July 3rd, 2012

The result of about 1400 times reading and logging the value of solar panel's output power over a 24-hour period starting from 00:00 hrs on July 3rd, 2012 is shown in Fig. 5.

As it is obvious from Fig. 5, solar panel's output power measured with 1 sample per minute is highly fluctuating. Logging the fluctuating power value in the artificial neural network training data sets would decrease the efficiency of the training process of the ANN and increase its training error. The solution to this problem is to increase the averaging rate of the measured output power.

At this point the system is modified to read the output power of the solar panel through computer's serial port at 5 second intervals. After 12 readings is completed (which corresponds to 60 seconds reading time), the average value of the last 12 samples is logged along with the exact time at the moment.

Fig. 6, shows the results of about 1400 measurements of the solar panel's output power with an averaging rate of 12 readings per minute over a 24-hour period on July 3rd,2012.

As shown in Fig. 6, increasing the averaging rate of the solar panel's output power measurement decreases the fluctuations in the logged data and makes it ready to be passed into the artificial neural network training data sets. Similar to the input values, the output value also has to be normalized before being passed to the training data set.

IV. Artificial Neural Network Training Process

As previously mentioned, it is aimed to develop an artificial neural network (ANN) which receives the values of the solar altitude angle, the solar azimuth angle and the solar angle of incidence as inputs and derive the estimated solar panel output power corresponding to each set of input.

The ANN needs to be trained with inputs and outputs collected formerly. After the training process completed, the ANN gets ready to derive proper outputs for the inputs given in training data set as well as generalizations for new inputs. The training process is done on a .data training file which is shown in Fig. 7.

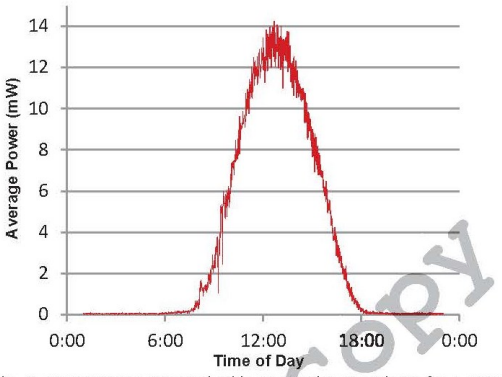

Fig. 6. Output power measured with 12 samples per minute for a 40W monocrystalline silicon solar panel over a 24-hour period on July 3rd, 2012

The first line in the training file indicates that the ANN goes through 1339 training paths with 3 inputs and 1 output. The next couple of lines consist of the input values which are $\gamma_{s,input}$, (5), $\alpha_{s,input}$, (9, 10) and θ_{input}, (13) in the first line and the normalized solar panel output value in the second line. These two lines represent the first training path for the ANN and are followed by 1338 other paths which are all formed in the same way with different input and output values.

The artificial neural network utilized in the solar panel fault detection system has multilayer feed-forward architecture with back-propagation algorithm. During the training process each training path is processed separately and inputs of each path are propagated through different layers of the network until they reach to the output layer.

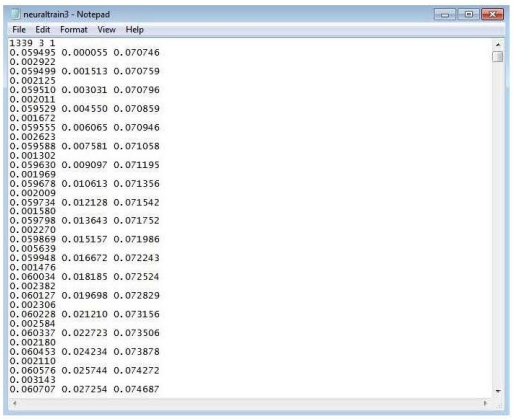

Fig. 7. Artificial neural network training data set

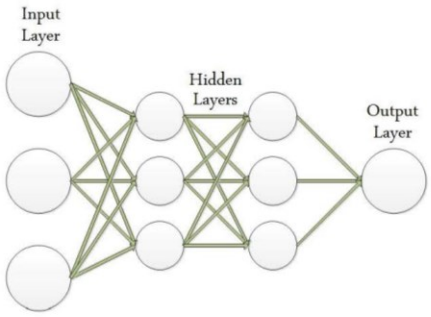

Fig. 8. The artificial neural network architecture utilized in the solar panel fault detection system

At this point the error of the training process is calculated with respect to the output specified to each input array in the training data set. After all the training paths are processed, the back-propagation algorithm is applied to adjust the weights on neurons in different layers of the network. The procedure continues until the training error falls below a preset threshold.

The architecture of the multilayer fully connected artificial neural network shown in Fig. 8, consists of an input layer, two hidden layers and an output layer. This ANN architecture with symmetric sigmoid activation function with steepness factor 1 is selected to be utilized in the solar panel fault detection system since it provides the lowest error during the training and execution phases.

Executing the training process, the ANN falls below the pre-set training error threshold 1.2×10^{-4} after 15215 epochs of back-propagation and at this point a .net file is created to be used for execution of the ANN with future inputs.

V. Execution Results of the Proposed Solar Panel Fault Detection System

At this point, having the artificial neural network trained with collected solar data, the solar panel fault detection system is ready to be executed. When the system is run, it connects to the computer's serial port to get the value of the solar panel output power every 5 seconds and calculate the average output power with 12 samples per minute. After calculating the average power for each minute, the system gets the time and calculates the values of $\gamma_{s,input}$ (5), $\alpha_{s,input}$ (9, 10) and θ_{input} (13) and feeds them as inputs to the artificial neural network shown in Fig. 8.

The inputs propagate through the network layers to reach the output layer. After the execution of the ANN is completed the output value is reconstructed from the normalized form and logged as the estimated output power for the corresponding time. At this point the root mean square error between the estimated and the actually measured output power values are calculated and logged as a percentage error with respect to the measured output power value.

If the calculated percentage error value falls below a pre-set threshold, the execution window of the fault detection system produces the message "System Performance Check: Successful" along with the exact time, measured power value, estimated power value and the root mean square error value. On the other hand, if the percentage error value exceeds the threshold, the system reports the message "System Performance Check: Fault Detected" again along with the previously mentioned values.

The solar panel output power values (measured vs. estimated) and the root mean square error between the measured and the estimated power values over a 24-hour period on July 6th, 2012 which was a clear, sunny day are shown in Fig. 9.

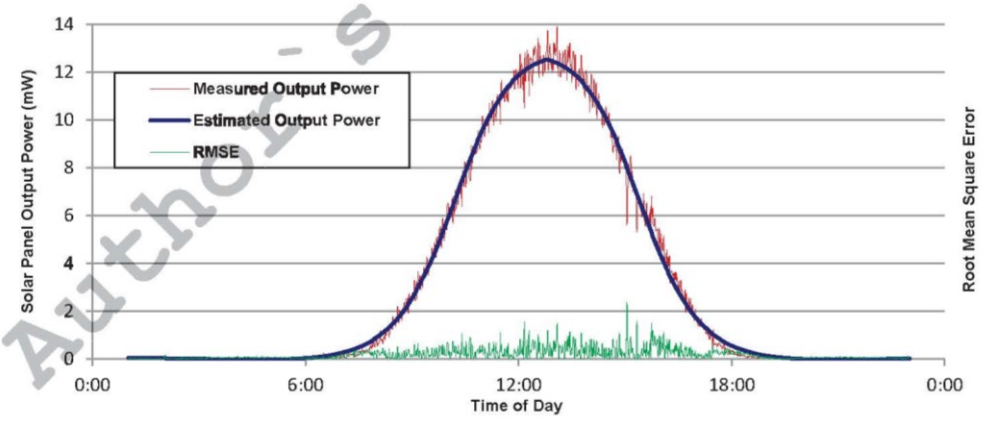

Fig. 9. Output power values (measured vs. estimated) and the root mean square error between the measured and the estimated output power values for a 40W monocrystalline silicon solar panel on July 6th, 2012.

TABLE I. AVERAGE PERCENTAGE RMSE BETWEEN THE MEASURED AND THE ESTIMATED OUTPUT POWER VALUES FOR DIFFERENT DAYLIGHT TIME INTERVALS ON JULY 6TH, 2012

DAYLIGHT TIME INTERVAL (HOURS)	AVERAGE RMSE (%)
12:30 – 13:30	3.309906
12:00 – 14:00	3.420657
11:30 – 14:30	3.188346
11:00 – 15:00	3.175156
10:30 – 15:30	3.57076
10:00 – 16:00	3.950062
9:30 – 16:30	4.602882
9:00 – 17:00	5.207249
8:30 – 17:30	5.554695
8:00 – 18:00	8.405882

Table I, shows the different values of the average percentage RMSE between the measured and the estimated solar panel output power for different daylight time intervals from 1 up to 12 hours on a clear, sunny day (July 6th, 2012).

The daylight time interval 8:00-18:00 corresponds to the period in which the solar panel operates effectively and the solar panel fault detection system is executed within this interval providing overall %RMSE values between 3.17% and 8.40%. These values may be compared to the RMSE values for different models of irradiance estimation introduced in [8].

Nguyen [9] indicates that in a solar panel/module consisting of 10 sub-modules each containing 10 solar cells interconnected by 2 different connection types (Simple Series-Parallel and Total-Cross-Tied), the effect of 6 solar cells being shaded or damaged results in 17% to 48% overall power loss based on the locations and connection types of the shaded/damaged solar cells. Respecting the above, the 15% RMSE value between the measured and the estimated output power is decided as threshold for the solar panel fault detection system.

Setting the RMSE threshold for the solar panel fault detection system to 15% provides the possibility of detecting any failure higher than 6% in a solar panel's surface [9].

VI. CONCLUSIONS

The artificial neural network based fault detection system provides 24-hour monitoring and real time fault detection of solar panels. The mechanism of the fault detection system relies on the position of the sun in the sky. During the data collection procedure, the sun's position is calculated and recorded along with the corresponding solar panel output power in the artificial neural network training data sets. The ANN is trained with the solar training data sets and derives the algorithms that relate the solar panel output power to the position of the sun in the sky.

At this point the artificial neural network is capable of estimating the output power of the solar panel with respect to the sun's position. The fault detection system is designed to measure the average output power of the solar panel with 12 samples per minute and compare it with the output power estimated by the ANN. If the root mean square error between the measured and the estimated output powers exceeds some pre-set threshold an error message is produced to report the RMSE value along with the measured and estimated output power values and system time.

Utilizing the solar panel fault detection system, any power loss due to damaged cells, shadows etc. is detected and reported immediately which increases the efficiency of the solar power stations and decreases the long term maintenance and support costs.

ACKNOWLEDGMENT

We would like to express our sincere thanks to our dear friend Reza Abrishambaf for his help and support through the various stages of this study.

REFERENCES

[1] P.A. Lynn, *Electricity from Sunlight: An Introduction to Photovoltaics*, West Sussex, UK: Wiley, 2010, pp. 1-23.

[2] E. Lorenz, J. Hurka, D. Heinemann and H.G. Beyer, "Irradiance forecasting for the power prediction of grid-connected photovoltaic systems," *IEEE J. Sel. Topics Appl. Earth Observations and Remote Sensing*, Vol. 2, No.1, pp. 2-10, Mar. 2009.

[3] M. Suri, T. Huld, T. Cebecauer and E.D. Dunlop, "Geographic aspects of photovoltaics in Europe: contribution of the PVGIS website," *IEEE J. Sel. Topics Appl. Earth Observations and Remote Sensing*, Vol. 1, No.1, pp. 34-41, Mar. 2008.

[4] S. Nissen, "Implementation of A Fast Artificial Neural Network Library (FANN)," Graduate dissertation, Dept. Comput. Sci., Univ. Copenhagen, Copenhagen, Denmark. 2003.

[5] K. Scharmer and J. Greif, *The European Solar Radiation Atlas Vol.1: Fundamentals and Maps*, Paris, France: Les Presses de l'Ecole des Mines, 2000, pp. 23-42.

[6] A. Luque and S. Hegedus, *Handbook of Photovoltaics Science and Engineering*, West Sussex, UK: Wiley, 2003, pp. 906-912.

[7] C.S. Solanki, *Solar Photovoltaics: Fundamentals, Technologies and Applications*, New Delhi, India: PHI Learning Private Limited, 2011, pp. 72-95.

[8] G. Notton, C. Cristofari, M. Muselli, P. Poggi and N. Heraud, "Hourly solar irradiations estimation: from horizontal measurements to inclined data," in *IEEE-ISEIM*, Corte-Ajaccio, France, 2006, pp. 234-239.

[9] D. D. Nguyen, "Modeling And Reconfiguration Of Solar Photovoltaic Arrays Under Non-Uniform Shadow Conditions," Ph.D. dissertation, Dept. Elect. Comput. Eng., Northeastern Univ., Boston, MA., 2008.

Appendix M: Analysis of Effects of Sun's Position in the Sky on Solar Radiation and Solar Panel Output Power

Moein Jazayeri, Sener Uysal, Kian Jazayeri, "Analysis of effects of sun's position in the sky on solar radiation and solar panel output power", in *Proceedings - IEEE AFRICON Conference*, Port Luis, Mauritius, 2013.

Abstract — **It is basically approved that the output power of a solar cell/module directly depends on the amount of solar irradiance which it receives from the sun. Also it is known that the irradiance values are not constant at any specific time interval. The changes in the position of the sun with respect to earth are one of the main reasons causing the variations in the amount of incoming sunlight and its energy to the earth's surface. The main focus of this paper is to analyze the effects of changes in the position of the sun in the sky on the incoming solar radiation during a whole year. Also the effects of such changes on the hourly values of solar radiation as well as the effects on the output power generated by a solar panel during a specific sample day is analyzed.**

Keywords—solar energy, solar power generation, solar radiation, irradiance, photovoltaic cells, data acquisition, data analysis

Analysis of Effects of Sun`s Position in the Sky on Solar Radiation and Solar Panel Output Power

Moein Jazayeri, Sener Uysal, *Member, IEEE*, and Kian Jazayeri
Electrical and Electronic Engineering Department, Eastern Mediterranean University
Famagusta, North Cyprus, Via Mersin 10 Turkey
moein.jazayeri@cc.emu.edu.tr
sener.uysal@emu.edu.tr
kian.jazayeri@cc.emu.edu.tr

Abstract — **It is basically approved that the output power of a solar cell/module directly depends on the amount of solar irradiance which it receives from the sun. Also it is known that the irradiance values are not constant at any specific time interval. The changes in the position of the sun with respect to earth are one of the main reasons causing the variations in the amount of incoming sunlight and its energy to the earth's surface. The main focus of this paper is to analyze the effects of changes in the position of the sun in the sky on the incoming solar radiation during a whole year. Also the effects of such changes on the hourly values of solar radiation as well as the effects on the output power generated by a solar panel during a specific sample day is analyzed.**

Keywords—solar energy, solar power generation, solar radiation, irradiance, photovoltaic cells, data acquisition, data analysis

I. Introduction

The importance of use of solar energy as a huge, reliable and clean source of renewable energy is assumed to be well-known by any individual energy consumer. This importance can best be sensed when the pollution caused by conventional energy sources and their limited amount are taken into the consideration. Despite the relatively low efficiency of the current solar power generators, the applications that employ solar energy as a power source are growing fast and there are lots of researches to improve the PV power generation efficiency. Sun tracking systems, solar concentrators, maximum power point tracking techniques etc. are all strategies and technologies used to obtain higher efficiency from the available sunlight.

Having an appropriate, precise and reliable knowledge of the available solar radiation is of the most important factors, which plays a great role during design and planning stage of almost any solar energy dependent application. The amount of incoming energy to the earth's surface highly depends on the position of the sun in the sky during different time intervals. Also some other factors like aerosols, water vapor etc. all have decreasing effects on the amount of incoming sunlight energy. Hence it is necessary for almost all applications to estimate, measure or calculate the real values of solar radiation for the specific applications sites. Taking the high expenses of measurement equipment and techniques into the consideration, a number of prediction and estimation models have been developed to obtain the required solar radiation data. Analysis of satellite data for irradiance forecasts, use of numerical weather prediction models, neural network based models for irradiance forecasts etc. are some of the methods which are used to determine the irradiance values for desired applications. Some prediction and estimation methods of solar radiation data are reviewed in [1] – [6].

In this paper it is aimed to analyze the effects of variations in the sun's position in the sky on the incoming solar radiation on a tilted solar panel. Also variations in the output power of a tilted solar panel are analyzed during a sample day, as a factor, which is directly related to the incoming irradiance values.

For the mentioned purposes a precise knowledge of solar radiation amount and determination of sun's position in the sky for the specific location of the observation site where the solar system is mounted is required as well as output power data obtained from the system. In the later parts of the paper, the methods, which are used to obtain the required data for the proposed analyses, are described and the results of the analyses are discussed.

II. Methodology

The information on the sun's position in the sky, incoming irradiance on tilted solar panels and output power of the panel, which is used during the study, form the basis of the analyses discussed in the present paper. In this part, the methods, which are used to obtain each set of the above information, are briefly explained. Electrical and Electronic Engineering Dept. of Eastern Mediterranean University in Northern Cyprus ($35^{\circ}8'51'' N, 33^{\circ}53'58'' E$) is chosen as the observation point.

A. Calculations of Solar Radiation Data

As it is mentioned before the purpose of this paper is to analyze the effects of changes in the position of the sun on the incoming solar radiation to the earth`s surface. For this purpose the method of calculation of radiation data introduced by [7] is used for solar radiation calculations. The monthly mean value of daily global irradiance data provided by "NASA Atmospheric Science Data Center" for the location of the observation point is used. The mentioned data source is averaged based on 22 years of data measurements. A brief

978-1-4673-5943-6/13/$31.00 ©2013 IEEE

review on the calculation procedure of the solar radiation components is given during the following sections.

1) *Calculation of Radiation Data on a Horizontal Surface:* Different factors utilized during the calculations of solar radiation data on a horizontal surface are listed as following;

a) Air Mass: The Air Mass factor is calculated using the following equation,

$$AM = \frac{1}{cos\theta_{ZS}} \quad (1)$$

Where,

θ_{ZS} : The Solar Zenith Angle

b) Solar Declination: The solar declination angle is calculated according to the following equation,

$$\delta = 23.45°sin\left[\frac{360(d_n + 284)}{365}\right] \quad (2)$$

Where,

d_n : The Julian Day Number

c) Extraterrestrial Irradiance: The daily mean value of the extraterrestrial irradiance over a horizontal surface for the observation point can be calculated as;

$$B_{0d}(0) = \frac{T}{\pi} B_0 \varepsilon_0 \left[-\frac{\pi}{180}\omega_S.\sin\delta.\sin\phi - \cos\delta\cos\phi\sin\omega_S\right] \quad (3)$$

Where,

T : Day length, in hours
B_0 : Solar constant (1367 W/m^2)
ω_s : Sunrise hour angle
ε_0 : Eccentricity correction factor

d) Clearness Index: Clearness index as a measure of the atmospheric transparency can be obtained as;

$$K_{TM} = \frac{G_{dm}(0)}{B_{0dm}(0)} \quad (4)$$

e) Beam Irradiance on a Horizontal Surface : The mean value of daily beam irradiance on a horizontal surface can be obtained as a result of extraction of the value of diffuse irradiance from the global irradiance. The value of daily beam irradiance on a horizontal surface can be calculated using the following equation,

$$B_{dm}(0) = G_{dm}(0) - D_{dm}(0) \quad (5)$$

Where, $D_{dm}(0)$ is the daily mean value of diffuse irradiance and is calculated as;

$$D_{dm}(0) = G_{dm}(0) \times F_{dm} \quad (6)$$

And, $F_{dm} = {D_{dm}(0)}/{G_{dm}(0)}$ is the diffuse fraction of the horizontal irradiance.

2) *Calculation of Solar Irradiance on Inclined Surfaces:* During this part, the calculation method of solar irradiance components on inclined solar panels is described using the data obtained in the previous part. In general the global irradiance falling on an inclined surface consists of three components, respectively named as direct irradiance, diffuse irradiance and albedo. Hence the general form of the equation defining the global solar irradiance on an inclined solar panel is defined as follows,

$$G(\beta,\alpha) = B(\beta,\alpha) + D(\beta,\alpha) + R(\beta,\alpha) \quad (7)$$

Where,

$G(\beta,\alpha)$: Global Solar Irradiance on an Inclined Surface
$B(\beta,\alpha)$: The Direct Solar Irradiance on an Inclined Surface
$D(\beta,\alpha)$: The Diffuse Solar Irradiance on an Inclined Surface
$R(\beta,\alpha)$: The Albedo Component of Solar Irradiance on an Inclined surface

a) Direct Irradiance on Inclined Surfaces: The direct irradiance component on an inclined surface is defined as,

$$B(\beta,\alpha) = Bmax(0,\cos\theta_s) \quad (8)$$

Where,

β : Tilt angle of the solar panel
α : Panel azimuth angle
θ_s : The incidence angle of sunlight rays on the panel
$B = \frac{B(0)}{\cos\theta_{ZS}}$: The direct irradiance on a surface normal to sunlight rays.

$B(0) = G(0) - D(0)$ is the beam irradiance on a horizontal surface.

$$G(0) = \left[\left(\frac{\pi}{T} \times \frac{\cos\omega - \cos\omega_s}{\frac{\pi}{180}\omega_s\cos\omega_s - \sin\omega_s}\right)(a + b\cos\omega)\right] \times G_{dm}(0) \quad (9)$$

Where,

$$a = 0.409 - 0.5016 \times \sin(\omega_s + 60) \quad (10)$$

$$b = 0.6609 + 0.4767 \times \sin(\omega_s + 60) \quad (11)$$

and,

$$D(0) = \left(\frac{\pi}{T} \times \frac{\cos\omega - \cos\omega_s}{\frac{\pi}{180}\omega_s \cos\omega_s - \sin\omega_s}\right) \times D_{dm}(0) \quad (12)$$

b) Diffuse Irradiance on Inclined Surfaces : In general anisotropic models have shown better results during the calculations of diffuse irradiance values. Accoring to these models the diffuse irradiance is assumed to be composed of two main components, respectively named as circumsolar component $D^C(\beta,\alpha)$, which directly comes from the sun`s direction and the isotropic component $D^I(\beta,\alpha)$, which comes from the entire celestial hemisphere. According to the mentioned model,

$$D(\beta,\alpha) = D^I(\beta,\alpha) + D^C(\beta,\alpha) \quad (13)$$

where,

$$D^I(\beta,\alpha) = D(0)(1-k_1)\frac{1+\cos\beta}{2} \quad (14)$$

$$D^C(\beta,\alpha) = \frac{D(0)k_1}{\cos\theta_{ZS}} max(0,\cos\theta_s) \quad (15)$$

and,

$k_1 = \frac{B}{B_0\varepsilon_0}$: Anisotropy Index

c) Albedo Irradiance on Inclined Surfaces : The albedo irradiance on inclined solar panels, $R(\beta,\alpha)$, can be obtained using the following equation,

$$R(\beta,\alpha) = \rho G(0)\frac{1-\cos\beta}{2} \quad (16)$$

Where ρ is the reflectivity of the ground and generally is taken as 0.2 when its value is not known.

3) Calculations of Daily Solar Irradiance on Inclined Surfaces: A general approach to calculate the monthly mean value of daily solar irradiance can be defined in three steps as follows,

1. Calculation of the hourly horizontal irradiance components $G_{hm}(0), D_{hm}(0), B_{hm}(0)$ from $G_{dm}(0)$
2. Calculation of the hourly solar irradiance values on inclined surfaces, $G_{hm}(\beta,\alpha), D_{hm}(\beta,\alpha), B_{hm}(\beta,\alpha)$
3. Integration of the hourly values over one day (24 hours) according to the following equation,

$$G_{dm}(\beta,\alpha) = \sum_{-\omega_s}^{\omega_s} G_{hm}(\beta,\alpha) \quad (17)$$

B. Calculations of Sun`s Position in the Sky

The position of the sun in the sky is basically explained using two main factors as followings;

i. Sun's altitude angle, (γ_s), which is a measure of sun's height in the sky

ii. Sun's azimuth angle, (α_s), which determines the position of the sun with respect to the south direction

In this paper the method described in [8] is used for derivation of information about the sun's position in the sky. These three factors are obtained as follows;

1) Solar Altitude Angle (γ_s)

$$\gamma_s = sin^{-1}(sin\varphi sin\delta + cos\varphi cos\delta cos\omega) \quad (18)$$

$$\delta = sin^{-1}\{0.3978\sin(j` - 80.2^0 + 1.92(\sin(j` - 2.80^0)))\} \quad (19)$$

$$j` = j \times \left(\frac{360}{365.25}\right) \quad (20)$$

$$\omega = 15(t-12) \quad (21)$$

Where,

φ : The latitude of the observation point
δ : The solar declination angle (Degrees)
$j`$: The Julian day number expressed as a day angle
ω : The solar hour angle (Degrees)

2) The Solar Azimuth Angle (α_s)

$$\cos\alpha_s = (\sin\varphi \sin\gamma_s - \sin\delta)/\cos\varphi\cos\gamma_s \quad (22)$$

$$\sin\alpha_s = \cos\alpha_s \sin\omega/\cos\gamma_s \quad (23)$$

If $\sin\alpha_s < 0$ $\alpha_s = -\cos^{-1}(\cos\alpha_s)$
If $\sin\alpha_s > 0$ $\alpha_s = \cos^{-1}(\cos\alpha_s)$

Where $0^\circ = South, 90^\circ = West$

3) Solar Angle of Incidence

$$\theta_s = \cos^{-1}[\cos(\beta)\cos(Z_s) + \sin(\beta)\sin(Z_s)\cos(\alpha_s - \alpha_m)] \quad (24)$$

Where,

β : Tilt angle of the solar collector ($Horizontal = 0^\circ$)
Z_s : Zenith Angle of the Sun
α_m : Module azimuth angle ($North = 0^0, East = 90^\circ$)

The sun's position in the sky for the observation point is calculated with 30 min. time intervals for a whole year.

C. Collection of Solar Panel Output Data

A 20W, 12V Polycrystalline Silicon solar panel is used and the output characteristics of the panel are measured and recorded. The panel specifications are given in Table I.

TABLE I. SOLAR PANEL PARAMETERS

Panel Size	21.7" x 13.8" x 0.98"
Number of cells and connections	36 (2x18)
Maximum Power (P_{max})	20 W
Maximum Power Voltage (V_{pm})	17.2 V
Maximum Power Current (I_{pm})	1.17 A
Open Circuit Voltage (V_{oc})	21.7 V
Short Circuit Current (I_{sc})	1.25 A

The panel is mounted at 17 m height from sea level on the roof of the Electrical and Electronics Eng. Dept., and is aligned toward South with a tilt angle of 45°. The terminals of the panel are connected to a constant valued resistive load and the output voltage, current and power characteristics are measured and recorded. An electronic circuit is constructed to measure and send the panel output characteristic data to a computer. A microprocessor in the circuit is responsible of these measurements which senses and sends the data to the computer with 1 min. time intervals. A program is developed using C programing language which saves the panel output characteristic data. Hence 1440 sets of panel output voltage, current and power data are recorded for each day.

III. ANALYSIS OF RESULTS

Results of analyses on the sun's position in the sky and effects of that on the incoming solar irradiance to the inclined solar panels and their output powers are discussed in this part. The analyses are based on calculation results and real-time measurement data.

As mentioned before, Electrical and Electronic Eng. Dept., Eastern Mediterranean University, Northern Cyprus ($35^{\circ}8'51''N, 33^{\circ}53'58''E$) is chosen as the observation point. All the calculations and real-time observations are based on this geographical location.

A. Analysis of Solar Radiation Data

As a result of calculations, the monthly average value of the daily extraterrestrial radiation falling on a horizontal surface is obtained using (3). Fig. 1, shows a general overview of the results. As it is obvious from the figure, the highest values belong to June with approximately 11.5 kW/m^2/day. This value is then followed by May and July with almost 11 kW/m^2/day. The monthly average values of Clearness Index, as a measure of atmospheric transparency, are obtained using (4). It is seen that the best amounts belong to June and July for the mentioned observation area.

The monthly average values of daily global, beam and diffuse irradiance falling on a horizontal surface, based on (5) and (6) are shown in Fig. 2. The results show that the value of the global irradiance as a combination of beam and diffuse components reach its maximum with approximately 8 kW/m^2/day in June and July and is then followed by May and August.

Based on the discussed method and according to the calculation results of the incoming irradiance on horizontal surfaces, the irradiance components for tilted panels are calculated using (7) – (17). The values are calculated for the mentioned test panel and the results are shown in Fig. 3.

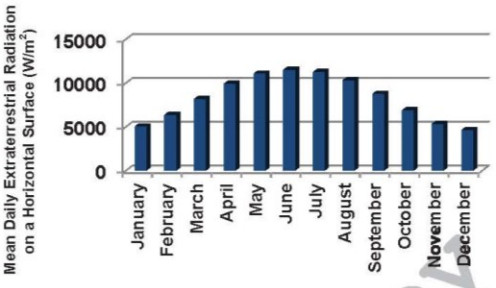

Fig. 1. Monthly Average of Daily Extraterrestrial Radiation on a Horizontal Surface

B. Analysis of the Effects of Sun's Position in the Sky on Panel Output Powers

In this part, the effects of variations in the Sun's position in the sky on the output power generated by a tilted solar panel are analyzed. The panel specifications are given in Table I.

The panel is mounted at 17 m height from sea level at the observation point and the panel power output data is recorded as described in the previous chapter. The data is recorded during a 24 hour time interval in July 3rd, 2012 which represents a clear summer sky with no cloud coverage. The sun's altitude angle and sunlight incidence angle values are also calculated for the same day according to (18) – (24).

The effects of the sun's position in the sky on hourly values of incoming global irradiance on a tilted panel is illustrated in Fig. 4. The hourly values of global solar irradiance are drawn against values of sun's altitude angle and incidence angle of sunlight from 05:30 AM – 18:30 PM for July 3rd, 2012. The calculations of sun's position data are made based on local solar time and the corresponding time for the incoming hourly global irradiance values is the local time at the observation point.

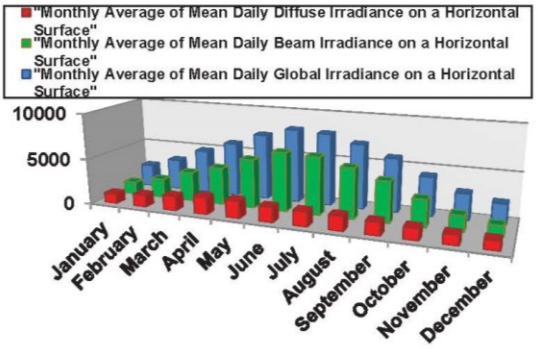

Fig. 2. Monthly Average Values of Solar Radiation Components on a Horizontal Surface

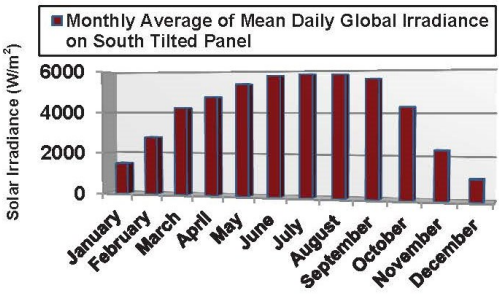

Fig. 3. Monthly Average Values of Mean Daily Solar Radiation Components for South Tilted Solar Panel

The figure shows that the sun`s altitude angle reaches its maximum value at 12:00 (LST) meaning that the sun will be at the maximum height at this time. At the same time the sunlight incidence angle is minimum and indicates that the sunlight rays come to the panel with the closest angle to perpendicular at this time. Taking the difference between the local solar time and local time at the observation point, it is obvious that the hourly values of global irradiance falling on the panel will be maximum with approximately 850 W/m^2 during the same time interval. The results clearly show that there is a direct relation between the sun`s position in the sky and hourly values of global irradiance falling on a tilted panel. According to the results, maximum hourly irradiance is falling on the panel when the sun reaches the maximum altitude and the incidence angle takes its minimum value.

The effects of incoming hourly global solar irradiance on the solar panel output power are also shown in Fig. 5. The data sets belong to July 3rd, 2012. The graphic is showing the variations for 05:30 AM – 18:30 PM. The figure clearly shows that the increasing values of hourly global irradiance have direct effects on the generated power by the solar panel. The output powers reach their maximum at 12:30 PM while the hourly global irradiance falling on the panel has the maximum value at the same time interval. The corresponding time for both panel power outputs and hourly values of global solar irradiance is local time at the observation point.

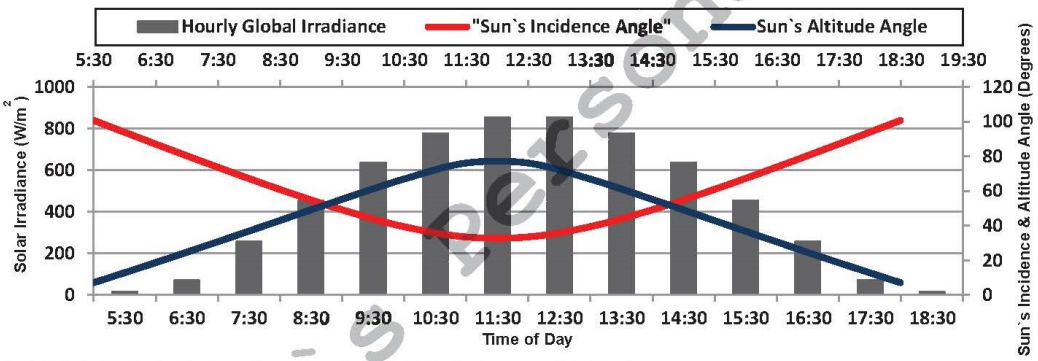

Fig. 4. Effects of Sun`s Position in the Sky on Incoming Global Solar Irradiance on a Tilted Panel

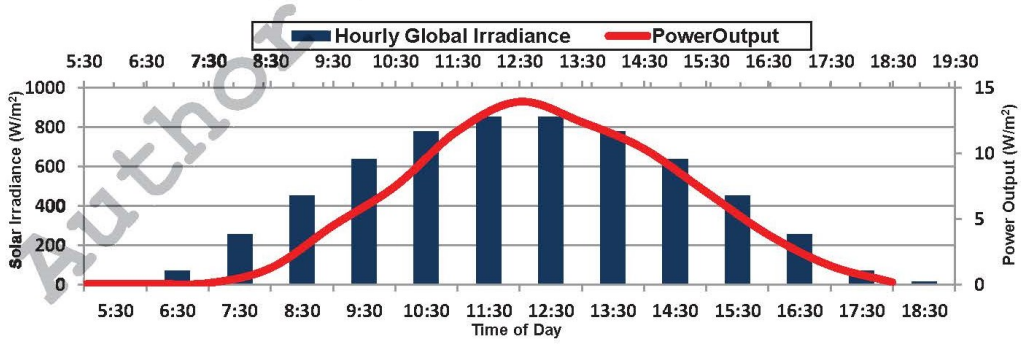

Fig. 5. Effects of Hourly Global Solar Irradiance on Panel Power Output

C. Analysis of the Effects of Sun`s Position in the Sky on Daily Global Radiation

This part of the paper involves analyses and results of the effects of variations in the sun`s position in the sky on monthly average values of daily global solar irradiance falling on a tilted panel during a whole year. For this purpose the effects of variations in sun`s elevation on radiation statistics are analyzed in a figure.

The effects of variations in solar altitude angle on monthly average of daily global irradiance values are shown in Fig. 6. The irradiance data are obtained according to the methods discussed in chapter II. Also the monthly average of sun`s altitude angles at 12:30 PM (LST) is taken into the consideration. The mentioned time interval is chosen because the sun`s altitude takes its maximum value at this time interval and the variations during a year will be clearly visible.

According to the figure it is approved that the increasing rate of sun`s height in the sky during a year has direct effects on the daily values of global solar irradiance. While sun`s altitude reaches its maximum at the same time interval during June and July, the monthly average value of daily global irradiance also takes the maximum value for these months.

As it is clearly visible in Fig. 6, although the sun`s altitude angle has a decreasing rate during July, August and September the monthly average value of daily global irradiance almost remains constant. It is thought that this behavior can be presumed ordinary as the variations between maximum and minimum values of sun`s altitude during each individual day happens in a smaller range compared to those of the previous months.

IV. Conclusions

Having a precise knowledge of the sun`s position in the sky and the incidence angle of sunlight plays an important role during design and preparation of solar energy applications. Also the power yield of solar energy systems directly depends on the irradiance values falling on solar generators. Various methods and equipment for measurement, prediction and estimation of solar irradiance values exist but due to high expenses of measurement equipment and methods, calculation methods of solar irradiance are preferred in some applications.

In this paper a method for calculation of solar radiation data is described and the calculations are made based on 22 year average values provided by NASA. As a result of calculations, the relationship between the sun`s position in the sky and incoming solar irradiance on inclined solar panels is analyzed. The results show that a direct relation exists between the sun`s height and solar angle of incidence and the hourly solar radiation amounts incident at an inclined solar panel at any time interval during a year. Increases in sun`s height cause decreases in solar angle of incidence with respect to perpendicular during each day and cause increases in the incoming values of solar radiation.

Also the relationships between the incoming solar radiation amount to inclined solar panels and the output power generated by the panels are discussed. The results show that increases in hourly solar radiation amounts falling on inclined solar panels as a result of increases in sun`s elevation cause the panel output power values to be increased. This result is valid for any individual day or specific time interval.

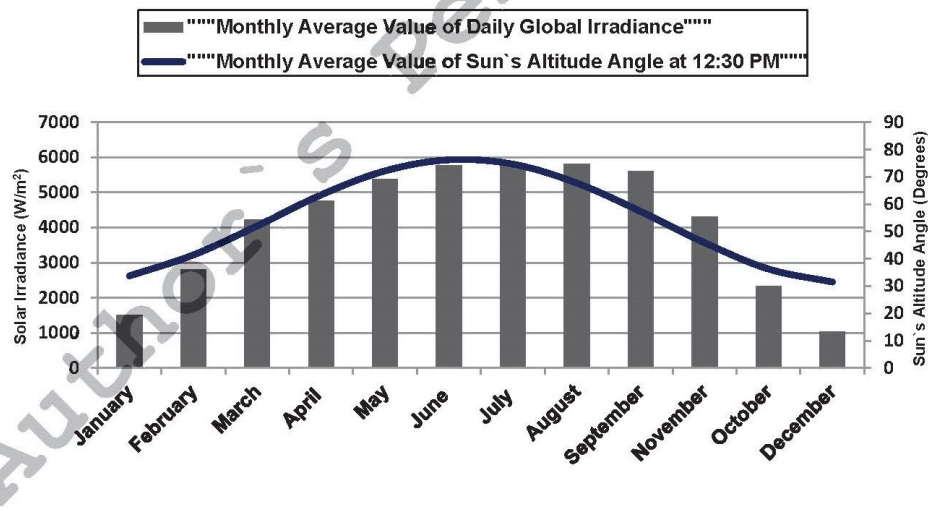

Fig. 6. Effects of Sun`s Altitude on Monthly Average of Global Daily Solar Irradiance

REFERENCES

[1] E.Lorenz, J.Hurka, D.Heinemann and H.G. Beyer, "Irradiance forecasting for power prediction of grid-connected photovoltaic systems," *IEEE J. Sel. Topics Appl. Earth Observations and Remote Sensing*, vol.2, pp.2-10, Mar. 2009.

[2] H. Bulut and O.Büyükalaca, "Simple model for the generation of daily global solar-radiation data in Turkey," *J. Applied Energy*, vol.84, pp.477-491, May 2007.

[3] S.S. Chandel and R.K. Aggarwal, "Estimation of hourly solar radiation on horizontal and inclined surfaces in Western Himalayas," *J. Smart Grid and Renewable Energy*, vol.2, pp.45-55, 2011.

[4] F.S. Tymvios, C.P. Jacovides, S.C. Michaelides, and C.Scouteli, "Comparative study of Angstrom's and artificial neural networks' methodologies in estimating global solar radiation," *J. Solar Energy*, vol.78, pp.752-762, June 2005.

[5] N.Z. Al-Rawahi, Y.H. Zurigat, and N.A. Al-Azri, "Prediction of hourly solar radiation on horizontal and inclined surfaces for Muscat/Oman," *J. Eng. Research*, vol.8, pp.19-31, 2011.

[6] M.Wittmann, H.Breikreuz, M.Schroedter-Homscjeidt, and M.Eck, "Case studies on the use of solar irradiance forecast for optimized operation strategies of solar thermal power plants," *IEEE J. Sel. Topics Appl. Earth Observations and Remote Sensing*, vol.1, pp.18-27, Mar. 2008.

[7] A. Luque and S. Hegedus, *Handbook of Photovoltaics Science and Engineering*, West Sussex, UK : Wiley, 2003, pp.905-933.

[8] K. Schamer, J. Greif, *The European Solar Radiation Atlas Vol.1: Fundamentals and Maps*, Les Presses de l'Ecole des Mines, Paris, 2000, pp.23-42.